The Dissertation Committee for Li Ma Certifies that this is the approved version of the following dissertation:

Textured Thin Metal Shells on Metal Oxide Nanoparticles with Strong NIR Absorbance and High Magnetization for Imaging and Therapy

Committee:

Keith P. Johnston, Supervisor

Marc D. Feldman, Co-Supervisor

Thomas E. Milner

Konstantin V. Sokolov

Charles B. Mullins

Gyeong S. Hwang

Textured Thin Metal Shells on Metal Oxide Nanoparticles with Strong NIR Absorbance and High Magnetization for Imaging and Therapy

by

Li Ma, B.E.; M.E.; M.A.

Dissertation

Presented to the Faculty of the Graduate School of

The University of Texas at Austin

in Partial Fulfillment

of the Requirements

for the Degree of

Doctor of Philosophy

The University of Texas at Austin

December 2010

Dedication

To my wife, son, parents and friends

Acknowledgements

A dissertation for the degree of Doctor of Philosophy is a valuable treasure for human being. The rule of treasure is equal to everybody. You can't take it with you when you leave. Some people think treasure equals to money, others think the real treasure is human being herself. When I look back to see what I have done for this dissertation, I really enjoy the procedure of digging these treasures out of the ground. The procedure of learning is the only important thing to achieve treasures and the degrees. I guess that is why we call this dissertation for Doctor of Philosophy, not Doctor of Chemical Engineering. I am lucky to be able to find these treasures earlier in my life. And I want to share them with you in this dissertation.

I sincerely thank all people who help me discovered the treasures and achieved the goal for my future career. They are my wife Xi Ke, my son Yuntao Ma and my parents who are always patient to support me for every choice I have made. They are my advisor Keith Johnston, who worked with me closely in the past 5.5 years and other advisors or sponsors: Marc Feldman, Thomas Milner, Konstantin Sokolov and Stanislav Emelianov who contributed a lot of time and helpful discussions with me. They are my people, who helped me in the treasure discovery procedure: Ameya Borwankar, Justina Tam, Jasmine Tam, Brian Willsey, Daniel Rigdon, Vidia Paramita, Davis Ingram, Tianyi Wang, Amit Paranjape, Joseph Villard, Kiran Cheruku, Timothy Larson, Travis Jenkins, Min Qu and Mohammad Mehrmohammadi. They are my lab mates, who always sit behind me to support: Andrea Miller, Avinash Murthy, Aileen Dinin, Dan Slanac, Mehul Patel, Xi Chen and Yunsheng Chen.

Gold nanoroses bless the people who deserve.

Textured Thin Metal Shells on Metal Oxide Nanoparticles with Strong NIR Absorbance and High Magnetization for Imaging and Therapy

Publication No._____

Li Ma, Ph.D.

The University of Texas at Austin, 2010

Supervisors: Keith P. Johnston and Marc D. Feldman

The ability of sub 100 nm nanoparticles to target and modulate the biology of cells will enable major advancements in cellular imaging and therapy in cancer and atherosclerosis. A key challenge is to load an extremely high degree of targeting, imaging, and therapeutic functionality into small, yet stable particles. A general mechanism is presented for thin autocatalytic growth on nanoparticle substrates (TAGS), as demonstrated for a homologous series of < 5 nm textured Au coatings on < 42 nm iron oxide cluster cores. Very low Au supersaturation levels are utilized to prevent commonly encountered excessive autocatalytic growth that otherwise produce thick shells. The degree of separation of nucleation to form the seeds from growth is utilized to control the morphology and uniformity of the thin Au coatings. The thin and asymmetric Au shells produce strong near infrared (NIR) absorbance with a cross section of ~10^{-14} m^2, whereas the high magnetic content per particles provides strong r2 spin-spin magnetic relaxivity of 200 $mM^{-1}s^{-1}$. TAGS may be generalized to a wide variety of

substrates and high energy coatings to form core-shell nanoparticles of interest in a variety of applications as diverse as catalysis and bionanotechnology.

High uptake of the nanoclusters by macrophages is facilitated by the dextran coating, producing intense NIR contrast both in cell culture and an in vivo rabbit model of atherosclerosis. A novel conjugation technique further allows covalent binding of anti-epidermal growth factor receptor (EGFR) monoclonal antibody (Ab) to the nanoclusters for highly selective targeting to EGFR over expressing cancer cells. AlexaFluor 488 tagged Ab nanocluster conjugates were prepared to correlate the number of conjugated Abs with the hydrodynamic diameter. The high targeting efficacy was evaluated by dark field reflectance imaging and atomic absorbance spectrometry (AAS). Colocalization of the nanoparticles by dual mode in-vitro imaging with dark field and fluorescence microscopy demonstrates the Abs remained attached to the Au surfaces. The extremely high curvature of the Au shells with features below 5 nm influence the spacing and orientations of the Abs on the surface, which has the potential to have a marked effect on biological pathways within cells. These targeted small multifunctional nanoclusters may solve some key molecular imaging challenges for cancer and atherosclerosis.

Table of Contents

List of Tables

List of Figures

Chapter 1: Introduction

1.1 APPLICATION OF MULTIFUNCTIONAL NANOCLUSTERS

Gold plasmonic nanostructures are receiving great attention as contrast agents for molecular optical imaging of tissue by optical coherence tomography (OCT)[1, 2], photoacoustic tomography[3-5], reflectance microscopy[6, 7] and two-photon luminescence[8] in atherosclerosis and cancer. The depth of light penetrates deeper in the near infrared (NIR) region (700–850 nm), where soft tissue, hemoglobin and water are the most transparent[9]. The surface plasmon resonance (SPR) of gold undergoes a red shift into the NIR region in confined geometries including nanoshells[2, 10, 11], nanorods[12, 13], nanocages[1] and aggregates of gold primary particles[6, 7, 14]. Antibody conjugated gold nanospheres have been assembled by cancer receptors to form aggregates with high NIR contrast for precancerous versus normal cells[6, 7].

However, all of them have intrinsic problems based on absorbance effectiveness in NIR, toxicity, size and stability. For example, gold nanospheres do not have a strong surface plasmon resonance peak in NIR region[7]. Further, the large size (over 100 nm) of typical NIR gold nanoparticles leads to short circulation times with i.v. injection, because of removal by the liver and spleen[15]. Further, to synthesize high quality gold nanorods, a strong capping ligand cetyl trimethylammonium bromide (CTAB) and a mediation agent $AgNO_3$ are often used, but these agents can be toxic and cannot be easily removed from the surface of the nanorods[16, 17] limiting their application to patients. Similar toxicity considerations are present in the synthesis of nanoparticles composed of a silica core with a gold shell, where (3-aminopropyl)-triethoxysilane (APTES) and tetrakis (hydroxymethyl) phosphonium chloride are commonly used as capping ligands to

functionalize the intermediate surfaces[18, 19]. Finally, the porous Au nanocages contain some Ag which can lead to toxicity in cell culture[1, 20].

We have fabricated thin gold coated iron oxide nanoclusters, called "nanoroses". The multifaceted surfaces tuning their absorption of light into the NIR region for both cellular imaging and photothermal therapy, where both applications minimize competition from surrounding cells and tissue to allow both diagnostics and therapy to be more selective. There are few examples that we are aware of where nano-composites for medical applications serve the dual role of diagnostics and therapy[5, 21-23]. Non-toxic or low toxic materials have been used to compose nanoroses. And the comprehensive purification processes ensure the residues from reactions will not present in the final products.

The application of NIR absorbing nanoparticles in biomedical imaging not only depends on the particle scattering or absorption cross-section, but also on cell uptake rate determined by nanoparticle size and surface coating[24-27]. For instance, we have coated the nanorose with dextran since macrophages pose dextran receptors. We have also developed the nanorose to be less than 50 nm in diameter, since particles in this small size range have minimum uptake by the liver and spleen. Therefore, a prolonged life time in blood stream maximizes the uptake of nanorose by macrophages associated with cancers and vulnerable plaques.

Inflammatory macrophages are an important early cellular marker that indicate and contribute to increased risk of plaque rupture in the coronary, cerebral, and peripheral circulations. Activation and recruitment of macrophages in “vulnerable” plaques can induce breakdown of a thin fibrous cap, decrease mechanical stability, and increase the risk of plaque rupture by local production of MMPs. Further, greater macrophage density is associated with increased plaque vulnerability[28, 29]. Thus, the selective targeting of

macrophages inside “vulnerable” plaques by nanoparticles can help to detect and visualize such type of plaques. The preliminary histological results showed the high sensitivity of proposed nanoparticles, nanoroses, to “vulnerable” atherosclerotic plaques because of the primary uptake of nanorose by live inflammatory macrophages. Meanwhile, other plaque constituents did not show considerable uptake of nanoroses; above all, affected inflammatory macrophages released the taken nanoroses after the apoptosis. Tumor associated macrophages also play important role in promoting tumor growth, invasion, metastasis, and angiogenesis[30-33]. Macrophage targeting via administration of NIR sensitive nanoparticles may enhance diagnosis and therapy for both these conditions.

Nanorose has a great potential to serve as a magnetic resonance imaging (MRI) contrast agent due to its high ratio of embedded magnetic materials, iron oxide, and excellent surface modification ability. MRI techniques are widely used in radiology to visualize the structure and function of the body. It provides detailed images of the body in any plane. The hydrogen nuclei (protons) found in abundance in the human align with the strong main magnetic field in MRI. A second electromagnetic field, which oscillates at radio frequencies and is perpendicular to the main field, is then pulsed to push a proportion of the protons out of alignment with the main field. These protons then drift back into alignment with the main field, emitting a detectable radiofrequency signal. Since protons in different tissues of the body realign at different speeds, the different structures of the body can be revealed. Contrast agents may be injected intravenously to enhance the appearance of blood vessels, tumors or inflammation. The relaxivity of MRI contrast agents depends on the molecular structure and kinetic of the complex. To increase the number of water molecules that are in the inner sphere of the complex, or to

slow down the molecular rotational correlation time, are possibilities to improve the water relaxivity[34].

Optical imaging yields excellent spatial resolution and is inexpensive, robust and portable, but it has limited penetration depth, field of view. MRI provides exceptional anatomic information and depth of imaging, but it suffers from limited spatial resolution. A combination of MRI and optical imaging can lead to the development of new approaches that will bridge the gaps in resolution and depth of imaging between these two modalities[22] For example, contrast agents consisting of conjugates of iron oxide particles and NIR fluorescent dye Cy5.5 were used for detection of enzymatic activity in lymph nodes in vivo[35]. The iron oxide portion was used to determine distribution of the contrast agent and the optical fluorescent moiety was used as a reporter of microenvironment.

1.2 OBJECTIVES

1.2.1 Control of the size and shape of nanoroses

The small particle size of the nanorose enhances transport rates in extracellular fluid, and within cells[36]. It also minimizes rapid clearance by the reticuloendothelial system, like liver or spleen[15, 26], especially with the flexible hydrophilic polyvinylalcohol (PVA) coating. We will lower the size of the nanorose by modifying the ratio of gold to iron oxide, as well as the initial concentrations of iron oxide nanoparticles, dextran, and reducing agent. Based on our extensive experimental studies, we have found some key factors which can affect the size and distribution of nanorose in the cluster formation process. The variation in the compositions of the reactants and reducing agents will

influence the nucleation and growth kinetics of the gold shells and the clustering of the primary particles to influence the final particle size and polydispersity. Previously, ~60 nm Au-coated magnetic iron oxide nanoparticles were formed with a molar Au:Fe precursor ratio of 2 after the first iteration[23]. In our study, the much smaller Au:Fe ratio 0.1 after all of the iterations led to slower reduction and a much smaller primary iron oxide-gold domains, on the order of 7-10 nm. A tunable ratio of Au to iron oxide cores can change the size of nanorose for both optical and magnetic properties. The dextran chains are known to coat only a fraction of the iron oxide surface, leaving exposed regions for the growth of the gold shells. The high concentration of dextran in the reaction will add more restriction to growth of the nanorose, therefore smaller sizes are usually achieved. But if the concentration is too high, the gold precursors are prevented from coating the iron oxide nanoparticles. Thus, depending on our applications, we can tune the size and iron ratio of nanoroses by changing the reactant ratios.

1.2.2 Synthesis antibody conjugated nanorose for targeted delivery

Molecular-specific imaging with spherical gold nanoparticles has been used to label epithelial cancer receptors on the surface of cells as well as in the intracellular imaging of actin dynamics[37]. Selective photothermal therapy to treat cancer cells has also been achieved using nanoshells, nanorods and spherical nanoparticles[1, 12, 13, 18]. Probes for recognition and targeting can include small peptides, antibodies and antibody fragments. Antibodies (Abs) are among the most widely used of these recognition moieties due to their high affinity and availability for a large number of established biomarkers. A critical step in the synthesis of molecular specific nanoparticles is the conjugation of probe molecules to nanoparticles.

We will synthesize molecular-specific nanorose bioconjugates to target epidermal growth factor receptors (EGFR) on the surface of cancer cells. The conjugates can be delivered to the cancer cells topically and imaged noninvasively with dark field microscope with NIR long pass filter in real time. We can evaluate the nanorose targeting efficiency and kinetics in vitro by optimizing the conjugated Ab numbers per nanorose to achieve a high delivery. The gold surfaces of nanoparticles will be functionalized as reported conjugation chemical reactions with dithiolaromatic PEG6-hydrazide as a linker[7, 21, 22, 37](Fig. 1.1 and Fig. 1.2). The dithiol group on one end of the linker will form covalent bonds with gold surface. The hydrazide group on the other end of the linker will react with the aldehyde group on the antibody's Fc region.

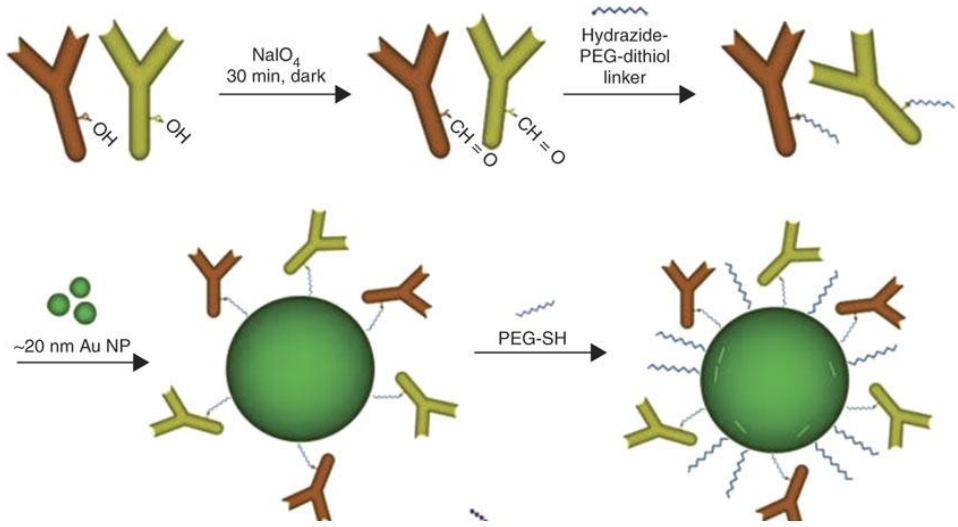

Figure 1.1 Schematic of the antibody conjugation to gold nanoparticle

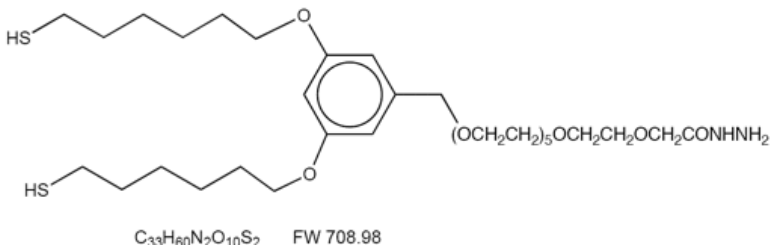

Figure 1.2 Structure of the dithiol linker with a hydrazide group on end

The numbers of antibodies that are conjugated to the nanoparticles can be verified using the following procedure. (i) Label antibodies with fluorescent dye using a standard labeling kit, for example, Alexa Fluor 360 or 594 (Invitrogen). (ii) Then, determine a linear calibration curve that relates the concentration of a fluorescently labeled antibody and fluorescence intensity. (iii) After attachment of fluorescently labeled Abs to gold nanoparticles, centrifuge the nanoparticles and measure fluorescence from the supernatant at the excitation emission wavelengths of the dyes that were used to tag each antibody. (iv) Use the calibration curves to determine the concentration of each antibody in the supernatant. Subtract these values from the initial concentrations to obtain the amount of antibody that is attached to nanoparticles.

There are several challenges to make these bioconjugated nanoroses. First, the surfaces of nanoroses have been partially covered with dextran molecules. But the thiol group of the linker can form a much stronger covalent bond with gold than the polar groups on dextran with gold. So we think the chances for these dithiol linkers to successfully compete with dextran molecules are very high. Second, after the antibody is attached, an additional stabilizer may be needed to provide steric stabilization. Based on our previous experiences, PVA can also serve as a good stabilizer for these antibody

conjugated nanoroses in water. Some other stabilizers have been reported with HS-gold binding, like PEG-SH (MW 5,000) or glutathione. Third, the special shape of nanorose brings in variable curvatures on the surface of gold shells. The binding strength of antibodies to different nanorose domains may change depending on curvatures. And the spatial configuration of these antibodies can have different effects on the attachment efficiency to the cells. These effects need to be characterized based on binding reaction kinetics and cell imaging techniques.

The targeted binding efficiency between Anti-EGFR conjugated nanoroses and cancer cell lines can be visualized by dark field (DF) microscope with long pass filters in the NIR reign, since cells are most transparent in NIR while nanoroses have very strong reflectance. The contrast enhancement of the nanoroses has been shown in our studies for the nanorose labeled macrophages. And the quantified binding rate can be achieved by doing elemental analysis with atomic absorption spectroscopy (AAS).

How cells interact with nanostructures at the molecular level remains poorly understood. Jiang et al [24] found the binding of gold nanospheres in the 2-100 nm size range to the membrane receptors strongly depends on nanoparticle size. Gratton et al[38] reported the internalization of specially designed, monodisperse hydrogel particles into HeLa cells as a function of size, shape, and surface charge. There are several papers on gold nanoparticle size and shape effects on the delivery into cancer cells[13, 24, 38]. For nanoroses, since the high curvatures on the primary particles on the nanorose surfaces are very different from large 50-100 nm spherical nanoparticles[23]. The nanorose offer many interesting shapes that may influence interactions of conjugated Abs with cell membranes. The interaction of the Abs on the curved surface with the receptors on the cell membranes may vary with curvature in ways that are currently poorly understood. Furthermore, two Abs near each other on the curved surfaces may increase strongly the

binding with the receptors[24, 38]. We are expecting to find some favorable features for cancer cell targeting related to particle surface curvatures and Ab binding density. We are going to compare different size nanoroses with nanospheres to see the relations between surface curvature and antibody binding. We will use well defined cancer cell line to deliver these nanoparticles with know antibody densities. The kinetics of the binding reaction can be monitored by UV-vis spectrometry. The remaining surface of Au will be passivated by mPEG-SH with different molecular weight. An optimum size, shape, antibody density, and surface coatings have to be investigated, so that the maximum nanorose delivery efficiency will be achieved.

1.3 DISSERTATION OUTLINE

Chapter 2 of the dissertation reported the ~30 nm stable uniformly-sized near infrared active, superparamagnetic nanoclusters (nanoroses) formed by kinetically controlled self-assembly of gold-coated iron oxide nanoparticles. The controlled assembly of nanocomposite particles into clusters with small primary particle spacings produces collective responses of the electrons that shift the absorbance into the NIR region. Despite only 12% by weight polymeric stabilizer, the particle size and NIR absorbance change very little in deionized water over 8 months. High uptake of the nanoclusters by macrophages is facilitated by the dextran coating, producing intense NIR contrast in dark field and hyperspectral microscopy, both in cell culture and an *in vivo* rabbit model of atherosclerosis. The experimental results show the ability of 20 to 50 nm nanoparticles to target macrophage cells will enable major advancements in cellular imaging and therapy in cancer and atherosclerosis. This chapter is primarily written by me with intensive discussions with Dr. Johnston, Dr Feldman and Dr Milner.

Chapter 3 presented a general mechanism for thin autocatalytic growth on nanoparticle substrates (TAGS) as demonstrated for a homologous series of < 5 nm textured Au coatings on 42 nm iron oxide cores. Very low Au precursor supersaturation levels are utilized to prevent commonly encountered thick shells due to excessive autocatalytic growth. The degree of separation of nucleation to form the seeds from growth is utilized to control the morphology and uniformity of the unusually thin Au coatings. The thin shells with high degrees of asymmetry shift the surface plasmon resonance to the NIR, with large extinction coefficients, even for particles with total hydrodynamic diameters less than 60 nm. This chapter is primarily written by me with intensive discussions with Dr. Johnston. Ameya Borwankar and Brian Willsey acquired some experimental data with analysis.

Chapter 4 extended TAGs mechanism to make a wide range of morphologies of Au shells on 42 nm iron oxide cluster cores, namely thin (5 nm) or thick (20-40 nm) smooth shells or thick (10-40 nm) knobby shells by tuning the nucleation and growth in the presence of a polymeric stabilizer. For high nucleation rates at high pH, Au seeds were deposited on a higher fraction of the iron oxide substrate particles leading to thinner coatings. At low pH values, slower nucleation led to less separation between nucleation and autocatalytic growth and, consequently, Au seeds on fewer particles, and thicker coatings. The knobby protrusions on the surface introduce high asymmetry and high aspect ratios that shift the SPR of Au into the NIR with strong extinction coefficients. This chapter is primarily written by me and Ameya with intensive discussions with Dr. Johnston. Ameya Borwankar and Brian Willsey acquired some experimental data with analysis.

Chapter 5 introduced a novel conjugation technique allowing covalent binding of anti-epidermal growth factor receptor (EGFR) monoclonal antibody (Ab) clone 225 to

the nanoclusters to realize highly selective targeting to EGFR over expressing cancer cells. AlexaFluor 488 tagged clone 225 nanocluster conjugates were prepared to correlate the number of conjugated antibodies with the hydrodynamic size of the naoclusters. For 1 to 74 Abs on a nanorose surface, the correlated hydrodynamic diameters varied from 35 to 78 nm, as measured by dynamic light scattering. A transition from sub-monolayer to multilayer aggregates of Abs on the nanoparticle surface was observed for 54 Abs and an overall particle diameter of 63 nm. The targeting efficacy of the conjugated nanoclusters was evaluated by the A431 cancer cell uptake characterized by atomic absorbance spectrometry. Dual mode in-vitro imaging studies with dark field reflectance microscopy and fluorescence microscopy demonstrate that these multifunctional nanoclusters may be used as NIR and fluorescent contrast agents for 'theranostisc' of EGFR expressing cancer cells. This chapter is primarily written by me with intensive discussions with Dr. Johnston. Justina Tam helped to acquire some experimental data with analysis.

1.4 REFERENCES

1. Skrabalak, S. E.; Chen, J.; Au, L.; Lu, X.; Li, X.; Xia, Y., Gold Nanocages for Biomedical Applications. *Advanced Materials (Weinheim, Germany)* **2007,** 19, 3177-3184.

2. Adler, D. C.; Huang, S.-W.; Huber, R.; Fujimoto, J. G., Photothermal Detection of Gold Nanoparticles Using Phase-Sensitive Optical Coherence Tomography. *Optics Express* **2008,** 16, 4376-4393.

3. Wang, Y.; Xie, X.; Wang, X.; Ku, G.; Gill, K. L.; O'Neal, D. P.; Stoica, G.; Wang, L. V., Photoacoustic Tomography of a Nanoshell Contrast Agent in the in Vivo Rat Brain. *Nano Letters* **2004,** 4, 1689-1692.

4. Shah, J.; Park, S.; Aglyamov, S.; Larson, T.; Ma, L.; Sokolov, K.; Johnston, K.; Milner, T.; Emelianov Stanislav, Y., Photoacoustic Imaging and Temperature Measurement for Photothermal Cancer Therapy. *Journal of biomedical optics* **2008,** 13, 034024.

5. Mallidi, S.; Larson, T.; Aaron, J.; Sokolov, K.; Emelianov, S., Molecular Specific Optoacoustic Imaging with Plasmonic Nanoparticles. *Optics Express* **2007,** 15, 6583-6588.

6. Sokolov, K.; Follen, M.; Aaron, J.; Pavlova, I.; Malpica, A.; Lotan, R.; Richards-Kortum, R., Real-Time Vital Optical Imaging of Precancer Using Anti-Epidermal Growth Factor Receptor Antibodies Conjugated to Gold Nanoparticles. *Cancer Research* **2003,** 63, 1999-2004.

7. Aaron, J.; Nitin, N.; Travis, K.; Kumar, S.; Collier, T.; Park, S. Y.; Jose-Yacaman, M.; Coghlan, L.; Follen, M.; Richards-Kortum, R.; Sokolov, K., Plasmon Resonance Coupling of Metal Nanoparticles for Molecular Imaging of Carcinogenesis in Vivo. *Journal of Biomedical Optics* **2007,** 12, 034007/1-034007/11.

8. Wang, H.; Huff, T. B.; Zweifel, D. A.; He, W.; Low, P. S.; Wei, A.; Cheng, J.-X., In Vitro and in Vivo Two-Photon Luminescence Imaging of Single Gold Nanorods. *Proceedings of the National Academy of Sciences of the United States of America* **2005,** 102, 15752-15756.

9. Weissleder, R., A Clearer Vision for in Vivo Imaging. *Nature Biotechnology* **2001,** 19, 316-317.

10. Hirsch, L. R.; Stafford, R. J.; Bankson, J. A.; Sershen, S. R.; Rivera, B.; Price, R. E.; Hazle, J. D.; Halas, N. J.; West, J. L., Nanoshell-Mediated near-Infrared Thermal Therapy of Tumors under Magnetic Resonance Guidance. *Proceedings of the National Academy of Sciences of the United States of America* **2003,** 100, 13549-13554.

11. Loo, C.; Lowery, A.; Halas, N.; West, J.; Drezek, R., Immunotargeted Nanoshells for Integrated Cancer Imaging and Therapy. *Nano Letters* **2005,** 5, 709-711.

12. Huang, X.; El-Sayed, I. H.; Qian, W.; El-Sayed, M. A., Cancer Cell Imaging and Photothermal Therapy in the near-Infrared Region by Using Gold Nanorods. *Journal of the American Chemical Society* **2006,** 128, 2115-2120.

13. Pissuwan, D.; Valenzuela, S. M.; Killingsworth, M. C.; Xu, X.; Cortie, M. B., Targeted Destruction of Murine Macrophage Cells with Bioconjugated Gold Nanorods. *Journal of Nanoparticle Research* **2007,** 9, 1109-1124.

14. Khlebtsov, B.; Zharov, V.; Melnikov, A.; Tuchin, V.; Khlebtsov, N., Optical Amplification of Photothermal Therapy with Gold Nanoparticles and Nanoclusters. *Nanotechnology* **2006,** 17, 5167-5179.

15. Brannon-Peppas, L.; Blanchette, J. O., Nanoparticle and Targeted Systems for Cancer Therapy. *Advanced Drug Delivery Reviews* **2004,** 56, 1649-1659.

16. Connor, E. E.; Mwamuka, J.; Gole, A.; Murphy, C. J.; Wyatt, M. D., Gold Nanoparticles Are Taken up by Human Cells but Do Not Cause Acute Cytotoxicity. *Small* **2005,** 1, 325-327.

17. Nikoobakht, B.; El-Sayed, M. A., Preparation and Growth Mechanism of Gold Nanorods (Nrs) Using Seed-Mediated Growth Method. *Chemistry of Materials* **2003,** 15, 1957-1962.

18. O'Neal, D. P.; Hirsch, L. R.; Halas, N. J.; Payne, J. D.; West, J. L., Photo-Thermal Tumor Ablation in Mice Using near Infrared-Absorbing Nanoparticles. *Cancer Letters (Amsterdam, Netherlands)* **2004,** 209, 171-176.

19. Pham, T.; Jackson, J. B.; Halas, N. J.; Lee, T. R., Preparation and Characterization of Gold Nanoshells Coated with Self-Assembled Monolayers. *Langmuir* **2002,** 18, 4915-4920.

20. Skrabalak, S. E.; Au, L.; Li, X.; Xia, Y., Facile Synthesis of Ag Nanocubes and Au Nanocages. *Nature Protocols* **2007,** 2, 2182-2190.

21. Aaron, J. S.; Oh, J.; Larson, T. A.; Kumar, S.; Milner, T. E.; Sokolov, K. V., Increased Optical Contrast in Imaging of Epidermal Growth Factor Receptor Using Magnetically Actuated Hybrid Gold/Iron Oxide Nanoparticles. *Optics Express* **2006,** 14, 12930-12943.

22. Larson, T. A.; Bankson, J.; Aaron, J.; Sokolov, K., Hybrid Plasmonic Magnetic Nanoparticles as Molecular Specific Agents for Mri/Optical Imaging and Photothermal Therapy of Cancer Cells. *Nanotechnology* **2007,** 18, 325101/1-325101/8.

23. Lyon, J. L.; Fleming, D. A.; Stone, M. B.; Schiffer, P.; Williams, M. E., Synthesis of Fe Oxide Core/Au Shell Nanoparticles by Iterative Hydroxylamine Seeding. *Nano Letters* **2004,** 4, 719-723.

24. Jiang, W.; Kim, B. Y. S.; Rutka, J. T.; Chan, W. C. W., Nanoparticle-Mediated Cellular Response Is Size-Dependent. *Nature Nanotechnology* **2008,** 3, 145-150.

25. Ferrari, M., Beyond Drug Delivery. *Nature Nanotechnology* **2008,** 3, 131-132.

26. Choi, H. S.; Liu, W.; Misra, P.; Tanaka, E.; Zimmer, J. P.; Ipe, B. I.; Bawendi, M. G.; Frangioni, J. V., Renal Clearance of Quantum Dots. *Nature Biotechnology* **2007,** 25, 1165-1170.

27. Chithrani, B. D.; Ghazani, A. A.; Chan, W. C. W., Determining the Size and Shape Dependence of Gold Nanoparticle Uptake into Mammalian Cells. *Nano Letters* **2006,** 6, 662-668.

28. Libby, P., Inflammation in Atherosclerosis. *Nature (London, United Kingdom)* **2002,** 420, 868-874.

29. Jaffer, F. A.; Libby, P.; Weissleder, R., Molecular and Cellular Imaging of Atherosclerosis: Emergency Applications. *Journal of the American College of Cardiology* **2006,** 47, 1328-1338.

30. Kimura, Y. N.; Watari, K.; Fotovati, A.; Hosoi, F.; Yasumoto, K.; Izumi, H.; Kohno, K.; Umezawa, K.; Iguchi, H.; Shirouzu, K.; Takamori, S.; Kuwano, M.; Ono, M., Inflammatory Stimuli from Macrophages and Cancer Cells Synergistically Promote Tumor Growth and Angiogenesis. *Cancer Science* **2007,** 98, 2009-2018.

31. Allavena, P.; Sica, A.; Solinas, G.; Porta, C.; Mantovani, A., The Inflammatory Micro-Environment in Tumor Progression: The Role of Tumor-Associated Macrophages. *Critical reviews in oncology/hematology* **2008,** 66, 1-9.

32. Biswas, S. K.; Sica, A.; Lewis, C. E., Plasticity of Macrophage Function During Tumor Progression: Regulation by Distinct Molecular Mechanisms. *Journal of Immunology* **2008,** 180, 2011-2017.

33. Nardin, A.; Abastado, J.-P., Macrophages and Cancer. *Frontiers in Bioscience* **2008,** 13, 3494-3505.

34. Hayat, M. A., Cancer Imaging. In Academic Press: 2007.

35. Josephson, L.; Kircher, M. F.; Mahmood, U.; Tang, Y.; Weissleder, R., Near-Infrared Fluorescent Nanoparticles as Combined Mr/Optical Imaging Probes. *Bioconjugate Chemistry* **2002,** 13, 554-560.

36. Reddy, S. T.; Swartz, M. A.; Hubbell, J. A., Targeting Dendritic Cells with Biomaterials: Developing the Next Generation of Vaccines. *Trends in Immunology* **2006,** 27, 573-579.

37. Kumar, S.; Harrison, N.; Richards-Kortum, R.; Sokolov, K., Plasmonic Nanosensors for Imaging Intracellular Biomarkers in Live Cells. *Nano Letters* **2007,** 7, 1338-1343.

38. Gratton, S. E. A.; Ropp, P. A.; Pohlhaus, P. D.; Luft, J. C.; Madden, V. J.; Napier, M. E.; De Simone, J. M., The Effect of Particle Design on Cellular Internalization Pathways. *Proceedings of the National Academy of Sciences of the United States of America* **2008,** 105, 11613-11618.

Chapter 2: Small Multifunctional Nanoclusters (Nanoroses) for Targeted Cellular Imaging and Therapy

The ability of 20 to 50 nm nanoparticles to target and modulate the biology of specific types of cells will enable major advancements in cellular imaging and therapy in cancer and atherosclerosis. A key challenge is to load an extremely high degree of targeting, imaging, and therapeutic functionality into small, yet stable particles. Herein we report ~30 nm stable uniformly-sized near infrared (NIR) active, superparamagnetic nanoclusters formed by kinetically controlled self-assembly of gold-coated iron oxide nanoparticles. The controlled assembly of nanocomposite particles into clusters with small primary particle spacings produces collective responses of the electrons that shift the absorbance into the NIR region. The nanoclusters of ~70 iron oxide primary particles with thin gold coatings display intense NIR (700 - 850 nm) absorbance with a cross section of $\sim 10^{-14}$ m^2. Because of the thin gold shells with an average thickness of only 2 nm, the r2 spin-spin magnetic relaxivity is 200 $mM^{-1}s^{-1}$, an order of magnitude larger than observed for typical iron oxide particles with thicker gold shells. Despite only 12% by weight polymeric stabilizer, the particle size and NIR absorbance change very little in deionized water over 8 months. High uptake of the nanoclusters by macrophages is facilitated by the dextran coating, producing intense NIR contrast in dark field and hyperspectral microscopy, both in cell culture and an *in vivo* rabbit model of atherosclerosis. Small nanoclusters with optical, magnetic and therapeutic functionality, designed by assembly of nanoparticle building blocks, offer broad opportunities for targeted cellular imaging, therapy, and combined imaging and therapy.

2.1 INTRODUCTION

Clinical imaging and/or therapy with multifunctional nanoparticles that target specific types of cells has the potential to transform health care in cancer, atherosclerosis and other diseases. When the nanoparticle diameters are reduced to 20 to 50 nm, the biological pathways in targeted cells can undergo profound changes.[1-5] Small nanoparticles, the size of small viruses, permeate barriers more rapidly including cell membranes and leaky vasculature in cancers. The efficacy of vaccines may be enhanced with ultrasmall 20 nm nanoparticles that can diffuse to the lymph nodes to target resident dendritic cells.[3] Multifunctional ultrasmall paramagnetic iron oxide particles (USPIO) particles (~30 nm) have been designed to detect and deliver chemotherapeutic agents directly into prostate cancer cells.[4] Antibody functionalized spherical gold particles target membrane receptors much more efficiently and modulate a variety of cell functions including cell death, as the size is reduced to 40-50 nm.[1, 2] Finally, prolonged circulation in the bloodstream (slow clearance by the liver and spleen) for small nanoparticles facilitates magnetic resonance imaging (MRI) contrast for imaging atherosclerosis and imaging of lymph nodal metastases in cancer.[5,6]

New opportunities in cellular optical imaging and therapy in intact tissues have been spawned by nanoparticles including gold nanoshells, nanorods, and nanocages with absorbances 10^3 fold those of organic dyes.[7-12] For these particle geometries, the surface plasmon resonance (SPR) peak of gold shifts to the NIR region (700 and 850 nm) where soft tissue, hemoglobin and water absorb weakly. Alternatively, gold nanospheres bioconjugated with antibodies have been assembled by cancer receptors to form NIR-active gold aggregates.[13, 14] Multifunctional imaging further provides complimentary

anatomic, functional, and molecular information at the cellular level needed to advance therapy. For example, the location of iron oxide nanoparticles may be imaged with MRI *in vivo*, while simultaneously detecting enzymatic activity in lymph nodes with NIR fluorescence upon subcutaneous injection.[15] Furthermore, multifunctional nanoparticles may be utilized for combined optical/MRI molecular imaging and photothermal therapy of cancer cells, and for molecular-specific optical image contrast enhancement using magnetic modulation.[16, 17]

A major challenge in nanotechnology and nanomedicine is to devise robust and broadly applicable synthetic strategies to pack sufficient multifunctionality into nanoparticles smaller than ~50 nm. The high surface energy of the nanoparticles make it challenging to control the geometry and composition, and furthermore, to maintain the structure and functional properties in physiological media or *in vivo*. The shapes and compositions of nanoparticles may be guided during condensation of atoms by selectively favoring growth of particular crystal facets to produce spheres, rods, wires, discs, cages, core-shell structures and many other shapes. [8, 10, 12, 18] A less common yet highly adaptable approach is to assemble ultrasmall spherical nanoparticles as the primary building blocks, rather than atoms, into 1D, 2D and 3D inorganic/organic nanocluster composites.[19-22] The size and shape of 3D composite nanoclusters have been controlled with block copolymer templates, DNA, proteins and viruses, primarily for the design of sensing and memory devices.[20] However, the sizes of the clusters have been well above 50 nm in nearly all cases, or the degree of functionality has been limited, because of the need for a large amount of templating and stabilizing agents. These agents have been required to control particle growth and to provide stability.

Herein, we demonstrate that primary iron oxide nanoparticles with thin gold coatings may be assembled into very stable ~30 nm nanoclusters with intense functionality, despite only a small amount of polymeric stabilizers. Unlike most previous studies of 3D clusters, the nanoparticle building block incorporates two inorganic materials, iron oxide and gold, rather than one, to provide multifunctionality. The nanoclusters composed of ~70 iron primary particles display intense NIR (700 - 850 nm) absorbance and r2 magnetic relaxivity (>200 $mM^{-1}s^{-1}$) in solution and strong optical contrast in targeted macrophages. The small average size and relatively low polydispersity of the nanoclusters are achieved by kinetic control of self-assembly, as a function of the iron oxide nanoparticle concentration and gold: iron oxide ratio, in the presence of dextran stabilizer. The intense optical and magnetic properties of the nanoclusters far exceed the values of the constituents.[23] The intense NIR absorbance is described in terms of the close proximity of the thin and asymmetric gold coatings on the primary nanoparticles. Sufficiently small spacing between the primary particles needed for the enhanced optical and magnetic properties is favored by the small concentration of dextran stabilizer on the starting primary iron oxide particles. The small size of the nanoclusters and the dextran surface coating are shown to facilitate high uptake by macrophages, which contain dextran receptors.[6] The high uptake and intense NIR absorbance are shown to provide high NIR contrast in dark field and hyperspectral microscopy, both in cell culture and an *in vivo* rabbit model of atherosclerosis. These properties are also utilized for photothermal destruction of nanocluster-laden macrophages.

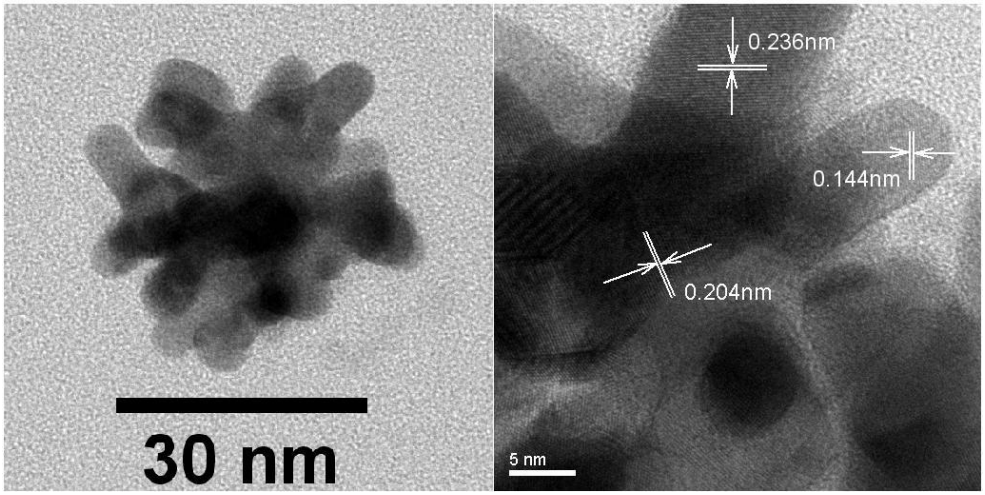

(a)

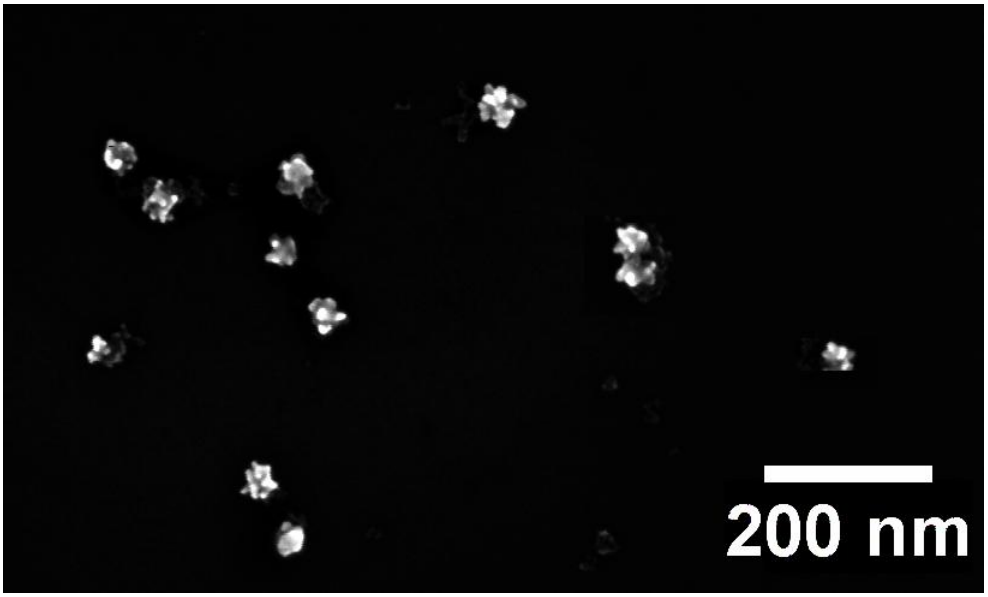

(b)

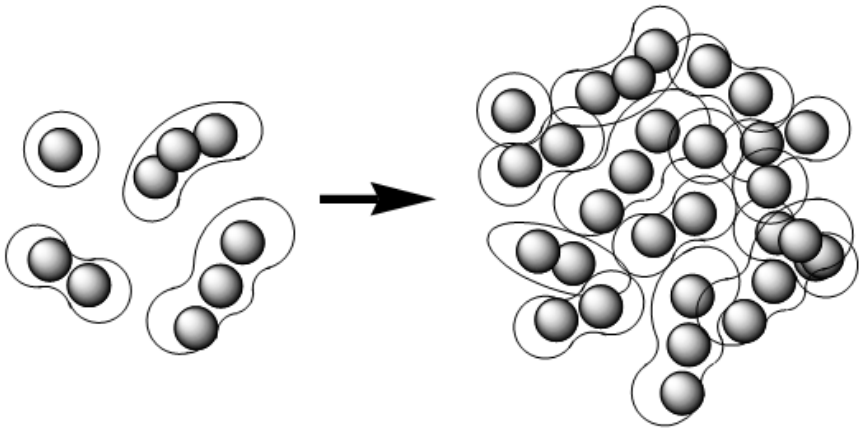

(c)

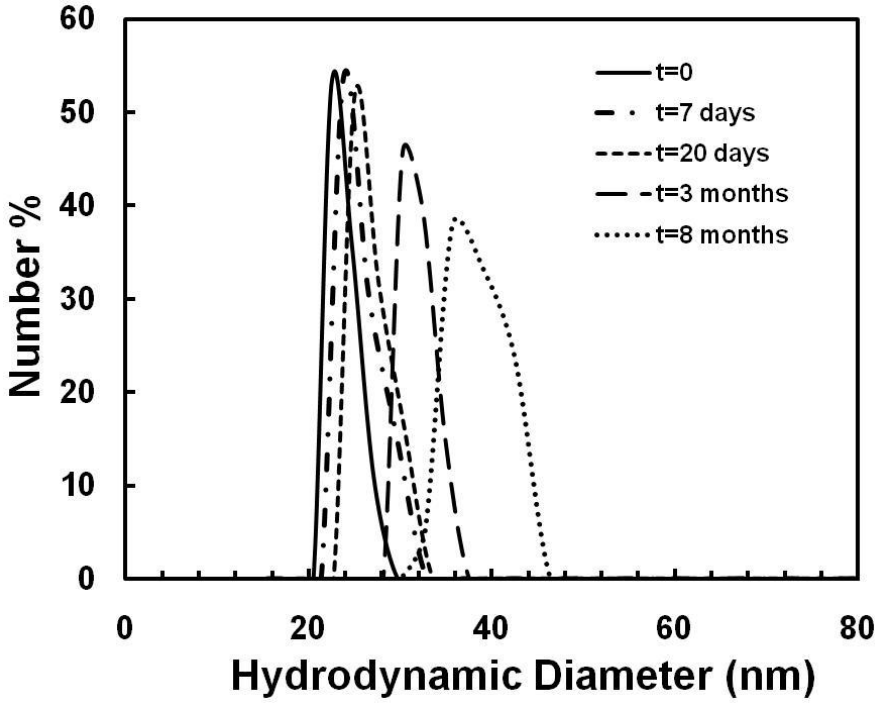

(d)

Figure 2.1 Size, shape and colloidal stability of nanoclusters (nanoroses) in deionized (DI) water. (a) High resolution transmission electron microscopy (TEM) images on an ultra thin carbon film substrate reveal an open nanocluster of iron oxide@Au primary core-shell particles. The most prevalent lattice spacing is found to be 0.236 nm for the (1 1 1) plane of Au. The (2 0 0) and (2 2 0) planes are also indicated. (b) Scanning electron microscopy (SEM) image of dried nanoroses on silicon wafer. (c) Schematic of

nanocluster of gold-coated iron oxide primary particles. (d) Hydrodynamic diameter in water from dynamic light scattering starts at 25 nm, and the small change in size up to 8 months at 4 ^{o}C indicating high colloidal stability.

2.2 RESULTS AND DISCUSSION

2.2.1 Synthesis, Structure and Stability

Nanoclusters were formed by the reduction of $HAuCl_4$ onto the surfaces of 5 nm iron oxide nanoparticles with hydroxylamine as a seeding agent. We will call these particular particles "nanoroses" to distinguish them from more general types of nanoclusters, and also to emphasize their intense properties, analogous to a rose's vibrant color.[20] The hydroxylamine adsorbs on the iron oxide particle surface and favors selective formation of gold on the iron oxide surface rather than in bulk solution.[24] Previously, ~ 60 nm Au-coated magnetic iron oxide nanoparticles without NIR absorbance were formed with a molar Au:Fe precursor ratio of 2:1 after the first iteration.[24] In our study, a much smaller Au:Fe ratio 1:10 by mole after all of the iterations led to much thinner gold domains. The dextran molecules on the iron oxide surface helped prevent the gold domains from growing too thick during reduction. The reaction resulted in ~30 nm relatively open clusters composed of much smaller primary particle domains. The primary domains are more easily discerned near the periphery in the TEM images (Figure 2.1a), but are somewhat masked towards the center, where the electrons pass through a much thicker cross-section. Because the gold shells are darker than the iron oxide cores in the TEM, and the cluster geometry is rather complex, it is not feasible to observe the shells directly.[25] The thickness of the gold shells may be estimated by subtracting the known 5 nm diameter of the iron oxide cores (Figure S1) from the size of the ~7-10 nm primary domains, as has been done previously.[25] The resulting shell

thickness is ~ 1 to 2.5 nm, and from the non-spherical shape of the primary domains, appears to vary along the surface of a given iron oxide core, as is the case for "nanoeggs" with asymmetric egg whites [26]

The gold coatings on iron oxide cores increase the attractive van der Waals forces between particles, given the much larger Hamaker constant for Au versus iron oxide. The balance of these attractive forces and the steric stabilization provided by dextran, along with the iron oxide and gold precursor concentrations, resulted in kinetic control of the cluster size with a relatively low polydispersity shown by dynamic light scattering (DLS) (Figure 2.1d). The small hydrodynamic diameter of the nanorose in DI water ranged from 23 ± 3 nm and 34 ± 2 nm over 7 separate experiments (Table 2.S1 in supporting information) The relatively low polydispersities of these clusters is also evident by SEM (Figure 2.1b). It changed relatively little, with an average of only 33 nm over 3 months and 39 nm in 8 months as shown in Figure 2.1d. Thus, the iron oxide cores helped prevent growth of gold domains and the dextran and PVA provided effective steric stabilization. The total polymer concentration was only 12% according to thermal gravimetric analysis (TGA), in contrast with larger amounts typically needed in block copolymer templated clusters.[20] In contrast, aggregation of gold nanoparticles by variation of surface charge in a recent study led to large micron-sized 3-D assemblies with NIR absorption.[27]

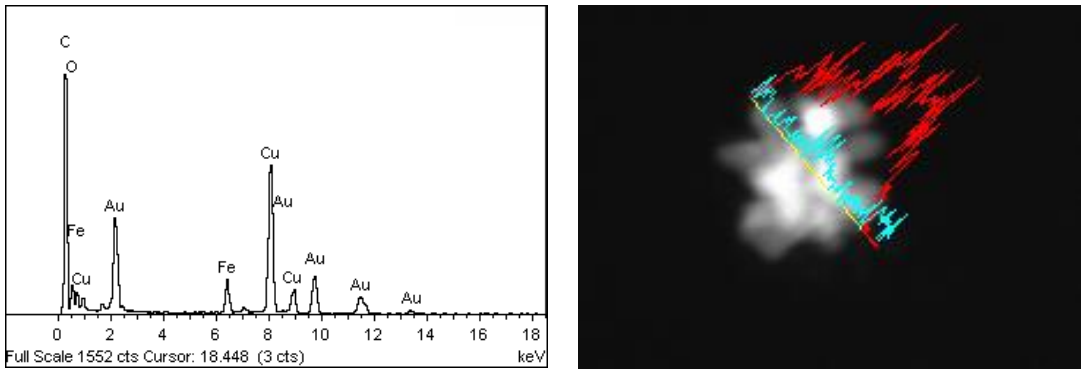

(a) **(b)**

Figure 2.2 Energy dispersive spectroscopy area scan and line scan coupled with STEM from one nanorose. STEM and EDS were performed on a field emission JEOL2010F transmission electron microscope equipped with an Oxford INCA EDS system. EDS line scan was performed with the microscope in STEM mode at 200kV accelerating voltage. C and Cu peaks are from TEM sample grid (Cu) and ultrathin carbon substrate. Red intensity is from Au and blue intensity is from Fe.

A variety of measurements indicate that the oligomeric domains that formed the nanoclusters in Figure 2.1a contained primary iron oxide cores, as depicted schematically in Figure 2.1c. An energy dispersive x-ray spectroscopy (EDS) line scan across the particle that shows Fe was present throughout the cluster diameter (Figure 2.2). This observation is consistent with the hydroxylamine seeded growth of gold on the iron oxide surface rather than that of pure gold particles. EDS measurements of 20 nanorose particles indicate that the Au:Fe mass ratio varied from 5:1 to 9:1, as shown in Figure 2.2. Smaller ratios of 3:1 to 4:1 were determined from flame atomic absorption spectroscopy (FAAS) as a consequence of the excess iron oxide particles (without gold coatings) in the dispersion, which were also seen by TEM in the very light particles near the nanorose surfaces in Figure 2.1a. If all of the iron oxide particles were coated with a uniform gold shell, the thickness for a 1:10 Au:Fe ratio would be less than 0.2 nm, which would not be possible. The gold nuclei grew on only a fraction of the iron oxide particles, and then

further growth of gold was favored on these Au sites. The nucleation of gold took place over a relatively small time period, given the relatively low polydispersity in the final cluster size. The calculated number of primary iron oxide particles for a 35 nm nanorose was approximately 70, from the molar Au:Fe ratio determined by EDS and the assumption that the occupied volume within an effective spherical nanorose (with diameter equivalent to the end-to-end distance) was approximately 50% (Supporting information).

2.2.2 Optical and magnetic properties in solution

The broad NIR absorbance of a colloidal nanorose dispersion shown in Figure 2.3 is relevant to tissue imaging and light-based therapy, and drops only 5% at 800 nm from the maximum at 730 nm. Colloidal and optical stability of the nanorose may be attributed to prevention against growth or collapse of the gold domains by the iron oxide cores and polymer stabilizers for both the primary domains and the external surfaces of the clusters. For a dispersion with 32 μg Au/ml, as determined by FAAS in Figure 2.3a, the extinction coefficient at the maximum absorbance (730 nm) was 0.025 $cm^2/\mu g$ Au. The original dispersion was diluted to this concentration to obtain an absorbance maximum in the range of 0.5 to 1. Assuming that gold occupies 50% of the volume of a nanorose with an end-end distance based on Figure 2.1a, the dispersion in Figure 2.3a contained 10^{10} nanoroses per ml and thus a particle extinction cross section $\sigma_{755\ nm} \sim 10^{-14}\ m^2$. Similar particle cross sections were observed for nanocages, nanorods and nanoshells.[12, 28] The nanorose extinction cross section at 755 nm is 6 orders of magnitude larger than that of freshly prepared indocyanine green dissolved in NaCl aqueous buffer solution ($1 \times 10^{-20}\ m^2$ at 778 nm), which has been investigated as a NIR dye for laser photothermal therapy.[29, 30]

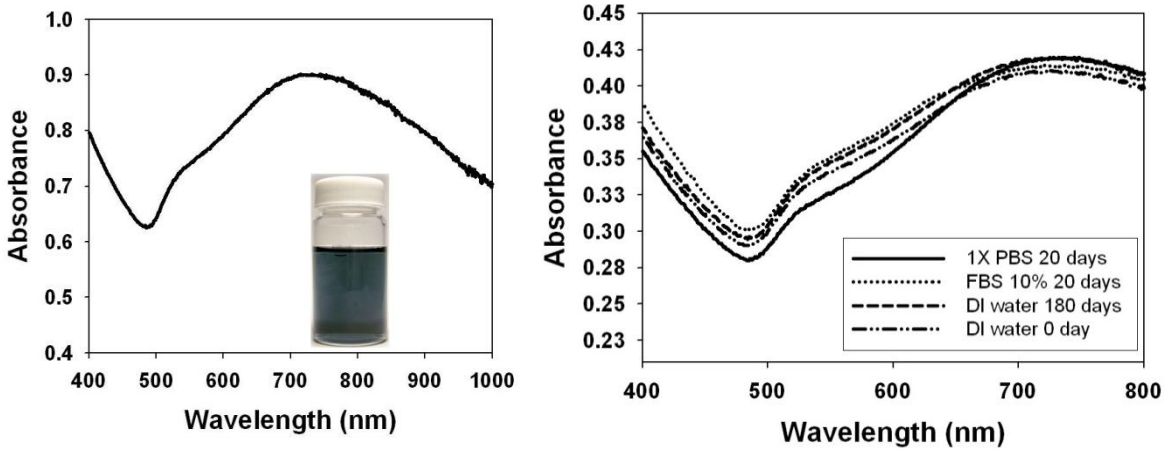

(a) **(b)**

Figure 2.3 UV-Vis-NIR absorbance spectra of colloidal nanorose dispersions in various media. **(**a) The blue dispersion in the inset indicates a strong absorbance in NIR region for 32 μg/ml gold, as quantified by the spectra with 1 cm path length. (b) A similar strong NIR absorbance was observed in DI water, 1× PBS solution and a DMEM supplemented with 10% FBS cell culture media, which was stable for ~180 days storage at 4 ^{o}C. The optical stability was consistent with the small change in size according to DLS in Figure 2.1d.

A further examination of the nanorose shape will now be used to explain the marked red shift in the SPR from 532 nm for a single spherical gold particle. For a single core-shell particle of gold on silica, the thickness of the shell to the core diameter must be in the range of 5 % to shift the SPR to 900 nm, according to Mie theory.[31, 32] For an average Au coating thickness of 0.7 nm on 5 nm diameter Fe_3O_4, the experimental SPR maximum shifted only to 600 nm, consistent with the above theoretical prediction.[25] Small red shifts were also observed for 1 nm gold shells on 10 nm diameter Fe_3O_4.[33] For our 5 nm iron oxide cores, a ~ 0.3 nm shell thickness would be required for an absorbance at 900 nm. Such thin shells of Au on iron oxide have not been reported. In

our study, thin gold layers with an average thickness of ~1 to 2.5 nm were observed. A uniform shell of this thickness on a single 5 nm iron oxide core would be too thick to produce this large SPR red shift.[8, 34] Instead, the red shift was caused by (1) collective responses of the electrons in the gold coatings on the closely-spaced primary particles within the clusters and (2) asymmetry in the thickness of the gold coatings on each particle. An analogous type of red shift has been observed for multiple spherical gold particles in close proximity.[14, 31, 35] In Figure 2.1a, short oligomers of primary particles (sub-clusters) are evident in the shape of relatively high aspect ratio rods or bent rods containing kinks where the particles touch, as indicated in the schematic in Figure 2.1c. The high aspect ratio of these rods contributes to the SPR red shift more strongly than in the case of a dense spherical cluster composed of uniformly spaced primary particles.[28, 31] The close approach of the primary particles coated with dextran is favored by the very low volume fraction of hydrated dextran in the shell (see supplemental section) of 24% in the original iron oxide particles. A red shift would also be produced by differential thickness of the shells on a given particle at various locations on the surface, as has been observed for nanoeggs and nanocups with off-centered cores.[26, 36] This shift results from reduced symmetry of the interactions between plasmon modes. The very thin shells in the nanorose primary particles are likely to exhibit these types of eccentric geometries, although it is difficult to distinguish between the iron oxide and gold by TEM for the complex cluster geometry.

A knowledge of the contribution of absorption versus scattering for the nanoclusters is important for understanding various optical imaging applications. A direct optical properties measurement technique was used to measure the absorption and scattering cross section of the nanorose dispersion with an integrating sphere.[37, 38]

Absorption coefficient and scattering coefficient were computed using equations (1) and (2):

$$\mu_a = \frac{1}{x}\frac{S_{a0} - S_a}{S_{a0}} \quad (1)$$

$$\mu_s = \frac{1}{x}\frac{S_s}{S_{s0}} \quad (2)$$

where xis the sample thickness (80 μm) and S_{a0} and S_a are the measured absorption radiant power with DI water and nanorose solution, respectively. The absorption cross section is given by μ_a divided by the number density. Samples were prepared at six nanorose concentrations (385, 193, 96, 77, 39 and 26 μg Au/ml) with corresponding nanorose number densities of 1.2×10^{11}, 0.6×10^{11}, 0.4×10^{11}, 0.24×10^{11}, 0.12×10^{11} and 0.08×10^{11} nanoroses/ml, respectively. For these concentrations, the absorption coefficient μ_a = 29.3, 19.2, 10.3, 7.6, 4.2 and 2.9 cm^{-1}, and the corresponding averaged absorption cross section $\sigma_a = (3.1 \pm 0.5) \times 10^{-14}$ m^2 were computed according to the six nanorose concentrations. Data suggest the scattering cross section (σ_s) is much smaller than the absorption cross section and beyond the sensitivity of measurements. According to Mie theory, the contribution from absorption relative to scattering increases for spheres as the diameter decreases, and for nanoshells as the shell thickness decreases, consistent with our results for extremely small and thin gold shells.[28] Experimentally, this behavior has been observed for nanocages with a decrease in the particle size.[12] The strong absortion for very small gold domains is beneficial for imaging techniques such as optical coherence tomography and photoacoustic spectroscopy and for photothermal therapy.[7, 8, 39]

The normalized saturation magnetization at 300 K was 34 emu/g Fe_3O_4 as measured by a superconducting quantum interference device (SQUID) magnetometer (Quantum Design MPMS) as shown in Figure 2.4a. To convert from magnetization per

total mass of particles to a basis of per mass of Fe_3O_4, the mass ratio of Au:Fe was 3:1 as determined by FAAS, and the polymer amount was 12% as determined by TGA. The magnetization approached the value of 39 emu/g Fe_3O_4 (54 emu/g Fe) for the original 5 nm iron oxide nanoparticles, indicating little interference from the gold coating. For single crystal Fe_3O_4, the saturation magnetization increased with an increase in size from 4 to 12 nm, as the loss from the surface effect decreased.[40, 41] In our case, the spins in adjacent primary iron oxide particles were not close enough to raise the mass magnetization over that of the individual primary particles, as has been seen previously for sub-100 nm polymer-coated iron oxide nanoparticles.[42]

The r2 transverse relaxivity measured with the 3.0 T MRI was 219 $mM^{-1}s^{-1}$ (Figure 2.4b) comparable to the high value obtained for solid iron oxide spheres formed in organic solvents at elevated temperatures. [40] This r2 value was over twice those typically obtained for iron oxide spherical particles, including Feridex I.V. (AMAG Pharmaceuticals, Inc.) approved for clinical use by the FDA.[40] Water protons experience an inhomogeneity in the external field produced by the local magnetic field gradient about the superparamagnetic iron oxide particles.[43] This gradient produces dephasing of the proton spins and increases the r2 relaxation rate. The r2 increases upon nanoparticle assembly into clusters that raise the cross-sectional area.[41, 43] For single crystal Fe_3O_4 nanoparticles, the increase in mass magnetization with an increase in size from 4 to 12 nm produces an increases r2.[40] However, the relationship between the cluster geometry and r2 is not well understood theoretically for complex cluster geometries, as in the case of nanorose.[23, 41, 43, 44] The high r2 is favored by the porous structure of the nanoclusters and the thin gold coatings (< 3 nm) that result in short distances between iron oxide surfaces and water molecules, which favor high local inhomogenities in the magnetic field. For more typical iron oxide particles with gold

shells thicker than 5 nm, the r2 is about an order of magnitude lower.[16] It is also enhanced by the iron oxide particles without gold coatings associated with the clusters that pack closely together. The higher r2 value for the nanorose relative to Feridex I.V. is manifested in improved negative contrast (lower T2 values and darker images) in MR imaging, as shown in Figure 2.4c. Furthermore, the images become darker with an increase in nanoparticle concentration.

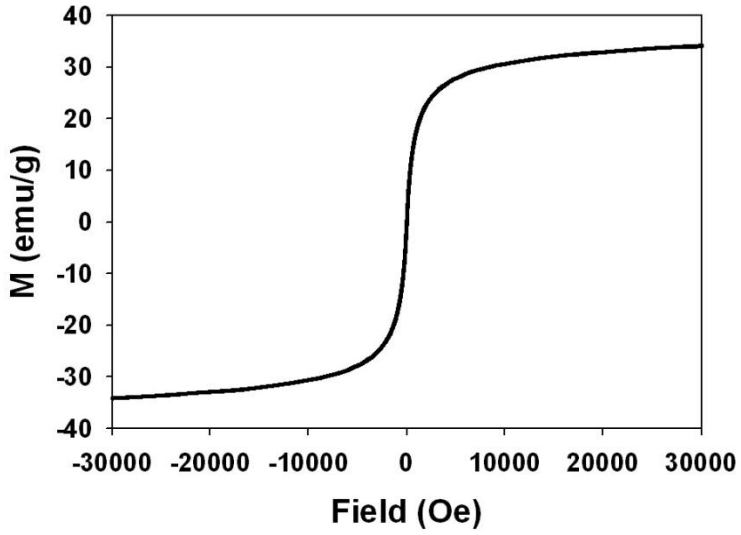

(a)

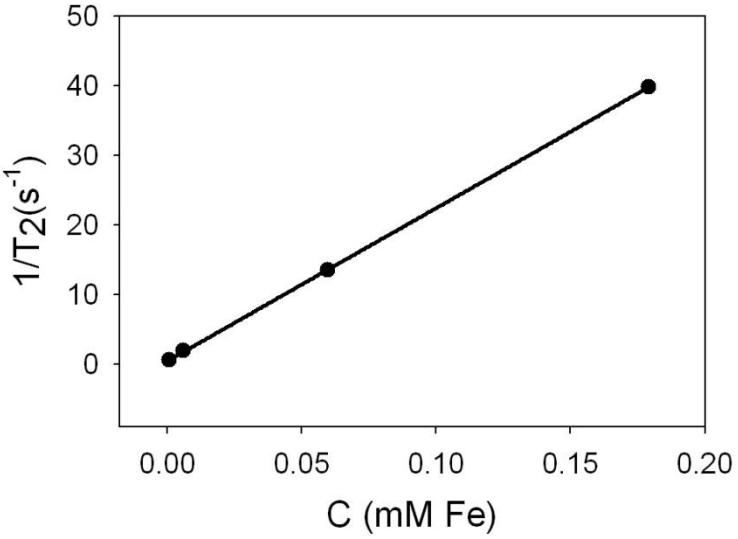

(b)

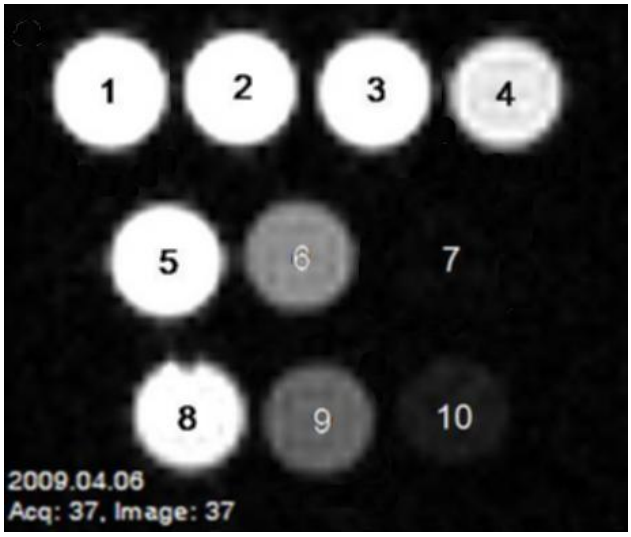

(c)

Figure 2.4 (a) Normalized nanorose magnetization per gram of Fe_3O_4vs field strength at 300K. (b) Reciprocal spin-spin relaxation time T_2 vs iron concentration in water. Relaxivity value (r_2) of 219 $mM^{-1}s^{-1}$ was determined from the slope. (c) A T2-weighted magnetic resonance fast spin echo images of syringes containing solutions of Feridex I.V. and nanorose in phosphate buffer saline and blood. Concentrations are based upon iron content. Tube: 1) Saline; 2-4) 1.75, 17.5 and 52.5 μg Fe/mL Feridex in saline; 5-7) 1.75, 17.5 and 52.5 μg Fe/mL nanorose in saline; 8-10) 1.75, 17.5 and 52.5 μg Fe/mL nanorose in blood. At equivalent iron concentrations, these results are consistent with Nanorose inducing shorter relaxation time than Feridex.

The nanorose clusters exhibit intense single- and multi-functionality whereby the NIR absorbance and magnetic relaxivity increase markedly upon assembly of the cluster, relative to the initial ~5 nm primary particles. Similarly-sized virus capsids in nature, are also assemblies of ~5 nm particles (proteins) with intense functionality. In the case of virus capsids and templated synthetic nanoclusters, the clusters are highly ordered assemblies of nanoparticles, in contrast with the disordered nanorose.[20] For nanorose, the disorder makes the cluster design and synthesis simpler and more adaptable, since templating agents such as block copolymers, DNA or proteins are not needed.

2.2.3 Cell Targeting, Imaging and Photothermolysis

Macrophages are implicated in every stage of atherosclerosis from lesion initiation to plaque rupture and clinical presentation.[45, 46] Tumor associated macrophages also play an important role in promoting tumor growth, invasion, metastasis, and angiogenesis.[47-50] Macrophage targeting via administration of NIR sensitive nanoparticles may enhance diagnosis and therapy for both these conditions. The targeted uptake of nanorose for enhancement of cellular imaging and also photothermolysis was investigated with primary peritoneal macrophages, which were isolated from C57/BL6 mice. These mice can develop the M2 phenotype associated with cancer.[51] We incubated 10^5 cells with nanorose in culture media for 24 hours. In Figure 2.5, for 10 μg Au/ml dose, the brown domains inside the cell under phase contrast mode (40 × objective lens) shows an extensive distribution of nanoroses. In the dark field mode, 610 to 800 nm light was reflected by nanorose-labeled macrophages producing strong contrast, relative to the unlabeled control.

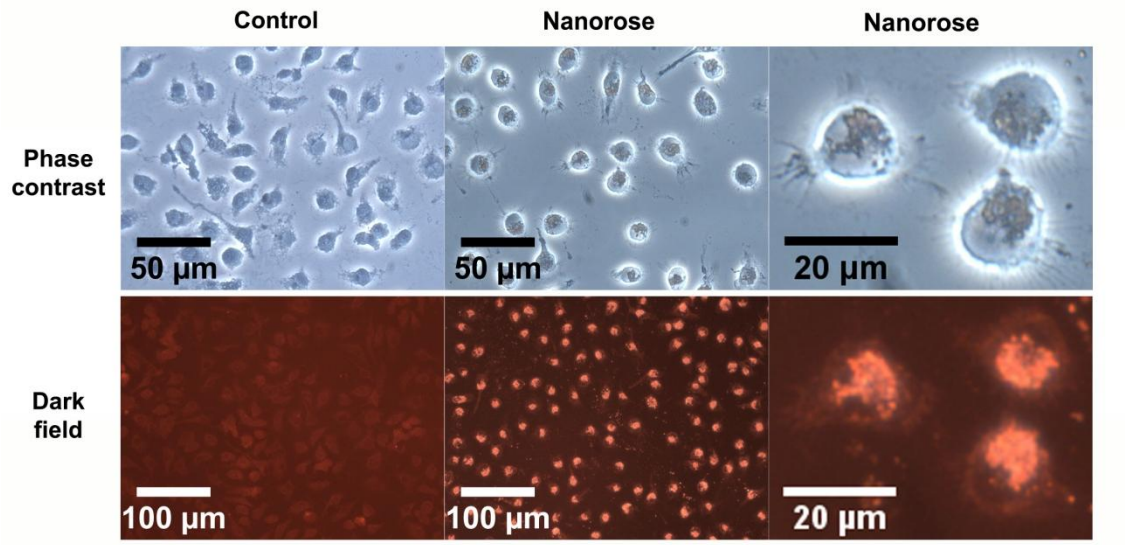

Figure 2.5 Phase contrast and dark field microscopy images of macrophages labeled with nanorose in DMEM supplemented with 10% FBS media. The left panels do not include nanoroses. The middle and right panels at two different levels of magnification include nanoroses at 10 µg Au/ml. The darkfield reflectance images (20× objective lens) included a 610 nm long pass filter in the path of illumination. All images were recorded with Xe lamp illumination.

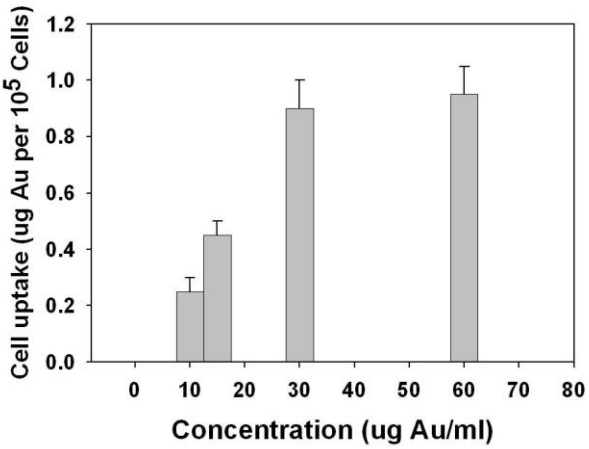

Figure 2.6 Strong uptake of nanoroses by macrophages as determined by flame atomic absorption spectroscopy for 10^5 cells.

A high optical contrast for labeled macrophages for a relatively low nanorose dose requires high cellular uptake and a strong absorbance cross-section per nanorose cluster. As shown in Figure 2.6 for a concentration of only 30 μg Au per ml culture media, the uptake reached saturation at 10^4 nanoroses per cell for 10^5 macrophages. This uptake level is far above the minimum value of a few hundred required to discriminate between nanorose-labeled versus unlabeled macrophages under dark field microscopy with a 40× objective lens. The optical densities, $\log_{10}$ (I_0/I_{sample}), of nanorose-loaded macrophages, were collected with a PARISS hyperspectral imaging instrument (Lightform, Inc.) in transmission bright field mode with a halogen illuminator (see supporting information). For the three nanorose concentrations indicated, 10^5 macrophages were incubated with nanoroses in DMEM culture medium supplemented with 10% FBS for 24 hours (Figure 2.7). A pronounced increase in absorbance was observed over this concentration range reaching 0.6 indicating the potential for high NIR contrast for optical imaging despite the relatively low nanorose dose.

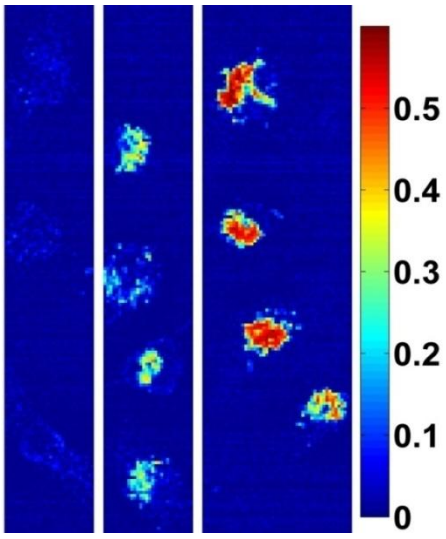

Figure 2.7 Hyperspectral microscopy images illustrating strong absorbance at 755 nm for nanorose in macrophages *in vitro*. The legend provides a color code for the optical density values up to 0.6. From left to right, macrophages were incubated with nanoroses (0.0, 1.0 and 10 μg Au per ml media) for 24 hours. Area averaged spectra on the same macrophages are shown in supporting information Figure 2.S3.

The high NIR absorbance of the nanorose may benefit photothermal cancer therapy of tumors containing macrophages. The macrophages were cultured in phenol-free DMEM plus 10% FBS media at 37 ℃ in 5% CO_2 for 24 hours before they were treated with nanoroses. In Figure 2.8, a monolayer of macrophages, which had engulfed nanoroses, was irradiated with a Q-switched alexandrite laser for a single 755 nm pulse of 50 ns duration and a 2 mm spot size providing a fluence of 18 J/cm^2. A HgCdTe infrared detector was used to measure the temperature after irradiation. Immediately after irradiation, Figure 2.8c shows a 0.7 ^{o}C increase over the 2 mm spot, indicating strong absorbance by the nanorose. The measured temperature increase represents an average value over the effective aperture at the air-cell interface. The actual temperature increase immediately adjacent to the small nanorose cluster is substantially larger and localized to a small volume. Outside yet close to the edge of the beam, macrophage cells in a bright field image (Supporting information Figure 2.S4) were stained brown indicating TUNEL positivity caused by heating. Identical laser irradiation without nanorose results in no change in phenotype and absence of TUNEL positivity. This positivity with nanorose present may suggest apoptosis, which would be of interest in the treatment of atherosclerosis and other macrophage-associated pathologies.

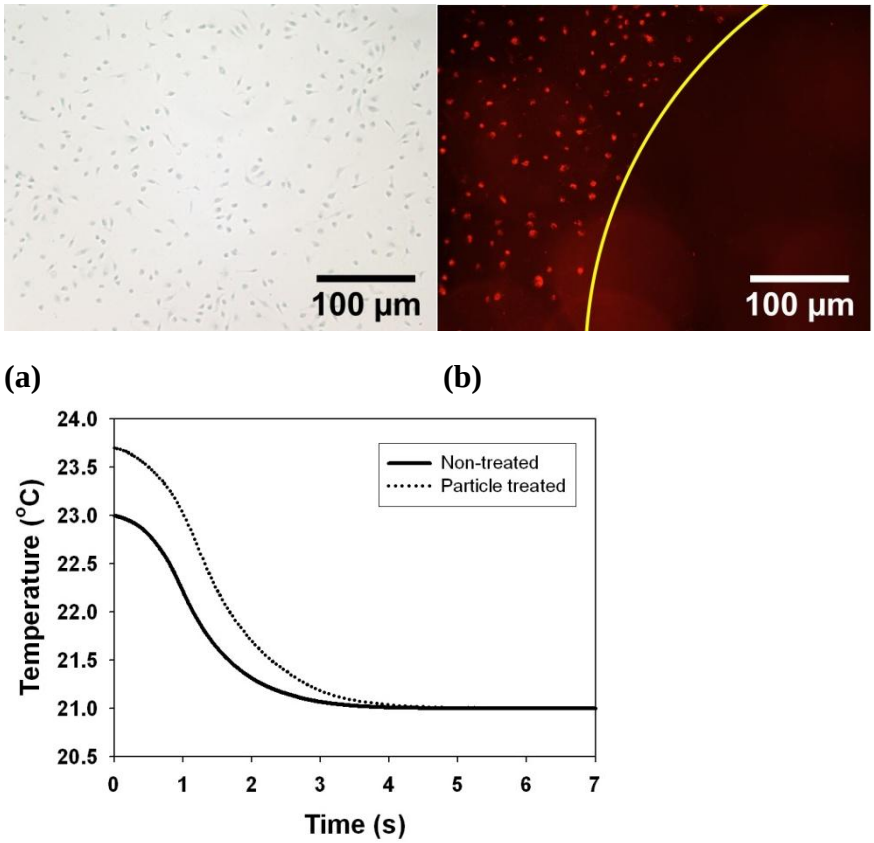

Figure 2.8 Laser photothermolysis of macrophages *in vitro* with a single 50 ns pulse at 755 nm at a fluence of 18 J/cm^2. (a) After irradiation without nanorose, a brightfield image with TUNEL staining indicates the macrophage membranes were intact. (b) After irradiation with nanorose, a darkfield image shows a zone of macrophage photothermolysis coincident with the laser beam. (c) Radiometric temperature following pulse radiation over an area with 2 mm diameter.

2.2.4 Macrophage Cell Uptake Specificity

To evaluate the specificity of targeting of macrophage cells associated with atherosclerosis, the uptake of nanorose among three major cell types including macrophages, endothelial cells (EC) and smooth muscle cells (SMC) in the aorta was evaluated. All cell lines were first allowed to reach confluence in LabTek chamber slides

(Supporting information). Each cell type was then treated with 1 μg/mL nanorose in 10% FBS DMEM/ endothelial cell (EC) growth media for 4 hours. Control samples were not treated with nanorose. After 4 hours of treatment all samples were washed 3 times with PBS and fixed in 5% formaldehyde.

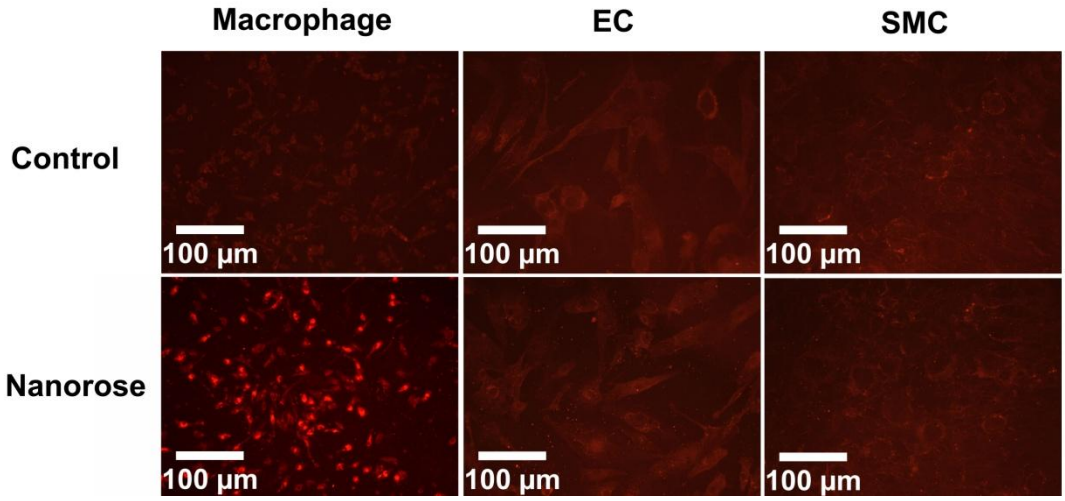

Figure 2.9 Specificity of nanorose into macrophages versus aortic endothelial cells and aortic smooth muscle cells by dark field microscopy with a 610 nm long pass filter. The top row is a control without incubation of nanorose. In the bottom row, the bright spots indicate NIR reflectance from nanorose in macrophage cells, at wavelengths above 610 nm, which is not evident for the other cells.

According to Figure 2.9, the dextran coated nanorose particles were taken up much more aggressively by macrophages than either aortic smooth muscle cells or aortic endothelial cells. The structures of the cells are shown in greater detail by dark field imaging without a filter in the supporting information (Figure 2.S5). This specificity is the basis for the following imaging experiments in macrophage cells associated with an atherosclerotic rabbit aorta.

2.2.5 Atherosclerotic Rabbit Aorta Imaging

Macrophage targeting and imaging may be used to enhance diagnosis and therapy of atherosclerosis. We performed *in vivo* cellular imaging of atherosclerosis in a double balloon injured fat-fed rabbit model known for high prevalence of macrophages (Figure 2.10).[52] We injected the injured New Zealand white rabbit (age = 6 months, weight = 3.3 kg) intravenously with 12 cc of a colloidal dispersion of nanoroses (1.37 mg Au/ kg body weight). The *in vivo* intravenous dose given to the rabbit is comparable to the currently FDA approved value of 100 mg for a single injection of gold sodium thiomalate (per a 70 kg human body) used in the treatment of rheumatoid arthritis.[53] Three days following gold nanorose injection, the rabbit was euthanized and aortic specimens were harvested. The plaque-based macrophages engulf nanorose following intravenous injection, as demonstrated via co-localization of macrophage immunohistochemistry (RAM-11 positive) and nanorose identified with both dark field microscopy and hyperspectral imaging (see Figure 2.10 legend for details). Nanoroses engulfed by the macrophages retain their strong NIR absorbance seen in solutions and cell culture (Figure 2.3 and 7). High nanorose uptake and absorbance, along with the absence of NIR reflective components of native rabbit aorta, provide high contrast between macrophages and surrounding tissue.

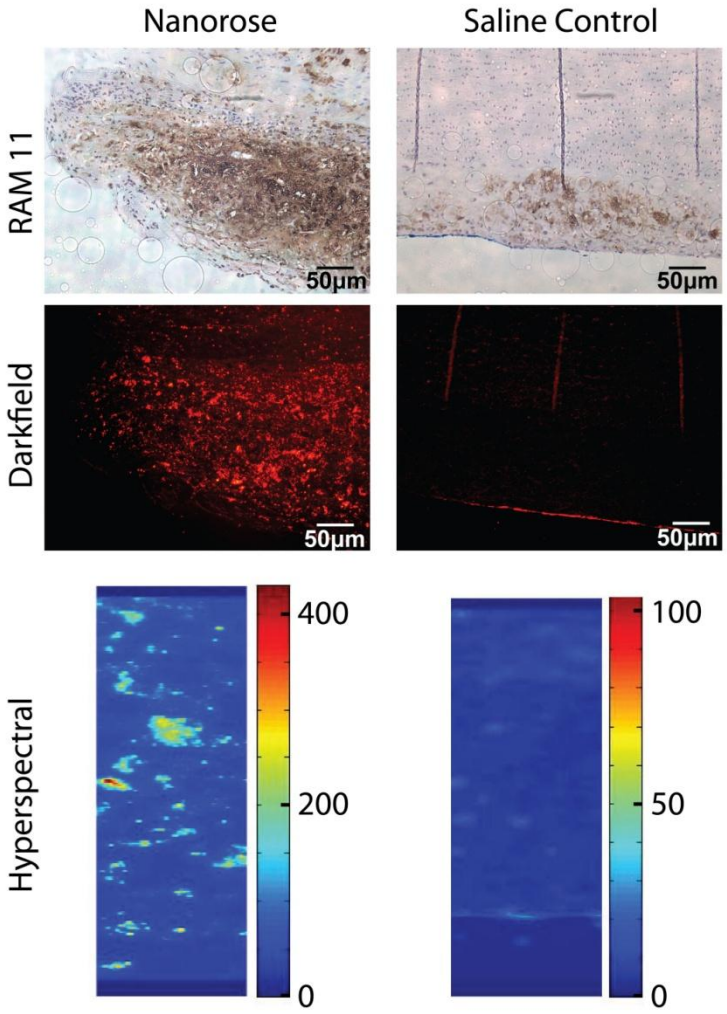

Figure 2.10 Histological sections of atherosclerotic rabbit aorta. Leftmost images are double-balloon injured aorta after intravenous injection with nanorose; rightmost images are from a saline-injected control rabbit. RAM 11 stain (brown color) shows macrophages are present in both rabbits. Dark field microscopy with a 610 nm long-pass filter shows nanorose in the double-balloon injured aorta only (bright red reflections). Hyperspectral images (integrated reflectance intensities of light between 610 and 800 nm) show nanorose (yellow-red intensities) within the macrophages (blue intensities) in the double-balloon injured aorta.

2.3 CONCLUSIONS

Strong NIR and magnetic functionality were loaded into very small ~30 nm nanoclusters that were relatively stable for 8 months. The nanoclusters were formed by kinetic assembly of Au/iron oxide nanocomposite building blocks with only a small amount of polymeric stablizers. The closely-spaced and asymmetric thin gold coatings on the primary particles and porosity of the nanoclusters favor high NIR absorbance as a result of collective responses of the electrons and reduced symmetry of the interactions between plasmon modes. The large degree of empty space in the clusters is beneficial for further addition of adsorbed or conjugated (onto gold) drugs, antibodies and aptamers.[15] The primary components of the particles, iron oxide, Au, dextran and poly vinyl alcohol (PVA), are acceptable for administration to humans, without the need for toxic surfactants or toxic metals. The small size of the nanoclusters and the dextran surface coating are shown to facilitate high uptake by macrophages, which contain dextran receptors.[6] The high uptake and intense NIR absorbance are shown to provide high NIR contrast in dark field and hyperspectral microscopy, both in cell culture and an *in vivo* rabbit model of atherosclerosis. A single 50 ns laser pulse at 755 nm is sufficient for photothermal destruction of nanocluster-laden macrophages. Small and stable nanoclusters of nanocomposite primary particles with strong multifunctionality, designed by this general approach, will offer broad opportunities for cellular imaging and altering cell biology, for the treatment of diseases such as atherosclerosis and cancer.

2.4 METHODS

2.4.1 Synthesis of iron oxide dispersion

The iron oxide nanoparticles were synthesized by using a modified method of Shen et al.[54] 15 ml of dextran aqueous solution (15% w/w) was titrated with 4 ml NH_4OH

(>25% w/w) to pH 11.7. The alkali-treated dextran solution was heated in a flask with magnetic stirring to 25 ℃ in a water bath. 5 ml fresh prepared 0.75 g $FeCl_3 \cdot 6H_2O$ and 0.32 g $FeCl_2 \cdot 4H_2O$ aqueous solution was gradually injected into the alkali-treated dextran solution after passing through a hydrophilic 0.2 μm filter. The black suspension was stirred for a half hour. The subsequent mixture was centrifuged at 10,000 rpm for 20 min. to remove the aggregates. The supernatant was decanted and dialyzed against DI water for 24 hrs. For a dialysis bag (Spectra/Pro 7, Spectrum Laboratories Inc.) with 25 kDalton molecular weight cut off, heavy metal ions, excess salts, ammonium and unbound dextran molecules were removed from the particle dispersion. To concentrate the dispersions and further remove free dextran from the particles, a centrifugal filter device (Ultracel YM-30, Millipore Co.) was used with a relative centrifugal force of 1500 × g. The size of the iron oxide nanoparticles in this supernatant measured by HRTEM was 5.2 ± 0.8 nm, and the pH was 7.3. The concentration of iron oxide from FAAS was 14.6 mg Fe/mL. After dilution to 0.1 mg/ml Fe, DLS gave an average hydrodynamic diameter of 14 nm at 25 ℃ (see supporting information Figure 2.S1).

2.4.2 Nanorose growth and purification

To synthesize the nanorose, 0.1 mL (14.6 mg Fe/ml) 5 nm dextran coated iron oxide nanoparticles were dispersed in 8.9 mL DI water and 100 μL 1% hydroxylamine seeding agent were added. 0.5 g of dextrose was used as a more mild reducing agent compared with sodium citrate which was used previously.[24] Before starting the Au precursor addition, 20 μL of 7% NH_4OH solution was added to the iron oxide dispersion to tune the pH to 9.0. A 100 μL aliquot of 6.348 mM $HAuCl_4$ aqueous solution was added to the stirred dispersion. After 10 minutes a second 100 μL aliquot was added. This procedure was repeated two more times for a total of 400 μL of $HAuCl_4$. A gradual

change in color from brown to dark brown occurred during the four aliquot additions and the pH decreased to 7.0. The dense gold-coated iron oxide particles were separated from the less dense uncoated particles by centrifugation at 6000 rpm for 6 mins. 1.6 ~ 2.3% iron oxide nanoparticles from the original reaction were incorporated in the nanorose precipitate as determined by FAAS. After decanting the supernatant, purified gold-coated iron oxide nanorose were redispersed in DI water. Dialysis bags were used to purify the nanoroses further against DI water for 24 hours and the dispersions were sterilized by passage through a 0.45 μm pore size Nylon filter. The purified particles were then concentrated by centrifugal filter devices (Ultracel YM-30, Millipore Co.) to 700 μg Au/ml in a total volume of 0.1 ml. The final product appeared dark blue in color to the unaided eye. To improve the steric stabilization of the nanorose clusters, 40 μL of 2% poly (vinyl alcohol) MW 22,000, was added to the dispersions. After 8 months storage, a small portion of the settled particles were re-dispersible by manual shaking without any visible aggregates.

2.4.3 Dynamic light scattering

Dynamic light scattering analysis was performed in triplicate on a custom-built apparatus (scattering angle: 90 ϑ) and the data were analyzed using a digital autocorrelator (Brookhaven BI-9000AT) and a non-negative least-squares (NNLS) routine (Brookhaven 9KDLSW32).[55] The dispersion concentration was 0.02-0.04 mg Au/mL which gave a measured count rate of approximately 300-400 kcps. All dispersions were filtered through a 0.2 μm filter and probe-sonicated for 2 min prior to measurement.

2.4.4 Determination of absorption and scattering with an integrating sphere

A lens coupled fiber optic laser (Opto Power, Inc.; Model FCTS/B) was used to irradiate a sample positioned inside an integrating sphere. The sample was positioned in a glass sample holder and consisted to two microscope slides displaced by 80 μm. The sample holder was positioned in the center of the integrating sphere and oriented perpendicular to the incident laser beam (3W, 800 nm, CW mode). A power meter (Newport, Inc.; Model 1935-C) was placed at a port of the integrating sphere oriented perpendicular to the laser beam. For absorption coefficient (μ_a) measurement, the radiant power was measured with the sample holder containing DI water and nanorose solution. The directly transmitted beam through the sample holder was contained within the integrating sphere and contributed to the measurement. For scattering coefficient (μ_s) measurement, the same procedure was followed except that the directly transmitted beam was allowed to exit the integrating sphere and did not contribute to the measurement.

2.4.5 In vitro magnetic resonance imaging

All MRI experiments were performed with a 3.0 T clinical MRI instrument (Trio, Siemens Medical Solutions) with a circularly polarized, transmit-receive knee coil. The resonant frequency was 123.208591 MHz. The microscopic transverse relaxation time (T2) was measured for various concentrations of nanorose particles by applying spin echo (SE) pulse sequences at room temperature with TR = 2 s and increasing the echo time (TE) for successive scans: TE = 7, 14, 28, 56, 112, 224, 448 and 896 ms. Other parameters included the number of acquisitions (NA) = 1, pixel resolution = 0.351 mm×0.351 mm, bandwidth 200 Hz/pixel and section thickness = 2 mm. Following data collection, regions of interest (ROIs) were drawn and the mean signal intensity in each tube was recorded. Nonlinear least-squares fitting was used to solve for T2 as a function of iron concentration in mM. The relaxivity value (r2 in $mM^{-1}s^{-1}$) for the nanorose

dispersion was calculated using T2 measurements done with a series dilution of colloidal suspension in water.

2.4.6 In vitro macrophage photothermolysis study

For photothermolysis, 1 mL of culture media containing 1 μg of nanorose was incubated in each well of a dual chamber slide for 24 hours followed by intensive 1×PBS washing to remove non-engulfed nanoparticles. The amounts of gold and iron in the engulfed nanorose were determined by FAAS. The macrophages were cultured for another 24 hours after each laser treatment before staining and microscopy imaging. A Candela Alexlazr© laser (Candela Corporation, Wayland, Massachusetts, USA) with a wavelength of 755 nm was used to irradiate the slides. Radiometric temperature was measured by focusing the IR radiation with a parabolic mirror onto an HgCdTe infrared detector (Fermionics Corporation, Simi Valley, CA, USA) with 11 microns cut-off wavelength. The measured voltage was calibrated to a temperature using a black body source.

2.4.7 Hyperspectral microscopy

The Pariss hyperspectral system was coupled to a Leica microscope and measured the spectra of transmitted light at each pixel in an image, for illumination with a halogen lamp (300 to 780 nm). A single vertical section of the sample image was projected onto a prism through a 25 μm slit, and a prism dispersed the one-dimensional image onto a two-dimensional Q-imaging Retiga EXi CCD detector, with spatial information encoded on one axis and spectral information on the orthogonal direction. The macrophage samples were laterally scanned via a piezoelectric stage to construct a three-dimensional

hyperspectral data cube. A blank slide containing 1×PBS was used to acquire spectrum of the illumination lamp.

2.4.8 Atherosclerotic rabbit model

All experimental procedures were performed in accordance with protocols approved by the University of Texas Institutional Animal Care and Use Committee. Atherosclerotic plaques rich in macrophages were induced in New Zealand white rabbits by double-balloon injury and high cholesterol, high fat feeding as previously reported.[52] The tissue specimens were fixed in 10% formalin for 24 hrs, processed for histology, and embedded in paraffin. An aortic specimen from a control rabbit was prepared. The control rabbit (age = 6 months, weight = 3.3 kg) was fed and injured in the same way, but received 12 cc of saline without any nanorose.

2.5 SUPPORTING INFORMATION

2.5.1 Reproducibility in particle size distribution

We performed 7 individual syntheses of nanorose at the standard conditions to determine the reproducibility in the particle size distribution as shown in Table 2.S1. The average size distribution of nanoroses falls between 23 ± 3 nm and 34 ± 2 nm for 95% of the volume of the distribution. This size distribution may be considered to be quite narrow given that the clusters are formed by kinetically controlled self-assembly.

Table 2.S1 Multiple Batches of Nanorose to Illustrate Reproducibility in the Particle Size Distribution by Dynamic Light Scattering

batch	hydrodynamic diameter (nm)	volume percentage (%)
1	25-32	98
2	26-34	93
3	19-32	94
4	22-33	97
5	19-33	98
6	23-36	95
7	24-35	96

2.5.2 Porosity of dextran in the shells about the iron oxide particles

The porosity of the dextran in the coating about the iron oxide nanoparticles was determined to better understand the availability of free space on the particle surface. This free space is required to form the gold coatings in the subsequent gold reduction step. As shown by TEM in Figure 2.S1c, the iron oxide core radius (r) was equal to 2.5 nm. The total hydrodynamic radius (R) equals to 7.0 nm determined by DLS (Figure 2.S1b). The porosity in the dextran shell can be expressed as 1- ($N_{Dextran}/N_{Fe3O4}$) $V_{Dextran}/V_{Shell}$, where the volume of a hydrated dextran molecule ($V_{Dextran}$) is calculated from the Stoke's radius of bulk hydrated dextran (2.36 nm, MW 10,000). [http://www.dextran.net/dextran-physical-properties.html] The volume of the shell is given by $V_{Shell} = 4/3\ \pi\ (R^3\text{-}r^3)$. The number of dextran molecules attached to one iron oxide nanoparticle $N_{Dextran} / N_{Fe3O4}$ is estimated from the mass ratio $m_{Dextran} /m_{iron\ oxide}$ of 1/2.92 determined by TGA (Figure 2.S2). Unbound dextran molecules are separated from bound dextran by centrifugation (at 10000 rpm). The volume of an iron oxide core V_{Fe3O4} is $4/3\ \pi\ (2.5\times10^{-7})^3 = 6.54\times10^{-20}$ cm^3 and $\rho_{Fe3O4} = 5.2 g \cdot cm^{-3}$. The number of dextran chains per iron oxide particle given by $N_{Dextran}/N_{Fe3O4} = (N_{AV} \cdot m_{Dextran}/MW_{Dextran}) / [m_{Iron\ oxide} / (_{Fe3O4} \cdot V_{Fe3O4})]$ is 6. From these equations and properties, the calculated porosity

in the shell is 0.76 in agreement with a previous determination by Shen[1]. The highly porous shell provides a high degree of free volume and thus iron oxide surface area for coating by gold in the nanorose cluster formation step.

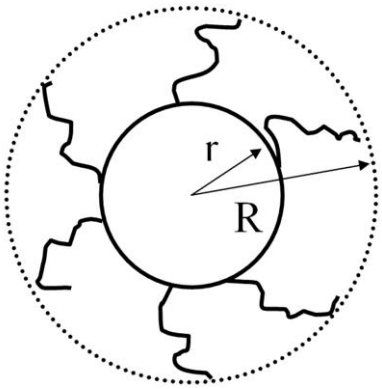

(a)

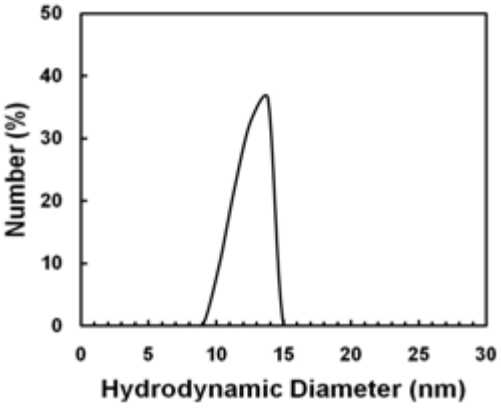

(**b**)

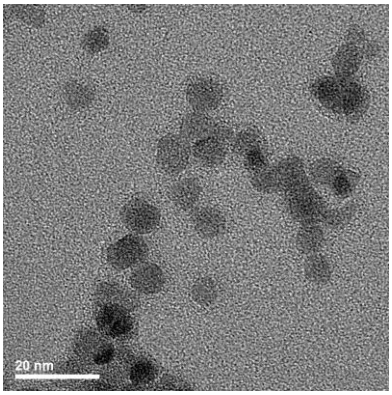

(c)

Figure 2.S1 (a) Schematic structure of dextran coating on 5 nm iron oxide nanoparticles. (b) Hydrodynamic diameter of dextran coated iron oxide nanoparticles dissolved in water. (c) HRTEM image of dextran coated 5 nm iron oxide nanoparticles on ultra thin layer carbon substrate.

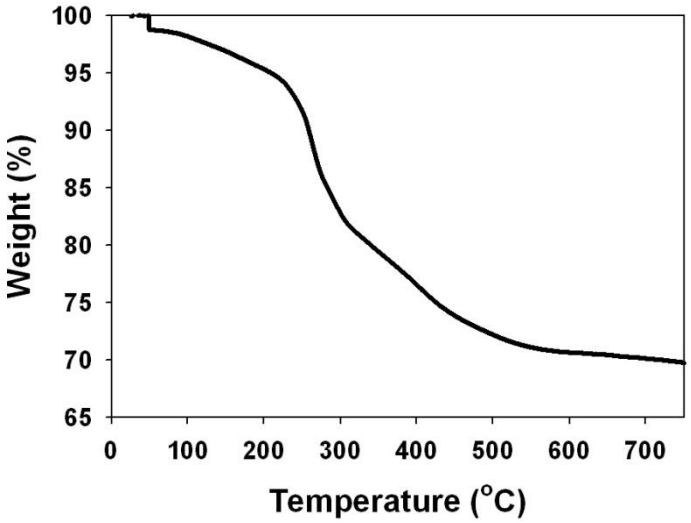

Figure 2.S2 TGA analysis of dried iron oxide nanoparticle precipitates after centrifugation. The weight loss from 105 ℃ to 800 ℃ is attributed to dextran thermolysis.

2.5.3 Estimation of number of particles per nanocluster

The number of iron oxide particles per nanocluster can be estimated from the Au:Fe molar ratio, r, determined by EDS and the geometric properties of the iron oxide particles and the nanorose cluster. The nanorose was modeled as an effective sphere with an occupied volume ϕ and diameter D_{NR}. The total occupied volume is just the sum of the volumes of the gold and iron oxide,

$$\phi V_{NR} = n_{Au}/\rho_{Au} + NV^{p}_{Fe3O4} \quad (1)$$

where, V_{NR} is the effective spherical volume of a nanorose, V^{p}_{Fe3O4} is the volume of a single iron oxide particle, N is the number of iron oxide particles per nanorose, and n and ρ are the number of moles and molar densities, respectively, of either Au or Fe_3O_4. The ratio of moles of Au to moles of Fe may be expressed as

$$r = n_{Au}/(3N\ \rho_{Fe3O4}\ V^{p}_{Fe3O4}) \quad (2)$$

where 3 is the moles of Fe in Fe_3O_4. Elimination of n_{Au} from eqs 1 and 2 yields

$N = \phi(D_{NR}/D_{Fe3O4})^3/[(3r(\rho_{Fe3O4/}\ \rho_{Au})+ 1]$ (3)

From Fig. 1, we choose D_{NR} = 35 nm (slightly larger than the hydrodynamic diameter) and ϕ~0.5. The molar densities are 0.0225 mol/cm^3 for Fe_3O_4 and 0.098 for Au and D_{Fe3O4} = 5 nm. For iron oxide, the diameter is 5 nm. For 20 nanorose particles, EDS measurements indicated that the Au:Fe mass ratio varied from 5:1 to 9:1, with an average of 8:1, which corresponds to a molar ratio r= 2.27. In addition, M_{Fe3O4} is 231.6 g/mol for Fe_3O_4 and M_{Au} is 196.97 g/mol, In this case, N ~ 70.

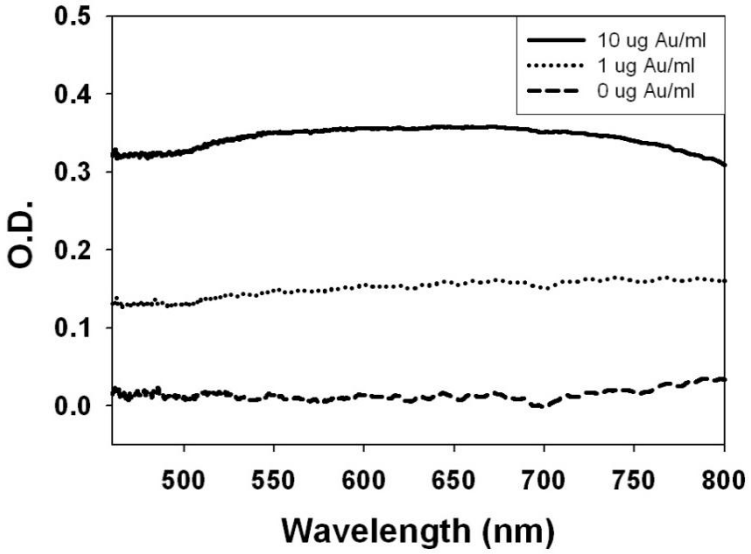

Figure 2.S3 Average optical density spectra v.s. incident light wavelength in macrophages labeled with different nanorose concentrations measured by hyperspectral microscopy. According to Figure 2.7, average OD values over 3 to 4 macrophage areas are collected between 460 nm and 800 nm spectra range. Note that the spectra broaden relative to the case of nanoparticles in solution due to aggregation of the nanoparticles inside macrophages.

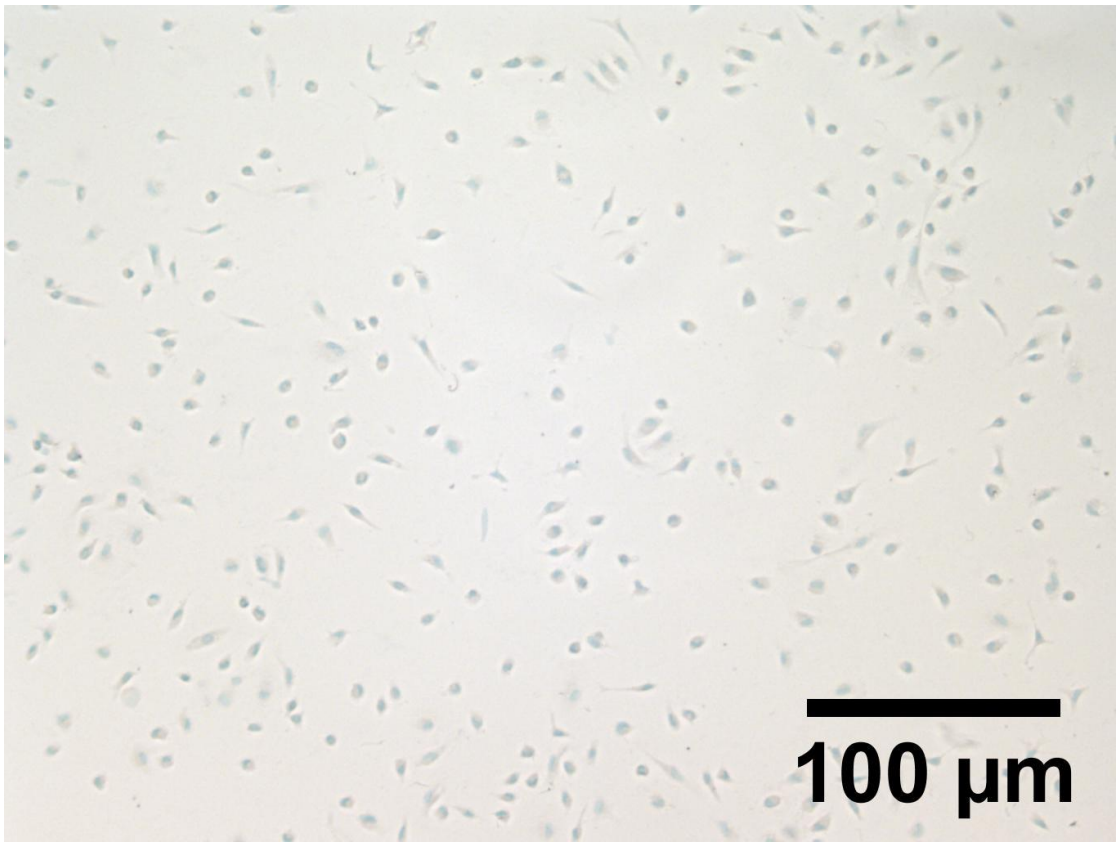

(a)

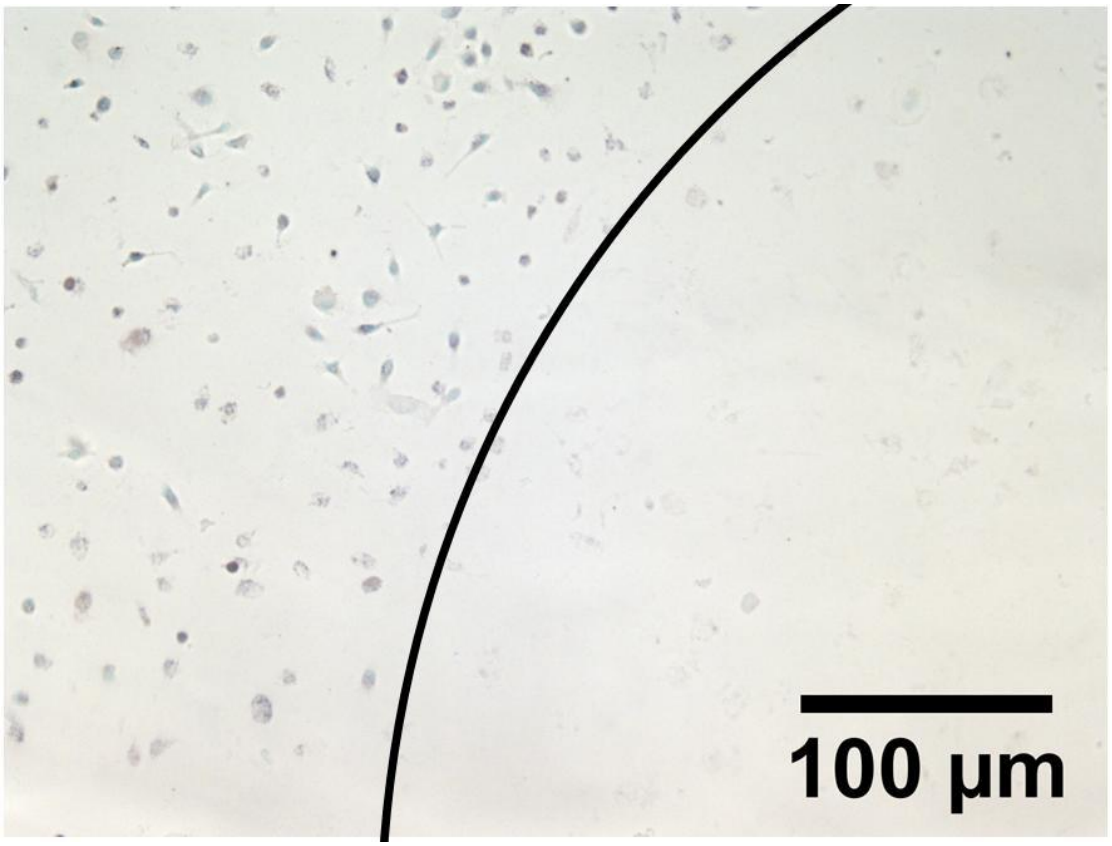

(b)

Figure 2.S4 Laser vaporization of macrophage cells in vitro. (a) A bright field image of the irradiated macrophages without nanorose shows the presence of macrophages with no damage to the membrane after irradiation. (b) A bright field image shows macrophages with nanorose near the boundary of the laser beam. The blue color after TUNEL staining indicates apoptosis was not present in Figure 2.S4a. In Figure 2.S4b, outside the beam to the left of the curve, brown stained macrophage cells were present indicating damage to the cell membrane likely as a result of apoptosis. Inside the beam to the right of the line, macrophages were destroyed due to the laser interaction with the nanoroses.

2.5.4 Rabbit endothelial cell preparation

Rabbits were first euthanized with phenobarbital by intraperitoneal anesthesia. Thoracic aortas were then harvested under sterile conditions and washed twice with sterile PBS. Adventitia was mechanically removed and aorta was longitudinally opened. To isolate endothelial cells, the aorta was immersed in 0.2% collagenase solution for 10 minutes

and the intima was gently scraped with a scalpel blade (Note: the remaining arterial wall tissue will be used for smooth muscle cell culture, see below). Digestion was terminated with endothelial cell growth medium containing 10% FBS and cells were centrifuged at 1200 rpm for 10 minutes (cells were then resuspended in sterile PBS and centrifuged under the same conditions again). The supernatant was discarded and endothelial cells (EC) were resuspended in EC growth medium containing 10% FBS. Cells were then seeded onto 6-well plates (collagen coated) and placed in 5% CO_2, 37 ℃ incubator. Media was changed regularly every 3 days.

2.5.5 Rabbit Smooth Muscle Cell Preparation

The arterial wall tissue obtained above (see EC cell preparation) was cut into 1 mm × 1 mm pieces and placed in DMEM containing 10% FBS. Explants were then seeded onto 6-well plates (collagen coated) and placed in a 5% CO_2, 37 ℃ incubator for 2 hours (No medium). Fresh DMEM containing 10% FBS was then added and media was regularly changed every 3 days.

Macrophage

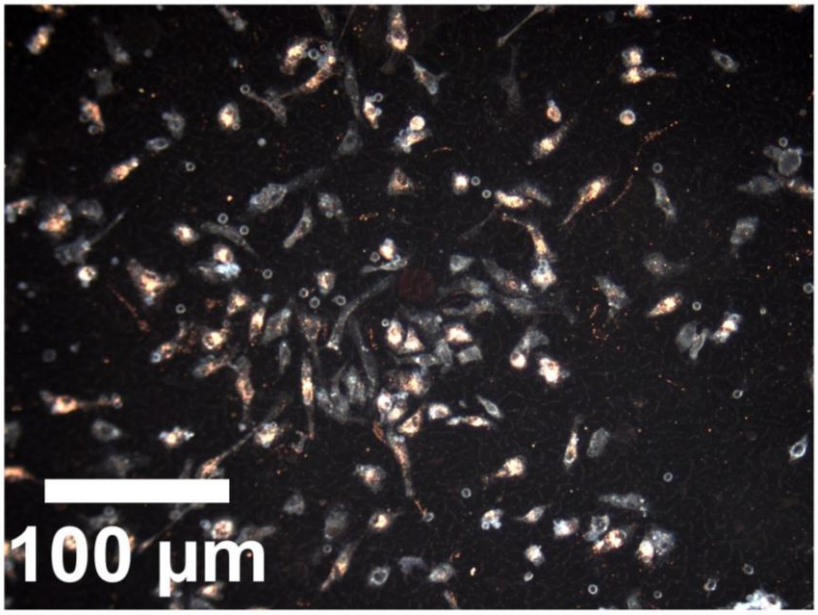

EC

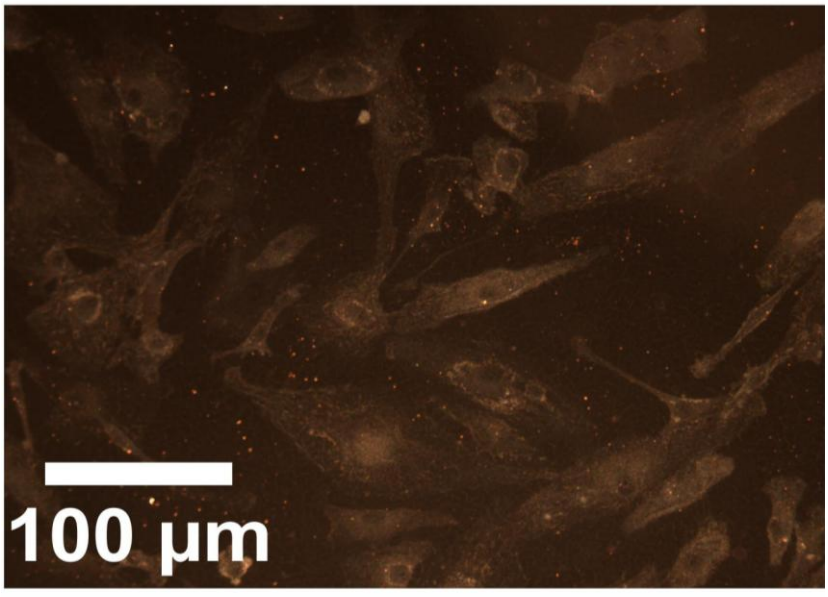

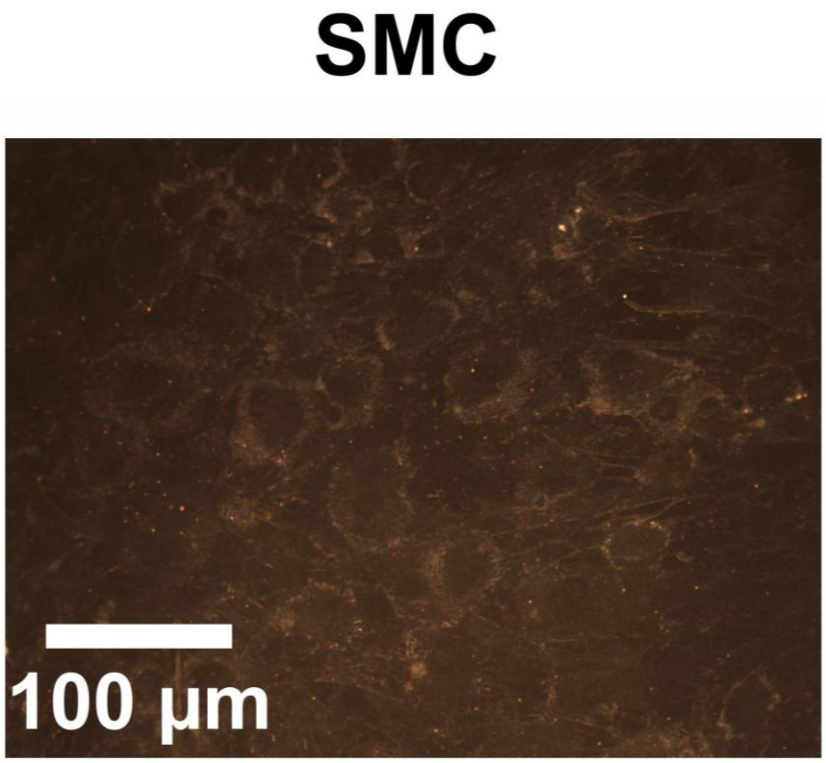

Figure 2.S5 Specificity of nanorose into macrophages versus aortic endothelial cells and aortic smooth muscle cells by dark field microscopy.

2.6 REFERENCES

1. Ferrari, M., Beyond Drug Delivery. *Nature Nanotechnology* **2008,** 3, 131-132.

2. Jiang, W.; Kim, B. Y. S.; Rutka, J. T.; Chan, W. C. W., Nanoparticle-Mediated Cellular Response Is Size-Dependent. *Nature Nanotechnology* **2008,** 3, 145-150.

3. Reddy, S. T.; Swartz, M. A.; Hubbell, J. A., Targeting Dendritic Cells with Biomaterials: Developing the Next Generation of Vaccines. *Trends in Immunology* **2006,** 27, 573-579.

4. Wang, A. Z.; Bagalkot, V.; Vasilliou, C. C.; Gu, F.; Alexis, F.; Zhang, L.; Shaikh, M.; Yuet, K.; Cima, M. J.; Langer, R.; Kantoff, P. W.; Bander, N. H.; Jon, S.; Farokhzad, O. C., Superparamagnetic Iron Oxide Nanoparticle-Aptamer Bioconjugates for Combined Prostate Cancer Imaging and Therapy. *ChemMedChem* **2008,** 3, 1311-1315.

5. Weissleder, R., Molecular Imaging in Cancer. *Science* **2006,** 312, 1168-1171.

6. Jaffer, F. A.; Libby, P.; Weissleder, R., Molecular and Cellular Imaging of Atherosclerosis: Emergency Applications. *Journal of the American College of Cardiology* **2006,** 47, 1328-1338.

7. Adler, D. C.; Huang, S.-W.; Huber, R.; Fujimoto, J. G., Photothermal Detection of Gold Nanoparticles Using Phase-Sensitive Optical Coherence Tomography. *Optics Express* **2008,** 16, 4376-4393.

8. Hirsch, L. R.; Stafford, R. J.; Bankson, J. A.; Sershen, S. R.; Rivera, B.; Price, R. E.; Hazle, J. D.; Halas, N. J.; West, J. L., Nanoshell-Mediated near-Infrared Thermal Therapy of Tumors under Magnetic Resonance Guidance. *Proc. Nat. Acad. Sci.* **2003,** 100, 13549-13554.

9. Loo, C.; Lowery, A.; Halas, N.; West, J.; Drezek, R., Immunotargeted Nanoshells for Integrated Cancer Imaging and Therapy. *Nano Letters* **2005,** 5, 709-711.

10. Huang, X.; El-Sayed, I. H.; Qian, W.; El-Sayed, M. A., Cancer Cell Imaging and Photothermal Therapy in the near-Infrared Region by Using Gold Nanorods. *Journal of the American Chemical Society* **2006,** 128, 2115-2120.

11. Pissuwan, D.; Valenzuela, S. M.; Killingsworth, M. C.; Xu, X.; Cortie, M. B., Targeted Destruction of Murine Macrophage Cells with Bioconjugated Gold Nanorods. *Journal of Nanoparticle Research* **2007,** 9, 1109-1124.

12. Skrabalak, S. E.; Chen, J.; Au, L.; Lu, X.; Li, X.; Xia, Y., Gold Nanocages for Biomedical Applications. *Advanced Materials* **2007,** 19, 3177-3184.

13. Sokolov, K.; Follen, M.; Aaron, J.; Pavlova, I.; Malpica, A.; Lotan, R.; Richards-Kortum, R., Real-Time Vital Optical Imaging of Precancer Using Anti-Epidermal Growth Factor Receptor Antibodies Conjugated to Gold Nanoparticles. *Cancer Research* **2003,** 63, 1999-2004.

14. Aaron, J.; Nitin, N.; Travis, K.; Kumar, S.; Collier, T.; Park, S. Y.; Jose-Yacaman, M.; Coghlan, L.; Follen, M.; Richards-Kortum, R.; Sokolov, K., Plasmon Resonance Coupling of Metal Nanoparticles for Molecular Imaging of Carcinogenesis in Vivo. *Journal of Biomedical Optics* **2007,** 12, 034007/1-034007/11.

15. Josephson, L.; Kircher, M. F.; Mahmood, U.; Tang, Y.; Weissleder, R., Near-Infrared Fluorescent Nanoparticles as Combined Mr/Optical Imaging Probes. *Bioconjugate Chemistry* **2002,** 13, 554-560.

16. Larson, T. A.; Bankson, J.; Aaron, J.; Sokolov, K., Hybrid Plasmonic Magnetic Nanoparticles as Molecular Specific Agents for Mri/Optical Imaging and Photothermal Therapy of Cancer Cells. *Nanotechnology* **2007,** 18, 325101/1-325101/8.

17. Aaron, J. S.; Oh, J.; Larson, T. A.; Kumar, S.; Milner, T. E.; Sokolov, K. V., Increased Optical Contrast in Imaging of Epidermal Growth Factor Receptor Using Magnetically Actuated Hybrid Gold/Iron Oxide Nanoparticles. *Optics Express* **2006,** 14, 12930-12943.

18. Yin, Y.; Alivisatos, A. P., Colloidal Nanocrystal Synthesis and the Organic-Inorganic Interface. *Nature* **2005,** 437, 664-670.

19. DeVries, G. A.; Brunnbauer, M.; Hu, Y.; Jackson, A. M.; Long, B.; Neltner, B. T.; Uzun, O.; Wunsch, B. H.; Stellacci, F., Divalent Metal Nanoparticles. *Science* **2007,** 315, 358-361.

20. Ofir, Y.; Samanta, B.; Rotello, V. M., Polymer and Biopolymer Mediated Self-Assembly of Gold Nanoparticles. *Chem. Soc. Rev.* **2008,** 37, 1814-1825.

21. Boal, A. K.; Ilhan, F.; DeRouchey, J. E.; Thurn-Albrecht, T.; Russell, T. P.; Rotello, V. M., Self-Assembly of Nanoparticles into Structured Spherical and Network Aggregates. *Nature* **2000,** 404, 746-748.

22. Lazarides, A. A.; Schatz, G. C., DNA-Linked Metal Nanosphere Materials: Structural Basis for the Optical Properties. *Journal of Physical Chemistry B* **2000,** 104, 460-467.

23. Berret, J.-F.; Schonbeck, N.; Gazeau, F.; El Kharrat, D.; Sandre, O.; Vacher, A.; Airiau, M., Controlled Clustering of Superparamagnetic Nanoparticles Using Block Copolymers: Design of New Contrast Agents for Magnetic Resonance Imaging. *Journal of the American Chemical Society* **2006,** 128, 1755-1761.

24. Lyon, J. L.; Fleming, D. A.; Stone, M. B.; Schiffer, P.; Williams, M. E., Synthesis of Fe Oxide Core/Au Shell Nanoparticles by Iterative Hydroxylamine Seeding. *Nano Letters* **2004,** 4, 719-723.

25. Wang, L.; Luo, J.; Fan, Q.; Suzuki, M.; Suzuki, I. S.; Engelhard, M. H.; Lin, Y.; Kim, N.; Wang, J. Q.; Zhong, C.-J., Monodispersed Core-Shell Fe3o4@Au Nanoparticles. *Journal of Physical Chemistry B* **2005,** 109, 21593-21601.

26. Knight, M. W.; Halas, N. J., Nanoshells to Nanoeggs to Nanocups: Optical Properties of Reduced Symmetry Core-Shell Nanoparticles Beyond the Quasistatic Limit. *New Journal of Physics* **2008,** 10.

27. Basu, S.; Pande, S.; Jana, S.; Bolisetty, S.; Pal, T., Controlled Interparticle Spacing for Surface-Modified Gold Nanoparticle Aggregates. *Langmuir* **2008,** 24, 5562-5568.

28. Jain, P. K.; Lee, K. S.; El-Sayed, I. H.; El-Sayed, M. A., Calculated Absorption and Scattering Properties of Gold Nanoparticles of Different Size, Shape, and Composition: Applications in Biological Imaging and Biomedicine. *Journal of Physical Chemistry B* **2006,** 110, 7238-7248.

29. Urbanska, K.; Romanowska-Dixon, B.; Matuszak, Z.; Oszajca, J.; Nowak-Sliwinska, P.; Stochel, G., Indocyanine Green as a Prospective Sensitizer for Photodynamic Therapy of Melanomas. *Acta Biochimica Polonica* **2002,** 49, 387-391.

30. Chen, W. R.; Adams, R. L.; Carubelli, R.; Nordquist, R. E., Laser-Photosensitizer Assisted Immunotherapy: A Novel Modality for Cancer Treatment. *Cancer Letters (Shannon, Ireland)* **1997,** 115, 25-30.

31. Khlebtsov, B.; Zharov, V.; Melnikov, A.; Tuchin, V.; Khlebtsov, N., Optical Amplification of Photothermal Therapy with Gold Nanoparticles and Nanoclusters. *Nanotechnology* **2006,** 17, 5167-5179.

32. Wang, H.; Goodrich, G. P.; Tam, F.; Oubre, C.; Nordlander, P.; Halas, N. J., Controlled Texturing Modifies the Surface Topography and Plasmonic Properties of Au Nanoshells. *Journal of Physical Chemistry B* **2005,** 109, 11083-11087.

33. Xu, Z.; Hou, Y.; Sun, S., Magnetic Core/Shell Fe3o4/Au and Fe3o4/Au/Ag Nanoparticles with Tunable Plasmonic Properties. *J. Am. Chem. Soc.* **2007,** 129, 8698-8699.

34. Pham, T.; Jackson, J. B.; Halas, N. J.; Lee, T. R., Preparation and Characterization of Gold Nanoshells Coated with Self-Assembled Monolayers. *Langmuir* **2002,** 18, 4915-4920.

35. Kumar, S.; Harrison, N.; Richards-Kortum, R.; Sokolov, K., Plasmonic Nanosensors for Imaging Intracellular Biomarkers in Live Cells. *Nano Letters* **2007,** 7, 1338-1343.

36. Wang, H.; Brandl, D. W.; Nordlander, P.; Halas, N. J., Plasmonic Nanostructures: Artificial Molecules. *Accounts of Chemical Research* **2007,** 40, 53-62.

37. Wilson, B. C.; Patterson, M. S.; Flock, S. T., Indirect Versus Direct Techniques for the Measurement of the Optical Properties of Tissues. *Photochemistry and photobiology* **1987,** 46, 601-8.

38. Patterson, M. S.; Wilson, B. C.; Wyman, D. R., The Propagation of Optical Radiation in Tissue. Ii: Optical Properties of Tissues and Resulting Fluence Distributions. *Lasers in Medical Science* **1991,** 6, 379-390.

39. Shah, J.; Park, S.; Aglyamov, S.; Larson, T.; Ma, L.; Sokolov, K.; Johnston, K.; Milner, T.; Emelianov Stanislav, Y., Photoacoustic Imaging and Temperature Measurement for Photothermal Cancer Therapy. *Journal of biomedical optics* **2008,** 13, 034024.

40. Jun, Y.-W.; Lee, J.-H.; Cheon, J., Chemical Design of Nanoparticle Probes for High-Performance Magnetic Resonance Imaging. *Angewandte Chemie, International Edition* **2008,** 47, 5122-5135.

41. Lee, J.-H.; Huh, Y.-M.; Jun, Y.-W.; Seo, J.-W.; Jang, J.-T.; Song, H.-T.; Kim, S.; Cho, E.-J.; Yoon, H.-G.; Suh, J.-S.; Cheon, J., Artificially Engineered Magnetic Nanoparticles for Ultra-Sensitive Molecular Imaging. *Nature medicine* **2007,** 13, 95-9.

42. Ditsch, A.; Laibinis, P. E.; Wang, D. I. C.; Hatton, T. A., Controlled Clustering and Enhanced Stability of Polymer-Coated Magnetic Nanoparticles. *Langmuir* **2005,** 21, 6006-6018.

43. Perez, J. M.; Josephson, L.; Weissleder, R., Use of Magnetic Nanoparticles as Nanosensors to Probe for Molecular Interactions. *ChemBioChem* **2004,** 5, 261-264.

44. Roch, A.; Gossuin, Y.; Muller, R. N.; Gillis, P., Superparamagnetic Colloid Suspensions: Water Magnetic Relaxation and Clustering. *Journal of Magnetism and Magnetic Materials* **2005,** 293, 532-539.

45. Ross, R., Atherosclerosis--an Inflammatory Disease. *The New England journal of medicine* **1999,** 340, 115-26.

46. Libby, P., Inflammation in Atherosclerosis. *Nature* **2002,** 420, 868-874.

47. Kimura, Y. N.; Watari, K.; Fotovati, A.; Hosoi, F.; Yasumoto, K.; Izumi, H.; Kohno, K.; Umezawa, K.; Iguchi, H.; Shirouzu, K.; Takamori, S.; Kuwano, M.; Ono, M.,

Inflammatory Stimuli from Macrophages and Cancer Cells Synergistically Promote Tumor Growth and Angiogenesis. *Cancer Science* **2007,** 98, 2009-2018.

48. Allavena, P.; Sica, A.; Solinas, G.; Porta, C.; Mantovani, A., The Inflammatory Micro-Environment in Tumor Progression: The Role of Tumor-Associated Macrophages. *Critical reviews in oncology/hematology* **2008,** 66, 1-9.

49. Biswas, S. K.; Sica, A.; Lewis, C. E., Plasticity of Macrophage Function During Tumor Progression: Regulation by Distinct Molecular Mechanisms. *Journal of Immunology* **2008,** 180, 2011-2017.

50. Nardin, A.; Abastado, J.-P., Macrophages and Cancer. *Frontiers in Bioscience* **2008,** 13, 3494-3505.

51. Bastos, K. R. B.; Alvarez, J. M.; Marinho, C. R. F.; Rizzo, L. V.; Lima, M. R. D. I., *Journal of Leukocyte Biology* **2002,** 71, 271-278.

52. Hyafil, F.; Laissy, J.-P.; Mazighi, M.; Tchetche, D.; Louedec, L.; Adle-Biassette, H.; Chillon, S.; Henin, D.; Jacob, M.-P.; Letourneur, D.; Feldman Laurent, J., Ferumoxtran-10-Enhanced Mri of the Hypercholesterolemic Rabbit Aorta: Relationship between Signal Loss and Macrophage Infiltration. *Arterioscler Thromb Vasc Biol* **2006,** 26, 176-81.

53. Shaw, C. F., III, Gold-Based Therapeutic Agents. *Chem. Rev.* **1999,** 99, 2589-2600.

54. Shen, T.; Weissleder, R.; Papisov, M.; Bogdanov, A., Jr.; Brady, T. J., Monocrystalline Iron Oxide Nanocompounds (Mion): Physicochemical Properties. *Magnetic Resonance in Medicine* **1993,** 29, 599-604.

55. Ryoo, W.; Webber, S. E.; Johnston, K. P., Water-in-Carbon Dioxide Microemulsions with Methylated Branched Hydrocarbon Surfactants. *Ind. Eng. Chem. Res.* **2003,** 42, 6348-6358.

Chapter 3: Growth of Textured Thin Au Shells on Iron Oxide Nanoparticles

A general mechanism is presented for thin autocatalytic growth on nanoparticle substrates (TAGS) as demonstrated for a homologous series of < 5 nm textured Au coatings on 42 nm iron oxide cores. Very low Au precursor supersaturation levels are utilized to prevent commonly encountered thick shells due to excessive autocatalytic growth. This approach extends the mechanism of seeded autocatalytic growth for the formation of pure metal nanoparticles to heterogeneous growth on a low energy substrate. The degree of separation of nucleation to form the seeds from growth is utilized to control the morphology and uniformity of the unusually thin Au coatings. The thin shells with high degrees of asymmetry shift the surface plasmon resonance (SPR) to the NIR, with large extinction coefficients, even for particles with total hydrodynamic diameters less than 60 nm. TAGS may be generalized to a wide variety of substrates and high energy coatings to form core-shell nanoparticles of interest in a broad range of applications including catalysis and bionanotechnology.

3.1 INTRODUCTION

Small nanoparticles (<100 nm) with a thin metal coating on a low surface energy metal oxide core are of interest in numerous applications including imaging contrast agents in nanomedicine,[1, 2] catalysis and electrocatalyis[3, 4] and sensors.[5, 6] For optical imaging and therapy in nanomedicine, the Au shells on magnetic cores are often too thick to shift the absorbance to the preferred near infrared (NIR) region.[7-9] Pure Au nanparticles (and other metals) are commonly synthesized by autocatalytic growth on Au seeds nucleated from soluble precursors[10, 11] or on pre-existing seeds.[12-14] Fine control of the size as well as low polydispersities may often be achieved by separating the nucleation from the growth stages.[15-19] In contrast, controlled growth of high surface energy Au shells on lower energy metal oxide cores is much less favorable; furthermore the lattice spacings are mismatched.[18, 20-24] To drive nucleation of Au seeds on unfavorable low energy iron oxide surfaces, high supersaturation values are often generated by utilization of Au^{3+}/Fe mass ratios on the order of 10.[7, 25, 26] Consequently, as the seeds are being nucleated, competitive autocatalytic growth of Au on Au often produces Au shells with thickness often larger than 10 nm.

The growth of a Au shell on an iron oxide core may be partially passivated with dynamic low molecular weight ligands, for example, citrate or thiols.[7, 25-28] The ligands must not inhibit too strongly the nucleation of the Au seeds, and simultaneously, must provide steric or electrostatic stabilization. A judicious balance of these factors has been accomplished to produce thin Au coatings on small iron oxide cores (<10 nm).[25, 26, 29] However, this approach has received little attention for larger cores (20-60 nm) where polymer steric stabilizers are required to counteract attractive VDW forces between the

particles.[2, 30] For a uniform shell on a 45 nm Fe_3O_4 spherical core, a shell thickness of 2.5 nm would require a Au/Fe ratio of 5:1 assuming 100% yield. Here, autocatalytic growth has been found to produce much thicker shells on a fraction of the iron oxide cores,[7] as further examined in this study. To date, reported Au coatings by direct growth of precursors on an iron oxide nanoparticle substrate range from 10 to 30 nm thick.[7-9, 31]

An alternative is to deposit pre-made Au seeds as small as 2 nm on a nanoparticle substrate, and to fill in spaces between the seeds by reduction of Au precursors to form Au shells,[32-36] as first demonstrated on silica.[37] Whereas in principle, the shells could be only slightly larger than the seeds, excessive autocatalytic growth produces shells on the order of 10 nm.[22, 30, 32, 34, 35] Novel concepts would be beneficial for synthesizing thin metal shells, and designing the shell texture, given these complexities of poor wetting by Au and excessive autocatalytic growth.

Herein, a general mechanism is presented for thin autocatalytic growth of metals on nanoparticle substrates (TAGS), and utilized to grow thin Au coatings on 42 nm iron oxide cores. The TAGS mechanism is shown to be a general extension of the seeded autocatalytic growth mechanism for pure nanoparticles[12, 14] to heterogeneous coatings on low energy substrate cores. The thickness and texture of the thin (< 5 nm) Au coatings are controlled by tuning the separation of the nucleation of the Au seeds on the iron oxide surface from the autocatalytic growth of the seeds. The Au coatings are either smooth (and relatively spherical) or characterized by knobby protrusions as shown for a series of morphologies in Scheme 3.1. Extremely low Au^{3+}/Fe ratios of 0.125-0.50 are investigated to attempt to prevent excessive autocatalytic growth. These low supersaturation levels will also inhibit undesired nucleation of Au seeds in the bulk solution. The Au^{3+}/Fe profile is varied during the reaction via a number of successive iterations or continuous addition of Au^{3+} precursor. This profile is designed to control the

fraction of iron oxide substrate particles that are seeded with Au. After reaction, the Au coated particles are separated by centrifugation from relatively naked (uncoated) iron oxide nanoclusters. Thiol terminated methoxy-polyethylene glycol (mPEG-SH, M_w = 20,000) is used for steric stabilization on the Au surfaces,[38] while simultaneously providing sufficient passivation of Au growth without too strongly inhibiting nucleation of Au seeds. The thiol group does not bind to iron oxide, which could otherwise interfere with the nucleation of Au seeds on its surface. The nanoparticles are characterized by TEM and DLS to determine the morphology and hydrodynamic diameter, and by atomic absorbance spectrometry to determine the Au/Fe mass ratio. Based on these results, it appears that the TAGS mechanism may be generalized in the future to form thin coatings on a wide range of low energy nanoparticle substrates with low precursor/substrate feed ratio, well controlled supersaturation profile and a polymeric stabilizer.

A secondary objective is to relate the surface plasmon resonance (SPR) of the nanoparticles to the asymmetries in the shell geometry. These asymmetries alter the interactions between plasmon modes and red-shift the SPR peak from 530 nm for symmetric systems, such as very thick uniform shells, to the NIR.[32, 33, 39, 40] For a peak maximum of 700 nm, according to Mie theory, $R_{total}/ R_{core} < 1.25$ is required for a Au shell on a spherical Fe_3O_4 core with a permittivity of ~ 6.[41-43] Thus, for cores on the order of 40 nm, the shells would have to be thinner than 5 nm, as reported in this study. Such thin shells have rarely been achieved previously.[2] Further asymmetry in geometry results from the non-spherical shape of the nanocluster core for the coated nanoparticles with either smooth (non-knobby) or knobby surfaces (Scheme 3.1). Related types of asymmetry have been demonstrated for Au rods,[44] nanocages,[18] nanorice,[33] nanoeggs (asymmetric egg white shells),[39] and smooth particles with faceted or tetracubic cores.[32] The high degree of magnetic and functionality and thin metal shell on relatively small

nanoparticles would be desirable for optical,[45, 46] magnetic or multimodal imaging and therapy[47, 48] with effective permeation of biological barriers.[2, 49, 50]

3.2 EXPERIMENTAL SECTION

3.2.1 Materials

All reagents used were analytical grade. Ferrous chloride, ammonium hydroxide, hydroxylamine hydrochloride and sodium hydroxide were purchased from Fisher Chemicals (Fairlawn, NJ), ferric chloride from Acros Organics (Morris Plains, NJ), and citric acid from EM Science (Gibbstown, NJ). Tetrachloroauric acid trihydrate ($HAuCl_4 \cdot 3H_2O$) was purchased from MP Biomedicals LLC. (Solon, OH) and mPEG-SH (MW 20,000) from Nanocs Inc. (New York, NY).

3.2.2 Kinetics of Nucleation and Growth of Au on Iron Oxide

Iron oxide nanoclusters coated with citrate were synthesized by hydrolysis of iron chlorides by modification of the method of Sahoo et al[51] as described in the supplementary section. The iron oxide nanoclusters were dispersed in 100 ml of deionized (DI) water at a concentration of 0.1 mg Fe/ml with rigorous stirring. 300 µL ammonium hydroxide (7 %) was added to adjust the pH to 9.3. 2.0 ml of 1 % (w/v) hydroxylamine hydrochloride was added as the reducing agent for the Au precursor along with 10 ml of 4 mg/ml mPEG-SH (PEG MW 20,000). 1 ml of the solution was transferred to a cuvette with a 1 cm path length, which was inserted into a Cary Varian 3E UV-Vis spectrophotometer. To start the reaction, the desired amount of Au chloride solution (2.5 mg Au/ml) was injected into the cuvette, and the absorbance of the solution

at 755 nm was measured at intervals of 0.0016 seconds for 5 minutes. After the absorbance reached a plateau, the absorbance spectrum was measured between 400 and 850 nm.

3.2.3 Coating Au on Iron Oxide Nanoclusters with Addition of Precursor in Iterations or Continuously

The exact above procedure was carried out in a 200 ml beaker with rigorous stirring. The $HAuCl_4$ solution (2.5 mg Au/ml) was divided equally into multiple aliquots for sequential iterations. Each iteration was separated by a 5 minute interval. After the last iteration, the stirred solution was allowed to stand for 30 min for mPEG-SH reaction with the Au surfaces. The reaction products were centrifuged at 6,000 rpm for 6 min. The supernatant was decanted and the precipitate were re-dispersed in a dilute mPEG-SH solution (0.2 mg/ml) and bath sonicated for 5 minutes to produce a stable colloidal suspension. For the continuous addition experiments, $HAuCl_4$ at a concentration of 0.5 mg Au/ml was added into the reaction mixture with a syringe pump at a rate of 0.1 ml/s.

3.2.4 Materials Characterization

Dynamic light scattering (DLS) measurements were performed in triplicate on a custom made Brookhaven Instruments ZetaPlus apparatus at a scattering angle of 90° and temperature of 25°C.[52] The concentrations of nanoparticle dispersions were adjusted with DI water to give a signal counting rate between 300-400 kcps. Prior to DLS measurements, the samples were bath sonicated for 2 minutes. The autocorrelation functions were analyzed with a non-negative least-squares (NNLS) method to determine distributions by volume.

Low resolution TEM was performed on a FEI Tecnai Spirit BioTwin at 80 kV accelerating voltage. High resolution TEM was performed on a field emission JEOL2010F at 200 kV accelerating voltage. A drop of the dispersion of particles after diluting it 40 times was put on a 400 mesh ultrathin carbon-coated copper TEM grid. Excess liquid was siphoned off using a tissue and the grid was allowed to dry in air.

The Au and iron oxide concentrations in the nanoparticle dispersions were obtained with a GBC 908AA flame atomic absorption spectrometer (GBC Scientific Equipment Pty Ltd) equipped with an air-acetylene flame furnace. The absorption of Au was recorded at 242.8 nm and iron at 248.3 nm. The instrument was calibrated using Au^{3+} or Fe^{3+} standard solutions before every set of measurements. All the measurements were carried on diluted samples so that the concentration of iron or Au in the diluted sample was between 1 and 5 μg/ml.

Thermogravimetric analysis (TGA) was performed using a Perkin–Elmer TGA 7 under nitrogen atmosphere at a gas flow rate of 20 ml/min. Nanoparticle samples were dried to powder in an oven at 100°C. Then samples were heated up to and held at 100°C in the TGA instrument for 20 minutes to remove any moisture. The samples were heated continuously from 100°C to 800 °C at a constant rate of 20 °C/min, and then held at 800°C for 30 minutes. Magnetization at 300 K was measured using a superconducting quantum interference device (SQUID) magnetometer (Quantum Design MPMS). The loss in mass due to adsorbed ligand from TGA was taken into account for normalization to the mass of iron oxide.

Scheme 3.1 Gold coatings on iron oxide nanoclusters

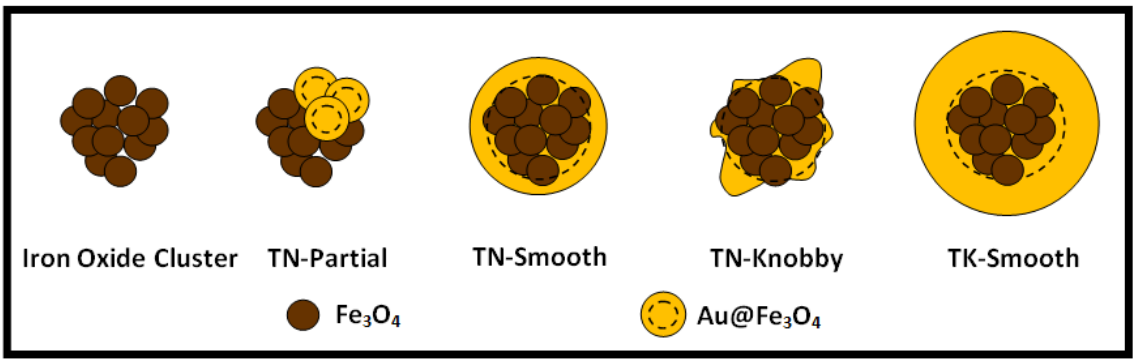

Scheme 3.2 Nucleation and growth of Au shells on iron oxide substrates by adding precursor with different profiles

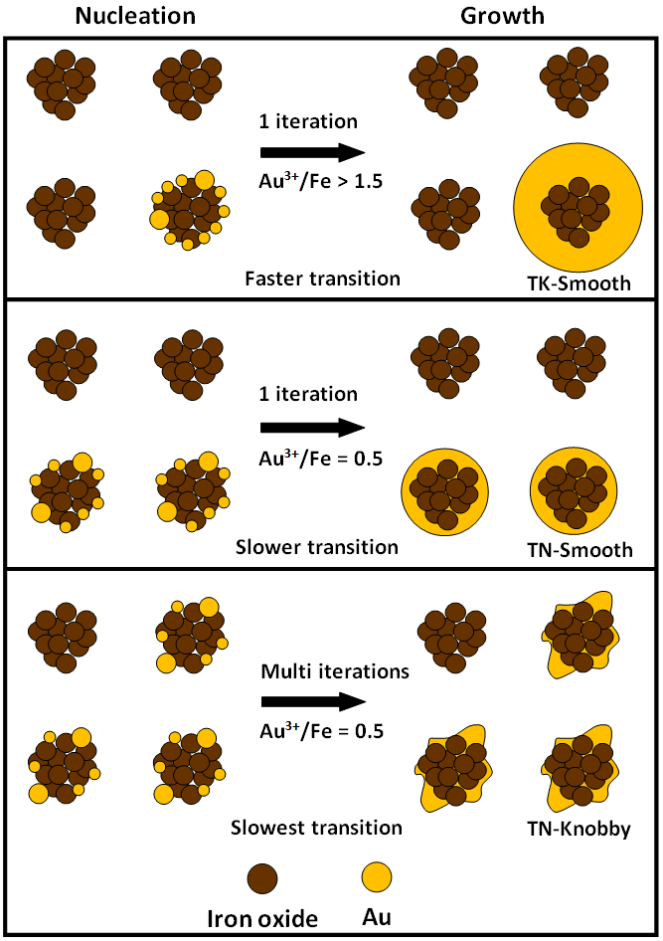

3.3 RESULTS

3.3.1 Au Nucleation and Growth Kinetics on Iron Oxide Substrates with a Single Iteration

The diameter of the starting citrate stabilized iron oxide nanoclusters without any added Au^{3+} was ~40 nm as shown by TEM in Figure 3.1A and more definitively by the DLS in Figure 3.2A. To coat the iron oxide cores, the feed Au^{3+}/Fe ratio was varied as shown in Figure 3.1. The mPEG-SH was present in initial mixture for bonding to the growing Au surfaces. For a complete monolayer of mPEG-SH on a 50 nm diameter Au nanoparticle surface, the estimated mPEG-SH/Au mole ratio would be 0.006 (Supporting Information). Thus, a higher mPEG-SH/Au^{3+} feed mole ratio of 0.08 was chosen for all experiments. At the lowest Au^{3+}/Fe ratio, a few darker 10-15 nm domains of Au were present, as shown in Figure 3.1B and Scheme 3.1 for a thin partial coating (TN-Partial) on the lighter iron oxide substrate, a consequence of the higher electron density for Au. As the Au^{3+}/Fe ratio increased progressively to 1.5, the size of the particles with thick relatively smooth (with very small knobby protrusions) Au coatings increased reaching 80 nm (TK-Smooth, Scheme 3.1).

The hydrodynamic diameters for the Au coated nanoclusters in the dispersion without centrifugation are shown in Figure 3.2 and Table 3.S1. For control experiments performed with iron oxide nanoparticles at the same mass concentration, low count rates of 5-20 kcps were observed, indicating very weak scattering of light from the 633 nm laser. After reaction, count rates were 400-500 kcps. Thus, the measured size distribution for a mixture of Au coated iron oxide nanoclusters in the presence of uncoated nanoclusters after reaction will be highly biased to the coated clusters, a beneficial result. The variance values for the hydrodynamic diameters were quite small (Figure 3.2 and Table 3.S1). The hydrodynamic diameters are in the same range as the

diameters in the TEM images, although the numbers of particles in the TEM images were too small for statistically significant determination of particle size. According to both the TEM images and DLS, the shell thickness increases monotonically with the Au^{3+}/Fe ratio. At Au^{3+}/Fe of 0.125 (TN-Partial), the hydrodynamic diameter is only 2 nm larger than for the initial naked iron oxide clusters. This value of 2 nm is well below the 12 nm end-to-end chain length of mPEG-SH (MW 20,000).[53] Only a small fraction of the surface is covered with Au and thiol groups on the polymer bound to Au. As Au^{3+}/Fe ratio increased to 0.5 (TN-Smooth), the measured mean hydrodynamic diameter was 57 nm, indicating a 7.5 nm shell thickness composed of a thin Au shell bound with flexible mPEG-SH molecules. Here the Au covered a much larger fraction of the surface as also seen by TEM, and thus a much larger amount of polymer was adsorbed. Much larger particles were formed at higher Au^{3+}/Fe ratios, and the hydrodynamic diameter reached 159 at a Au^{3+}/Fe ratio of 6 (TK-Smooth). At this high ratio, 30 nm pure Au nanoparticles were also present, as shown in Figure 3.2B by DLS.

The absorbance spectra of the Au coated nanoparticles were obtained by subtraction of the initial iron oxide specta given in Figure 3.2C. At a Au^{3+}/Fe ratio of 0.125 (TN-Partial), a relatively broad absorbance is present in the visible and NIR regions from 500 to 850 nm, despite the extremely low amount of Au. For Au^{3+}/Fe ratios of 0.25-0.5 in Figure 3.2C (TN-Smooth), the absorbance peak in the visible region increased to a greater extent than absorbance above a wavelength of 700 nm. For Au^{3+}/Fe ratios from 1 to 6, the SPR peaks were blue shifted as the shells became much thicker (TK-Smooth). SPR peak maxima on the order of 600 nm have been observed often for thick Au shells on iron oxide.[15,28,36,38,40,41]

To better understand the mechanism, the kinetics of Au nucleation and growth were monitored *in situ* by UV-Vis spectrometry at 755 nm. In Figure 3.3A, the

absorbance of Au on substrate for Au^{3+}/Fe mass ratio 0.125 -0.5 reached a plateau within the first 30 s. The height of the plateau increased with the Au^{3+}/Fe ratio suggesting a greater degree of nucleation and growth, consistent with thicker shells in Figure 3.1. When Au^{3+}/Fe ratio was raised higher to 1.0 or 1.5, the kinetics became even faster and the plateau height further increased as shown in Figure 3.3B. These results suggest that the large heterogeneous surface area of iron oxide was sufficient to achieve rapid nucleation. However, for Au^{3+}/Fe ratios of 3.0 and 6.0, the absorbance increased continuously for 5 min without reaching a plateau.

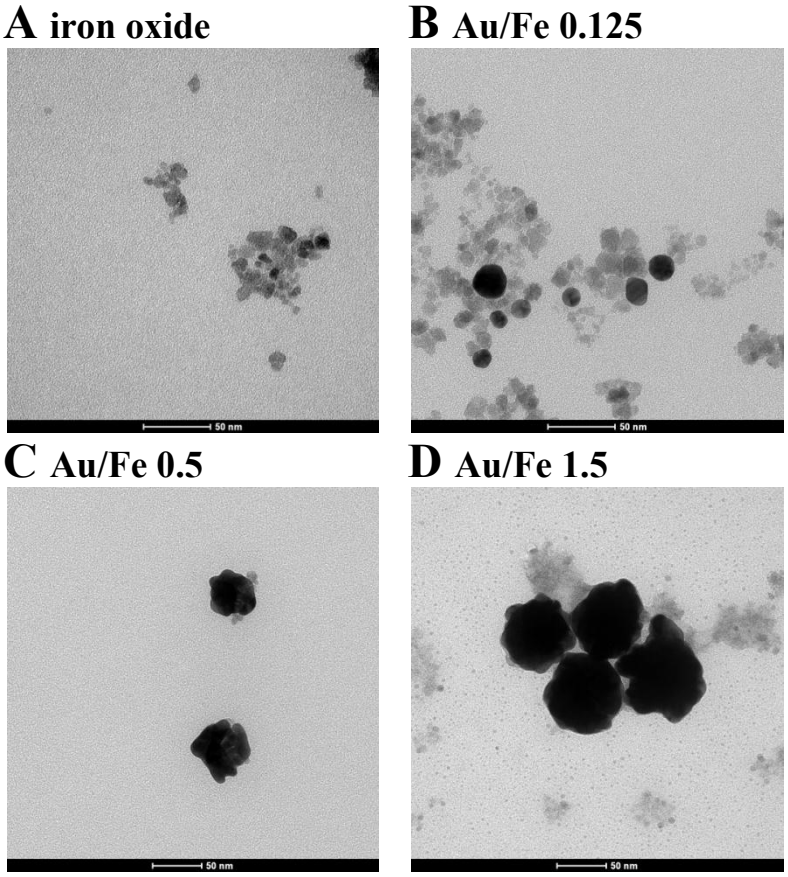

Figure 3.1 TEM images of gold on iron oxide made from Au/Fe mass ratio 0, 0.125, 0.5 and 1.5 with a single iteration.

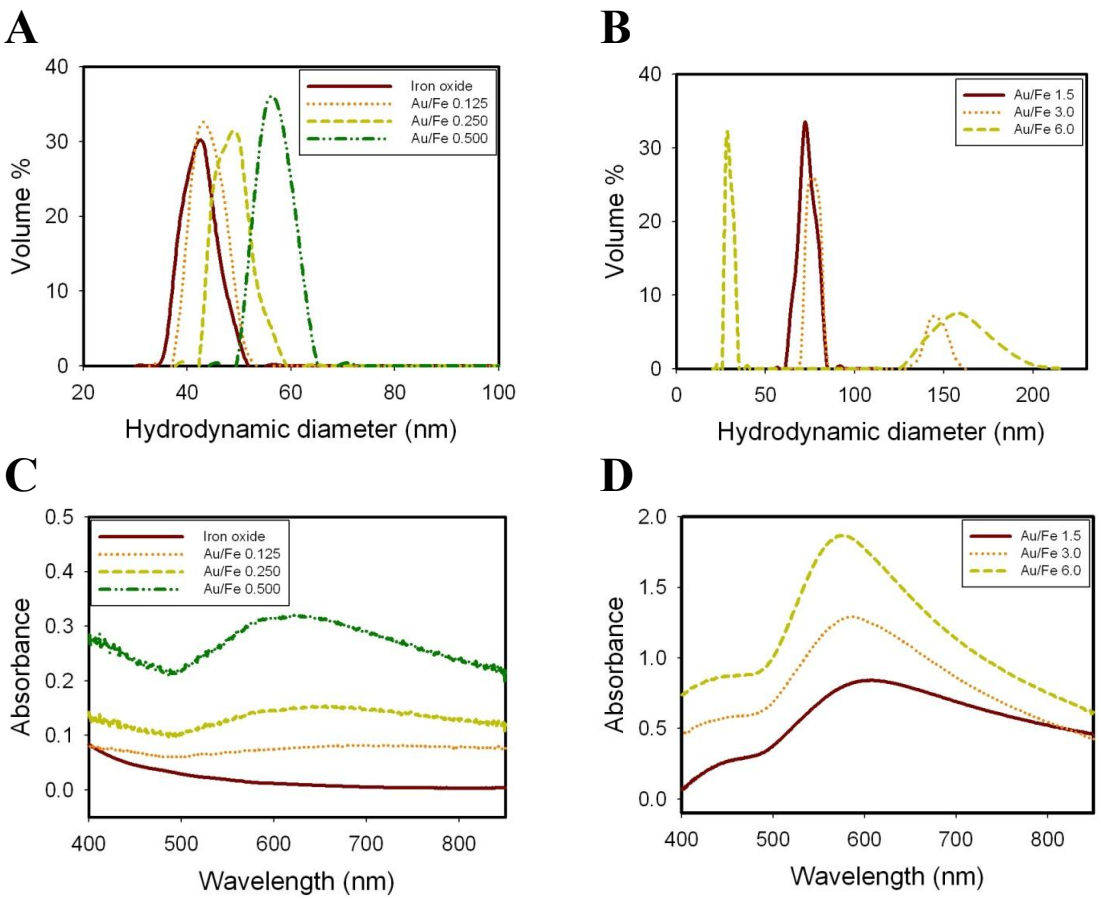

Figure 3.2 Hydrodynamic diameters A, B and Equilibrium absorbance spectra C, D of synthesized gold coated iron oxide nanoparticle dispersion with a single iteration after iron oxide base line deduction without centrifugation.

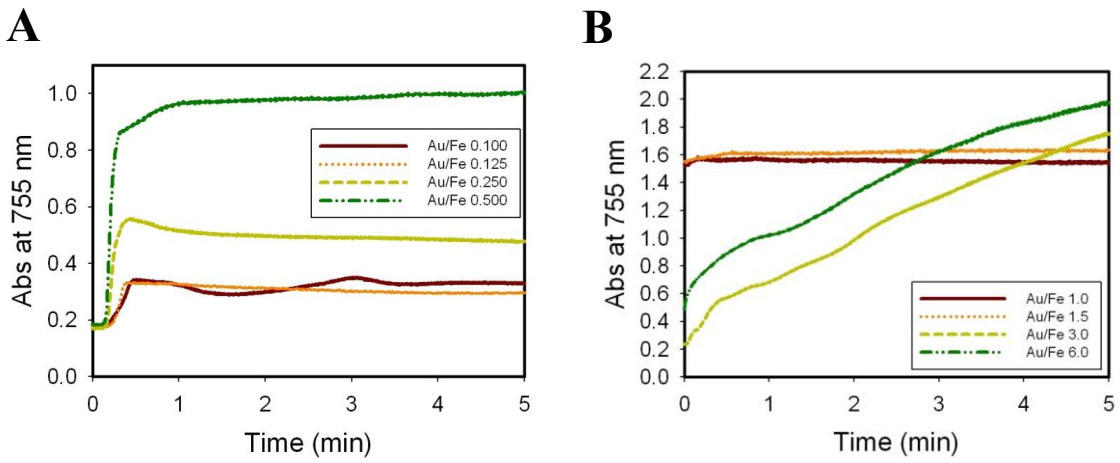

Figure 3.3 Au nucleation and growth kinetics monitored by real absorbance of gold on iron oxide at 755 nm in situ for a single iteration. A, Low Au/Fe mass ratio 0.1 - 0.5; B, high Au/Fe 1.0 - 6.0.

3.3.2 Au Nucleation and Growth Kinetics on Iron Oxide Substrates with Multiple Iterations

The number of iterations of Au^{3+} precursor addition was varied for a total Au^{3+}/Fe ratio of 0.5 to control the morphology. A smooth, relatively round (TN-Smooth), Au coated particle texture is shown in Figure 3.4A for a single iteration, similar to the TEM image in Figure 3.1C. For 3 equal iterations, the coatings were thinner and with knobby protuberances on the surface of the clusters (Figure 3.4B, TN-Knobby). This trend continued as the number of iterations increased from 3 to 5. According to DLS, the mean hydrodynamic diameters of Au coated iron oxide nanoparticles decreased from 61 nm to 57 nm as the number of iterations increased from 1 to 5 as shown in Figure 3.5A and Table 3.2. This decrease in size was also evident in the TEM images (Figure 3.4).

Furthermore, the Au/Fe ratio from AAS decreased by a factor of ~3 with this decrease in hydrodynamic diameter, and consequently, shell thickness (Table 3.1).

To provide insight, a simple geometric model was used to estimate the thickness of a uniform shell on a 42 nm spherical iron oxide core (despite the actual nonspherical nanocluster geometry) from the mass values obtained by AAS (Supplemental information). The calculated Au shell thicknesses ranging from 0.75-2.0 nm (Table 3.1) were below the thicknesses obtained by subtracting the core value of 42 nm from the hydrodynamic diameter (Table 3.2), which ranged from 7.5-9.5 nm (Table 3.2). This difference indicates an approximate thickness of the mPEG-SH layer, as well as uncertainty from the presence of uncoated iron oxide particles and the complex geometry.

The behavior of the SPR for the samples after centrifugation are shown in Figure 3.5B. For one iteration, the absorbance spectrum was similar to that in Figure 3.2C (which was not centrifuged), for the thin relatively round and smooth coating (TN-Smooth). However, for 3 or 5 iterations, the absorbance shifted progressively into the NIR region and became broader and flatter as the shell became thinner and the knobby protrusions became larger (TN-Knobby, Scheme 3.1). To our knowledge, this type of morphology and spectra has been reported only once previously for so called nanoroses, however, only one type of reaction condition and particle was investigated.[2] The extinction coefficients per weight of gold at 755 nm were higher for these particles as we can see in Table 3.1 and their value increased with an increase in the number of iterations.

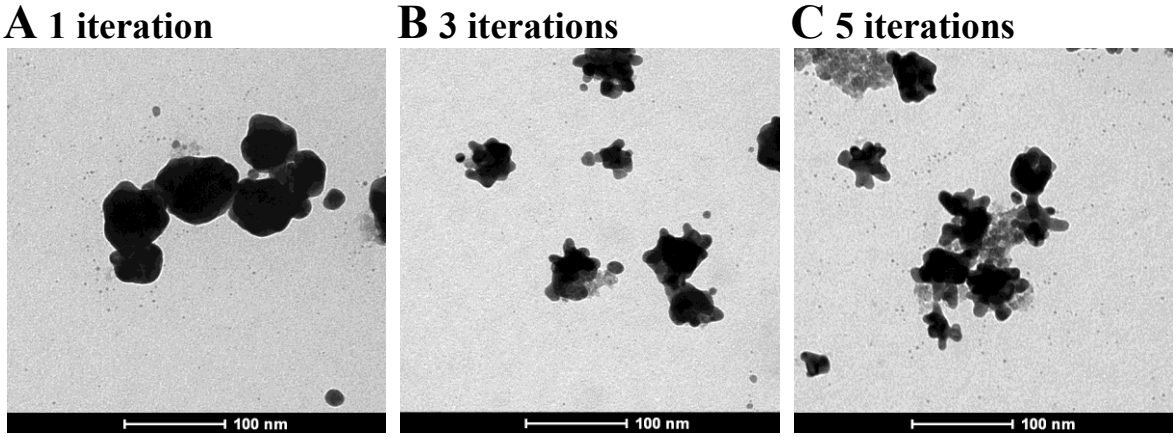

Figure 3.4 TEM images of gold coated iron oxide nanoparticles made from a total Au/Fe mass ratio of 0.50 with varying numbers of iterations. All samples were prepared from reactant mixture after centrifugation separation at 6000 rpm for 6 mins.

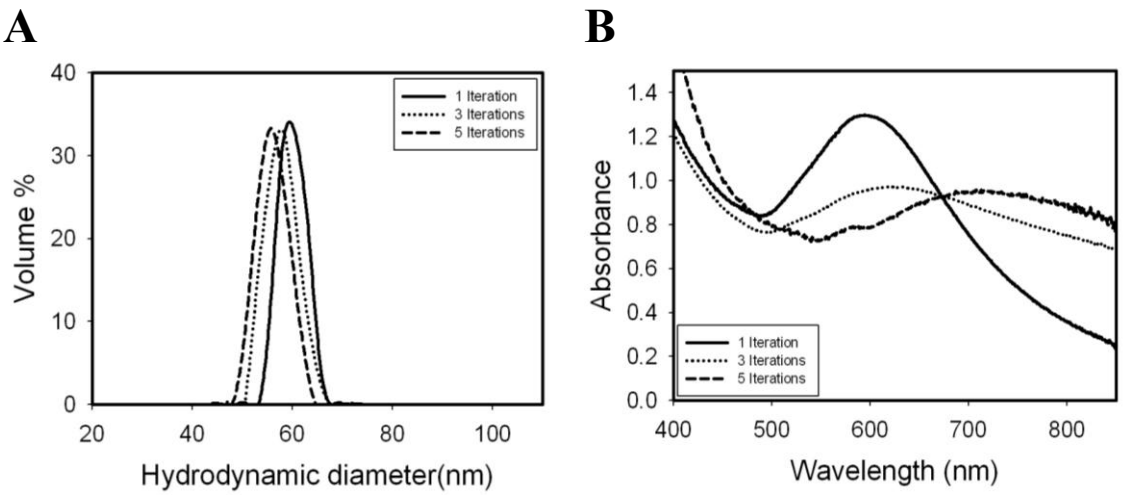

Figure 3.5 The hydrodynamic diameters A and absorbance spectra B of gold coated iron oxide nanoparticles made from a total Au/Fe mass ratio of 0.50 with varying numbers of iterations.

Table 3.1 Elemental analysis of gold coated iron oxide nanoparticles made from a total Au/Fe mass ratio of 0.50 with different iterations.

	Au/Fe	Au %	Fe %	Estimated total diameter (nm)	Extinction Coefficient ($cm^2/\mu g$ Au)
1 iteration	2.40	17.20	3.70	46.0	0.040
3 iteration	1.30	9.90	3.60	44.3	0.043
5 iteration	0.84	5.20	3.00	43.5	0.050

Table 3.2 Mean Size and Standard Deviation of Textured Thin Gold Coated Iron Oxide Nanoparticles
Au/Fe=0.5, reached with different iterations

Au/Fe ratio	Mean (nm)	Variance (nm)	% Standard deviation
1 iteration	61	2.6	4.3
3 iterations	59	3.0	5.1
5 iterations	57	3.2	5.6

3.3.3 Au Nucleation and Growth Kinetics on Iron Oxide Substrates with Continuous Precursor Addition

The number of iterations was raised to infinity by adding the Au^{3+} precursor continuously to an iron oxide dispersion. Here Au chloride (0.5 mg Au^{3+}/ml) was injected with a syringe pump at a rate of 0.1 ml/s for 2 mins. For the uncoated iron oxide nanoclusters on the order of 40 nm, the primary particle size was 8 nm (Figure 3.6A). For a total Au^{3+}/Fe ratio 0.5, high resolution TEM images (Figure 3.6B and 6C) after centrifugation reveal lattice fringes from Au and Fe_3O_4 crystalline domains. The lattice spacing of 0.244 nm in the interior of the cluster from an 8 nm primary spherical particle indicated the (3 1 1) plane of Fe_3O_4 in Figure 3.6C, which is quite different from any other Fe_3O_4 or Au lattice planes. Two Au crystalline facets for the (1 1 1) and (2 0 0) orientations correspond to 0.236 nm and 0.204 nm d-spacings, respectively for Au. These Au shells on the exterior of the cluster are only a few nm thick and are highly curved, as a

consequence of the curvature of the surfaces of the iron oxide primary particles in the core.

The total feed Au^{3+}/Fe ratio was varied to attempt to manipulate the thickness and shape of the Au shells, as shown in the TEM images in Figure 3.7. At an Au^{3+}/Fe ratio of 0.125, a few spherical 12-15 nm darker spots are evident on the lighter iron oxide nanoclusters in Figure 3.7A and 7D (TN-Partial), indicating an extremely thin Au coating. In addition, extremely small 1 nm Au particles, which may be considered Au embryos or seeds may be observed on the surface of the iron oxide clusters (Figure 3.7D). The mean hydrodynamic diameter by DLS of these Au coated iron oxide nanoclusters was 51 nm DLS (Table 3.4). At a higher Au^{3+}/Fe ratio of 0.25, the number of Au-coated domains on the iron clusters increased as observed by TEM in Figure 3.7B and 7E. Consistent with these thicker coatings, the hydrodynamic diameter increased to 54 nm (Table 3.4). At the highest Au^{3+}/Fe ratio of 0.5, the shells became progressively thicker and the mean hydrodynamic diameter increased to 61 nm (Table 3.4, TN-Knobby). According to AAS, the final Au/Fe ratio increased monotonically as expected with the initial Au^{3+}/Fe ratio, consistent with the TEM and DLS results.

Based on the final Au/Fe ratio from AAS, the theoretical (assuming a simple spherical core and uniform shell) shell thickness ranged from 0.2 to 0.6 nm, as the Au^{3+}/Fe ratio varied from 0.125 to 0.5. The observed thicknesses by TEM were uneven on the partially coated iron oxide cores. Thus the thicknesses in the coated patches of the surface, on the order of a few nm, were higher than the theoretical mean thickness for a simple core-spherical shell model. The thicker shells determined from DLS include the thickness of the adsorbed polymer on Au coated regions of the nanocluster surface, with an end-to-end distance of 12 nm, and also complications from the non-spherical nanocluster geometry.

The absorbance spectra may be correlated with the morphologies observed by TEM and the diameters by DLS. In Figure 3.8B, the absorbance intensity increased in the entire spectral range as the feed Au^{3+}/Fe ratio increased. In addition, the SPR peak shifted to the NIR region as the Au shell thickness was increased. At an Au^{3+}/Fe ratio of 0.5 the maximum in SPR was above 700 nm for the particles with knobby surfaces according to the TEM images in Figure 3.7(TN-Knobby, Scheme 3.1). The shells were still thin according to the DLS sizes in Figure 3.8A. Similar spectral changes with size were found for Au^{3+} precursor added by 5 iterations (Figure 3.S1, Table 3.S2). The extinction coefficient per weight of gold at 755 nm was observed to decrease as the added Au^{3+}/Fe ratio increased as can be seen in Table 3.3.

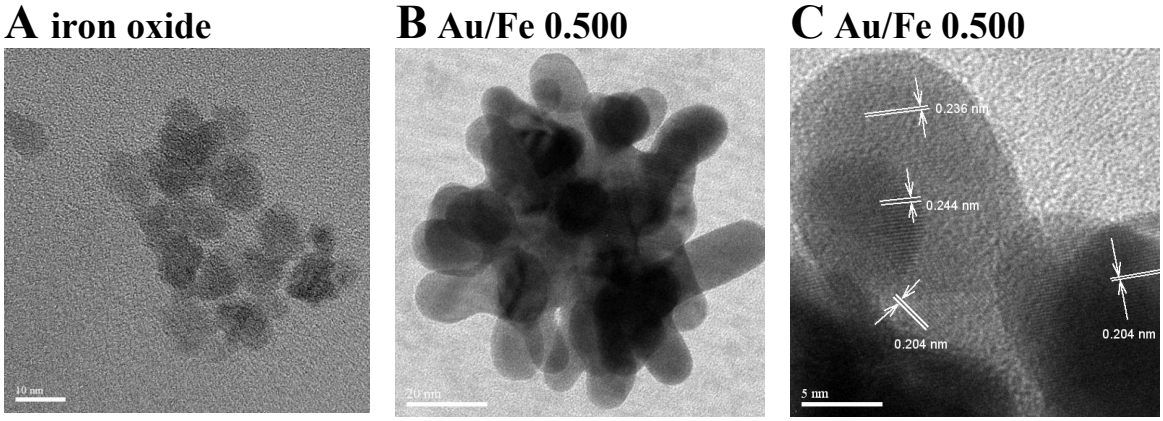

Figure 3.6 HRTEM images of iron oxide nanocluster A and gold coated iron oxide nanoparticle B. A magnified image of the upper tip from B indicating thin gold coating on Fe_3O_4 nanoparticles C.

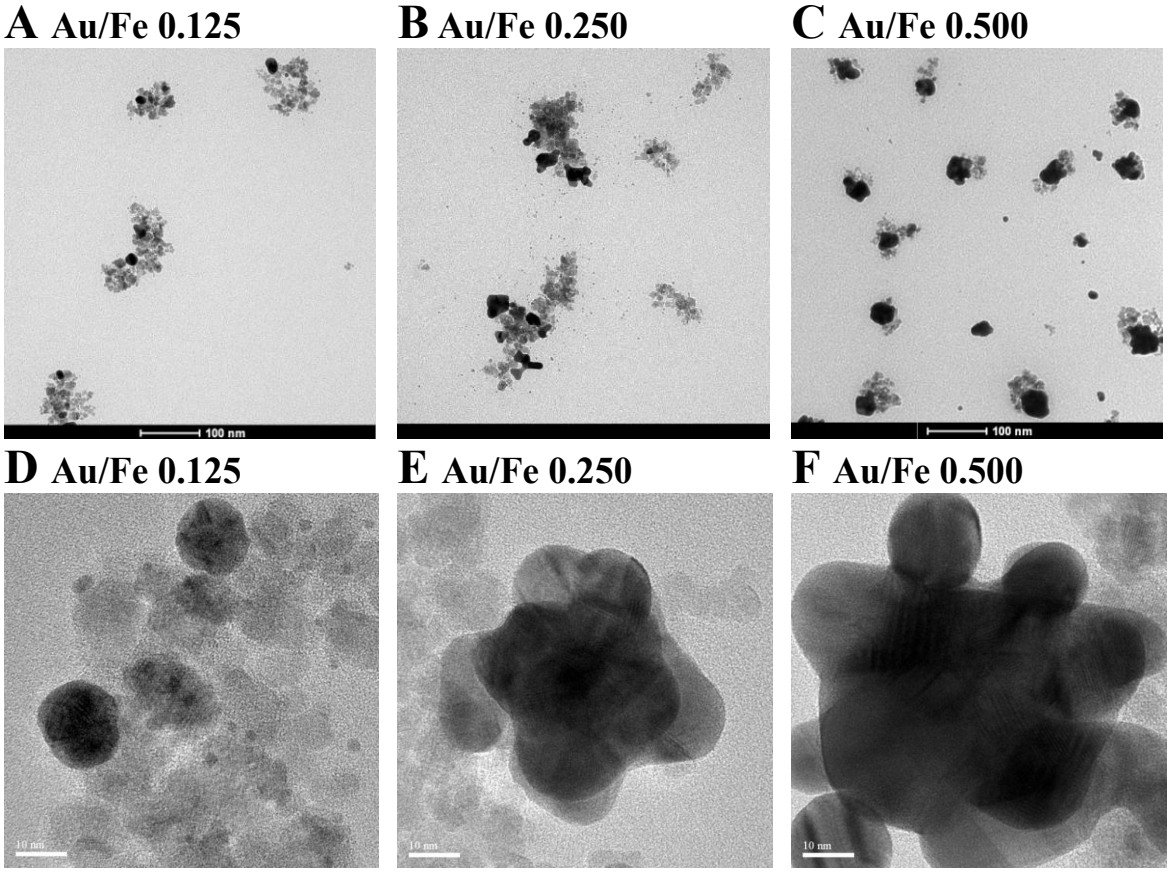

Figure 3.7 TEM images of the morphology evolution of thin gold shells on iron oxide substrates. Specimens were prepared by taking samples at Au/Fe mass ratio 0.125 (A, D), 0.25 (B, E) and 0.50 (C, F) from the continuous addition of gold precursor experiment and then being separated by centrifugation.

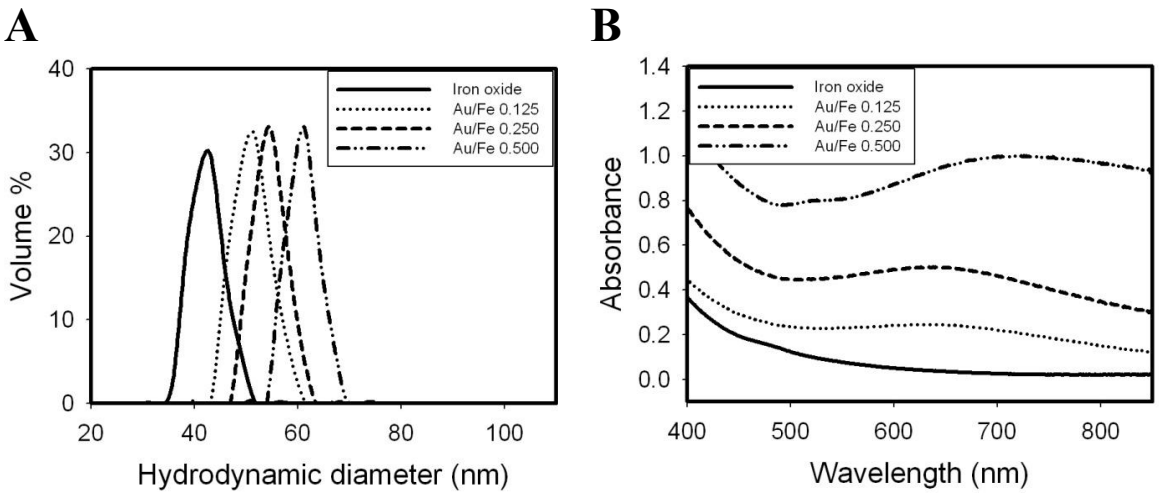

Figure 3.8 The evolution of hydrodynamic diameters A with the addition of gold precursor continuously and absorbance spectra B for increased gold to iron ratios accordingly. mPEG-SH/Au mole ratio was fixed at 0.08 for all experiments.

Table 3.3 Elemental Analysis of Textured Thin Gold Coated Iron Oxide Nanoparticles by AAS
Au/Fe= 0.5 was reached with continuous addition of Au precursor.

Au/Fe ratio	Final Au/Fe ratio	% Fe yield	% Au yield	Estimated total diameter (nm)	Extinction Coefficient ($cm^2/\mu g$ Au)
0.125	0.145	3.8	4.6	42.3	0.061
0.250	0.281	4.0	5.3	42.5	0.051
0.500	0.691	4.6	7.2	43.2	0.050

Table 3.4 Mean Size and Standard Deviation of Textured Thin Gold Coated Iron Oxide Nanoparticles
Au/Fe= 0.5 was reached with continuous addition of Au precursor.

Au/Fe ratio	Mean (nm)	Variance (nm)	% Standard deviation
Iron oxide	42	3.2	7.5
0.125	51	3.4	6.8
0.25	54	3.1	5.7
0.5	61	3.0	4.8

3.3.4 The Separation of Au Coated Iron Oxide Nanoparticles from Uncoated Ones by Centrifugation

The degree of separation of the Au coated and uncoated iron oxide particles may be estimated from the sedimentation coefficient, $S = (1-\rho_1/\rho_2)*m/f$, where ρ_1 is the density of the solvent, ρ_2 and m are the density and the mass of the particle, respectively, and f is the friction factor. The densities of Au coated versus uncoated iron oxide can be very different given the bulk densities of 19.3 and 5.2 g/cm^3 for Au and Fe_3O_4, respectively. The predictions of the model in Table 3.S3 indicate that a centrifugation speed on the order of 5,000-6,000 rpm is sufficient to move the Au-coated particles to the bottom of the centrifuge tube in ~ 6 min. However, at this speed the sedimentation of the uncoated particles is relatively low, and thus it should be possible to concentrate the coated particles in the precipitate.

Based on the theoretical predictions, the centrifugation speed, for 6 min, was varied for the case of the particles produced in 5 iterations according to Figure 3.9. For each Au^{3+}/Fe ratio, the Au yield in the precipitate increased significantly for an increase in speed from 2,000 to 10,000 rpm, and the yield decreased in the supernatant. The Au yields in the precipitate were higher for the higher initial Au^{3+}/Fe ratios, which produced thicker shells as expected. Thus, these changes in yields were observed in regions of centrifugation speeds as expected from the theoretical predictions of the sedimentation coefficient, based on the Au coatings. The detailed elemental analysis data for Au and Fe before and after centrifugation are shown in Table 3.S4. After centrifugation under all conditions, the Fe yield in the precipitates was less than 10% of the total in the nanoclusters prior to separation. From a practical point of view, the uncoated iron oxide may be recycled.

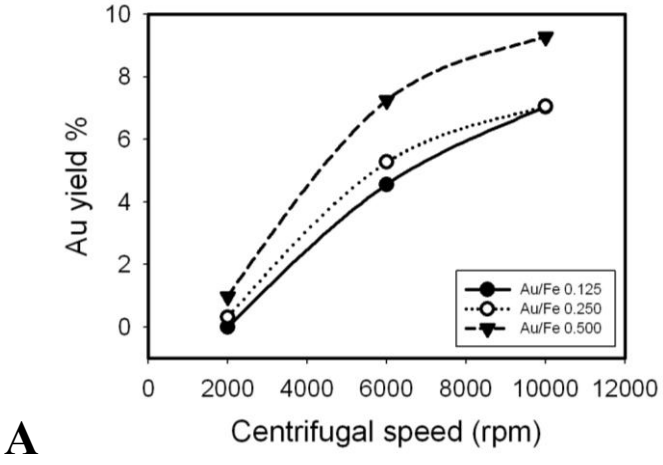

A

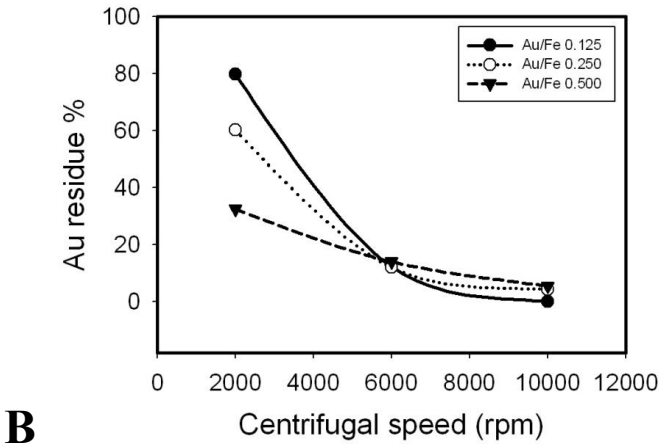

B

Figure 3.9 Au yield in precipitate and Au residue in supernatant after centrifugation at different speed for 6 mins. The yield and residue were calculated as a percentage of initially added gold precursor. Au precursor was added by 5 iterations.

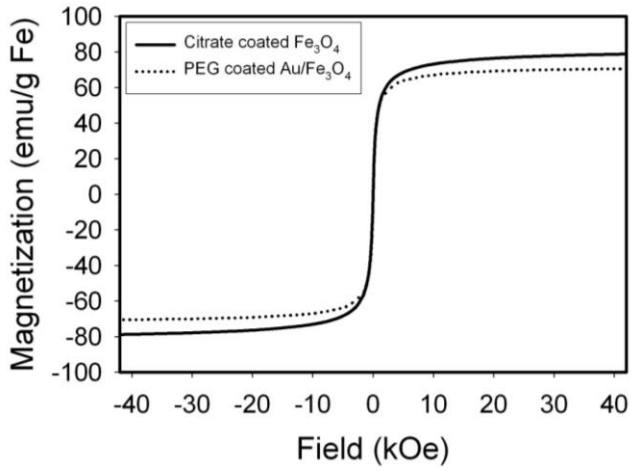

Figure 3.10 Normalized magnetization of dried iron oxide nanoclusters and thin gold coated iron oxide nanoparticles at 300K.

3.3.5 Magnetic Properties of the Au Coated Iron Oxide Nanoparticles

The magnetization of dried powders prepared from uncoated iron oxide nanoclusters and Au coated iron oxide nanoclusters synthesized at a total Au^{3+}/Fe ratio 0.5 with 5 iterations (TN-Knobby) after centrifugation was measured by a SQUID at 300 K. The measured magnetization values were normalized by the mass of Fe based on citrate/Fe_3O_4 mass ratio, mPEG-SH/particle ratio determined by TGA analysis and Au/Fe ratio determined by AAS (Figure 3.S3, Supporting Information). The magnetization increased rapidly for an applied magnetic field from 0 to ±5 kOe (0.5 Tesla) and reached saturation quickly below 10 kOe (1.0 Tesla) as shown in Figure 3.10. The normalized saturation magnetization of Au coated iron oxide nanoparticles is 70 emu/g Fe compared with 78 emu/g Fe for citrate coated iron oxide nanoclusters. Thus, the influence of the thin Au coatings on the iron oxide surfaces produced limited surface defects that potentially may degrade the magnetization. Given the particle Au/Fe ratio of 0.84 from

AAS, the saturation magnetization of TN-Knobby nanoparticles is 32 emu/g particles. This high magnetization per particle weight reflects the unusually high mass fraction of magnetic iron oxide material given the exceptionally thin Au coating, compared to many previous particles with much thicker coatings.[32, 34]

3.4 DISCUSSION

In order to explain the range of experimental morphologies shown in Scheme 3.1, a general mechanism is presented to describe thin autocatalytic growth on substrates (TAGS). Briefly, the thermodynamic driving force for nucleation and growth is characterized for reduction of Au^{3+} on Au surfaces in contrast with homogeneous reduction in solution. Next, a brief summary of the seeded autocatalytic growth mechanism is presented for formation of pure Au nanoparticles, to serve as background. The primary focus is on the TAGS mechanism to describe the formation of the various thin Au coatings on iron oxide substrates. The discussion ends by relating the behavior of the SPR spectra for the Au coated nanocomposites to the particle morphologies.

3.4.1 Autocatalytic nucleation and growth of pure Au nanoparticles

Hydroxylamine has been used to selectively promote growth of Au on Au surfaces relative to homogeneous nucleation of Au from soluble precursors.[12, 13] The cell potential for reduction of Au by hydroxylamine to Au^o on a Au metal surface in eq. (1)

$$2Au^{3+} + 6NH_2OH \Leftrightarrow 3N_2 + 6H_2O + 6H^+ + 2Au^0_{(metal)} \quad (1)$$

$$2Au^{3+} + 6NH_2OH \Leftrightarrow 3N_2 + 6H_2O + 6H^+ + 2Au^0_{(atom)} \quad (2)$$

is 1.936 V, based on eqns. (S1) to (S6) in the supplemental section. This potential is far more thermodynamically favorable than the value of -1.244 V to form a single Au^o atom

homogeneously described in eq. (2). Thus, hydroxylamine adsorbed on an iron oxide surface may be expected to favor nucleation of Au seeds on the surface, relative to undesired homogeneous nucleation to form pure Au nanoparticles in bulk.

A mechanism of homogenous nucleation to produce Au seeds followed by growth on the seeds has been widely used to synthesize nanoparticles of controlled size with narrow polydispersity.[14] Homogenous nucleation to form Au seeds

$$nAu^{3+} \xrightarrow{k_1} nAu^0 \ (nucleation) \qquad (3)$$

may compete with growth on the Au seeds

$$nAu^{3+} + nAu^0 \xrightarrow{k_2} 2nAu^0 \ (growth) \qquad (4)$$

where n is chosen arbitrarily to define the number of Au atoms in one Au seed. The growth reaction is autocatalytic in that the Au surface in the product is also a reactant.

The resulting rate expressions are[10, 19]:

$$\frac{d[Au^0]}{dt} = k_1[Au^{3+}] + k_2[Au^{3+}][Au^0] \qquad (5)$$

$$[Au^0] = [Au^{3+}]_0 - [Au^{3+}] \qquad (6)$$

$$\frac{d[Au^0]}{dt} = k_1[Au^{3+}] + k_2[Au^{3+}]([Au^{3+}]_0 - [Au^{3+}]) \qquad (7)$$

where k_1 and k_2 are rate constants for nucleation and growth, respectively, and $[Au^{3+}]_0$ is the initial concentration of precursor. The values if k_2 will be relatively large given the much greater thermodynamic driving force for reduction of Au^{3+} on a Au surface than for homogeneous nucleation. The initial rate of formation of Au^0 by homogeneous nucleation will be slow, given the growth (second term) in eq. (7) will be zero. As Au^0 increases, the contribution the second term in eq. (7) will become prevalent. Eventually when Au^{3+} is highly depleted, the rate slows down progressively, resulting in a well-known sigmoidal shape kinetics curve.[10, 14] For a decrease in $[Au^{3+}]_o$, the relative contribution of the growth step becomes smaller in eq.(7) relative to nucleation. For example, after half of $[Au^{3+}]_o$ reacts, the rate is proportional to $k_1 + k_2[Au^{3+}]_o/2$. For a given nucleation rate, a

decrease in the growth rate will lead to more nuclei, and thus a larger number of smaller final particles. Thus, a delay in autocatalytic growth provides more separation of nucleation and growth, leading to smaller particles and lower polydispersity in the seeded growth mechanism.[15]

3.4.2 Heterogeneous nucleation and growth of Au shells on substrates for a single iteration at a relatively low Au^{3+}/Fe ratio

The kinetics for formation of Au shells on iron oxide substrate particles exhibited a sigmoidal shape in Figure 3.3, as seen in previous studies for pure Au nanoparticles.[10, 14] Thus, we chose to extend the model for homogeneous nucleation and growth (eq. 3-4) to the heterogeneous case with substrate particles. An important additional degree of freedom must be considered, the fraction of the iron oxide substrates that become covered with seeds during the nucleation phase, and how this influences subsequent growth. Furthermore, the energy barrier for the formation of Au seeds is lowered by the heterogeneous iron oxide substrate. The barrier is further lowered by the adsorbed hydroxylamine on the iron oxide surfaces.[7]

A mechanism for thin autocatalytic growth on substrates (TAGS) is shown in Scheme 3.2 for three levels of separation of nucleation and growth. The substrate (core) may be a nanocluster (brown), or another shape, for example, a sphere (not shown). In each case, the region to the left of the arrow depicts the end of the nucleation phase, prior to the rapid autocatalytic growth to the final product on the right.

The scenario for a Au^{3+}/Fe ratio of 1.5 added in one iteration is given in the top panel in Scheme 3.2 and the first column in Table 3.5. In the experiments in Figure 3.1-3, a Au^{3+}/Fe ratio of 1.5 provided nucleation of Au seeds on a very limited number of iron oxide nanoparticles, as indicated by TEM. Given the high $[Au^{3+}]_0$, for an Au^{3+}/Fe ratio

above 1.5[7], the autocatalytic growth rate is relatively high as given by the second term of eq. (7). Therefore, the time for nucleation to produce Au seeds is short before the autocatalytic growth on the seeds becomes dominant. Given the short nucleation time, Au seeds are deposited on a small fraction of the substrate particles as indicated schematically. Rapid growth on a small number of substrates, or equivalently, relatively small separation between nucleation and growth, results in relatively thick shells as shown in Figure 3.1D and top panel of Scheme 3.2. These TK-Smooth (Scheme 3.1) Au shells (~ 10 nm) are commonly observed as Au^{3+}/Fe ratios are typically > 1.5.[7, 22, 30, 32, 34, 35]

The middle panel in Scheme 3.2 describes the behavior at a lower Au^{3+}/Fe ratio of 0.125-0.5 and a single iteration of precursor addition. The second column in Table 3.5 describes this behavior relative to the higher Au^{3+}/Fe ratios in the top panel. For slower autocatalytic growth at a lower Au^{3+}/Fe ratio, Au seeds are nucleated on more iron oxide substrate particles. Here the transition time from nucleation to growth is longer. The longer nucleation time allows deposition of Au seeds on a larger fraction of substrate particles, and thus, a smaller number of seeds on each substrate. Upon spreading the Au seeds on more substrate particles, the amount of Au per substrate (shell thickness) decreases upon completion of growth. This mechanism is consistent with the thinner shells as shown experimentally in Figure 3.1C, 4A and Scheme 3.2, relative to the thicker shells in the top panel at higher Au^{3+}/Fe ratios. Thus, greater separation between nucleation to form Au seeds on the substrate and autocatalytic growth at a lower Au^{3+}/Fe ratios, and consequently lower supersaturation, is a novel strategy to form extremely thin shells. Although TN-Smooth (Scheme 3.1) Au shells have been achieved on small iron oxide substrates (~10 nm diameter)[25, 26, 29, 54-56] with low MW ligands, they have not been reported for substrates larger than 20 nm, where polymeric stabilizers are needed.

3.4.3 Heterogeneous nucleation and growth of Au shells on substrates with iterative or continuous Au^{3+} addition

Given the decrease in the shell thickness with a decrease in $[Au^{3+}]_0$ for the first two panels in Scheme 3.2 and in Figure 3.2, it would seem desirable to continue this trend further. However the total amount of final Au deposited would become too low. To overcome this stoichiometric limitation, Au^{3+} may be fed to the system in multiple iterations or continuously but at much higher Au^{3+}/Fe ratios.[7] Here we explain this strategy with the TAGS mechanism, as the very thin shells in Figure 3.6 have rarely been reported for substrates > 20 nm. For this comparison, the middle panel is to the bottom panel as the first column is to the second column in Table 3.5. The early $[Au^{3+}]$ values are extremely low such that Au seeds may be nucleated on iron oxide substrates with minimal growth, as shown in Figure 3.7D, and the bottom panel in Scheme 3.2. After each iteration Au^{3+} is depleted, the next iteration produces a very small increase of Au. If little Au^{o} surface is present, the new iteration will grow more seeds predominantly, still with limited transition to autocatalytic growth (eq. 7) as shown in the bottom panel of Scheme 3.2 and in high resolution TEM in Figure 3.7 for low Au^{3+}/Fe ratios. With delayed autocatalytic growth, the Au seeds are deposited on an even larger fraction of iron oxide nanoclusters than for a single iteration (middle panel), and with fewer Au seeds deposited per particle (Figure 3.7A versus Figure 3.4A). Thus, Au shells grew on more substrate particles for a constant overall Au^{3+}/Fe ratio of 0.5, resulting in thinner shells as shown in Figure 3.4 and Table 3.2. This sequence is shown experimentally in Figure 3.7 with high resolution TEM for continuous addition.

In addition to tuning shell thickness with multiple iterations or continuous Au addition, the shape may also be manipulated, as shown experimentally in Figure 3.4 and

in the bottom panel of Scheme 3.2. The shape is controlled by the spatial distribution of nuclei deposited on each substrate particle. The relatively large number of Au seeds nucleated on each seeded substrate particle in the middle panel (relative to the lower panel) led to round shells during growth (Figure 3.4A). For the same total Au^{3+}/Fe of 0.5, under continuous Au^{3+} addition, the smaller number of seeds on each substrate (Figure 3.7A), provided more asymmetric sites for Au growth. Subsequent asymmetric growth led to knobby protrusions on a thin shell, as shown schematically in the bottom panel of Scheme 3.2 and the final particle morphology in Figure 3.7C and F. The greater fraction of coated substrate particles with Au seeds for continuous addition also plays a significant role. With less growth of Au per particle, the tendency of knobby shapes to be filled in to minimize interfacial area is lower than in the case of one iteration, where autocatalytic growth is more prevalent. To our knowledge, the formation of TN-Knobby shells (Scheme 3.1) by tuning the separation of nucleation and growth with low supersaturation values has not been reported previously.

In TAGS, a bimodal distribution of coated and uncoated particles is produced intentionally. The uncoated iron oxide substrate serve as a reservoir for nucleation of Au seeds at low Au^{3+}/Fe ratios to inhibit the autocatalytic growth of Au to form thick shells. After reaction, the coated particles are concentrated in the precipitate during centrifugation. The polydispersity in hydrodynamic diameter of these coated particles was very low (Table 3.2 and 4), indicating good separation between nucleation and growth, and prevention of aggregation by the polymer coatings.

3.4.4 Passivation and steric stabilization with mPEG-thiol

The Au coated particles would not be stable against aggregation without steric stabilization, except for the case of the TN-partial particles with very small amounts of

Au. The destabilizing attractive VDW forces between the iron oxide nanoclusters (without Au) are lowered in part by the porosity in the nanoclusters, and electrostatic repulsion from the citrate ions. Once the fraction of Au on the substrates becomes significant, the much stronger VDW forces for the Au versus iron oxide often cause aggregation.[30] In a recent study, 30 nm Au coated iron oxide nanoclusters with ~ 83% Au have been stabilized with physisorbed dextran (MW 10,000) on the surface.[2]

A chemically bound stabilizer such as mPEG-SH[38] with an end to end distance of 12 nm was found to be sufficient to provide particle stabilization. By assuming a complete monolayer of mPEG-SH (MW 20,000) on a 50 nm spherical Au nanoparticle surface, the estimated mPEG-SH/Au mole ratio would be 0.006 (Supporting Information). Thus, a higher mPEG-SH/Au^{3+} feed mole ratio of 0.08 was chosen for all Au coating experiments. mPEG-SH does not bind significantly to Fe_3O_4, which otherwise could inhibit nucleation of Au seeds on the surface. During TAGS, the polymer binds to the growing Au surfaces and provides passivation to prevent excessive growth. However the spaces between the anchored polymeric chains do not overinhibit growth, which is quite different from previous papers for heavily coated cores.[25, 29] As these surfaces are partially passivated by polymer, nucleation to form Au seeds at new sites on Fe_3O_4 are favored. Another interesting effect is that the time for polymer diffusion to the Au surfaces increases as the autocatalytic growth rate decreases, by the variation of Au^{3+} concentrations in Table 3.5. Thus passivation by polymer may further accentuate the formation of thinner coatings as a function of the transition time from nucleation to growth. Finally, these shifts may also influence particle shape by spreading the Au seeds on more substrate particles.

Table 3.5 The effects of Au^{3+} precursor addition profiles

Property	Faster growth on Au seeds	Slower growth on Au seeds
Initial Au^{3+}/Fe ratio (supersaturation)	Higher	Lower
Autocatalytic growth rate in early stage	Faster (less time for seed nucleation)	Slower (more time for seed nucleation)
Transition from nucleation to growth	Sooner (less separation between nucleation and growth)	Later (more separation between nucleation and growth)
Shell thickness	Thicker (e.g. rounder shells)	Thinner (e.g. knobby shells)
Role of polymer	Less time to adsorb and less restriction on growth	More time to adsorb and more restriction on growth (favors new nucleation)
Au yield in precipitate after centrifugation	Larger	Smaller

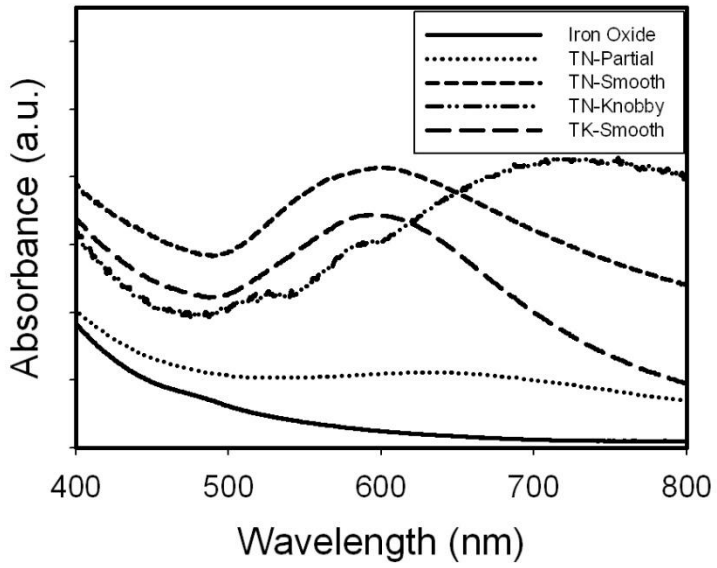

Figure 3.11 SPR spectra evolution from uncoated iron oxide nanoclusters to Au coated particles with different shell thickness and geometry. The arbitrary absorbance units were chosen to illustrate the spectra changes of the 4 particle classes shown in Scheme 3.1.

Table 3.6 Particle properties for different classes

	TN-Partial Figure 3.7A	TN-Knobby Figure 3.4C	TN-Smooth Figure 3.4A	TK-Smooth Figure 3.1D
Initial Au^{3+}/Fe mass ratio	0.125	0.5	0.5	1.5
Au^{3+} iterations	1	5	1	1
Final Au/Fe mass ratio	0.15	0.84	2.40	5.09
Extinction Coefficient (cm^2/μg Au)	0.061	0.050	0.040	0.029
Cross-section (10^{-15} m^2)	0.298	1.421	3.202	5.047
Hydrodynamic diameter (nm)	51	57	61	73
Absorbance peak max (nm)	Flat	730	620	600

3.4.5 SPR Spectra for various particle morphologies

Mie theory may be used to predict shifts in the SPR of a uniform Au shell on a spherical core with a given permittivity as a function of R_{total}/ R_{core}. Asymmetry in geometry from spherical Au nanoparticles produces hybridization between dipoles, quadrupoles and higher modes that cause spectral shifts to the NIR region.[32, 40] For a peak maximum of 700 nm, $R_{total}/ R_{core} < 1.2$ is required for a silica core with a permittivity of 2.0.[38] For an Fe_3O_4 core with a permittivity in the range of 5.5 - 6.1,[32] this value is $R_{core} < 1.25$ on the basis of calculations and experiments for an Au_2S core with a permittivity of 5.4.[41-43] For 2-3 nm Au shells on small iron oxide cores (< 10 nm diameter) R_{total}/ R_{core} is too large for NIR absorbance.[25, 26, 29, 54-56] Likewise, for relatively thin 5 nm Au shells on 18 nm iron oxide cores, where $R_{total}/ R_{core} = 1.56$, the SPR peak maximum was 590 nm.[36] The SPR peak of TK-Smooth nanoparticles with thicker Au shells (>20 nm) on small 9

nm iron oxide spherical cores was below 580 nm (Figure 3.11),[7] and approached that of pure Au spheres. In nearly all of these syntheses for cores in the range of 10 to 60 nm where autocatalytic growth led to shells such that $R_{total}/ R_{core} > 1.25$, the absorbance was limited in the NIR region.

Highly asymmetric cores may provide significant absorbance in the NIR for particles with smooth shells. Such behavior was observed for >8.5 nm thick Au shells on relatively large non-spherical iron oxide substrates (50-60 nm faceted or cubic).[32, 34] For our 7 nm smooth Au shells on relatively large 42 nm iron oxide nanocluster cores ($R_{total}/ R_{core} = 1.33$) (TN-Smooth in Scheme 3.1, Figure 3.1 C and Figure 3.4 A), the broad SPR peak shifted to 600 nm with significant absorbance in the NIR region (Figure 3.11).

The extremely thin, knobby Au shells on the iron oxide nanocluster cores in Figure 3.6B contributed to the strongest absorbance in the NIR region (Scheme 3.1, Figure 3.11). For spherical 42 nm cores the maximum predicted Au thickness would be 5 nm for $R_{total}/ R_{core} = 1.25$. The Au domains on the nanoclusters were thinner than 5 nm. The asymmetric shell thickness about the nanocluster core surface, as is evident in the knobby protrusions, encompasses attributes of high aspect ratios, as in the case of Au rods and nanorice[33] as well as nanoeggs[39] (asymmetric egg white shells). The combination of all of these asymmetries leads to the very broad NIR absorbance in contrast with sharper peaks for a single mode such as Au nanorods.[44] Related spectral behavior were observed for recently reported asymmetric Au coatings on iron oxide clusters,[2] however, only for a single morphology.

3.5 CONCLUSIONS

Autocatalytic growth of metal shells on metal oxide nanoparticle cores is often excessive as a result of the high metal/metal oxide ratios which are utilized to overcome

poor wetting on the low energy substrate. To mitigate the growth, we have introduced a general alternative concept of thin autocatalytic growth on nanparticle substrates (TAGS). The TAGS mechanism may be considered a generalization of the well-known seeded growth mechanism for pure nanoparticles[10, 12-14] to seeded growth of metals on heterogeneous low energy substrates. Low total metal precursor/metal oxide ratios (0.125-0.50 for Au^{3+}/Fe) are chosen to coat a small fraction of the substrate nanoparticles with unusually thin smooth or thin knobby Au shells (< 5 nm) on a 42 nm iron oxide cores. Multiple iterations or continuous addition of Au^{3+} precursor produce the smallest supersaturation values. During nucleation of Au seeds on a given substrate particle, the slow autocatalytic growth, at low supersaturation values, consumes a smaller amount of Au^{3+}. Consequently, new Au nuclei are seeded on a larger fraction of the iron oxide substrate particles, such that subsequent growth results in thinner shells. In essence, the lower supersaturation provides greater separation of nucleation of seeds and growth on them. Coated particles, with relatively monodisperse hydrodynamic diameters distributions, are separated efficiently from uncoated particles by centrifugation, given the large differences in the densities of Au and iron oxide. A covalently bonded polymer, mPEG-SH, provides steric stabilization against van der Waals attraction, while simultaneousy providing passivation of the growth of the Au coating. The less than 5 nm thin coatings along with asymmetry in shell geometries alter the interactions between plasmon modes and shift the SPR peak to the NIR region, with high cross sections, despite the small overall nanoparticle size. Additional asymmetry is introduced with the nanocluster cores, in contrast with spherical cores. Even further asymmetry and thus the largest red shifts are observed for the highly asymmetric thin knobby shells on nanocluster cores. The thin shells on small nanoparticles produce strong NIR cross sections, while maximizing available effectiveness of the magnetic component. The high

degree of multifunctionality in a total particles smaller than 60 nm is desirable for optical, magnetic or multimodal imaging and therapy, with effective permeation of biological barriers.[1, 2, 8, 9, 31, 45-48, 57, 58]

3.6 SUPPORTING INFORMATION

3.6.1 Iron Oxide Nanocluster Synthesis

0.86 g $FeCl_2$ and 2.35 g $FeCl_3$ were dissolved completely in 40 ml deionized (DI) water by sonication. 0.05 g citric acid was dissolved in 2 ml DI water. Both these solutions were injected into a 3-necked reaction flask that had been evacuated twice and nitrogen flow was maintained during the reaction to avoid oxygen. The reactant solution was stirred and heated up to 95°C, and 10 ml of ammonia (28-30%) was injected to initiate Fe_3O_4 nucleation. After one hour, the reactor was cooled down to room temperature slowly and the product was centrifuged at 6000 rpm for 6 minutes. The resulting completely clear supernatant was decanted and the precipitated particles were re-dispersed by probe sonication in 25 ml of buffer solution containing citric acid (20 mg/ml) with NaOH at a pH of 5.2. This centrifugation and re-dispersion procedure was repeated 2 more times until all the particles were well dispersed in the buffer solution. The dispersion was then dialyzed against DI water for 24 hours using a 25 kDa dialysis bag (Spectra/Pro 7, Spectrum Laboratories Inc.) to remove excess citrate.

Table 3.S1 Mean Size and Standard Deviation of Gold Coated Iron Oxide Nanoparticles in Figure 3.2.

Au^{3+}/Fe ratio	Mean (nm)	Variance (nm)	% Standard deviation
0.125	44	2.9	7.0
0.250	49	3.1	6.5
0.500	57	3.0	5.3
1.5	73	4.6	6.3
3.0	73 and 146	2.5 and 5.6	3.4 and 3.8
6.0	30 and 159	1.9 and 15.6	6.3 and 9.8

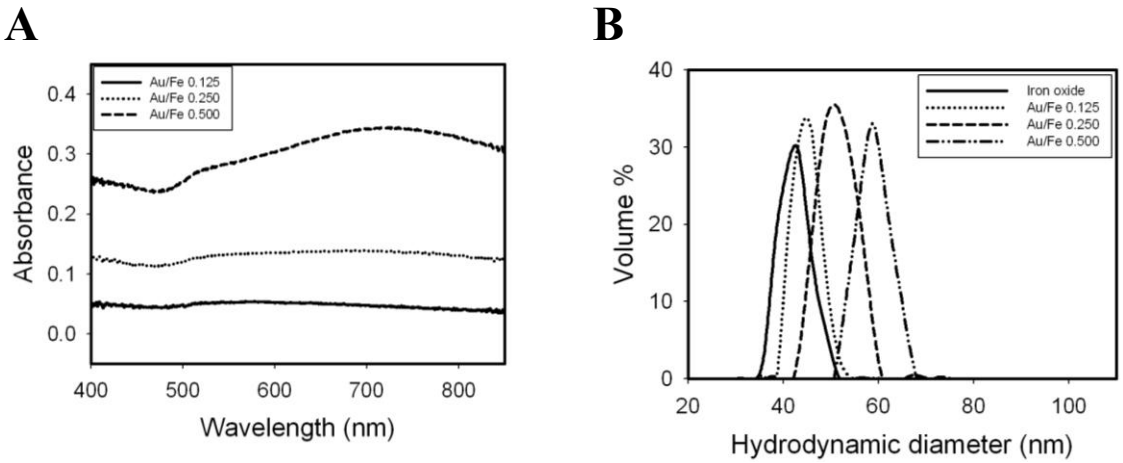

Figure 3.S1 The evolution of absorbance spectra and hydrodynamic diameters at selected step of the 5 iteration addition of gold precursor at a total Au/Fe mass ratio of 0.50. Iteration sequence: Au/Fe mass ratio = 0.05, 0.10, 0.125, 0.25, 0.5.

Table 3.S2 Mean Size and Standard Deviation of Textured Thin Gold Coated Iron Oxide Nanoparticles
Au/Fe= 0.5, reached with 5 Iterations

Au/Fe ratio	Mean (nm)	Variance (nm)	% Standard deviation
Iron oxide	42	3.2	7.5
0.125	45	2.8	6.1
0.25	51	3.6	7.0
0.5	58	3.3	5.7

3.6.2 The estimation of gold shell thickness on the iron oxide nanoclusters

The Fe_3O_4 nanocluster core was assumed to be a 42 nm diameter (R_{Fe3O4} = 21 nm) sphere with a porosity of $\phi = 0.3$ based on the morphology on TEM images and hydrodynamic diameters measured by DLS. 70 % of the entire volume of the spherical iron oxide cluster was assumed to be occupied by the Fe_3O_4 primary particles. V_{Core} = (1-ϕ) 4/3 πR^3. The mass of iron oxide cluster (M_{Fe3O4}) can be calculated as $M_{Fe3O4} = V_{Core} \cdot \rho_{Fe3O4}$ with the density of iron oxide $\rho_{Fe3O4} = 5.2 g \cdot cm^{-3}$. Based on Au/Fe mass ratio measured by AAS, the mass of gold coating the iron oxide was calculated M_{Au}= Au/Fe · $V_{Core} \cdot \rho_{Fe3O4} \cdot 0.72$. Knowing the density of gold $\rho_{Au} = 19.8 g \cdot cm^{-3}$, the volume of gold V_{Au} was calculated. The total volume of the coated cluster was calculated $V = V_{Core} + V_{Au}$. By assuming the Au coated cluster to be a perfect sphere, $R_{Au+Fe3O4} = (3V/4\pi)^{1/3}$. The gold shell thickness was calculated as $R_{Au+Fe3O4} - R_{Fe3O4}$.

3.6.3 The estimation of centrifugation speed for particle sedimentation

For a spherical particle, the centrifugation process is governed by sedimentation coefficient without considering diffusion. Therefore, this estimation does not take into account steric or electrostatic interactions between particles.[1]

$S = (1-\rho_1/\rho_2)*m/f$ (1)

ρ_1 = density of the solvent ($g \cdot cm^{-3}$)

ρ_2 = density of the particle ($g \cdot cm^{-3}$)

m = mass of the particle (g)

f = friction factor ($g \cdot s^{-1}$)

The density of solvent was assumed to be close to water at 300K, $\rho_1 = 1.0$ ($g \cdot cm^{-3}$). The density of gold coated iron oxide particles was calculated as $\rho_2 = (M_{Au} + M_{Fe3O4})/V$. Knowing the particle diameter (D) and the viscosity of the solvent (η), we can calculate the friction factor f. In this case, a viscosity $\eta = 0.001$ $kg \cdot m^{-1}s^{-1}$ from water at 300k was used for diluted particle reactant mixture.

$$f = \pi * \eta * D \qquad (2)$$

η = viscosity of the solvent ($kg \cdot m^{-1}s^{-1}$)

D = particle diameter (m)

$$S = \ln(l_1/l_2)/(\omega^2 * t) \qquad (3)$$

l_1 = initial distance of the particle from the axis of the centrifuge

l_2 = final distance of the particle from the axis of the centrifuge

ω = angular speed of rotation of the centrifuge (s^{-1})

t = time for which the centrifugation is carried out (s)

Assuming the centrifugation duration 360 s, we can calculate the centrifugation speed required to precipitate the particles from initial position to the bottom of the centrifuge tube (I1/I2=3.2/3.97).

3.6.4 The thermodynamic driving force for reduction of Au^{3+} on gold surfaces versus homogeneous reduction in solution

The thermodynamic driving forces of the autocatalytic growth of gold on Au^0 metal and homogeneous nucleation from Au^0 atom can be derived from reduction potentials.

$$Au^+ + e^- \Leftrightarrow Au^0_{(metal)} \quad \text{(S1)}$$

$$Au^+ + e^- \Leftrightarrow Au^0_{(atom)} \quad \text{(S2)}$$

$$Au^0_{(atom)} \Leftrightarrow Au^0_{(metal)} \quad \text{(S3)}$$

The reduction potential versus NHE for $Au^0_{(metal)}/Au^+$ is 1.68 V and for $Au^0_{(atom)}/Au^+$ is -1.5 V.[2,3] From eq. (S3) = (S1) - (S2), cell potential of $Au^0_{(metal)}/Au^0_{(atom)}$ is 3.18 V.

$$Au^{3+} + 3e^- \Leftrightarrow Au^0_{(metal)} \quad \text{(S4)}$$

$$Au^{3+} + 3e^- \Leftrightarrow Au^0_{(atom)} \quad \text{(S5)}$$

The reduction potential versus NHE for $Au^0_{(metal)}/Au^{3+}$ is 1 V.[3,4] From eq. (S5) = (S4) – (S3), the reduction potential versus NHE for $Au^0_{(atom)}/Au^{3+}$ is -2.18 V.

$$N_2 + 2H_2O + 2H^+ + 2e^- \Leftrightarrow 2NH_2OH \quad \text{(S6)}$$

The reduction potential versus NHE for NH_2OH/N_2 is -0.936 V.[5]

$$2Au^{3+} + 6NH_2OH \Leftrightarrow 3N_2 + 6H_2O + 6H^+ + 2Au^0_{(metal)} \quad \text{(S7) same as eq. (1)}$$

From eq. (S7) = (S4) - (S6), E_{cell} = 1.936 V.

$$2Au^{3+} + 6NH_2OH \Leftrightarrow 3N_2 + 6H_2O + 6H^+ + 2Au^0_{(atom)} \quad \text{(S8) same as eq. (2)}$$

From eq. (S8) = (S5) - (S6), E_{cell} = -1.244 V.

Table 3.S3 Calculated centrifugation speed for sedimentation of gold coated iron oxide nanoparticles

	Au/Fe ratio	Diameter (nm)	Centrifugation (rpm)
Iron oxide	0.00	42.0	8303
Au coated iron oxide	0.84	43.5	6415
	1.30	44.3	5776
	2.40	46.0	4859
	3.80	48.0	4188

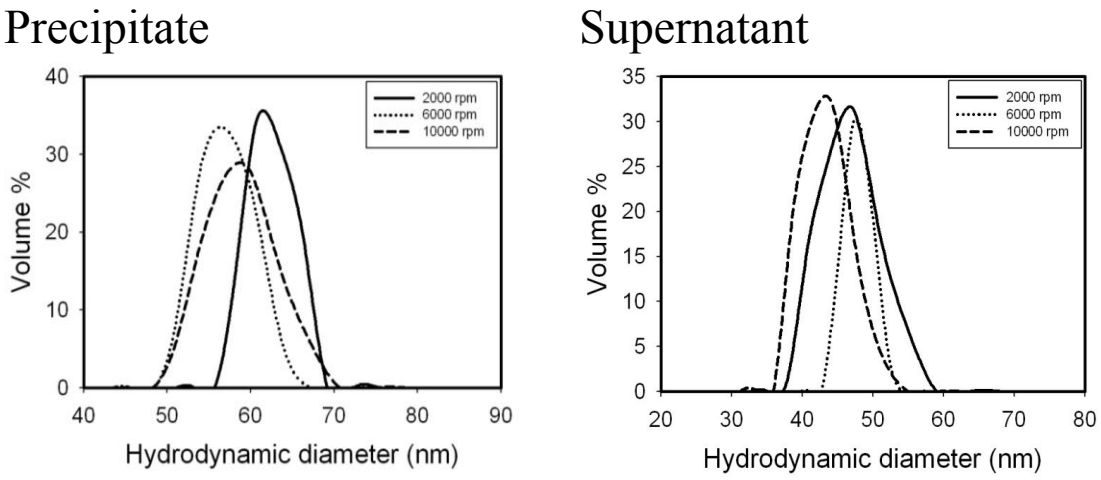

Figure 3.S2 Hydrodynamic diameter distribution of nanoparticles in precipitate and supernatant after centrifugation under different speeds. Au precursor was added by 5 iterations at Au/Fe mass ratio 0.500.

The hydrodynamic diameters of nanoparticles in the precipitate and supernatant phases were measured after centrifugation for the case of Au^{3+}/Fe of 0.5. The size distribution of particles in the supernatant was almost identical to that of the uncoated iron oxide nanoclusters. The mean hydrodynamic diameter of Au coated particles in the precipitate at the lowest speed of 2000 rpm were larger than those at the higher speeds, indicating fewer of the smaller particles settled with the weakest centrifugal force.

Table 3.S4 Detailed elemental analysis results of Fe and Au before and after centrifugation

Sample	Initial Au/Fe ratio	Final Au/Fe ratio	% Fe yield	% Au yield
0.125 R	0.125	0.094	100.3	88.8
0.25 R	0.250	0.264	100.8	108.6
0.5 R	0.500	0.445	100.4	100.9
0.125 2000 S	0.125	0.093	90.7	79.8
0.125 6000 S	0.125	0.014	92.5	12.2
0.125 10000 S	0.125	0	91.0	0
0.125 2000 P	0.125	0	0.82	0
0.125 6000 P	0.125	0.145	3.83	4.6
0.125 10000 P	0.125	0.095	7.84	7.0
0.25 2000 S	0.250	0.137	106.7	60.3
0.25 6000 S	0.250	0.030	98.2	12.0
0.25 10000 S	0.250	0.011	98.5	4.3
0.25 2000 P	0.250	0.073	1.1	0.3
0.25 6000 P	0.250	0.281	4.0	5.3
0.25 10000 P	0.250	0.176	9.7	7.1
0.5 2000 S	0.500	0.151	94.8	32.5
0.5 6000 S	0.500	0.068	90.8	14.0
0.5 10000 S	0.500	0.028	86.6	5.5
0.5 2000 P	0.500	0.396	1.1	1.0
0.5 6000 P	0.500	0.691	4.6	7.2
0.5 10000 P	0.500	0.465	8.8	9.3

* R indicated reactant before centrifugation
S indicated supernatant after centrifugation
P indicated precipitate after centrifugation

Table 3.S5 Mass balance sheet of Fe and Au after centrifugation

		Au/Fe 0.125	Au/Fe 0.25	Au/Fe 0.5
Fe	2000 rpm	92 %	98 %	96 %
	6000 rpm	96 %	93 %	95 %
	10000 rpm	99 %	98 %	95 %
Au	2000 rpm	89.9 %	55.8 %	33.2 %
	6000 rpm	19.4 %	15.3 %	21.1 %
	10000 rpm	7.9 %	10.4 %	14.6 %

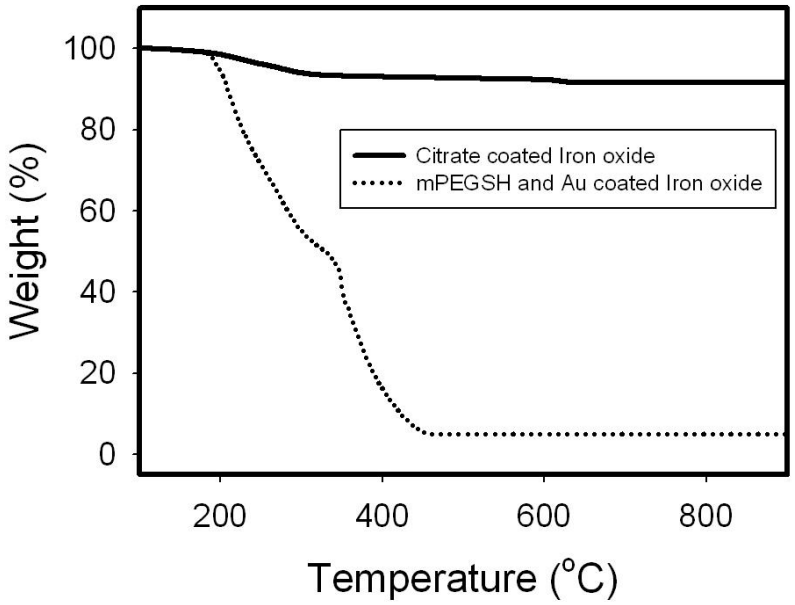

Figure 3.S3 TGA measurements of citrate coated iron oxide nanoclusters, mPEG-SH and gold coated iron oxide nanoparticles. At 900 ^{o}C, 9.5 % weight loss occurred from citrate and 95.0 % weight loss occurred from mPEG-SH.

3.7 REFERENCES

1. Hirsch, L. R.; Stafford, R. J.; Bankson, J. A.; Sershen, S. R.; Rivera, B.; Price, R. E.; Hazle, J. D.; Halas, N. J.; West, J. L., Nanoshell-mediated near-infrared thermal therapy of tumors under magnetic resonance guidance. *Proc. Nat. Acad. Sci.* **2003,** 100, (23), 13549-13554.

2. Ma, L. L.; Feldman, M. D.; Tam, J. M.; Paranjape, A. S.; Cheruku, K. K.; Larson, T. A.; Tam, J. O.; Ingram, D. R.; Paramita, V.; Villard, J. W.; Jenkins, J. T.; Wang, T.; Clarke, G. D.; Asmis, R.; Sokolov, K.; Chandrasekar, B.; Milner, T. E.; Johnston, K. P., Small Multifunctional Nanoclusters (Nanoroses) for Targeted Cellular Imaging and Therapy. *Acs Nano* **2009,** 3, (9), 2686-2696.

3. Mazumder, V.; Chi, M. F.; More, K. L.; Sun, S. H., Core/Shell Pd/FePt Nanoparticles as an Active and Durable Catalyst for the Oxygen Reduction Reaction. *Journal of the American Chemical Society* **2010,** 132, (23), 7848-7849.

4. Zhang, J.; Sasaki, K.; Sutter, E.; Adzic, R. R., Stabilization of platinum oxygen-reduction electrocatalysts using gold clusters. *Science* **2007,** 315, (5809), 220-222.

5. Anker, J. N.; Hall, W. P.; Lyandres, O.; Shah, N. C.; Zhao, J.; Van Duyne, R. P., Biosensing with plasmonic nanosensors. *Nat. Mater.* **2008,** 7, (6), 442-453.

6. Stewart, M. E.; Anderton, C. R.; Thompson, L. B.; Maria, J.; Gray, S. K.; Rogers, J. A.; Nuzzo, R. G., Nanostructured plasmonic sensors. *Chemical Reviews* **2008,** 108, (2), 494-521.

7. Lyon, J. L.; Fleming, D. A.; Stone, M. B.; Schiffer, P.; Williams, M. E., Synthesis of Fe Oxide Core/Au Shell Nanoparticles by Iterative Hydroxylamine Seeding. *Nano Letters* **2004,** 4, (4), 719-723.

8. Larson, T. A.; Bankson, J.; Aaron, J.; Sokolov, K., Hybrid plasmonic magnetic nanoparticles as molecular specific agents for MRI/optical imaging and photothermal therapy of cancer cells. *Nanotechnology* **2007,** 18, (32), 325101/1-325101/8.

9. Aaron, J. S.; Oh, J.; Larson, T. A.; Kumar, S.; Milner, T. E.; Sokolov, K. V., Increased optical contrast in imaging of epidermal growth factor receptor using magnetically actuated hybrid gold/iron oxide nanoparticles. *Optics Express* **2006,** 14, (26), 12930-12943.

10. Watzky, M. A.; Finke, R. G., Transition metal nanocluster formation kinetic and mechanistic studies. A new mechanism when hydrogen is the reductant: Slow, continuous nucleation and fast autocatalytic surface growth. *Journal of the American Chemical Society* **1997,** 119, (43), 10382-10400.

11. Ji, X.; Song, X.; Li, J.; Bai, Y.; Yang, W.; Peng, X., Size Control of Gold Nanocrystals in Citrate Reduction: The Third Role of Citrate. *Journal of the American Chemical Society* **2007,** 129, (45), 13939-13948.

12. Brown, K. R.; Natan, M. J., Hydroxylamine Seeding of Colloidal Au Nanoparticles in Solution and on Surfaces. *Langmuir* **1998,** 14, (4), 726-728.

13. Brown, K. R.; Walter, D. G.; Natan, M. J., Seeding of colloidal Au nanoparticle solutions. 2. Improved control of particle size and shape. *Chemistry of Materials* **2000,** 12, (2), 306-313.

14. Jana, N. R.; Gearheart, L.; Murphy, C. J., Evidence for seed-mediated nucleation in the chemical reduction of gold salts to gold nanoparticles. *Chemistry of Materials* **2001,** 13, (7), 2313-2322.

15. Yin, Y.; Alivisatos, A. P., Colloidal nanocrystal synthesis and the organic-inorganic interface. *Nature (London, United Kingdom)* **2005,** 437, (7059), 664-670.

16. Talapin, D. V.; Rogach, A. L.; Haase, M.; Weller, H., Evolution of an ensemble of nanoparticles in a colloidal solution: Theoretical study. *Journal of Physical Chemistry B* **2001,** 105, (49), 12278-12285.

17. Park, J.; Joo, J.; Kwon, S. G.; Jang, Y.; Hyeon, T., Synthesis of monodisperse spherical nanocrystals. *Angew Chem Int Edit* **2007,** 46, (25), 4630-4660.

18. Xia, Y.; Xiong, Y. J.; Lim, B.; Skrabalak, S. E., Shape-Controlled Synthesis of Metal Nanocrystals: Simple Chemistry Meets Complex Physics? *Angew Chem Int Edit* **2009,** 48, (1), 60-103.

19. Finney, E. E.; Finke, R. G., Nanocluster nucleation and growth kinetic and mechanistic studies: A review emphasizing transition-metal nanoclusters. *Journal of Colloid and Interface Science* **2008,** 317, (2), 351-374.

20. Jeong, U.; Teng, X.; Wang, Y.; Yang, H.; Xia, Y., Superparamagnetic colloids: controlled synthesis and niche applications. *Advanced Materials (Weinheim, Germany)* **2007,** 19, (1), 33-60.

21. Zeng, H.; Sun, S., Syntheses, properties, and potential applications of multicomponent magnetic nanoparticles. *Advanced Functional Materials* **2008,** 18, (3), 391-400.

22. Lim, J.; Tilton, R. D.; Eggeman, A.; Majetich, S. A., Design and synthesis of plasmonic magnetic nanoparticles. *Journal of Magnetism and Magnetic Materials* **2007,** 311, (1), 78-83.

23. Yu, H.; Chen, M.; Rice, P. M.; Wang, S. X.; White, R. L.; Sun, S. H., Dumbbell-like bifunctional Au-Fe3O4 nanoparticles. *Nano Letters* **2005,** 5, (2), 379-382.

24. Shevchenko, E. V.; Bodnarchuk, M. I.; Kovalenko, M. V.; Talapin, D. V.; Smith, R. K.; Aloni, S.; Heiss, W.; Alivisatos, A. P., Gold/iron oxide core/hollow-shell nanoparticles. *Advanced Materials (Weinheim, Germany)* **2008,** 20, (22), 4323-4329.

25. Park, H.-Y.; Schadt, M. J.; Wang, L.; Lim, I. I. S.; Njoki, P. N.; Kim, S. H.; Jang, M.-Y.; Luo, J.; Zhong, C.-J., Fabrication of Magnetic Core@Shell Fe Oxide@Au Nanoparticles for Interfacial Bioactivity and Bio-separation. *Langmuir* **2007,** 23, (17), 9050-9056.

26. Xu, Z.; Hou, Y.; Sun, S., Magnetic Core/Shell Fe3O4/Au and Fe3O4/Au/Ag Nanoparticles with Tunable Plasmonic Properties. *Journal of the American Chemical Society* **2007,** 129, (28), 8698-8699.

27. Hostetler, M. J.; Wingate, J. E.; Zhong, C. J.; Harris, J. E.; Vachet, R. W.; Clark, M. R.; Londono, J. D.; Green, S. J.; Stokes, J. J.; Wignall, G. D.; Glish, G. L.; Porter, M. D.; Evans, N. D.; Murray, R. W., Alkanethiolate gold cluster molecules with core diameters from 1.5 to 5.2 nm: Core and monolayer properties as a function of core size. *Langmuir* **1998,** 14, (1), 17-30.

28. Leff, D. V.; Ohara, P. C.; Heath, J. R.; Gelbart, W. M., Thermodynamic Control of Gold Nanocrystal Size - Experiment and Theory. *J Phys Chem-Us* **1995,** 99, (18), 7036-7041.

29. Wang, L.; Luo, J.; Fan, Q.; Suzuki, M.; Suzuki, I. S.; Engelhard, M. H.; Lin, Y.; Kim, N.; Wang, J. Q.; Zhong, C.-J., Monodispersed Core-Shell Fe3O4@Au Nanoparticles. *Journal of Physical Chemistry B* **2005,** 109, (46), 21593-21601.

30. Rasch, M. R.; Sokolov, K. V.; Korgel, B. A., Limitations on the Optical Tunability of Small Diameter Gold Nanoshells. *Langmuir* **2009,** 25, (19), 11777-11785.

31. Oh, J.; Feldman, M. D.; Kim, J.; Condit, C.; Emelianov, S.; Milner, T. E., Detection of magnetic nanoparticles in tissue using magneto-motive ultrasound. *Nanotechnology* **2006,** 17, (16), 4183-4190.

32. Levin, C. S.; Hofmann, C.; Ali, T. A.; Kelly, A. T.; Morosan, E.; Nordlander, P.; Whitmire, K. H.; Halas, N. J., Magnetic-Plasmonic Core-Shell Nanoparticles. *Acs Nano* **2009,** 3, (6), 1379-1388.

33. Wang, H.; Brandl, D. W.; Le, F.; Nordlander, P.; Halas, N. J., Nanorice: A Hybrid Plasmonic Nanostructure. *Nano Letters* **2006,** 6, (4), 827-832.

34. Goon, I. Y.; Lai, L. M. H.; Lim, M.; Munroe, P.; Gooding, J. J.; Amal, R., Fabrication and Dispersion of Gold-Shell-Protected Magnetite Nanoparticles: Systematic Control Using Polyethyleneimine. *Chemistry of Materials* **2009,** 21, (4), 673-681.

35. Lim, J. K.; Majetich, S. A.; Tilton, R. D., Stabilization of Superparamagnetic Iron Oxide Core-Gold Shell Nanoparticles in High Ionic Strength Media. *Langmuir* **2009,** 25, (23), 13384-13393.

36. Lim, J.; Eggeman, A.; Lanni, F.; Tilton, R. D.; Majetich, S. A., Synthesis and single-particle optical detection of low-polydispersity plasmonic-superparamagnetic nanoparticles. *Adv Mater* **2008,** 20, (9), 1721-1726.

37. Oldenburg, S. J.; Averitt, R. D.; Westcott, S. L.; Halas, N. J., Nanoengineering of optical resonances. *Chemical Physics Letters* **1998,** 288, (2,3,4), 243-247.

38. Kumar, S.; Aaron, J.; Sokolov, K., Directional conjugation of antibodies to nanoparticles for synthesis of multiplexed optical contrast agents with both delivery and targeting moieties. *Nat. Protocols* **2008,** 3, (2), 314-320.

39. Knight, M. W.; Halas, N. J., Nanoshells to nanoeggs to nanocups: optical properties of reduced symmetry core-shell nanoparticles beyond the quasistatic limit. *New Journal of Physics* **2008,** 10, (Oct.).

40. Hu, Y.; Noelck, S. J.; Drezek, R. A., Symmetry Breaking in Gold-Silica-Gold Multilayer Nanoshells. *Acs Nano* **2010,** 4, (3), 1521-1528.

41. Averitt, R. D.; Westcott, S. L.; Halas, N. J., Linear optical properties of gold nanoshells. *J Opt Soc Am B* **1999,** 16, (10), 1824-1832.

42. Wu, D. J.; Xu, X. D.; Liu, X. J., Influence of dielectric core, embedding medium and size on the optical properties of gold nanoshells. *Solid State Commun* **2008,** 146, (1-2), 7-11.

43. Prodan, E.; Nordlander, P.; Halas, N. J., Electronic structure and optical properties of gold nanoshells. *Nano Letters* **2003,** 3, (10), 1411-1415.

44. Huang, X.; El-Sayed, I. H.; Qian, W.; El-Sayed, M. A., Cancer Cell Imaging and Photothermal Therapy in the Near-Infrared Region by Using Gold Nanorods. *Journal of the American Chemical Society* **2006,** 128, (6), 2115-2120.

45. Shah, J.; Park, S.; Aglyamov, S.; Larson, T.; Ma, L.; Sokolov, K.; Johnston, K.; Milner, T.; Emelianov Stanislav, Y., Photoacoustic imaging and temperature measurement for photothermal cancer therapy. *Journal of biomedical optics* **2008,** 13, (3), 034024.

46. Paranjape, A. S.; Kuranov, R.; Baranov, S.; Ma, L. L.; Villard, J. W.; Wang, T.; Konstantin, S.; Feldman, M. D.; Johnston, K. P.; Milner, T. E., Depth resolved photothermal OCT detection of macrophages in tissue using nanorose. *Biomedical Optics Express* **2010,** 1, (1), 2-16.

47. Mehrmohammadi, M.; Oh, J.; Ma, L.; Yantsen, E.; Larson, T.; Mallidi, S.; Park, S.; Johnston, K. P.; Sokolov, K.; Milner, T.; Emelianov, S.; Ieee, Imaging of iron oxide nanoparticles using magneto-motive ultrasound. In *2007 Ieee Ultrasonics Symposium Proceedings, Vols 1-6*, Ieee: New York, 2007; pp 652-655.

48. Qu, M.; Mallidi, S.; Mehrmohammadi, M.; Ma, L. L.; Johnston, K. P.; Sokolov, K.; Emelianov, S., Combined photoacoustic and magneto-acoustic imaging. *Conf Proc IEEE Eng Med Biol Soc* **2009,** 2009, 4763-6.

49. Ferrari, M., Beyond drug delivery. *Nature Nanotechnology* **2008,** 3, (3), 131-132.

50. Jiang, W.; Kim, B. Y. S.; Rutka, J. T.; Chan, W. C. W., Nanoparticle-mediated cellular response is size-dependent. *Nature Nanotechnology* **2008,** 3, (3), 145-150.

51. Sahoo, Y.; Goodarzi, A.; Swihart, M. T.; Ohulchanskyy, T. Y.; Kaur, N.; Furlani, E. P.; Prasad, P. N., Aqueous Ferrofluid of Magnetite Nanoparticles: Fluorescence Labeling and Magnetophoretic Control. *Journal of Physical Chemistry B* **2005,** 109, (9), 3879-3885.

52. Ryoo, W.; Webber, S. E.; Johnston, K. P., Water-in-Carbon Dioxide Microemulsions with Methylated Branched Hydrocarbon Surfactants. *Industrial & Engineering Chemistry Research* **2003,** 42, (25), 6348-6358.

53. Fetters, L. J.; Lohse, D. J.; Richter, D.; Witten, T. A.; Zirkel, A., CONNECTION BETWEEN POLYMER MOLECULAR-WEIGHT, DENSITY, CHAIN DIMENSIONS, AND MELT VISCOELASTIC PROPERTIES. *Macromolecules* **1994,** 27, (17), 4639-4647.

54. Caruntu, D.; Cushing, B. L.; Caruntu, G.; O'Connor, C. J., Attachment of Gold Nanograins onto Colloidal Magnetite Nanocrystals. *Chemistry of Materials* **2005,** 17, (13), 3398-3402.

55. Lo, C. K.; Xiao, D.; Choi, M. M. F., Homocysteine-protected gold-coated magnetic nanoparticles: synthesis and characterization. *Journal of Materials Chemistry* **2007,** 17, (23), 2418-2427.

56. Mandal, M.; Kundu, S.; Ghosh, S. K.; Panigrahi, S.; Sau, T. K.; Yusuf, S. M.; Pal, T., Magnetite nanoparticles with tunable gold or silver shell. *Journal of Colloid and Interface Science* **2005,** 286, (1), 187-194.

57. Weissleder, R., Molecular Imaging in Cancer. *Science* **2006,** 312, (5777), 1168-1171.

58. Josephson, L.; Kircher, M. F.; Mahmood, U.; Tang, Y.; Weissleder, R., Near-Infrared Fluorescent Nanoparticles as Combined MR/Optical Imaging Probes. *Bioconjugate Chemistry* **2002,** 13, (3), 554-560.

Chapter4: Tuning the Nucleation and Growth of Au Shells on Iron Oxide Nanoclusters

A general strategy is presented for controlling the morphology of thin metal shells on low energy nanoparticle substrates, despite the unfavorable wetting. A wide range of morphologies of Au shells on 42 nm iron oxide cluster cores, namely thin (5 nm) or thick smooth shells (20-40 nm) or thick knobby (10-40 nm) shells, was produced by tuning the nucleation and growth in the presence of a polymeric stabilizer. For high nucleation rates at high pH, Au seeds were deposited on a higher fraction of the iron oxide substrate particles leading to thinner coatings. At lower pH values, slower nucleation led to less separation between nucleation and autocatalytic growth and, consequently, Au seeds on fewer particles, and thicker coatings. The Au coated nanoclusters were characterized by dynamic light scattering to determine the hydrodynamic diameter, TEM, atomic absorption spectroscopy to determine the mass ratio of Au to iron, thermogravimetric analysis to determine the amount of polymer on the surface, and UV-vis-NIR spectroscopy to characterize the peak of the surface plasmon resonance (SPR). The knobby protrusions on the surface introduce high asymmetry and high aspect ratios that shift the SPR of Au into the NIR with strong extinction coefficients. This general mechanism of thin autocatalytic growth on nanoparticle substrates is shown to be highly versatile for producing a homologous series of metal shells of varying thickness and shape. The intensity absorbance in the NIR region, along with the magnetic functionality is of interest in multimodal imaging in nanomedicine.

4.1 INTRODUCTION

Small nanoparticles (40 to 50 nm) with metal coatings on low energy metal oxide cores may be utilized for imaging and therapy in biomedicine,[1-5] catalysis, and sensors.[6] Pure metal nanoparticles are often formed by homogeneous nucleation to form seeds followed by autocatalytic growth on the seeds[7-12], as described by the kinetic model of Watzky and Finke.[13] The control of the thickness and uniformity of Au shells on iron oxide cores is highly challenging given the poor wetting of the high surface energy shell on the low energy core, as well as the large mismatch in lattice spacings.[14, 15] To attempt to overcome these challenges, Au seeds may be nucleated from Au precursors on the substrate nanoparticles[16-18] or may be pre-made separately and attached to the cores.[19-26] High Au^{3+}/Fe mass ratios on the order of 10 are utilized to provide high supersaturation to nucleate the Au seeds or to fully coat the particles. Unfortunately, high supersaturation leads to excessive autocatalytic growth resulting in very thick Au shells, and in the extreme case, homogenous nucleation of Au in the solution.[22, 23, 25, 27] For coated nanoparticles larger than 20 nm, van der Waals attraction may produce aggregation. The particles may be stabilized sterically with a polymer to avoid aggregation, but without impeding nucleation and growth.[20, 25]

We have demonstrated recently[28] the controlled growth of Au shells on 42 nm iron oxide cores by Textured Autocatalytic Growth on a nanoparticle Substrate (TAGS). Very low Au supersaturation levels were utilized to mitigate commonly encountered excessive autocatalytic growth that otherwise produces thick shells. The morphology of the Au shells was tuned by varying the precursor addition history all at a pH of 9.3. At low supersaturation levels, Au seeds were nucleated on a sufficient number of iron oxide

substrate particles prior to growth, such that the subsequent growth resulted in shells thinner than 5 nm, as shown in Scheme 4.1. Thin knobby shells were formed on particles with a hydrodynamic diameter of about 55-60 nm with high degrees of asymmetry, which produces red shifts in the SPR, as has been demonstrated for Au rods and nanorice[22] as well as nanoeggs[29] (asymmetric egg white shells).

The objective of this study was to tune the relative rates of nucleation and growth during TAGS by varying a solution condition, in this case the initial pH. The pH was varied to produce thick smooth shells or thick knobby shells on ~42 nm iron oxide cluster cores with total particle hydrodynamic diameters from 55 to 180 nm, as shown in Scheme 4.1. These morphologies compliment our recently reported smaller Au coated nanoparticles (<60 nm) with iron oxide cores and thin smooth or knobby shells.[28] The Au^{3+}/Fe ratio was only 0.5 relative to commonly used values of 3-27 in order to minimize autocatalytic growth.[25, 27] Low Au^{3+}/Fe ratios were utilized to coat only a fraction of the iron oxide particles, which were then separated from the uncoated substrate particles by centrifugation. To guide this strategy, the effect of pH on homogenous nucleation and growth of pure Au nanoparticles was also investigated.[30, 31] The TAGS mechanism for heterogeneous nucleation and growth is shown to be highly versatile for producing a homologous series of metal shells of varying thickness and shape. In essence, it is an extension of the seeded growth mechanism developed for pure metal nanoparticles.[11, 13] The polymer mPEG-SH (M_w = 20,000 g/mol) was bonded covalently to the Au shells during growth to provide steric stabilization. Since mPEG-SH does not coat iron oxide, it selectively passivates autocatalytic growth of Au on Au. Thus, the selective passivation was utilized to spread Au seeds onto more iron oxide cores, which gave rise to thinner coatings, as a function of mPEG-SH concentration.

The SPR of Au is tuned over a wide range from 700 to 850 nm by varying the thickness and texture of the Au shells for a wide range of particle diameters. For the thick knobby shells, the high asymmetry in particle shape is shown to produce much larger red shifts than for smooth shells[21, 27] as a result of hybridization between different plasmon modes.[29, 32] The large amount of Au in the thick knobby shells offers the potential of large absorbance cross-sections/particle. NIR applications of Au based nanoparticles include optical coherence tomography,[33-36] photothermal therapy,[4, 37-39] photoacoustic imaging,[40-42] combined photoacoustic imaging and photothermal therapy[5, 43, 44] as well as other types of optical imaging.[45-47] Nanoparticles with a high NIR absorbance and a high magnetic payload for a high magnetic susceptibility are of widespread interest in multimodal imaging.[39]

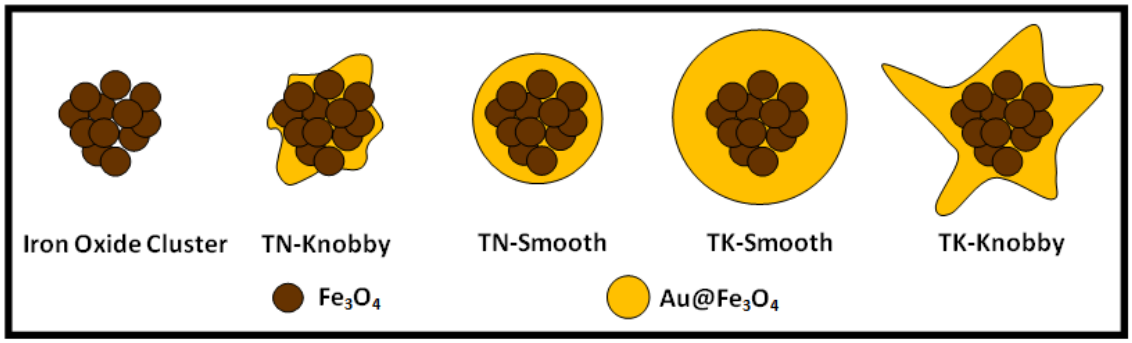

Scheme 4.1 Schematic showing a homologous series of morphologies of gold coatings on iron oxide nanoclusters.

4.2 Experimental Section

4.2.1 Materials

All reagents used were analytical grade. Ferrous chloride, ammonium hydroxide, hydroxylamine hydrochloride, nitric acid and sodium hydroxide were purchased from

Fisher Chemicals (Fairlawn, NJ). Ferric chloride was purchased from Acros Organics (Morris Plains, NJ). Citric acid was purchased from EM Science (Gibbstown, NJ). $HAuCl_4$ trihydrate was purchased from MP Biomedicals LLC. (Solon, OH). mPEG-SH was purchased from Nanocs Inc. (New York, NY).

4.2.2 Coating Au on iron oxide nanoclusters

Iron oxide nanocluster synthesis was done by a modification of the Sahoo method[48], as described recently.[28] These nanoclusters were dispersed in DI water to produce 100 ml of 0.1 mg Fe/ml dispersion with vigorous stirring. 320 μL of 7% by weight ammonium hydroxide was added to adjust the pH to 9.3. For different initial pH values, correspondingly lower amounts of ammonium hydroxide were added to the reaction mixture. 2.0 ml of 1 % (w/v) hydroxylamine hydrochloride was added as the reducing agent for the Au precursor. A desired amount of 4 mg/ml mPEG-SH (PEG MW 20,000) solution was added to provide steric stabilization. 2 ml of $HAuCl_4$ solution (2.5 mg Au/ml) was added to the reaction mixture to get a Au^{3+}/Fe mass ratio of 0.5 in all cases. From visual observation, the color of the initial iron oxide dispersion was brown and did not change for a few seconds after addition of the Au precursor. Next, the dispersion became slightly turbid, and the color rapidly changed to greenish-brown. When the color change to greenish brown started, the reactions were quenched with 1% nitric acid down to a pH of below 6 to ensure minimal further nucleation. As shown in the Supporting Information, the same results were obtained by following the same procedure without the acid quenching. In essence, the acid quenching had a minimal if not negligible effect. The solution was allowed to stand with constant stirring for half an hour to allow time for further mPEG-SH reaction with the surface of Au coatings. The reaction mixture was then centrifuged at 6,000 rpm for 6 minutes in order to separate the

Au coated particles from the uncoated iron oxide particles. The precipitates were re-dispersed by using 1 ml of dilute mPEG-SH solution (0.2 mg/ml) and bath sonicated for four to five minutes to produce a colloidally stable suspension.

4.2.3 Materials characterization

UV-visible absorbance spectra were obtained with a Cary Varian 3E UV-visible spectrophotometer with a polystyrene cuvette with a path length of 1 cm, relative to DI water as a baseline. All samples were diluted so that the absorbance was below 1.5. Dynamic light scattering (DLS) measurements were performed in triplicate on a custom made Brookhaven Instruments ZetaPlus dynamic light scattering apparatus at a scattering angle of 90° and temperature of 25°C.[49] Nanoparticle dispersion concentrations were adjusted with DI water to give a signal count rate between 300-400 kcps. Prior to DLS measurements, the samples were bath sonicated for 2 minutes. The correlation functions were analyzed with a non-negative least-squares (NNLS) method. TEM images were obtained using a FEI Tecnai Spirit BioTwin at 80 kV accelerating voltage. A drop of the dispersion of particles, which had been diluted about 40 times, was put on a 400 mesh ultrathin carbon-coated copper grid. Excess liquid was siphoned off using a tissue and then the grid was allowed to dry in air.

The Au and Fe concentrations in the nanoparticle dispersions were measured with a GBC 908AA flame atomic absorption spectrometer (GBC Scientific Equipment) equipped with an air-acetylene flame furnace at a detector wavelength of 242.8 nm and 212 nm, respectively. The instrument was calibrated using Au^{3+} or Fe^{3+} standard solutions before every set of measurements. The concentrations of Fe or Au were measured at concentrations between 1 and 5 μg/ml.

4.3 RESULTS

4.3.1 Effect of pH on kinetics of formation of pure Au nanoparticles

To monitor the kinetics of Au nanoparticle formation at various pH values, the absorbance was monitored every 0.033 seconds for a reaction mixture containing 0.1726 mg/ml of $HAuCl_4$ (0.1 mg/mL Au^{3+}), 0.2 mg/ml hydroxylamine and 0.12 mg/ml mPEG-SH. The SPR of the Au particles was monitored at 530 nm, where it is known to be a maximum.[19, 23, 30] The pH was adjusted with ammonium hydroxide. A sigmoidal curve of absorbance versus time was observed as shown in Figure 4.1, as expected for homogeneous nucleation of Au.[11, 50-52] The initial slow increase represents nucleation of Au particles, followed by a rapid upturn caused by autocatalytic growth on the Au surfaces, and finally a leveling off as Au^{3+} is highly depleted. The half-life for reaction increased progressively from ~ 1 min. at pH 9.3 to 7 min. at pH 6.8. At pH 4.16 the reaction rate was negligible. Furthermore, the maximum slope decreased as pH was lowered. Finally, the height of the absorbance plateau was similar for pH 6.8 and above, but was not reached at lower pH values in 20 min.

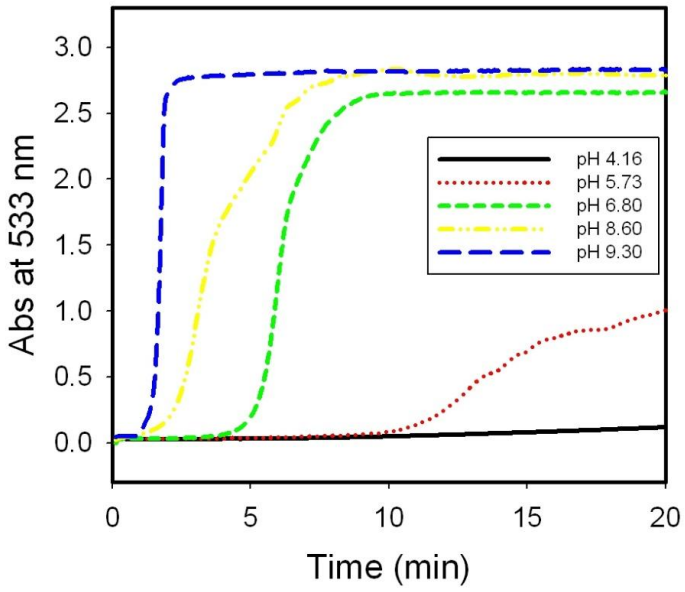

Figure 4.1 Hydroxylamine catalyzed reduction of $HAuCl_4$ to produce pure gold particles at different initial pH values (before $HAuCl_4$ was added). The reaction mixture contained 0.02% NH_2OH and 0.12 mg/mL mPEG-SH. $HAuCl_4$ was added to produce a final concentration of 0.1726 mg/mL.

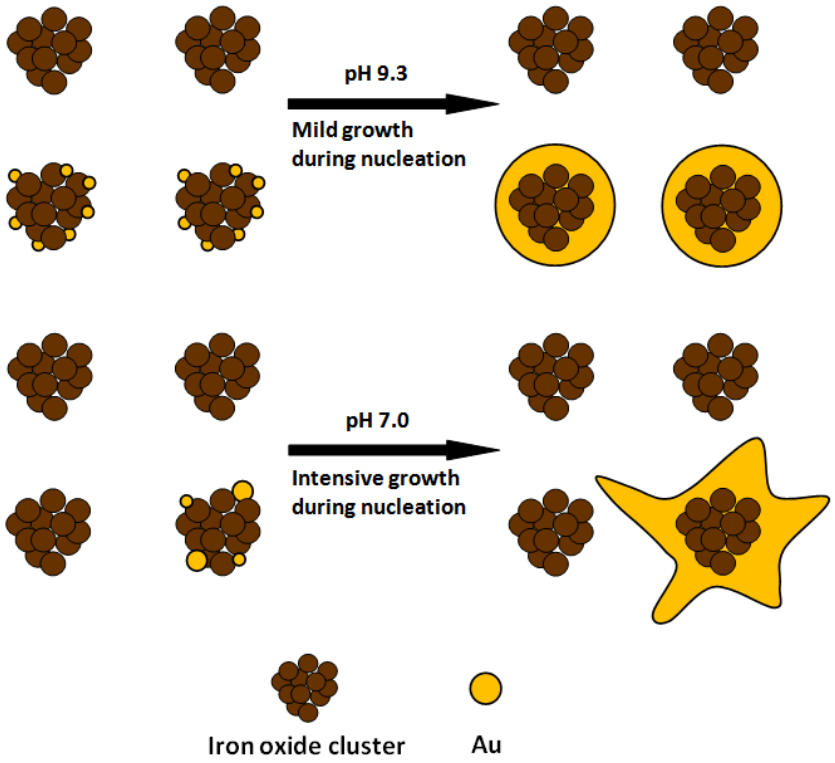

Scheme 4.2 Schematic showing the effect of changing the initial pH on nucleation and growth of the gold shells. The arrow indicates the transition to autocatalytic growth.

4.3.2 Effect of pH on nucleation and growth of Au coatings on iron oxide at high polymer concentration

Upon addition of the Au^{3+}, the time for the color change to greenish brown ranged from 16 s to 1 s for pH values of 9.3 and 7, respectively, as shown in Table 4.1. The slower color change at high pH at first may appear surprising given the faster homogeneous nucleation of pure Au nanoparticles in Scheme 4.2. In the discussion section, this slower color change will be examined in detail and in terms of more rapid nucleation and subsequently delayed autocatalytic growth. TEM images of Au coated iron oxide particles are shown in Figure 4.2 for various values of initial pH. The hydrodynamic diameter of the iron oxide core was 42 nm. At the highest initial pH of 9.3,

the smallest particles were produced (about 60 nm). The particle surface was relatively smooth. At a pH of about 8.6, the size increased to about 100 nm and knobby protrusions became evident on the surface. These knobs were even more pronounced at pH 7, and the size increased to about 125 nm. Quantitative size distributions were obtained by DLS, as shown in Figure 4.3a. The coated particle size increased monotonically with a decrease in pH, reaching 175 nm at pH 6. The standard deviation also increased (Supporting Information Tables S1, S2 and S3). This increase in size was consistent with the thicker Au coatings observed by TEM. Furthermore, the Au/Fe ratio in the product measured by Atomic Absorption Spectroscopy increased from 2.7 at pH 9.3 to about 5 for the lower pH values as shown in Table 4.1. The yields of Au and Fe in the precipitate are also shown in Table 4.1. The yield of iron was higher for the particles with thinner Au coatings at high pH, and was somewhat lower for the thicker Au coatings at lower pH. The Au yield was approximately constant at 20%. The extinction coefficient per μg of Au at 755 nm increased as pH decreased.

The visual color of the resulting particle dispersions became progressively bluer and less pink as the initial pH was lowered as shown in Figure 4.3b. The absorbance maximum was about 630 nm for pH 9.3. The absorbance peak was progressively red-shifted and also became flatter and broader with very high NIR absorbance from 700 to 850 nm as seen in the spectra (Figure 4.3b). The value of the extinction coefficient for these particles at 755 nm is very high and is observed to increase with a decrease in the pH from 9.3 to 7 (Table 4.1). The cross-section of these particles is comparable to the values for nanocages, nanorods and nanoshells on the order of 10^{-14} m^2, relative to a value on the order of 10^{-20} m^2 for indocyanine green.[39, 53] To our knowledge, strong NIR absorbance has rarely been reported for iron oxide cores in this size range.[20, 25, 27]

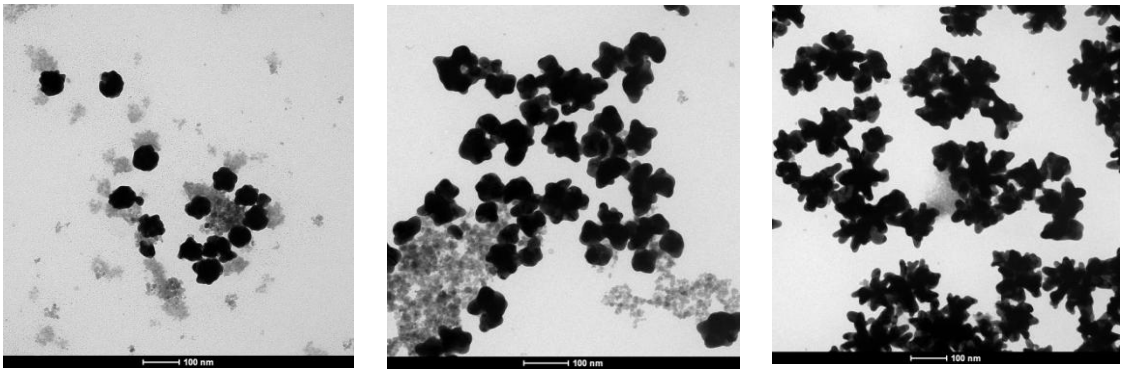

a b c

Figure 4.2 TEM images of the final gold coated iron oxide nanoclusters for different initial pH values (a) pH 9.3 (b) pH 8.6 and (c) pH 7, with an initial Au^{3+}/Fe mass ratio of 0.5 and a mPEG-SH to gold mole ratio of 0.08. The particles were separated by centrifugation. The scale bar for all the images is 100 nm.

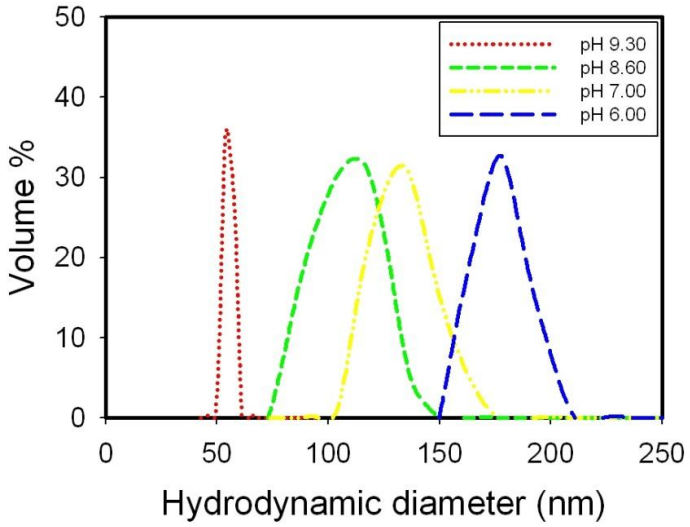

a

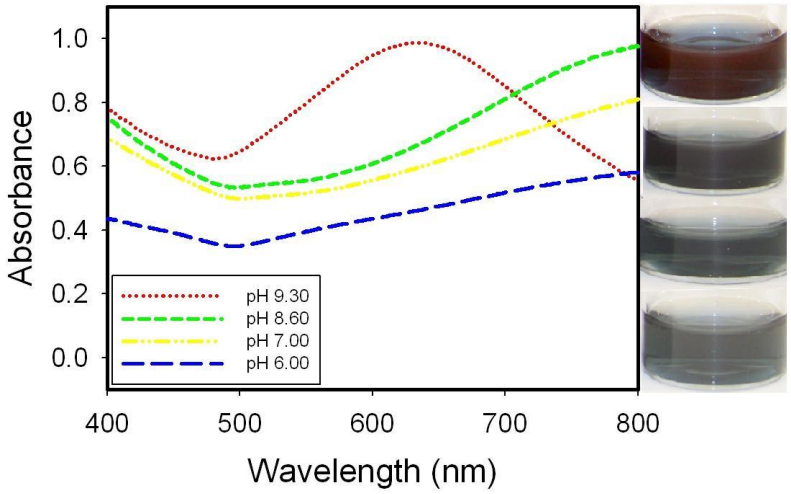

b

Figure 4.3 a. Effect of initial pH on coated cluster hydrodynamic diameter measured by DLS. b. Absorbance spectra . The inserted photo shows the color of the diluted Au coated iron oxide nanoparticles in aqueous dispersion after centrifugation (from top to bottom, initial pH 9.30, 8.60, 7.00 and 6.00).

Table 4.1 Properties of the particles synthesized at different initial pH values stabilized with 400 μg/ml mPEG-SH.

Starting pH	9.3	8.6	7.0	6.0
Time for color change (s)	16	6	1	<1
Au/Fe ratio in product	2.70	4.13	6.43	7.71
Extinction coefficient at 755 nm (cm^2/μg Au)	0.041	0.059	0.059	0.026
% Yield (Au)	19.8	17.2	20.4	21.4
% Yield (Fe)	3.7	2.1	1.6	1.4
Hydrodynamic diameter (nm)	55	105	132	178

Table 4.2 Size distribution moments for nanoclusters produced with different initial pH values.

pH	μ1	μ3
9.3	1.00	0.998
8.6	1.04	0.980
7.0	1.02	0.990
6.0	1.01	0.996

4.3.3 Calculation of size distribution moments

In order to determine whether the growth of Au on the clusters led to significant coagulation between Au coated iron oxide nanoclusters, size distribution moments were calculated for the DLS data. The size distribution moments, μ_1 and μ_3, are defined as

$$\mu_1 = \frac{r_3}{r_h} = \frac{\sqrt[3]{\sum r_i^3 / N_{Tot}}}{N_{Tot} / \sum \frac{1}{r_i}} \quad \text{.....(1)}$$

$$\mu_3 = \frac{r_1}{r_3} = \frac{\sum r_i / N_{Tot}}{\sqrt[3]{\sum r_i^3 / N_{Tot}}} \quad \text{.....(2)}$$

where r_1 is the arithmetic mean radius, r_3 is the cube mean radius, r_h is the harmonic mean radius, and N_{Tot} is the total number of particles in the system. When $\mu_1 = \mu_3 = 1$, the size distribution moments reflect a monodisperse system where clusters have been formed by condensation. Size distribution moments where $\mu_1 < 1.25$ and $\mu_3 > 0.905$ as shown in Table 4.2 suggest that coagulation of the Au coated iron oxide cores was not present.[54]

4.3.4 Effect of mPEG-SH concentrations on the morphology

The concentration of a passivating ligand may be used to control growth of Au nanoparticles.[55] For the above experiments a high mPEG-SH/Au molar ratio of 12.6 was used. In this section, the mPEG-SH/Au molar ratio was used to further manipulate the growth by influencing passivation and steric stabilization at different pH values. For an initial pH of 9.3, a series of Au coated nanoparticles with relatively smooth shells are shown by TEM for the four mPEG-SH concentrations in Figures 4a-d. The particle hydrodynamic diameter (shown in Figure 4.4f) started at 55 nm with a high mPEG-SH concentration and increased as the polymer concentration was lowered indicating less passivation. The peak in the UV-vis spectrum (shown in Figure 4.4g) became less prominent (flatter) and was red shifted as the shell became thicker. For an initial pH of

8.6, a representative TEM image shown in Figure 4.2b reveals a slightly knobby morphology. At an initial pH of 7, the knobby protrusions were much larger (Figure 4.2c). The hydrodynamic diameters from DLS were about 105-125 nm (Figure 4.5a) for the pH 8.6 reaction, and 130 to 150 nm (Figure 4.5c) for pH 7. For each reaction pH, the hydrodynamic diameter increased slightly with a decrease in the concentration of mPEG-SH. For the pH 8.6 reaction, the peak of the UV-vis spectrum (Figure 4.5b) was at 800-825 nm with a very high intensity of absorbance and therefore a high extinction coefficient and cross section (Supporting information Table 4.S4). The red shift was even larger for the pH 7 reaction. All of the properties for particles synthesized at either pH 8.6 or pH 7 were relatively insensitive to the concentration of mPEG-SH, unlike the results for the pH 9.3 reaction in Figure 4.4.

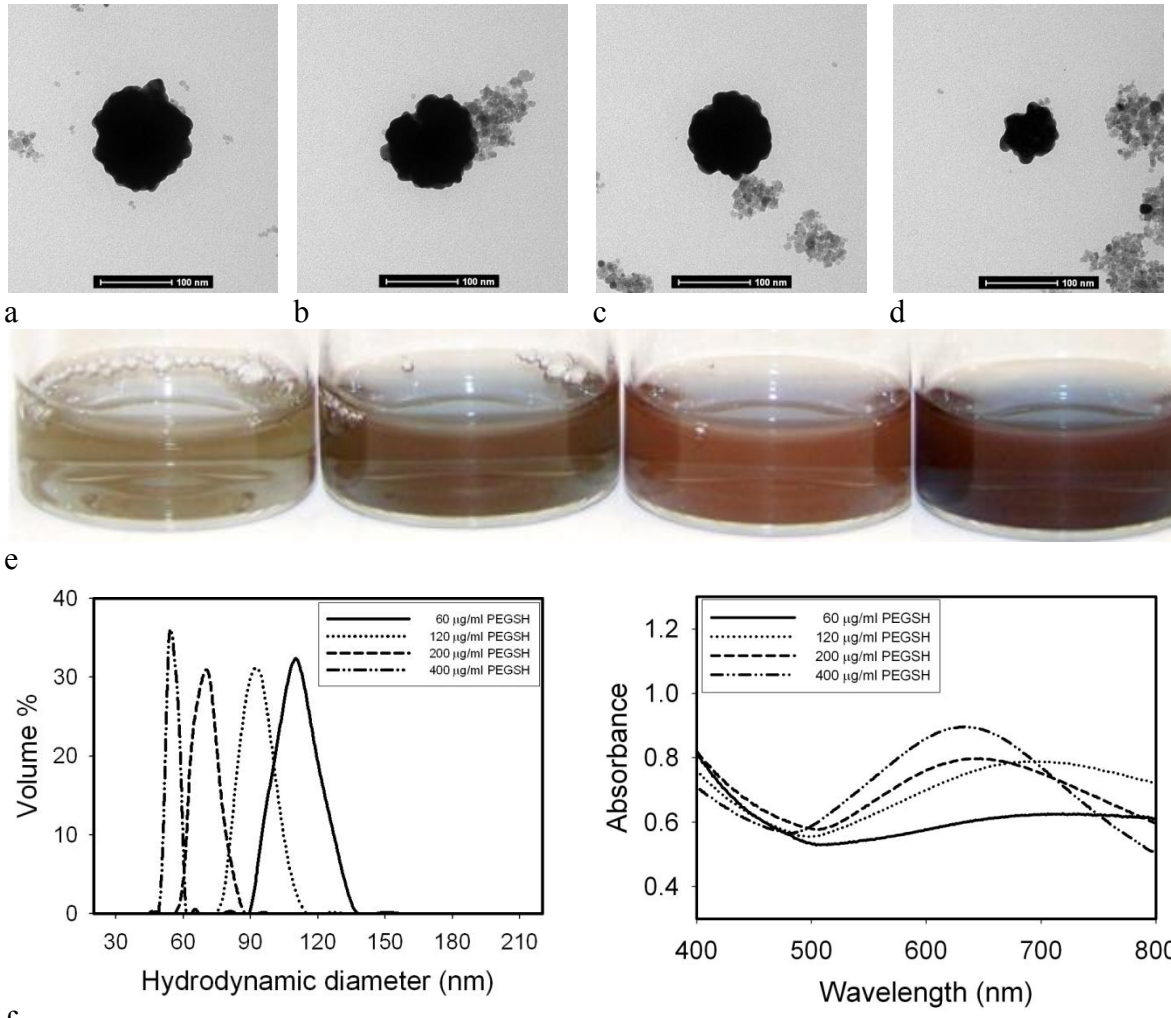

Figure 4.4 Effect of mPEG-SH/Au ratio on coated cluster properties for an initial Au^{3+}/Fe ratio of 0.5 and pH of 9.3. Morphology based on the TEM images (a) 60 µg/mL (b) 120 µg/mL (c) 200 µg/mL and (d) 400 µg/mL mPEG SH. The scale bar for all the images is 100 nm. The color of the resulting dispersions is shown in the photograph (e) below each corresponding TEM image. (f) hydrodynamic diameter (g) absorbance (absolute).

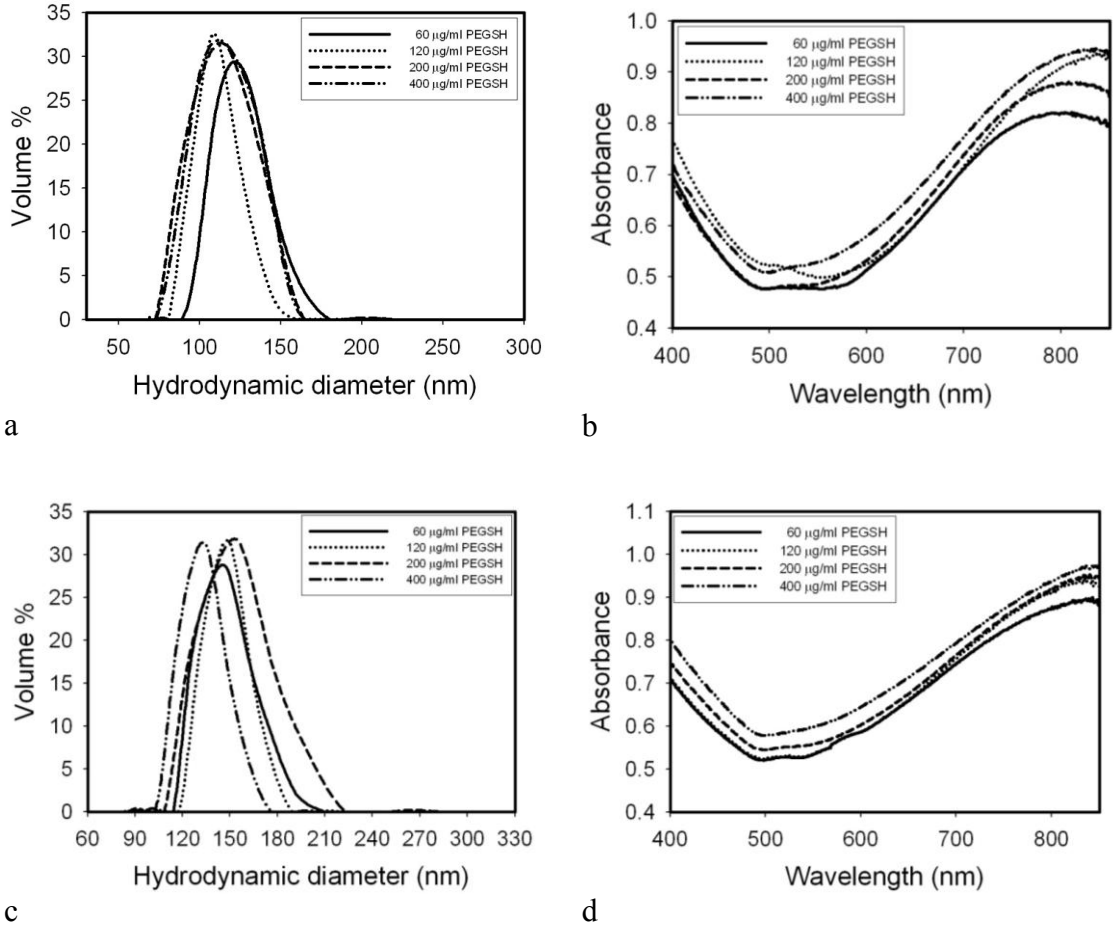

Figure 4.5 Effect of mPEG-SH/Au ratio on particle properties at pH values 8.6 and 7. Particle hydrodynamic diameter distributions by DLS for an initial pH of 8.6 (a) and 7.0 (c). The absorbance spectrum of the particles is shown in figure (b) initial pH of 8.6 and (d) initial pH of 7. The initial Au^{3+}/Fe mass ratio is 0.5. The reaction mixtures were quenched with HNO_3 to pH 6.0 after they turned turbid.

4.4 DISCUSSION

The changes in morphology upon changing a reaction condition, particularly the pH, will be explained in terms of a recently presented mechanism,[28] Textured Autocatalytic Growth on a Nanoparticle substrate (TAGS). We consider the

morphologies in this study as well as those in a recent study[28] where Au^{3+} precursor addition profiles were varied. Together the two studies cover a broad range of morphologies of Au shells of varying shape and thickness as can be seen in Scheme 4.1 and Figure 4.6.

4.4.1 Homogeneous nucleation and autocatalytic growth to form pure metal nanoparticles

The reduction potential for formation of a Au atom by reduction with hydroxylamine is -1.244 V. [7-9, 11, 56, 57]

$$2Au^{3+} + 6NH_2OH \Leftrightarrow 3N_2 + 6H_2O + 6H^+ + 2Au^0_{(atom\ or\ metal)}$$

In contrast, the reduction potential is thermodynamically much more favorable, 1.936 V, to form Au^o on a heterogeneous Au surface. Thus, it will be important to prevent excessive growth on the surfaces of Au seeds relative to nucleation of Au seeds from solution onto the iron oxide substrates.

The process of nucleation and autocatalytic growth of pure metal nanoparticles, is described quantitatively in the model developed by Watzky and Finke[13] and in studies of the growth of Au nanoparticles.[30, 31, 58] Nucleation of Au is described by

$$n\,Au^{3+} \xrightarrow{k_1} n\,Au^0 \qquad (1)$$

and growth on a Au surface by

$$n\,Au^{3+} + n\,Au^0 \xrightarrow{k_2} 2n\,Au^0 \qquad (2)$$

Based on (1) and (2),

$$\frac{d[Au^0]}{dt} = k_1[Au^{3+}] + k_2[Au^{3+}][Au^0] \qquad (3)$$

where k_1 is the rate constant for nucleation of Au seeds and k_2 is the growth rate.

Since $[Au^0] = [Au^{3+}]_0 - [Au^{3+}]$ (4)

$\frac{d[Au^0]}{dt} = k_1[Au^{3+}] + k_2[Au^{3+}]([Au^{3+}]_0 - [Au^{3+}])$ (5)

The value of n may be assumed to be the number of atoms needed to form a critical nucleus, above which growth is thermodynamically favorable.[59, 60] The growth is autocatalytic in that $[Au^0]$ in the product is a reactant. This type of nucleation and growth produces a sigmoidal shape as was demonstrated in Figure 4.1. In some cases, reactions 1 and 2 are fully separated and growth is performed on pre-made Au seeds. As the number of seeds increases, the particle size decreases for a fixed amount of Au reacted.[11, 60] In other cases, the degree of separation between nucleation and growth is manipulated to control the particle size.[13] As the separation increases, growth on a larger number of nuclei produces smaller particles.[11, 60]

4.4.2 Mechanism of nucleation and growth of thin Au films on iron oxide substrates

The autocatalytic growth mechanism in equations 1 to 5 may be extended to describe heterogeneous nucleation and growth of a Au shell on a nanoparticle substrate. A Au^{3+} ion may be reduced to form a new Au nucleus on an iron oxide surface or may attach to a growing Au surface already present on the substrate. Thus, it may be expected that changes in the relative values of k_1 and k_2 with pH would have the potential to influence the morphology of thin Au shells. Experimentally, thinner shells were observed for higher pH values in Figure 4.2 and 3a and Table 4.1, as shown schematically in Scheme 4.2. The figures on the left hand side of the arrow represent the particles at the end of the nucleation process, while those on the right represent the final particles. At a higher pH, the rapid reduction of Au^{3+} (as seen for homogeneous nucleation in Figure

4.1) may be expected to form Au nuclei on a larger fraction of the iron oxide particles, and with more nuclei per particle on these particles. The relatively large k_1 relative to k_2 describes more rapid nucleation and thus greater separation of nucleation and growth. For a fixed amount of total Au reduced, growth on a larger fraction of substrate particles, leads to relatively thin shells. When the nucleation to form seeds was more rapid at higher pH (larger k_1 relative to k_2), the greater separation of nucleation and growth led to thinner shells on a large number of substrate particles. Thus, the delay in growth provides more separation of nucleation and growth, leading to smaller particles and lower polydispersity in the seeded growth mechanism.

At low pH, the formation of nuclei (seeds) is slower and thus a smaller fraction of the substrate particles contains seeds, and with fewer seeds on these particles. Consequently, a fixed amount of Au reduced on fewer substrates will lead to thicker coatings. In each case, rapid autocatalytic growth takes place on the Au seeds, given the favorable surface energy for growth. Here the smaller degree of separation of nucleation and growth leads to growth on fewer particles. The rapid increase in Au shell thickness produces the more rapid color changes seen in Table 4.1. For a relatively small number of seeds/particle, rapid preferential growth in certain radial directions forms the highly asymmetric shells with knobby protuberances, as seen in the TEM images (Figure 4.2).

In our recent study,[28] the TAGS mechanism was introduced for controlling the degree of separation of nucleation and growth to control the Au shell morphology at a fixed pH of 9.3. The low value of the Au^{3+}/Fe ratio on the order of 0.5 relative to the value of 3-27 prevalent in the literature was used to produce much thinner Au coatings.[19, 22, 23, 25, 27] The rate and number of iterations of Au addition were varied to achieve this control. After half of the $[Au^{3+}]_o$ reacts, the rate is proportional to $k_1 + k_2[Au^{3+}]_o/2$. In the limit of continuous addition of Au precursor, small values of $[Au^{3+}]_o$ mitigate the

autocatalytic growth relative to nucleation, resulting in the thinnest shells. Conversely, in the current paper, nucleation was affected by changing a solution property, the pH of the reaction mixture, to manipulate the balance between nucleation and growth.

A widely used approach for growth of homogeneous nanoparticles utilizes rapid nucleation followed by slow growth and Ostwald ripening to focus the particle size to a narrow distribution. [59-62] Because growth of gold on gold is autocatalytic, unreacted Au precursor will be reduced rapidly onto any Au nuclei that are present. Thus, this conventional approach is not applicable given the inability to produce a slow growth step.

4.4.3 Effect of polymer: passivation and steric stabilization

For the relatively large iron oxide cores with a diameter of 40 nm and Au coatings, steric stabilization is necessary to prevent flocculation.[20, 25] The strong and selective binding of the mPEG-SH (20,000 g/mol), with an end-to-end distance of about 12 nm, to Au and not to iron oxide provided sufficient steric stabilization.[55, 63-66] At high pH (Figures 4a-g) where nucleation was fastest, the particle size increased as the mPEG-SH concentration was reduced. This increase reflects lower passivation of autocatalytic growth of Au on Au and spreading of Au seeds on fewer iron oxide particles. At lower pH values where nucleation was slower, and the separation of nucleation and growth was much smaller, the passivation of growth with mPEG-SH concentration had little effect on the particle size (Figures 5a-d). Here, growth during nucleation was sufficiently fast that the altered passivation effect of the polymer at different concentration was minor as expected. Therefore, the passivation of growth with bound polymer is more important for the case of larger separation of nucleation and growth, where the thinnest Au shells are formed.

4.4.4 Homologous series of shell morphologies by TAGS

A homologous series of high energy shells on a lower energy nanoparticle substrate is shown in Figure 4.6 and Table 4.3. In Figure 4.6 from left to right, the final ratio of Au/Fe in the particles and the particle size increases monotonically as can be seen in Table 4.3, reflecting less separation between nucleation and growth. This trend is a consequence of greater autocatalytic growth on fewer substrate particles. Although this study was performed with iron oxide clusters, the same concept would be expected to be applicable to spherical cores or other metal oxide substrates. For cores in the range of 40-50 nm, thick smooth Au shells (TK-Smooth) have been reported with shell thicknesses above 10 nm.[12, 17, 19-21, 23, 25, 67] The thin knobby shell morphology (TN-Knobby) and the thin smooth were reported in our recent work,[28] and thick knobby coated particles were introduced in the current work. As we can also see in Table 4.3, we get higher extinction coefficients for the particles with greater asymmetry associated with them.

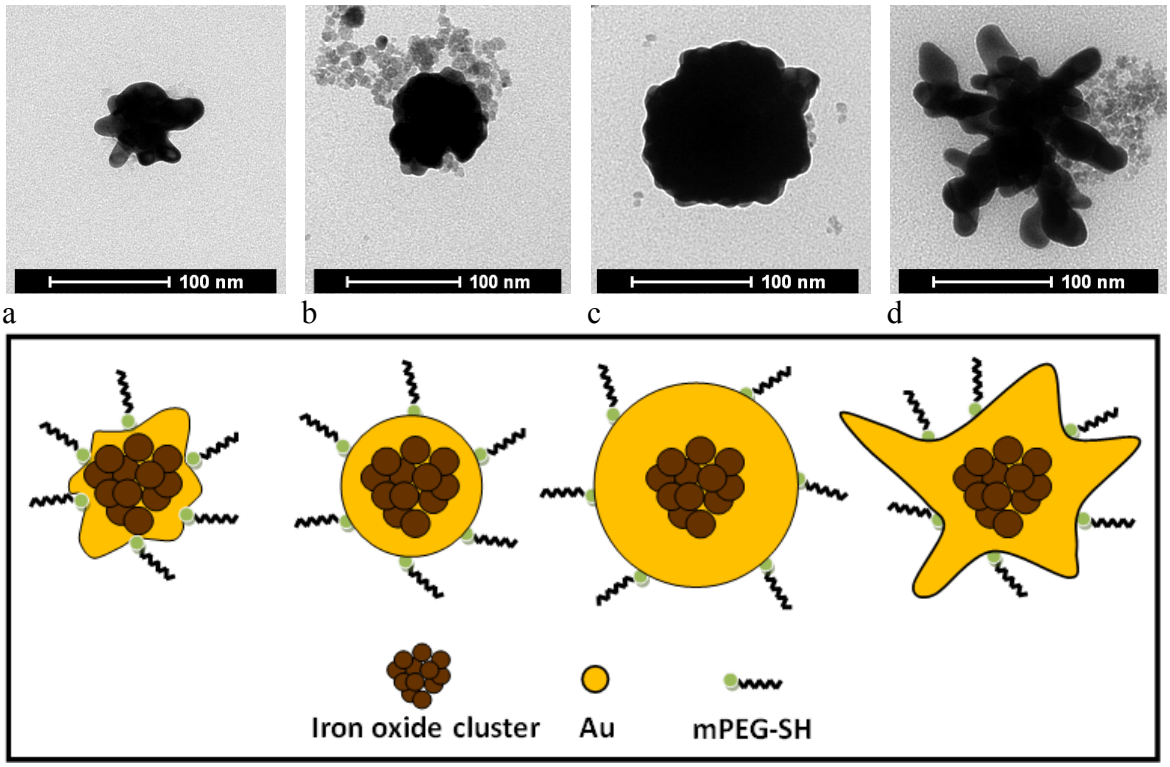

Figure 4.6 Morphology of the four classes of particles made (a) Thin knobby coated particles (b) Thin smooth coated particles (c) Thick smooth coated particles (d) Thick knobby coated particles and (e) A schematic representation of the four types of particles to depict the corresponding TEM images.

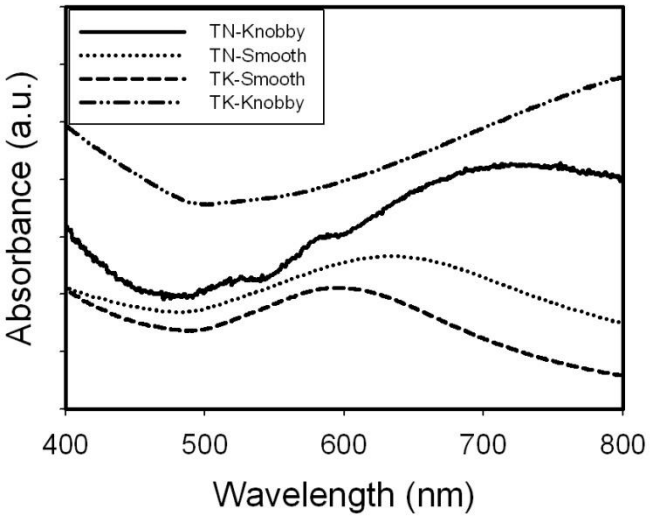

Figure 4.7 Absorbance spectra of four classes gold coated iron oxide nanoclusters (TN knobby and TN smooth from Ma et al. 2011) [28]

Table 4.3 Particle properties for different classes of particles all with an added gold to iron mass ratio of 0.5

	TN-Knobby[28]	TN-Smooth	TK-Smooth[28]	TK-Knobby
Starting pH	9.3	9.3	9.3	7.0
Initial Au^{3+}/Fe mass ratio	0.5	0.5	1.5	0.5
Au^{3+} iterations	5	1	1	1
Final Au/Fe mass ratio	0.84	2.70	5.09	6.43
Extinction coefficient at 755 nm (cm^2/μg Au)	0.051	0.041	0.029	0.059
Hydrodynamic diameter (nm)	55	60	105	132
Absorbance peak max	730	620	700	850

4.4.5 SPR behavior

The SPR behavior is shown in Figure 4.7 and quantified in Table 4.3 corresponding to the homologous series of Au shells on 42 nm iron oxide cluster substrates in Figure 4.6. The peak wavelength has been tuned from ~ 600 nm to as high as 850 nm. Asymmetries in the shapes of the core and shell enhance the absorbance in NIR region, as a result of hybridization between dipoles, quadrupoles and higher modes.[23, 32 29] Consider a uniform Au shell on spherical iron oxide cores, as described by Mie theory. To shift SPR peak to above 700 nm, the condition is $R_{total}/ R_{core} < 1.25$ for an Fe_3O_4 core with a permittivity in the range of 5.5 - 6.1[23] (predicted from Au_2S with a permittivity of 5.4).[23, 32, 43, 68] For smooth Au shells thinner than 5 nm (TN-smooth) where $R_{total}/ R_{core} = 1.25$, a broad SPR peak is centered about 600 nm, as shown in Figure 4.7. For thicker smooth shells the peak shifts to the blue as R_{total}/ R_{core} becomes larger.

In the case of knobby shells of varying thickness, the SPR peaks were strongly red-shifted to the NIR region (Figure 4.7). The knobby protrusions on the surface introduce high asymmetry and high aspect ratios, as has been observed in related morphologies including rods, nanoeggs[29] and nanorice[22]. In the case of 100-150 nm particles with TK-Knobby shells, the curves were red shifted to the greatest degree from 700nm to 900 nm even though $R_{total}/ R_{core} >> 1.25$. Thus the SPR may be tuned in the NIR for knobby shells over a wide range of total nanoparticle hydrodynamic diameters from 60 to 150 nm. The extinction coefficient of the particles at 755 nm is also very high and varies with morphology as can be seen in Table 4.3. The intensity of absorbance for these particles is therefore very high leading to high values of cross-section ($\sim 10^{-14}$ m^2). The extinction coefficient is higher for particles with knobby shells due to their asymmetries. Particles with thick smooth shells have a lower extinction coefficient due to their low absorbance in this spectral region as do particles with thin smooth shells.

4.5 CONCLUSIONS

The relative rates of nucleation and growth were tuned with a solution property, pH, to produce smooth shells from 5 to 40 nm thick, as well as 20 to 40 nm thick knobby shells, on ~42 nm iron oxide core nanoclusters. For a low Au^{3+}/Fe ratio of 0.5, low supersaturation values mitigate otherwise excessive autocatalytic growth. At low Au^{3+}/Fe ratios, intentionally, only a small and controlled fraction of substrate nanoparticles were coated with Au. For high nucleation rates at high pH, Au seeds were deposited on a higher fraction of the iron oxide substrate particles leading to thinner coatings. At lower pH values, slower nucleation led to less separation between nucleation and autocatalytic growth and, consequently, Au seeds on fewer particles, and thicker coatings. Covalently bound mPEG-SH on the Au shells provided steric stabilization and also passivated autocatalytic growth of Au. As the mPEG-SH concentration was lowered, less passivated shells at high pH became thicker, and eventually the concentration became too low for steric stabilization. The ability to control Textured Autocatalytic Growth on the nanoparticles Substrates (TAGS), while simultaneously providing sufficient steric stabilization, enables synthesis of Au shells on nanoparticles cores with total particle sizes in the range of 60 to 150 nm. Together, the tuning of the TAGS mechanism with a solution property, pH in the current study, as well as the precursor addition rate in our recent study[28] offers a broad platform for designing a wide range of smooth and knobby shell thicknesses on metal oxide cores. Thus, the TAGS mechanism for controlling the separation of nucleation and growth at low supersaturation values to coat high surface energy metals on metal oxide substrates may be expected to be general and applicable to a wide range of materials.

In most previous studies,[17, 19, 20, 25, 27, 55] the Au coatings were smooth and sufficiently thick that the peak maximum was in the visible region. The wide range of novel Au coated iron oxide nanoclusters with diameters from 60 to 150 nm were utilized to gain insight into NIR SPR behavior for highly asymmetric Au shell geometries. NIR SPR behavior with high cross-sections was demonstrated for both thin[28] or thick knobby shells, and thin smooth shells[28]. Broad peaks in the range of 700 to 900 nm were produced by the high aspect ratios and asymmetries in the geometries of the cores and shells (Figure 4.7). In many cases, the extinction coefficient per mass of Au in the NIR region (Table 4.3) was quite large for such small nanoparticles.

4.6 SUPPORTING INFORMATION

Table 4.S1 This table contains data for the size distributions for the particles produced by using a starting pH of 9.3 and a Au^{3+}/Fe ratio of 0.5. This is the same data as shown in graph form in Figure 4.4f.

Polymer concentration (mg/mL)	Mean (nm)	% Standard deviation
60	110.5	8.3
120	92.6	7.6
200	70.0	7.8
400	55.2	4.2

Table 4.S2 This table contains data for the size distributions for the particles produced by using a starting pH of 8.6 and a Au^{3+}/Fe ratio of 0.5. This is the same data as shown in graph form in Figure 4.5a.

Polymer concentration (mg/mL)	Mean (nm)	% Standard deviation
60	124.2	12.7
120	110.1	12.2
200	114.4	17.3
400	105.8	15.2

Table 4.S3 This table contains data for the size distributions for the particles produced by using a starting pH of 7.0 and a Au^{3+}/Fe ratio of 0.5. This is the same data as shown in graph form in Figure 4.5c.

Polymer concentration (mg/mL)	Mean (nm)	% Standard deviation
60	146.8	11.2
120	147.2	9.0
200	152.2	14.0
400	132.3	10.2

Table 4.S4 Summary of the reaction conditions and the properties of the resulting particles for a Au^{3+}/Fe feed ratio of 0.5.

pH	PEG-SH/Au feed ratio (mole/mole)	Au/Fe product mass ratio	Absorbance Maximum wavelength (nm)	Extinction Coefficient (cm^2/μg Au)	% Yield (Au)	% Yield (Fe)
9.3	0.01	1.89	720	0.042	11.8	3.1
9.3	0.02	2.43	700	0.051	16.2	3.3
9.3	0.04	2.47	650	0.044	17.3	3.5
9.3	0.08	2.70	630	0.041	19.8	3.7
8.6	0.01	3.15	800	0.053	22.8	3.6
8.6	0.02	3.62	800	0.056	20.1	2.8
8.6	0.04	4.48	800	0.056	19.6	2.2
8.6	0.08	4.13	800	0.059	17.2	2.1
7.0	0.01	3.52	850	0.055	20.6	2.9
7.0	0.02	3.92	850	0.057	23.2	3.0
7.0	0.04	5.14	850	0.057	22.6	2.2
7.0	0.08	6.43	850	0.059	20.4	1.6

Proof of acid quenching not affecting the final properties of the particles

The final properties of the particles resulting from the reaction are not affected much due to quenching the reaction mixture by adding nitric acid. This is evidenced in the figures below in which the properties for the particles produced without quenching are compared to the properties of the particles produced with quenching and as can be seen the particles

have almost identical properties. The DLS sizes agree well with each other for both the values of pH and the uv-visible spectra have the same characteristics.

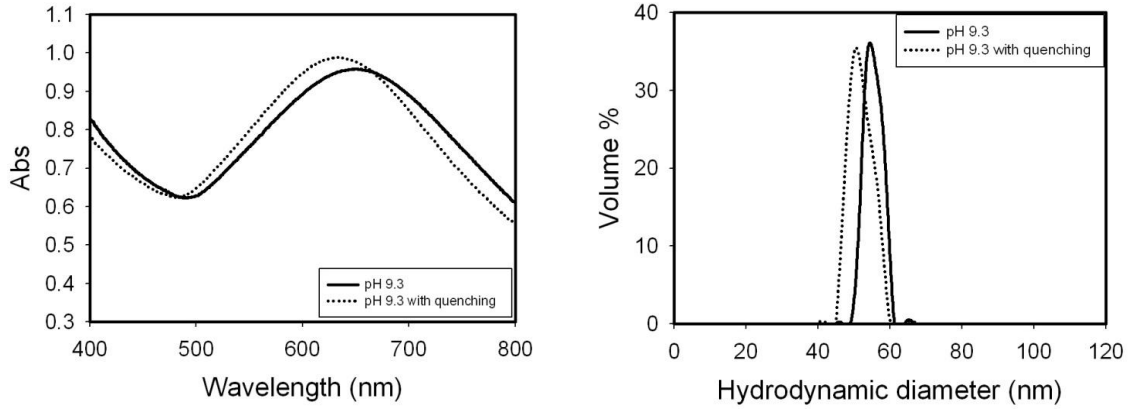

a b

Figure 4.S1 The UV-visible spectra a and the DLS data b for the particles resulting from an initial pH of 9.3 with and without acid quenching were compared.

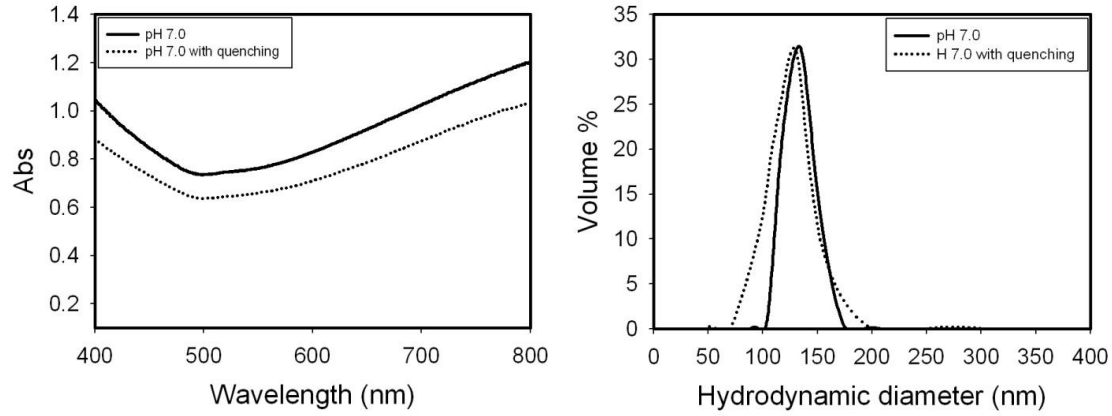

a b

Figure 4.S2 The UV-visible spectra a and the DLS data b for the particles resulting from an initial pH of 7.0 with and without acid quenching were compared.

4.7 REFERENCES

1. Ferrari, M., Beyond drug delivery. *Nature Nanotechnology* **2008,** 3, (3), 131-132.

2. Choi, H. S.; Liu, W.; Misra, P.; Tanaka, E.; Zimmer, J. P.; Ipe, B. I.; Bawendi, M. G.; Frangioni, J. V., Renal clearance of quantum dots. *Nature Biotechnology* **2007,** 25, (10), 1165-1170.

3. Nel, A. E.; Madler, L.; Velegol, D.; Xia, T.; Hoek, E. M. V.; Somasundaran, P.; Klaessig, F.; Castranova, V.; Thompson, M., Understanding biophysicochemical interactions at the nano-bio interface. *Nat. Mater.* **2009,** 8, (7), 543-557.

4. Hirsch, L. R., Nanoshell-mediated near-infrared thermal therapy of tumors under magnetic resonance guidance. *Proceedings of the National Academy of Sciences* **2003,** 100, (23), 13549-13554.

5. Lal, S.; Clare, S. E.; Halas, N. J., Nanoshell-Enabled Photothermal Cancer Therapy: Impending Clinical Impact. *Accounts Chem. Res.* **2008,** 41, (12), 1842-1851.

6. Stewart, M. E.; Anderton, C. R.; Thompson, L. B.; Maria, J.; Gray, S. K.; Rogers, J. A.; Nuzzo, R. G., Nanostructured plasmonic sensors. *Chemical Reviews* **2008,** 108, (2), 494-521.

7. Brown, K. R.; Lyon, L. A.; Fox, A. P.; Reiss, B. D.; Natan, M. J., Hydroxylamine seeding of colloidal au nanoparticles. 3. Controlled formation of conductive Au films. *Chemistry of Materials* **2000,** 12, (2), 314-323.

8. Brown, K. R.; Natan, M. J., Hydroxylamine seeding of colloidal Au nanoparticles in solution and on surfaces. *Langmuir* **1998,** 14, (4), 726-728.

9. Brown, K. R.; Walter, D. G.; Natan, M. J., Seeding of colloidal Au nanoparticle solutions. 2. Improved control of particle size and shape. *Chemistry of Materials* **2000,** 12, (2), 306-313.

10. Jana, N. R.; Gearheart, L.; Murphy, C. J., Seed-mediated growth approach for shape-controlled synthesis of spheroidal and rod-like gold nanoparticles using a surfactant template. *Advanced Materials* **2001,** 13, (18), 1389-1393.

11. Jana, N. R.; Gearheart, L.; Murphy, C. J., Evidence for seed-mediated nucleation in the chemical reduction of gold salts to gold nanoparticles. *Chemistry of Materials* **2001,** 13, (7), 2313-2322.

12. Park, J.; Joo, J.; Kwon, S. G.; Jang, Y.; Hyeon, T., Synthesis of Monodisperse Spherical Nanocrystals. *Angewandte Chemie International Edition* **2007,** 46, (25), 4630-4660.

13. Watzky, M. A.; Finke, R. G., Transition metal nanocluster formation kinetic and mechanistic studies. A new mechanism when hydrogen is the reductant: Slow, continuous nucleation and fast autocatalytic surface growth. *Journal of the American Chemical Society* **1997,** 119, (43), 10382-10400.

14. Lim, J. K.; Tilton, R. D.; Eggeman, A.; Majetich, S. A., Design and synthesis of plasmonic magnetic nanoparticles. *Journal of Magnetism and Magnetic Materials* **2007,** 311, (1), 78-83.

15. Shevchenko, E. V.; Bodnarchuk, M. I.; Kovalenko, M. V.; Talapin, D. V.; Smith, R. K.; Aloni, S.; Heiss, W.; Alivisatos, A. P., Gold/Iron Oxide Core/Hollow-Shell Nanoparticles. *Advanced Materials* **2008,** 20, (22), 4323-4329.

16. Xu, X.; Liu, F.; Yu, K.; Huang, W.; Peng, B.; Wei, W., A Kinetic Model for Nanocrystal Morphology Evolution. *ChemPhysChem* **2007,** 8, (5), 703-711.

17. Wang, L.; Park, H.-Y.; Lim, S. I. I.; Schadt, M. J.; Mott, D.; Luo, J.; Wang, X.; Zhong, C.-J., Core@shell nanomaterials: gold-coated magnetic oxide nanoparticles. *Journal of Materials Chemistry* **2008,** 18, (23), 2629-2635.

18. Park, H. Y.; Schadt, M. J.; Wang, L.; Lim, I. I. S.; Njoki, P. N.; Kim, S. H.; Jang, M. Y.; Luo, J.; Zhong, C. J., Fabrication of magnetic core @ shell Fe oxide @ Au nanoparticles for interfacial bioactivity and bio-separation. *Langmuir* **2007,** 23, (17), 9050-9056.

19. Oldenburg, S. J.; Averitt, R. D.; Westcott, S. L.; Halas, N. J., Nanoengineering of optical resonances. *Chemical Physics Letters* **1998,** 288, (2,3,4), 243-247.

20. Rasch, M. R.; Sokolov, K. V.; Korgel, B. A., Limitations on the Optical Tunability of Small Diameter Gold Nanoshells. *Langmuir* **2009,** 25, (19), 11777-11785.

21. Caruntu, D.; Cushing, B. L.; Caruntu, G.; O'Connor, C. J., Attachment of gold nanograins onto colloidal magnetite nanocrystals. *Chemistry of Materials* **2005,** 17, (13), 3398-3402.

22. Wang, H.; Brandl, D. W.; Le, F.; Nordlander, P.; Halas, N. J., Nanorice: A hybrid plasmonic nanostructure. *Nano Letters* **2006,** 6, (4), 827-832.

23. Levin, C. S.; Hofmann, C.; Ali, T. A.; Kelly, A. T.; Morosan, E.; Nordlander, P.; Whitmire, K. H.; Halas, N. J., Magnetic-Plasmonic Core-Shell Nanoparticles. *Acs Nano* **2009,** 3, (6), 1379-1388.

24. Lim, J. K.; Majetich, S. A.; Tilton, R. D., Stabilization of Superparamagnetic Iron Oxide Core−Gold Shell Nanoparticles in High Ionic Strength Media. *Langmuir* **2009,** 25, (23), 13384-13393.

25. Goon, I. Y.; Lai, L. M. H.; Lim, M.; Munroe, P.; Gooding, J. J.; Amal, R., Fabrication and Dispersion of Gold-Shell-Protected Magnetite Nanoparticles: Systematic Control Using Polyethyleneimine. *Chemistry of Materials* **2009,** 21, (4), 673-681.

26. Zhang, Q.; Ge, J.; Goebl, J.; Hu, Y.; Sun, Y.; Yin, Y., Tailored Synthesis of Superparamagnetic Gold Nanoshells with Tunable Optical Properties. *Advanced Materials* **2010**, n/a-n/a.

27. Lyon, J. L.; Fleming, D. A.; Stone, M. B.; Schiffer, P.; Williams, M. E., Synthesis of Fe oxide core/Au shell nanoparticles by iterative hydroxylamine seeding. *Nano Letters* **2004,** 4, (4), 719-723.

28. Ma, L. L.; Borwankar, A.; Willsey, B.; Yoon, K. Y.; Tam, J. O.; Sokolov, K.; Feldman, M. D.; Milner, T. E.; Johnston, K. P., Growth of Textured Thin Au Shells on Iron Oxide Nanoparticles. *Prepare for Submitting* **2011**.

29. Knight, M. W.; Halas, N. J., Nanoshells to nanoeggs to nanocups: optical properties of reduced symmetry core-shell nanoparticles beyond the quasistatic limit. *New Journal of Physics* **2008,** 10, (Oct.).

30. Yang, S.; Wang, Y.; Wang, Q.; Zhang, R.; Ding, B., UV irradiation induced formation of Au nanoparticles at room temperature: The case of pH values. *Colloids and Surfaces A: Physicochemical and Engineering Aspects* **2007,** 301, (1-3), 174-183.

31. Ji, X. H.; Song, X. N.; Li, J.; Bai, Y. B.; Yang, W. S.; Peng, X. G., Size control of gold nanocrystals in citrate reduction: The third role of citrate. *Journal of the American Chemical Society* **2007,** 129, (45), 13939-13948.

32. Hu, Y.; Noelck, S. J.; Drezek, R. A., Symmetry Breaking in Gold-Silica-Gold Multilayer Nanoshells. *Acs Nano* **2010,** 4, (3), 1521-1528.

33. Chen, J.; Saeki, F.; Wiley, B. J.; Cang, H.; Cobb, M. J.; Li, Z. Y.; Au, L.; Zhang, H.; Kimmey, M. B.; Li, X. D.; Xia, Y., Gold nanocages: Bioconjugation and their potential use as optical imaging contrast agents. *Nano Letters* **2005,** 5, (3), 473-477.

34. Loo, C.; Lin, A.; Hirsch, L.; Lee, M. H.; Barton, J.; Halas, N. J.; West, J.; Drezek, R., Nanoshell-enabled photonics-based imaging and therapy of cancer. *Technol. Cancer Res. Treat.* **2004,** 3, (1), 33-40.

35. Kim, C. S.; Wilder-Smith, P.; Ahn, Y. C.; Liaw, L. H. L.; Chen, Z. P.; Kwon, Y. J., Enhanced detection of early-stage oral cancer in vivo by optical coherence

tomography using multimodal delivery of gold nanoparticles. *Journal of Biomedical Optics* **2009,** 14, (3).

36. Sokolov, K.; Follen, M.; Aaron, J.; Pavlova, I.; Malpica, A.; Lotan, R.; Richards-Kortum, R., Real-time vital optical imaging of precancer using anti-epidermal growth factor receptor antibodies conjugated to gold nanoparticles. *Cancer Res.* **2003,** 63, (9), 1999-2004.

37. Larson, T. A.; Bankson, J.; Aaron, J.; Sokolov, K., Hybrid plasmonic magnetic nanoparticles as molecular specific agents for MRI/optical imaging and photothermal therapy of cancer cells. *Nanotechnology* **2007,** 18, (32), 325101/1-325101/8.

38. Huang, X. H.; Jain, P. K.; El-Sayed, I. H.; El-Sayed, M. A., Plasmonic photothermal therapy (PPTT) using gold nanoparticles. *Lasers Med. Sci.* **2008,** 23, (3), 217-228.

39. Ma, L. L.; Feldman, M. D.; Tam, J. M.; Paranjape, A. S.; Cheruku, K. K.; Larson, T. A.; Tam, J. O.; Ingram, D. R.; Paramita, V.; Villard, J. W.; Jenkins, J. T.; Wang, T.; Clarke, G. D.; Asmis, R.; Sokolov, K.; Chandrasekar, B.; Milner, T. E.; Johnston, K. P., Small Multifunctional Nanoclusters (Nanoroses) for Targeted Cellular Imaging and Therapy. *Acs Nano* **2009,** 3, (9), 2686-2696.

40. Aaron, J. S.; Oh, J.; Larson, T. A.; Kumar, S.; Milner, T. E.; Sokolov, K. V., Increased optical contrast in imaging of epidermal growth factor receptor using magnetically actuated hybrid gold/iron oxide nanoparticles. *Optics Express* **2006,** 14, (26), 12930-12943.

41. Xu, M. H.; Wang, L. H. V., Photoacoustic imaging in biomedicine. *Rev. Sci. Instrum.* **2006,** 77, (4).

42. Wang, L. V., Prospects of photoacoustic tomography. *Med. Phys.* **2008,** 35, (12), 5758-5767.

43. Anker, J. N.; Hall, W. P.; Lyandres, O.; Shah, N. C.; Zhao, J.; Van Duyne, R. P., Biosensing with plasmonic nanosensors. *Nat. Mater.* **2008,** 7, (6), 442-453.

44. Kim, J. W.; Galanzha, E. I.; Shashkov, E. V.; Moon, H. M.; Zharov, V. P., Golden carbon nanotubes as multimodal photoacoustic and photothermal high-contrast molecular agents. *Nat. Nanotechnol.* **2009,** 4, (10), 688-694.

45. Wu, S. P.; Lee, I.; Ghoroghchian, P. P.; Frail, P. R.; Zheng, G.; Glickson, J. D.; Therien, M. J., Near-infrared optical Imaging of B16 melanoma cells via low-density lipoprotein-mediated uptake and delivery of high emission dipole strength tris (porphinato)zinc(II) fluorophores. *Bioconjugate Chem.* **2005,** 16, (3), 542-550.

46. Diagaradjane, P.; Orenstein-Cardona, J. M.; Colon-Casasnovas, N. E.; Deorukhkar, A.; Shentu, S.; Kuno, N.; Schwartz, D. L.; Gelovani, J. G.; Krishnan, S., Imaging epidermal growth factor receptor expression in vivo: Pharmacokinetic and biodistribution characterization of a bioconjugated quantum dot nanoprobe. *Clin Cancer Res* **2008,** 14, (3), 731-741.

47. Ke, S.; Wen, X. X.; Gurfinkel, M.; Charnsangavej, C.; Wallace, S.; Sevick-Muraca, E. M.; Li, C., Near-infrared optical imaging of epidermal growth factor receptor in breast cancer xenografts. *Cancer Research* **2003,** 63, (22), 7870-7875.

48. Sahoo, Y.; Goodarzi, A.; Swihart, M. T.; Ohulchanskyy, T. Y.; Kaur, N.; Furlani, E. P.; Prasad, P. N., Aqueous ferrofluid of magnetite nanoparticles: Fluorescence labeling and magnetophoretic control. *J. Phys. Chem. B* **2005,** 109, (9), 3879-3885.

49. Ryoo, W.; Webber, S. E.; Johnston, K. P., Water-in-Carbon Dioxide Microemulsions with Methylated Branched Hydrocarbon Surfactants. *Industrial & Engineering Chemistry Research* **2003,** 42, (25), 6348-6358.

50. Qiu, P. H.; Mao, C. B., Seed-mediated shape evolution of gold nanomaterials: from spherical nanoparticles to polycrystalline nanochains and single-crystalline nanowires. *J. Nanopart. Res.* **2009,** 11, (4), 885-894.

51. Chen, R.; Wu, J. L.; Li, H.; Cheng, G.; Lu, Z.; Che, C. M., Fabrication of gold nanoparticles with different morphologies in HEPES buffer. *Rare Metals* **2010,** 29, (2), 180-186.

52. Sakai, T.; Alexandridis, P., Mechanism of gold metal ion reduction, nanoparticle growth and size control in aqueous amphiphilic block copolymer solutions at ambient conditions. *J. Phys. Chem. B* **2005,** 109, (16), 7766-7777.

53. Chen, W. R.; Adams, R. L.; Carubelli, R.; Nordquist, R. E., Laser-photosensitizer assisted immunotherapy: A novel modality for cancer treatment. *Cancer Letters* **1997,** 115, (1), 25-30.

54. Friedlander, S. K., *Smoke, Dust, and Haze: Fundamentals of Aerosol Dynamics, Second Edition*. Oxford University Press: 2000; p 432 pp.

55. Oh, E.; Susumu, K.; Goswami, R.; Mattoussi, H., One-Phase Synthesis of Water-Soluble Gold Nanoparticles with Control over Size and Surface Functionalities. *Langmuir* **2010,** 26, (10), 7604-7613.

56. Huang; W., Dissolution of copper thin films in hydroxylamine-based solutions. *International Journal of Mineral Processing* **2003,** 72, (1-4), 365-372.

57. Gachard, E.; Remita, H.; Khatouri, J.; Keita, B.; Nadjo, L.; Belloni, J., Radiation-induced and chemical formation of gold clusters. *New J. Chem.* **1998,** 22, (11), 1257-1265.

58. Cao, L.; Zhu, T.; Liu, Z., Formation mechanism of nonspherical gold nanoparticles during seeding growth: Roles of anion adsorption and reduction rate. *Journal of Colloid and Interface Science* **2006,** 293, (1), 69-76.

59. Yin, Y.; Alivisatos, A. P., Colloidal nanocrystal synthesis and the organic–inorganic interface. *Nature* **2005,** 437, (7059), 664-670.

60. Talapin, D. V.; Rogach, A. L.; Haase, M.; Weller, H., Evolution of an ensemble of nanoparticles in a colloidal solution: Theoretical study. *Journal of Physical Chemistry B* **2001,** 105, (49), 12278-12285.

61. Murray, C. B.; Kagan, C. R.; Bawendi, M. G., Synthesis and characterization of monodisperse nanocrystals and close-packed nanocrystal assemblies. *Annu. Rev. Mater. Sci.* **2000,** 30, 545-610.

62. Murray, C. B.; Norris, D. J.; Bawendi, M. G., Synthesis and characterization of nearly monodisperse CdE (E = sulfur, selenium, tellurium) semiconductor nanocrystallites. *Journal of the American Chemical Society* **1993,** 115, (19), 8706-8715.

63. Sakura, T.; Takahashi, T.; Kataoka, K.; Nagasaki, Y., One-pot preparation of mono-dispersed and physiologically stabilized gold colloid. *Colloid Polym. Sci.* **2005,** 284, (1), 97-101.

64. Hostetler, M. J.; Wingate, J. E.; Zhong, C. J.; Harris, J. E.; Vachet, R. W.; Clark, M. R.; Londono, J. D.; Green, S. J.; Stokes, J. J.; Wignall, G. D.; Glish, G. L.; Porter, M. D.; Evans, N. D.; Murray, R. W., Alkanethiolate gold cluster molecules with core diameters from 1.5 to 5.2 nm: Core and monolayer properties as a function of core size. *Langmuir* **1998,** 14, (1), 17-30.

65. Gilbert, S. E.; Cavalleri, O.; Kern, K., Electrodeposition of Cu nanoparticles on decanethiol-covered Au(111) surfaces: An in situ STM investigation. *J Phys Chem-Us* **1996,** 100, (30), 12123-12130.

66. Fetters, L. J.; Lohse, D. J.; Richter, D.; Witten, T. A.; Zirkel, A., CONNECTION BETWEEN POLYMER MOLECULAR-WEIGHT, DENSITY, CHAIN DIMENSIONS, AND MELT VISCOELASTIC PROPERTIES. *Macromolecules* **1994,** 27, (17), 4639-4647.

67. Wang, L.; Luo, J.; Maye, M. M.; Fan, Q.; Rendeng, Q.; Engelhard, M. H.; Wang, C.; Lin, Y.; Zhong, C.-J., Iron oxide–gold core–shell nanoparticles and thin film assembly. *Journal of Materials Chemistry* **2005,** 15, (18), 1821.

68. Wu, D. J.; Xu, X. D.; Liu, X. J., Influence of dielectric core, embedding medium and size on the optical properties of gold nanoshells. *Solid State Commun* **2008,** 146, (1-2), 7-11.

Chapter 5: Selective Targeting of Antibody Conjugated Multifunctional Nanoclusters (Nanoroses) to Epidermal Growth Factor Receptors in Cancer Cells

The ability of smaller than 100 nm antibody nanoparticle conjugates to target and modulate the biology of specific cell types may enable major advancements in cellular imaging and therapy in cancer. A key challenge is to load an extremely high degree of targeting, imaging, and therapeutic functionality into small, yet stable particles. A versatile method called thin autocatalytic growth on substrate (TAGs) has been developed in our previous study to separate the nucleation of gold seeds onto iron oxide nanoparticles followed by limited growth to form ultra-thin and asymmetric gold coatings. The 35 nm asymmetric thin gold coated iron oxide nanoclusters produce exceptional near infrared (NIR) absorbance and superparamagnetism for an enhanced r_2 spin-spin relaxivity. Herein, a novel conjugation technique further allows covalent binding of anti-epidermal growth factor receptor (EGFR) monoclonal antibody (Ab) clone 225 to the nanoclusters to realize highly selective targeting to EGFR over expressing cancer cells. AlexaFluor 488 tagged clone 225 nanocluster conjugates were prepared to correlate the number of conjugated antibodies with the hydrodynamic size of the naoclusters. For 1 to 74 Abs on a nanorose surface, the correlated hydrodynamic diameters varied from 35 to 78 nm, as measured by dynamic light scattering (DLS). A transition from sub-monolayer to multilayer aggregates of Abs on the nanoparticle surface was observed for 54 Abs and an overall particle diameter of 63 nm.

The targeting efficacy of the conjugated nanoclusters was evaluated by the A431 cancer cell uptake characterized by dark field reflectance imaging and atomic absorbance spectrometry (AAS) essay analysis on Au element. Dual mode *in-vitro* imaging studies

with dark field reflectance microscopy and fluorescence microscopy demonstrate that these multifunctional nanoclusters may be used as NIR and fluorescent contrast agents for 'theranostisc' of EGFR expressing cancer cells.

5.1 INTRODUCTION

Development of multifunctional nanoparticles to monitor targeted drug delivery non-invasively and to determine the therapeutic response rapidly will provide a new paradigm for cancer treatment in the clinic. Whereas, nanoparticles are typically used either for molecular imaging or therapy,[1-7] recent efforts are underway to do both simultaneously. For example, magnetic resonance imaging (MRI) and ultrasound imaging have been utilized to monitor temperature changes during photothermal therapy.[7-9] However, nanoparticles possessing multifunctional properties for achieving both molecular imaging and real time feedback on therapeutic efficacy for cancer treatment are not yet utilized in the clinic. Thus, a key challenge in nanomedicine is to synthesize therapeutic nanoparticles coated with biomarkers for high targeting efficiency and with strong near infrared (NIR) absorbance and/or magnetic properties for imaging and therapy.[10]

In passive delivery of polyethylene glycol (PEG) coated gold nanoparticles, the particles permeate leaky vasculatures and accumulate in tumor interstitial space.[11, 12] An antibody (Ab) or small antibody fragment may be coated on the particle surface to target biomarker receptors and greatly enhance accumulation at the tumor site.[10, 13] There are two key conjugation protocols available for attachment of peptides or proteins on the surface of nanoparticles. In the first or indirect method, functional groups, for example, COOH, on the polymer coatings of the nanoparticle surfaces are conjugated to primary

amine groups, which may be on either the Fc (nonbinding region) or Fab region (binding region).[14] For example, EDC/Sulfo-NHS chemistry has been widely adopted for nanospheres,[13, 14] nanoshells[3] and nanorods.[15] In a recent study of gold nanorods with this method, the total gold accumulation in xenograft tumor models was only marginally improved in comparison with nontargeted controls.[15] In the direct method, the Fc region of an Ab is first coupled with a low molecular weight heterobifunctional linker such as dithiol-PEG-hydrazide(MW 708.97), whereby the dithol group is conjugated directly to the Au surface. The coupling is achieved with a selective reaction between the hydrazide end group and an aldehyde, formed by mild oxidation of a carbohydrate side chain on the Fc region.[16-21] Selective binding to the Fc region of an Ab is beneficial for maximizing the biological activity of the Fab binding regions.[19, 20, 22-24] This conjugation strategy allows for the multiplexing of various glycosylated antibodies on a single nanoparticle for monitoring therapeutic agents in vivo.[25, 26] Thus, the high surface density of gold atom conjugation sites serves as a high versatile substrate for binding of these multiple types of functional biomolecules with relatively simple conjugation chemistry.

In cancer nanomedicine, an extremely high degree of targeting, NIR absorbance, magnetization and therapeutic functionality must be loaded into small, yet stable particles. Particles in the range of 35 to 65 nm are highly effective in bypassing the reticuloendothelial system (RES) (liver and spleen).[27-29] Gold coated iron oxide particles are of interest for both magnetic and optical functionality, and may exhibit relatively low toxicity.[7, 10, 30] To drive nucleation of Au seeds on unfavorable low energy iron oxide surfaces, high supersaturation values are often utilized, with Au^{3+}/Fe mass ratios in the order of 10.[30-32] Excessive autocatalytic growth often produces shells on the order of 10 nm.[33-37] The surface plasmon resonance (SPR) for the thick shells is typically in the

visible, rather than the NIR region. Furthermore, the thick shells take up space needed for the Abs, and other functional components such as iron oxide, given the limitation of the small overall particle size. To address these severe space requirements, 35 nm multifunctional iron oxide nanoparticles were designed with very thin Au shells (< 5 nm), yet strong NIR absorbance (cross section of ~10^{-14} m^2 at 755 nm).[7] For cancer imaging/therapy, it would be desirable to conjugate Abs onto this type of small multifunctional nanoparticle, while achieving colloidal stability. Very recently, it has been found that the particle curvature and shape impact cellular targeting as seen for nanocages,[38] ellipsoids, rods, cylinders and disks, in addition to spheres.[39-41] The design of multifunctional nanoparticles with various surface curvatures and control of the density and orientation of Abs on the surface has the potential to have a large impact on cellular uptake and therapy in nanomedicine.

Herein, we have conjugated monoclonal anti-EGFR antibodies to multifunctional nanoparticles (nanorose) composed of thin knobby Au coatings on magnetic iron oxide cores, with a tunable number, from 1 to 74, of conjugated Abs. As the number of Abs increased, the hydrodynamic diameter measured by dynamic light scattering (DLS), increased from 35-78 nm. High surface coverage of Abs is favored by the high density of conjugation sites supplied by Au atoms on the surface and the low cross sectional area of the heterobifunctional dithiol-PEG-hydrazide (MW 708.97) linker. The thin Au shells and the low MW linker take up relatively little space, leaving substantial room for other functional components (iron oxide) and Abs, despite the small overall particle size. Furthermore, because the Au shells are so thin, the amount of steric stabilizer (mPEG-SH, MW 5,000) needed to counteract VDW forces may be expected to be unusually low relative to more common particles with thicker Au shells.[34] The number of clone 225 Abs conjugated to the nanorose was tuned from sub-monolayer to multilayer coverage as

characterized by labeling the Abs with AlexaFluor 488 fluorophore. For 54 Abs, the hydrodynamic diameter indicated coverage of a monolayer for Abs, in agreement with the prediction of a geometric model, by assuming a circular area for the Fab region.

Highly uptake of conjugated nanorose for A431 skin cancer cells was observed with dark field and fluorescence microscopy, as quantified by flame atomic absorption spectroscopy (AAS). The intensive orange color under dark field indicates high NIR scattering by the thin Au shells on nanorose in agreement with previous hyperspectral images in macrophage cells for nanorose without Ab conjugation.[7] Fluorescence images show strong green emission from AlexaFluor 488 tagged clone 225 Abs inside cancer cells indicating the Abs stayed attached to the Au surfaces. The uptake of nanorose conjugated with an Ab monolayer reached 7000 particles/cell, more than previously reported for 50 nm Au spheres[42] with the same Ab and cell type. The high uptake is discussed in terms of the small hydrodynamic diameter, high degree of Ab conjugation, and the influence of the highly curved surfaces on the Ab orientations. These particles with NIR imaging, magnetic and therapeutic multifunctionality in a small overall particle size would be of interest in advancing molecular specific imaging combined with therapy.

5.2 EXPERIMENTAL SECTION

5.2.1 Materials

Monoclonal anti-EGF receptor antibody clone 225 (Sigma: E2156) and monoclonal anti-rabbit immunoglobulin clone RG-16 (Sigma: I0138) were obtained from Sigma-Aldrich Co. The antibody stock solutions were first purified by using a 100,000 molecular weight cutoff (MWCO) centrifugal filter (Amicon Ultra-4, Millipore Co.).

Briefly, 200 µL (1.5 mg/mL) clone 225 stock solution was transferred into one filter device with 3 mL HEPES (pH 7.4, 40 mM) addition. The filter device was centrifuged for 14 mins at 3,220 xg. 300 µL HEPES was used to form a solution of the antibody at a final concentration of 1 mg/ml. Dithiol-alkane aromatic PEG_6-$NHNH_2$ ($C_{33}H_{60}N_2O_{10}S_2$, MW 708.97, SensoPath Technologies Inc., Bozeman, MT, USA), mPEG-SH (MW 5,000) from Nanocs Inc. (New York, NY, USA), PEG (MW 14,000) and $NaIO_4$ (213.89 MW) from Sigma-Aldrich Co. were used.

5.2.2 Antibody conjugation to nanorose

The 35 nm diameter thin gold coated iron oxide "nanorose" particles were assembled by using dextran as a stabilizer as reported in our previous paper.[7] Nanorose particles (2.4 mg Au) were then redispersed after centrifugation at 4,629 xg for 6 mins by using a 50 µL of 0.05 mg/ml (10^{-5} M) mPEG-SH water solution and 2 ml DI water to reach a concentration of ~ 1 mg Au/ml. The heterogeneous linker (dithiol-PEG-hydrazide) was used to covalently attach monoclonal antibodies to gold surfaces.[19, 43] Briefly, the linker (MW 709 Da) consists of a short polyethylene glycol chain terminated at one end by a hydrazide group and at the other end by di-thiol groups. 300 µg clone 225 antibodies at a concentration of 1 mg/mL were first mixed with 300 µL of 10 mM $NaIO_4$ for 45 minutes at room temperature under mild agitation and protection from light. Here, the hydroxyl moieties on the antibodies' Fc region were oxidized to aldehyde groups. Then, one aliquot of dithiol-PEG-hydrazide linkers (5 µL, 50mM in ethanol) was added to the oxidized antibodies for 30 minutes. The hydrazide portion of the heterogeneous linker readily reacted with aldehydes on antibodies' Fc region to form a stable linkage. The unreacted linker and salts were removed with a 100,000 MWCO centrifugal filter (Millipore Co.) at 3,220 xg for 14 mins. The antibodies (clone 225-PEG-dithiol)

remained on the filter and were resuspended in 300 μL HEPES (pH 7.4, 40 mM). After purification, the modified antibodies were mixed with nanoroses and dispersed in 30 mL of HEPES for 8 hours at 4 ^{o}C on a shaker. Stable covalent bonds were formed between the gold surfaces and the linker's dithiol groups during mixing. Subsequently, mPEG-SH (MW 5,000) molecules were added to passivate the gold surface on the nanoparticles unoccupied by antibodies. Nanorose conjugates were centrifuged at 4,629 xg for 6 mins and re-suspended in 2 mL HEPES (pH 7.4, 40mM). The concentrated nanorose-clone 225 conjugates were stored at 4^{o}C for further characterization and cell targeting. To measure non-specific binding of nanoparticles to cancer cells, anti-rabbit IgG (clone RG-16) antibodies that do not specifically bind to cancer cells were also conjugated to nanoroses by following the same procedure as for the clone 225.

5.2.3 Cell culture and nanoparticle targeting

EGFR (+) human epithelial carcinoma cells (A431 keratinocyte) were cultured in petri dishes using a 50/50 (v/v) mixture of phenol/serum free DMEM medium at 37 ^{o}C in a 5% CO_2 incubator till 80% confluence. Cells were harvested from plate by using trypsin and incubated for 5 mins. They were harvested and resuspended in 1 mL culture medium for cell counting. 10^6 cells/ml suspensions were typically harvested for nanoparticle labeling. Then, a designated number of cells were mixed with a known number of nanoparticles dispersed in 2 mL culture medium and allowed to interact for 60 mins on a shaker at room temperature. After labeling, the cells were centrifuged at 201xg for 3 mins to remove unbound particles in supernatant and re-suspended in 1×PBS. After a second round centrifugation at the same conditions to minimize impurities, the particle labeled cells were dissolved in 0.5 ml 1 mM HNO_3 for AAS elemental analysis. The

labeled cells were also re-dispersed in 1×PBS for optical microscope imaging. EGFR (-) MDA-MB-435 breast cancer cells were cultured and labeled under the same conditions as the control cell line.

5.2.4 Au elemental analysis in the labeled cells

After redispersing the nanoparticle labeled cells, the Au concentrations in the cell was obtained by flame atomic absorption spectroscopy (GBC Scientific Equipment Pty Ltd, 908AA, Melbourne, Australia). The apparatus was equipped with an air-acetylene flame furnace. The absorption of Au was recorded at 242.8 nm. The instrument was calibrated using Au^{3+} standard solutions before every set of measurements. All measurements were carried in diluted samples so that the concentration of Au was between 1 and 5 μg/ml.

5.2.5 Hydrodynamic diameter measurement of Abs conjugated nanoparticles

Dynamic light scattering (DLS) measurements were performed in triplicate on a custom made Brookhaven Instruments dynamic light scattering apparatus at a scattering angle of 90° and temperature of 25℃. [44] Abs conjugated nanoparticle dispersion concentrations were adjusted with 1×PBS to give a scattering signal counting rate between 300-400 kcps. Prior to DLS measurements, the samples were bath sonicated for 2 minutes. The autocorrelation functions were analyzed with a non-negative least-squares (NNLS) method to determine distributions by volume.[44]

5.2.6 Fluorescent labeling and UV-Vis spectrometry

Alexa Fluor 488 monoclonal antibody labeling kit (Invitrogen Co.) was used to label modified antibodies (clone 225-PEG-dithiol) by following the provided procedure.

The fluorophore has a tetrafluorophenyl ester moiety that reacts efficiently with primary amines on the Abs to form stable dye-protein conjugates. The excitation and emission measurements were performed at the absorption peak (494 nm) of the Alexa Fluor 488 dye by using a BioTek Synergy HT multi-mode microplate reader (BioTek Instruments, Inc.). To precisely determine the absorbance or emission of the Abs on the nanorose, freshly prepared background solutions for baseline subtraction were analyzed simultaneously with samples in a 96-well plate. The concentrations of the fluorescent clone 225 were measured from the absorbance at wavelengths of 280 nm and 494 nm in a 1 cm optical path length cuvette according to the formula suggested by the guide in the fluorescent labeling kit:

$$\text{clone 225 concentration (mg/ml)} = \frac{(A_{280} - A_{494} \times 0.11) \times 160000}{203000} \quad (1)$$

The molecular weight of the clone 225 antibody was 160,000 g/mole, and the absorbance cross section was 203,000 cm^{-1} M^{-1}. A linear correlation between the emission intensity at 519 nm of the Alexa Fluor 488 labeled clone 225-PEG-dithiol versus concentration with a correlation coefficient r = 0.9986 was determined as shown in Figure 5.1.

After mixing of the fluorescently labeled clone 225-PEG-dithiol to nanoroses as described in the antibody conjugation procedure, centrifugation at 4,629 xg for 6 mins was used to separate the conjugated nanoroses in the pellet from unbound antibodies in the supernatant. The fluorescence emission intensity of the supernatant for an excitation and emission wavelength of 494 nm and 519 nm, respectively, was measured to determine the concentration unbound antibodies by comparing with the correlation curve. The average amount of attached antibodies to nanorose was determined by subtracting the unbound antibodies from total.

5.2.7 Dark field reflectance imaging and fluorescent imaging

Dark field reflection images were captured with a Leica DM 6000 upright microscope using Xenon illumination along with a 20× dark-field objective (0.5 NA) and a Retiga EXi camera with 12-bit ultra-sensitive CCD camera detector, for imaging in a RGB mode (Q-imaging, Inc.). In dark-field microscopy, a sample is illuminated by a cone of light outside of the imaging angular acceptance aperture. The large scattering angle allows detection of highly scattering objects (such as nanoroses) with very little background signal. Fluorescence images were captured from the same microscope under fluorescence mode by collecting 520 nm emission signals (emission peak at 519 nm of Alexa Fluor 488) with an excitation wavelength at 490 nm (absorption peak at 494 nm of Alexa Fluor 488).

Scheme 5.1 Geometric properties of antibody layers on model spherical particle surfaces (approximately to scale).

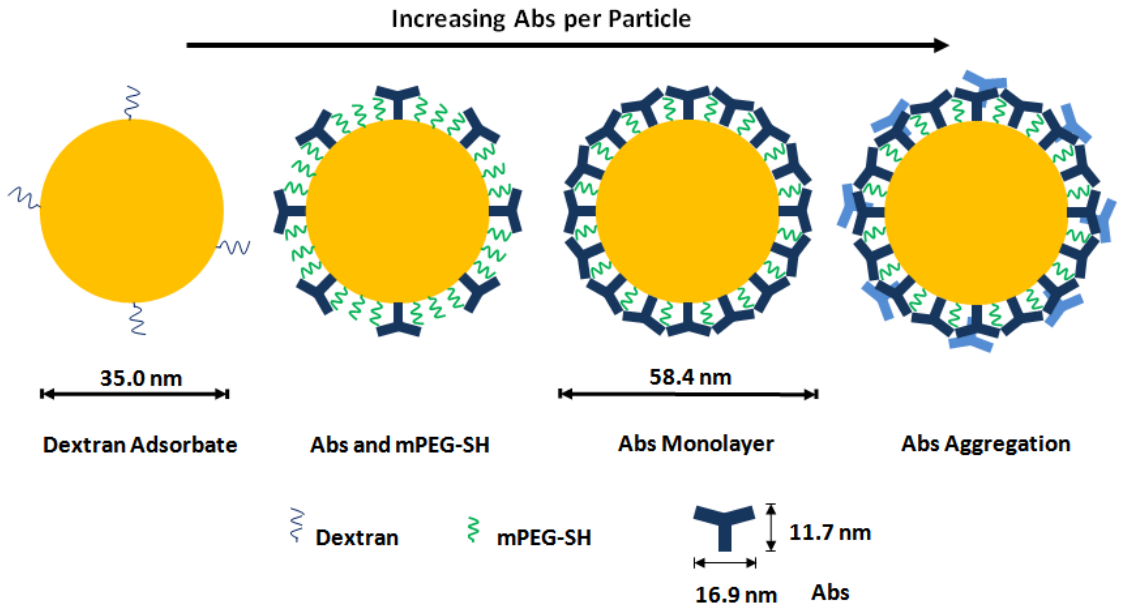

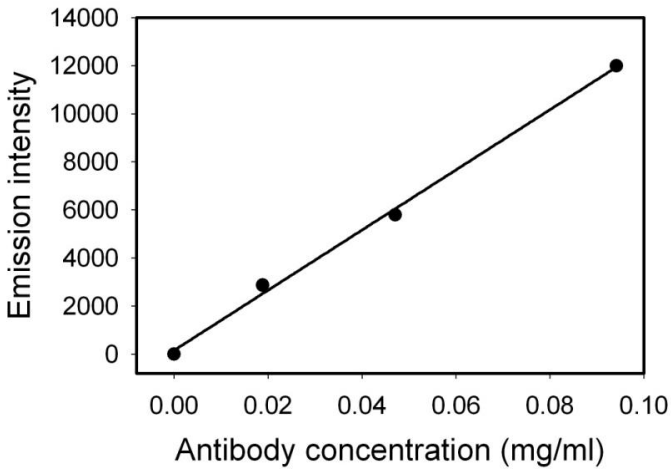

Figure 5.1 Calibration curve for emission intensity (arbitrary units) at 519 nm of AlexaFluor 488 labeled clone 225 antibody versus concentration. The excitation was performed at the absorption peak maximum of 494 nm of the AlexaFluor 488 dye. A correlation coefficient r = 0.9986 was determined.

5.3 RESULTS

5.3.1 Number of clone 225 Abs conjugated to nanorose and hydrodynamic diameter

The average number of conjugated clone 225 antibodies on one nanorose was determined from fluorescence for the Alexa Fluor 488 labeled clone 225 antibody based on the calibration curve in Figure 5.1 between emission intensity and . A predetermined amount (Table 5.1) of Alexa Fluor 488 labeled clone 225-PEG-dithiol from a concentrated stock solution (0.565 mg/ml) was mixed with 6.2×10^{11} nanorose particles dispersed in 10 ml HEPES for the conjugation reaction. The number of nanorose particles was determined from elemental analysis by AAS.[7] As shown in Table 5.1, the number of covalently attached clone 225 molecules per nanorose particle increased monotonically with the initially mixed antibody amount. When 303 clone 225-PEG-dithiol molecules were mixed with one nanorose particle, 54 were attached as determined by the calibration curve (Figure 5.1). This number is on the order of a monolayer as will be quantified in detail in the discussion section.

The hydrodynamic diameter of the nanorose particles with different numbers of conjugated antibodies were measured in 1×PBS dispersion, before and after filtration with a 0.22 μm filter, by DLS (Figure 5.2). As shown in Table 5.1, the hydrodynamic diameters increased monotonically from 33 nm to 80 nm as the attached number of clone 225 molecules increased from 1 to 74. The vast majority of the particle hydrodynamic diameter distribution by volume was in the primary peak. A small secondary peak (~ 10 % by volume) was observed with a larger size, indicating a small population of particle aggregates (Figure 5.2A and Table 5.1). After filtration with a 0.22 μm pore size syringe filter, the second peak from particle aggregates was fully removed as shown by DLS (Figure 5.2B and Table 5.1). The hydrodynamic sizes of the non-aggregated

particles (smaller peak) did not change significantly in the filtration process. This stability of the particles suggests that the antibody molecules and mPEG-SH were effective in providing steric stabilization.

The absorbance spectra of nanoroses (TEM image in Figure 5.3B) were obtained before and after antibody conjugation (Figure 5.3A). The very small change in spectra indicated high colloidal stability and stability in the Au shells for the particles. In addition, the Abs contributed little to the absorbance as expected, given the extremely strong cross section for the SPR of Au. In each case, a large shift to the NIR, relative to the spectra for Au spheres, is cause by asymmetry in the thin Au shells[7] as described below. We also determined the absorbance spectra for more well-known[30] spherical control particles with a 50 nm diameter and thick gold shells (TEM image in Figure 5.3B) on the same iron oxide core as for the nanorose in Figure 5.3A. At 755 nm, the extinction coefficients for the nanorose particles with thin asymmetric shells (0.0537-0.0563 $cm^2/\mu g$ Au) were over five times those of the control particles with thick smooth gold shells (0.0085-0.0106 $cm^2/\mu g$ Au) as shown in Table 5.2. For similar particles, ~ 20 nm thick smooth gold shells on ~10 nm iron oxide cores are often too thick to shift the SPR peak of pure gold at 530 nm to the preferred NIR region.[16, 17, 30] The 6 order of magnitude larger extinction cross section of the antibody conjugated nanorose particles (10^{-14} m^2)[7] compared with antibody conjugated fluorophore, like indocyanine green dye or Cy5.5,[26, 45, 46] is highly desirable for NIR optical imaging and therapy in cancer.

A

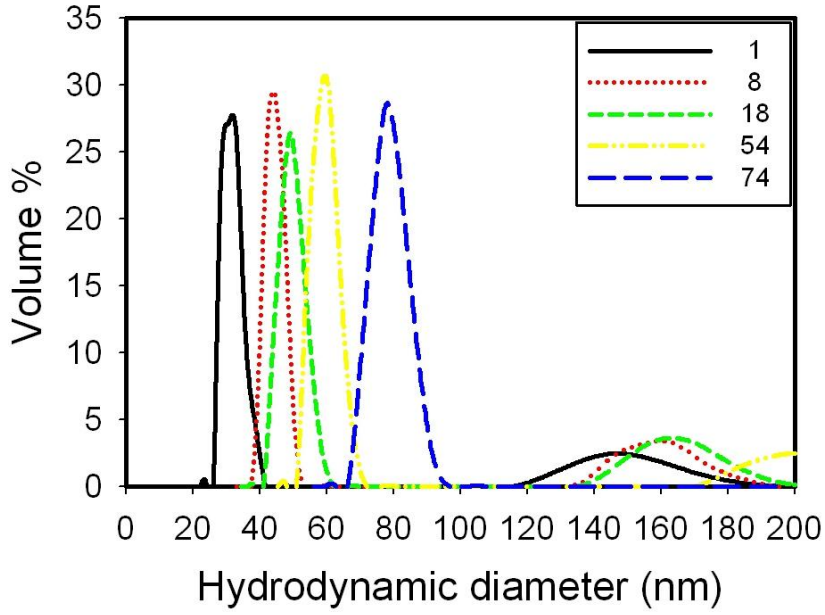

B

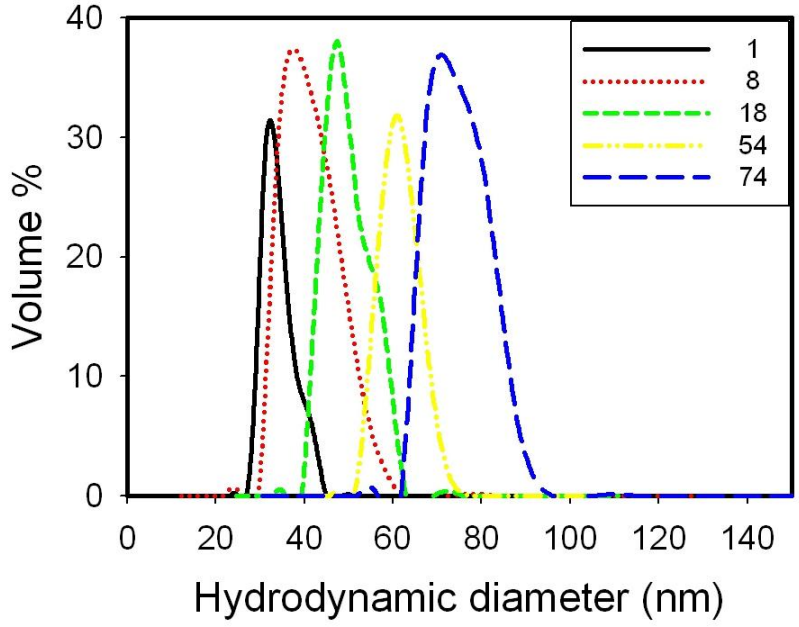

Figure 5.2 Hydrodynamic diameter of clone 225 conjugated nanoroses. A. before filtration B. after passing a 0.22 µL filter. Insert gives numbers of Abs per particle.

Table 5.1. Clone 225 conjugation to 6.2×10^{11} nanorose particles and hydrodynamic diameter by dynamic light scattering.

Feed Ab mass (μg)	Feed Ab molecules/ nanorose	Conjugated Ab mass (μg)	Conjugated Ab molecules/ nanorose	Diameter volume %	Diameter after filtration
2.00	12	0.1800	1	33 ±3 nm, 92%	35 ±4 nm
9.98	60	1.2570	8	45 ±3 nm, 89%	44 ±6 nm
20.02	121	3.0030	18	51 ±4 nm, 87%	50 ±5 nm
50.18	303	8.9674	54	61 ±4 nm, 92%	63 ±5 nm
99.80	604	12.1990	74	80 ±5 nm, 91%	78 ±7nm

A

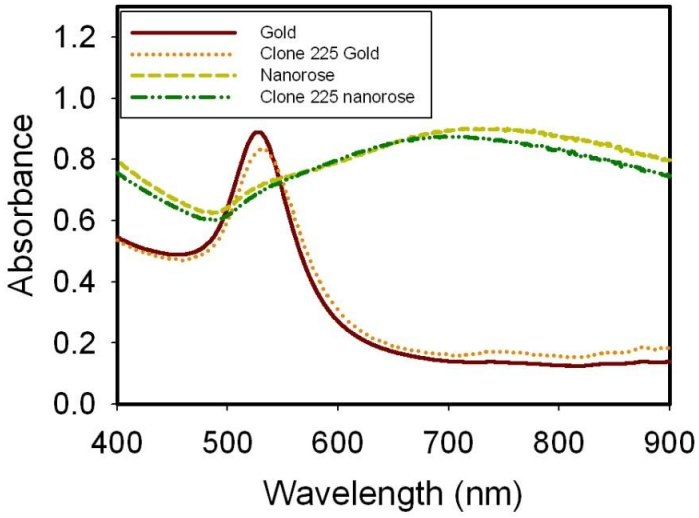

B

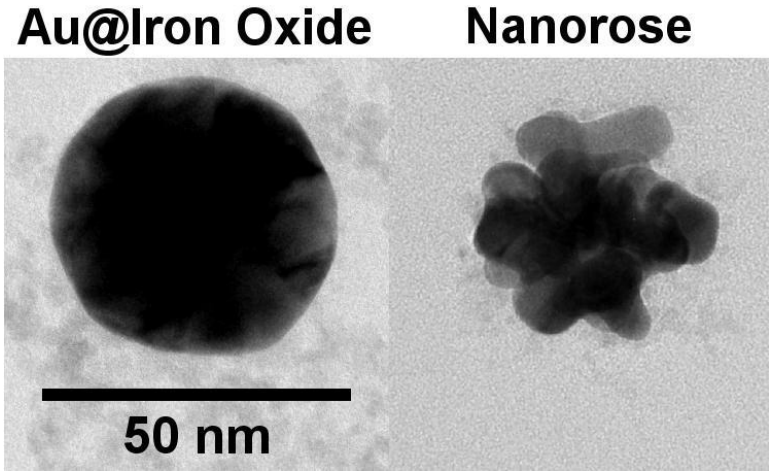

Figure 5.3 Extinction spectra (A) and TEM images (B) of thick gold shell coated iron oxide nanoparticle (Au@Iron Oxide) and nanorose. All spectra were normalized for 16 μg Au/ml dispersion as quantified by AAS with 1 cm optical path length. TEM images were acquired before conjugation.

Table 5.2. Measured Extinction Coefficient at 755 nm of Thick Gold Coated Iron Oxide Nanoparticles and Nanorose particles.

	Thick Au w/o Ab	Thick Au with Ab	Nanorose w/o Ab	Nanorose with Ab
Extinction coefficient ($cm^2/\mu g$ Au)	0.0085	0.0106	0.0563	0.0537

5.3.2 Selective cellular uptake with dosage response

Dark field microscopy images were used to compare the targeting selectivity of A431 cancer cells for the specific clone 225 conjugated nanoroses versus the non-specific anti-rabbit IgG (RG-16) conjugated nanoroses (Control). In each case, the experiments were performed with the sample containing 54 antibody molecules per nanorose, in which the coverage was on the order of a monolayer. Since empty cells scatter light much more weakly in the visible and NIR regions (400-900 nm) (Figure 5.4A) relative to metal nanoparticles, the reflected light from the nanoparticles was much brighter than for the cells under dark field. The A431 cells harvested from one petri dish were divided equally and cultured with different dosage of nanorose particles. The images were acquired under the same microscope and camera settings. As shown in Figures 4A-C the non-specific anti-rabbit IgG conjugated nanoroses accumulate very little in the A431 cells, even with the highest dosage (4.0×10^5 RG-16 nanoroses/cell). On the contrary, an orange signal intensity appeared in the A431 cells treated with the specific clone 225 conjugated nanoparticles, even with a dosage of 1.0×10^4 clone 225 nanoroses/cell (Figure 5.4D. Similar orange colors have been observed in macrophage cells incubated with non-specific dextran-coated nanorose without Abs.[7] The orange intensity increased

monotonically with dosage. At the highest level tested (4.0×10^5 clone 225 nanoroses/cell), the intense reflectance signal was at the limit of detector.

The nanorose particle cell uptake was quantified by AAS elemental analysis by averaging over 10^5 to 10^6 A431 cells treated with different particle dosages. Figure 5.5 shows the cell uptake increased from 10 to 609 particles per cell with increased dosage from 1.0×10^4 to 4.0×10^5 of anti-rabbit IgG conjugated nanoroses. The cell uptake for clone 225 conjugated nanoroses increased from 543 to 7175 particles per cell under the same dosage range. A factor of 54× higher cell uptake was achieved for clone 225 conjugated nanoroses versus control under lowest dosage and a factor of 12× higher versus control under highest dosage. The cell uptake reached a maximum value of ~7000 particles per cell at the dosage of 4.0×10^5 nanoroses/cell for clone 225 conjugated nanoroses.

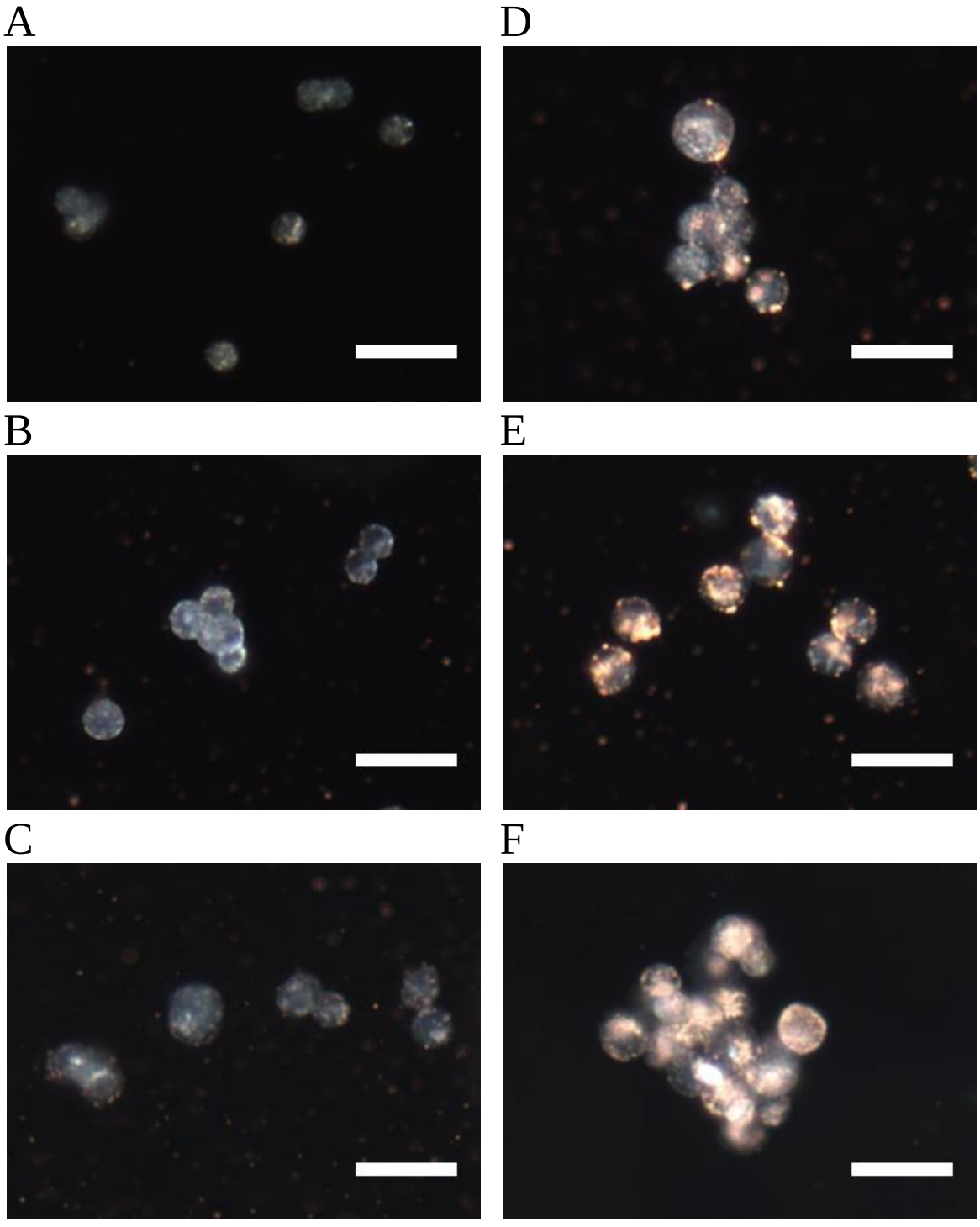
A
D
B
E
C
F

Figure 5.4 Dark field microscopy images of A431 cells treated with different dosages of clone 225 conjugated nanoroses (right column) relative to control experiments using anti-rabbit IgG (clone RG-16) conjugated nanoroses (left column) under the same experimental conditions. A, B and C represent typical images with dosages of 0, 5.0×10^4 and 4.0×10^5 RG-16 nanoroses/cell. D, E and F represent typical images with dosage of 1.0×10^4, 5.0×10^4, 4.0×10^5 nanoroses/cell. Scale bar is 25 μm.

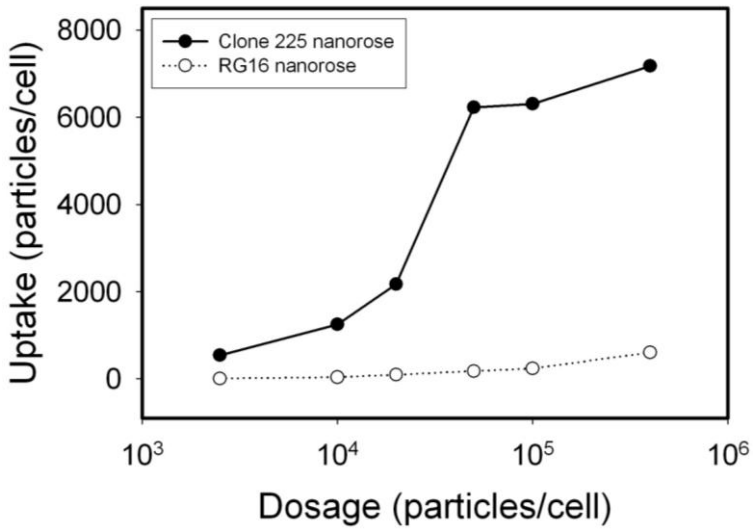

Figure 5.5 Cell uptake of clone 225 and RG-16 conjugated nanoroses. 10^5 to 10^6 A431 cells were incubated with 2.5×10^3, 1.0×10^4, 2.0×10^4, 5.0×10^4, 1.0×10^5, 4.0×10^5 nanoroses/cell for 1 hr.

5.3.3 Low cell uptake in EGFR(-) control cancer cells

To demonstrate the EGFR targeting specificity of clone 225 conjugated nanorose particles to EGFR (+) A431 cancer cells, negative control EGFR (-) MDA-MB-435 breast cancer cells were cultured and labeled under the same conditions. For both dextran coated nanoroses (2.0×10^4 nanoroses/cell) without Abs and clone 225 conjugated nanoroses (2.0×10^4 or 4.0×10^5 nanoroses/cell), dark field microscopy images show very little orange reflective intensity in these EGFR (-) MDA-MB-435 cells (Figure 5.6)

compared with the as EGFR (+) A431 cells (Figure 5.4 DEF). Thus, nonspecific endocytosis of the clone 225 conjugated nanorose particles to non-EGFR over-expressing cells was very limited. Therefore, the specific interactions of these nanoparticles with the receptors on the EGFR (+) A431 cancer cells were required for the large uptake.

A

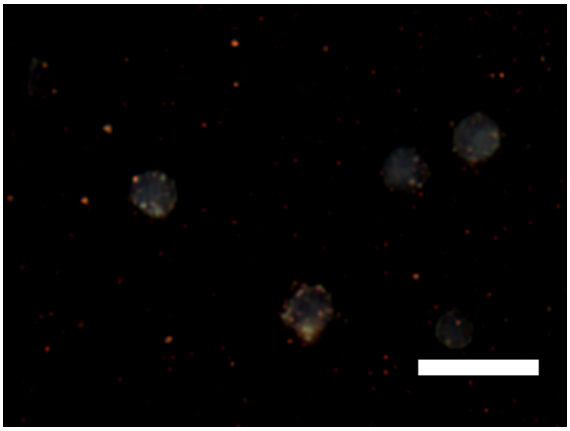

B

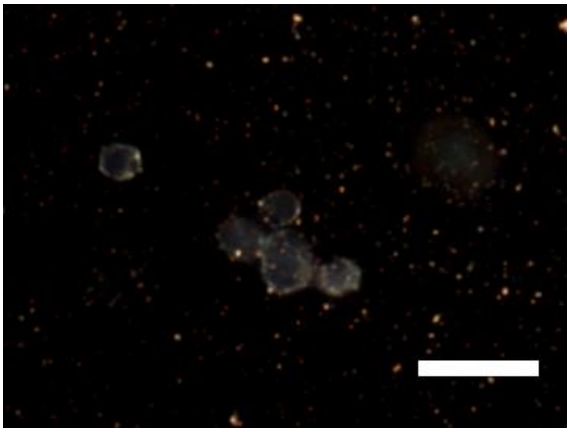

C

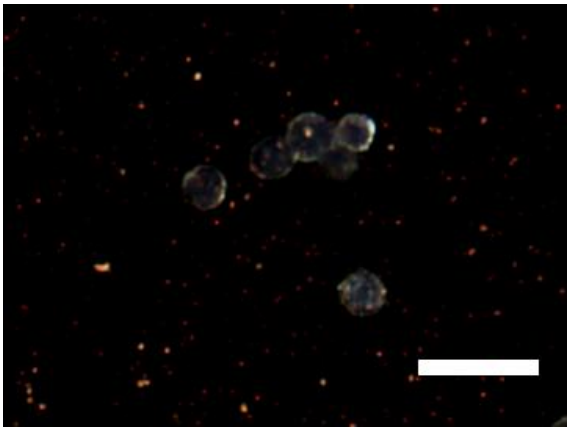

Figure 5.6 Dark field microscopy images of EGFR negative control MDA-MB-435 cells treated with clone 225 conjugated nanoroses for 1 hr. A, 2.0×10^4 unconjugated nanoroses/cell (control); B, 2.0×10^4 particles/cell; C, 4.0×10^5 particles/cell. Scale bar is 25 μm.

5.3.4 NIR and fluorescent dual mode imaging of clone 225 conjugated nanorose targeted to A431 cancer cells

Not only was the Alexa Fluor 488 label used to quantify the average number of conjugated antibodies per nanorose particle, but it was also be used for simultaneous fluorescence imaging (right column in Figure 5.7) with dark field reflectance imaging (left column). Image D0 shows very weak auto-reflectance signal without nanoparticles under dark field mode as has been shown in Figure 5.4A. Upon viewing under fluorescence mode simultaneously (F0, Figure 5.7) with an excitation light source at 490 nm, a signal was not present at the detection wavelength (520 nm), indicating lack of autofluorescence of the cells. With 5.0×10^4 nanoroses/cell, image D1 shows a strong reflectance signal in NIR region (as seen in Figure 5.4E). The fluorescence image F1 shows no signal indicating no fluorescence emission without Alexa Fluor 488 labels. Image D2 and F2 were acquired with Alexa Fluor 488 labeled clone 225 nanorose at the same dosage. D2 shows a similar imaging contrast and orange signal intensity as D1, suggesting the reflectance intensity under dark field mode is not affected by changing particle surface coating with fluorophore. A green fluorescent signal emitted from Alexa Fluor 488 was observed in image F2, localizing the cell profiles in the same location as shown in D2. Upon observing the images more carefully, a wide range of intensities is present in D2 showing high contrast for various degrees of aggregation of nanoparticles. Less contrast in intensity is evident in the fluorescence images. Dual mode Images were also obtained for nanoparticles with only 18 antibodies per nanorose at the same dosage (5.0×10^4 nanoroses/cell) in D3 and F3. Similar signal intensities were observed as in D2 and F2, indicating the targeting efficacy did not drop off significantly with a reduction in the number of Abs per particle. Again, higher contrast in intensity was in dark field imaging than by fluorescence (D3).

Dark field image (D)

D0

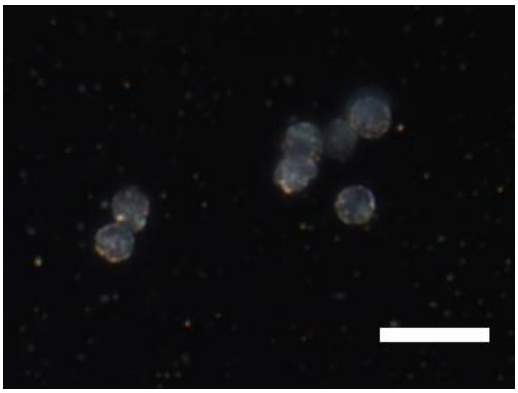

D1

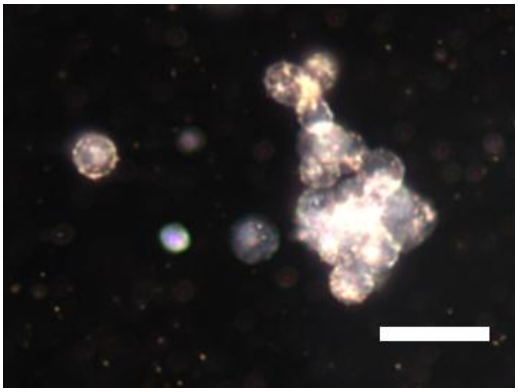

D2

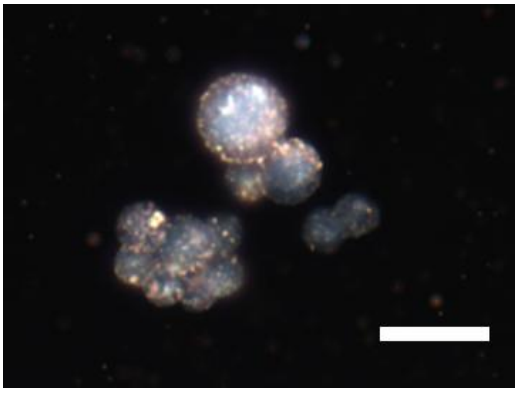

Fluorescence image (F)

F0

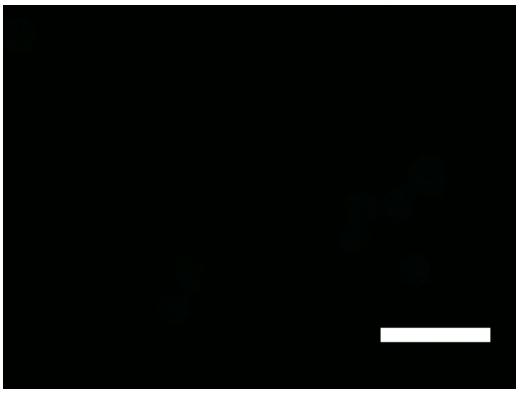

F1

F2

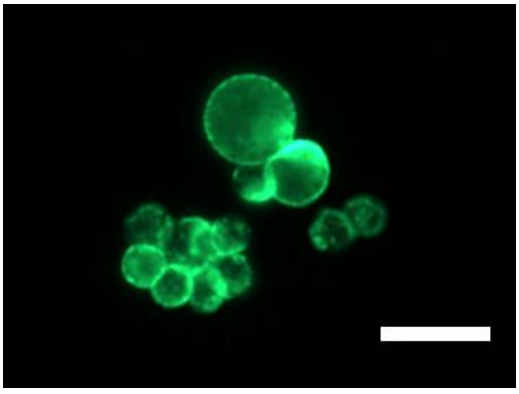

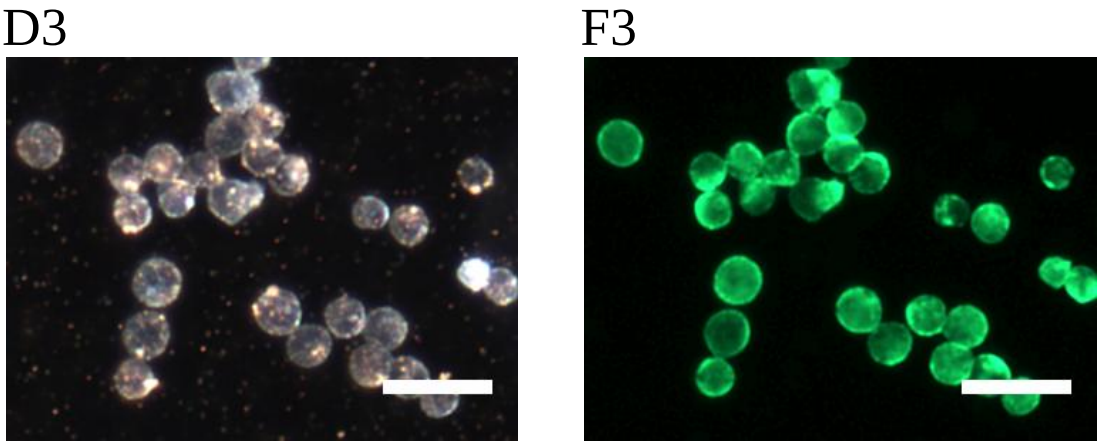

Figure 5.7 Dark field (D) and fluorescent (F) microscopic images of A431 cells incubated with clone 225 conjugated nanoroses for 1 hour. 0, cells without nanoparticles as control; 1, 54 antibodies per nanorose without fluorescent label; 2, Same as (1) with AlexaFluor 488 label; 3, same as (2) with 18 antibodies per nanorose. A particle dosage of 5.0×10^4 nanoroses/cell applied to 1-3 experiments. Scale bar is 25 μm.

5.4 DISCUSSION

5.4.1 Packing of optical and magnetic functionality, along with antibody linker and antibody in a small overall particle size

The design of a nanoparticle with a high degree of functionality and antibodies conjugated to the surface requires highly efficient use of space. This challenge can become severe as the particle diameter becomes smaller than 100 nm. The mass ratio of the various components in conjugated nanoparticles was estimated from AAS and the number of conjugated Ab, as shown in Table 5.S1 (Supporting Information). Typical mass ratios were 3.20 % for an Ab monolayer, 27.69 % for Fe cores and 69.21 % for the Au coating. For nanorose with thin Au coatings, the final Au/Fe mass ratio of 2.5 was much smaller than values of 10 for previously reported particles with spherical thick Au

shells (~20 nm shell thickness).[30] Au was still the predominant component in the particle by volume, illustrating the importance of designing very thin Au shells (< 5 nm) to reserve a large amount of space for additional functionality and Abs.

For nanorose particles, the unusually thin Au shells were synthesized by tuning the separation of the nucleation of the Au seeds on the iron oxide surface from the autocatalytic growth on the seeds.[47] To drive nucleation of Au seeds on unfavorable low energy iron oxide surfaces, high supersaturation values have often been generated by utilization of Au^{3+}/Fe mass ratios on the order of 10.[30-32] Consequently, as the seeds were nucleated, competitive autocatalytic growth of Au on Au often produced Au shells with thickness larger than 10 nm. Recently[47] and in the current study, extremely low Au^{3+} supersaturation values were applied to prevent excessive autocatalytic growth. The Au^{3+} addition profiles were varied during the reaction via a number of successive iterations to control the fraction of iron oxide substrate particles that were seeded.

In optical imaging and phototherapy applications, the Au shells on magnetic cores are often too thick to shift the surface plasmon resonance (SPR) peak to the preferred NIR region (Figure 5.3A).[16, 17, 30] For nanorose particles, the thin Au shells with high degrees of asymmetry shifted the SPR to the NIR, with an extinction coefficient at 755 nm five times higher than for 50 nm spherical thick Au shells on iron oxide (Figure 5.3 and Table 5.2), despite the overall small diameter of 35 nm. Related types of asymmetry have been demonstrated for Au nanorod,[4] nanocage,[48] nanorice,[49] nanoegg (asymmetric egg white shell),[50] and smooth Au shell with faceted or tetracubic core.[33] These asymmetries alter the interactions between plasmon modes and shift the SPR peak of gold nanospheres from 530 nm for symmetric systems to the NIR.[33, 49-51] In addition to nanorose, Au nanocages are also extremely small and exhibit strong NIR absorbance as a result of the morphology.[38]

Gold has a high Hamaker constant, and thus polymer steric stabilizers are often required to prevent van der Waals attraction between Au coated nanoparticles. For example, a 10 nm polymer (HS-PEG-COOH, MW 5kDa) shell was necessary to prevent colloid aggregation for 60 nm Au nanoparticles in buffered saline, prior to conjugation of targeting agents.[13] For indirect conjugation of Abs to functional groups on polymeric coatings on Au surfaces, a sufficient amount of polymer is needed to provide the required number of conjugation sites. For the low MW bifunctional linker on Abs in the present study, the length of linker is negligible, and the density of conjugation sites (Au atoms) is extremely high. For nanorose, only thin polymer coatings are needed for steric stabilization given weaker attraction for the thin Au shells, with a polymer loading of only 12 wt%, as shown recently.[7] The weak van der Waals forces for nanorose particles with thin Au shells and high porosity reduce the attraction forces between particles, and thus allow for very thin layers of steric stabilizers. Thus, a total thickness of only ~14 nm (Table 5.1) for a monolayer of Abs with low MW polymer stabilizers (mPEG-SH, MW 5kDa) was achieved on the 35 nm thin Au coated iron oxide nanoparticles. The unusually small volume of the thin Au shells in nanorose is highly beneficial for providing space for other types of functionality, in this case, magnetic functionality and an Ab monolayer.

Table 5.3. Occupied surface area per Ab on nanorose and Au sphere

	Nanorose	Au sphere
Diameter (nm)	35	18
Conjugated Abs/particle	54	9
Occupied surface area/Ab (nm^2)	71.2	113.0

5.4.2 Packing of antibodies on the highly curved nanorose surface

The number of antibodies for formation of a monolayer was calculated from two simple geometric models to evaluate the measured surface coverage. The Fc region binds to the Au surface, while the Fab chains extend outward and occupy more surface area, as shown in Figure 5.8. Thus we choose to define an effective radius R from the center of the nanoparticle to the Fab region. In our case, a nanoparticle diameter of 35 nm and an antibody length of 11.7 nm give R = 29.2 nm.[52] In the first model, the area of the Fab region was assumed to be circular with a diameter of 16.9 nm (Figure 5.8). For an individual antibody, half of the end-to-end length 16.9 nm for the two Fab chains gives a radius of r=8.45 nm.[52] Therefore, one Ab will occupy a circular area of 224 nm^2 on the surface of the particle at R. For a 2D monolayer of circles on a flat surface, where is the hexagonal close packed density (0.9069), the number of Abs

$$N_{Abs} = \frac{\text{Surface Area of Effective Sphere}}{\text{Area Occupied by Individual Antibody}} = \frac{4\pi R^2}{\pi r^2/\varepsilon}$$

Thus, a total of 43 antibodies per particle is calculated for a monolayer of close packed antibodies, assuming the native structure is maintained in the non-aggregated state.

In the second geometric model, the area of the Fab region is assumed to be a rectangle with length L=16.9 nm and width W= 4 nm[52]. In this case, the surface area per antibody (W Ł) is 67.6 nm^2, such that $N_{Abs} = 4\pi R^2/(W Ł) = 144$. As is expected, the number of Abs is larger for rectangles that pack more efficiently on the surface. On the basis of the circular cross-section geometric model, the particle (Table 5.1) was covered by approximately one monolayer with 54 Abs. The effective experimental area was 71.2

nm^2/Ab. The hydrodynamic diameter of 63 nm was close to the value of 58.4 nm predicted from R for a monolayer. The change of total hydrodynamic diameter with N_{Abs} may be attributed to a hybridization between the longer Ab chain length of 11.7 nm[52] and the shorter mPEG-SH (M_W 5,000) end-to-end chain length of 3.3 nm[53] (Scheme 5.1). Thus for N_{Abs} values of 8 and 18, the hydrodynamic diameter fell between 35 nm and 63 nm for a monolayer. For the case with 74 Abs, N_{Abs} is above the monolayer value. The additional Abs beyond a monolayer is more likely to cause denaturation and aggregation from intermolecular interactions.[54, 55] The aggregation may even trigger an immune response and decrease the targeting efficacy.[52]

In a recent study using clone 225, the same conjugation protocol and characterization methods were used for 18 nm spherical Au substrate particles. [19, 20] In this case, 9 Abs were conjugated to each Au sphere. This corresponding area/Ab was 113.0 nm^2, somewhat larger than the value of 71.2 nm^2 for nanorose. Compared with the Au spheres with a radius of 9 nm, the radius of the protuberances (~ 5 nm, Figure 5.3B) on the surface of nanorose led to a higher actual surface area, than the surface area of a sphere with an equivalent radius of 17.5 nm. The surface roughness raised the Ab packing capacity by ~ 1.6 times. Furthermore, the varying orientations of the Abs as a result of surface roughness may further allow for higher Ab densities.

High surface coverage of Abs is also favored by the high density of conjugation sites supplied by Au atoms on the nanorose surface and the low cross sectional area of the linker. In our case, the area of the short bifunctional linker with a MW 708.97 is very small. Only the steric repulsion from Abs appeared to limit the binding capacity as shown in our monolayer calculation. In contrast, an intermediate MW linker (HS-PEG-COOH, MW 5kDa) has been used for conjugation on Au nanospheres.[13] In this study N_{Abs} was not reported. For the indirect conjugation method, intermediate or high MW

polymers are first used to stabilize the nanoparticle. Here the fraction of conjugation sites on the polymer coating can be well below unity, unlike the case for pure Au atoms in the direct method. The resulting decrease in the number of binding sites, as well as increase of the steric repulsion between the coating polymer chains, may lower the N_{Abs}/particle. Therefore, the high density of atomic Au binding sites on nanorose for low MW linkers were beneficial for achieving a full monolayer coverage in the present study.

Another direct conjugation method is to adsorb the antibody to Au, but without the formation of covalent bonds, as has been demonstrated with Herceptin (MW 145 kDa). For 40 nm Au spheres, up to 200 protein molecules can be absorbed , which would correspond to 33 nm^2 per protein.[28] This high Ab density suggests multilayer absorption. Without covalent bonding of the Ab, it may be more difficult to control the Ab orientation than for conjugation with thiol-based bifunctional linkers.

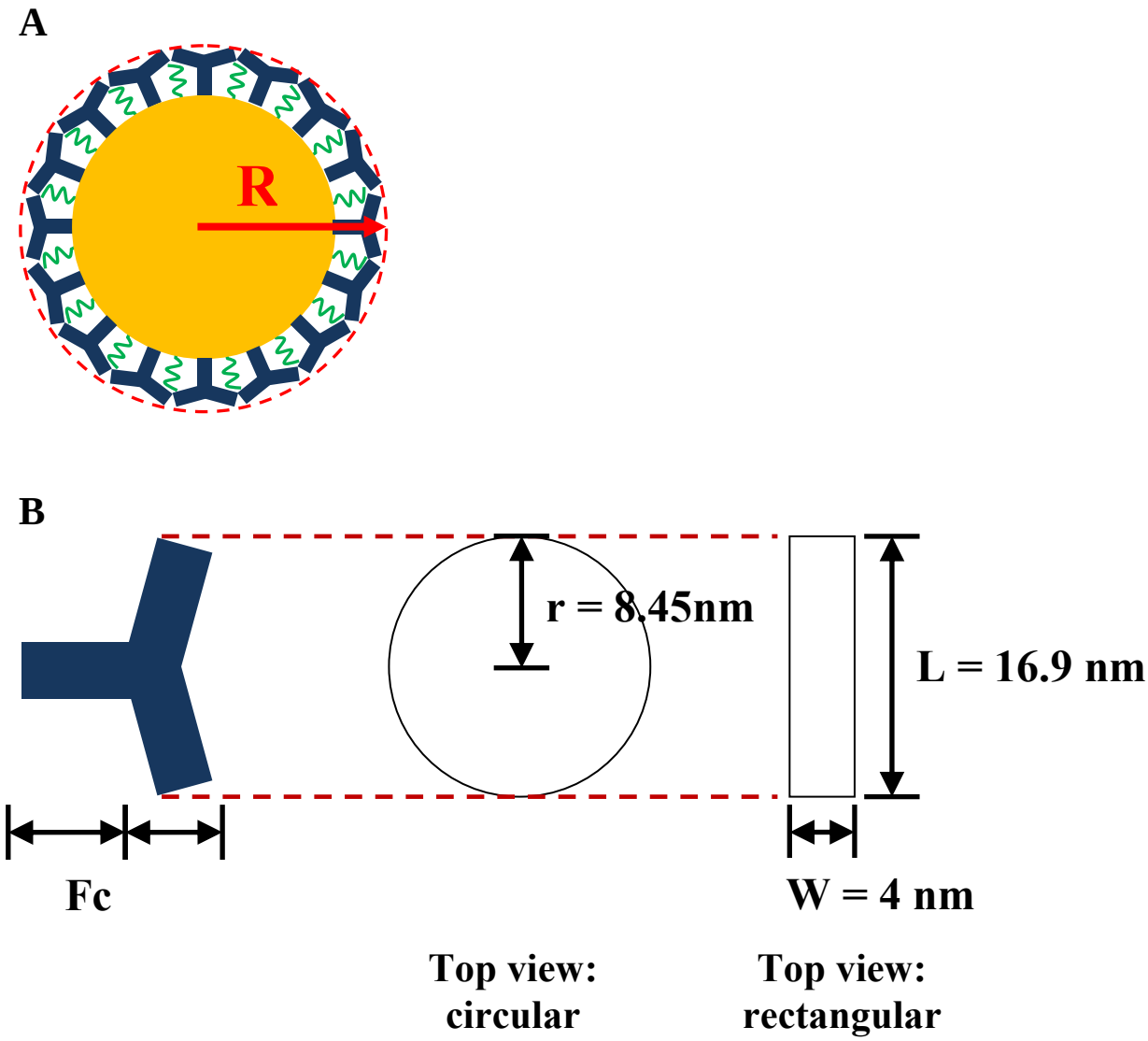

Figure 5.8 **A,** The surface area of the particle is determined based on the nanoparticle and antibody assembly, having R = 29.2 nm. **B,** The area occupied per antibody is calculated using a circular, unaggregated model as well as a rectangular, close packed aggregated model. The radius of the circular model, r, is the length of a Fab chain, 8.45 nm. The length of the rectangular model, L, is the length of two Fab chains, 16.9 nm. The width of the rectangular model, W, is the width of a Fab chain, 4 nm.

5.4.3 Effects of particle size, curvature and shape on selective targeting

Studies have shown EGFR is over-expressed in human cancer cells and play a role in promoting tumor cell proliferation, invasion and metastasis.[56] Therefore, EGFR has been identified as molecular target for cancers.[26, 57] Clone 225 (Cetuximab, Erbitux)[25, 58] is a human-mouse chimeric anti-EGFR antibody that binds to the extracellular domain of EGFR with high affinity, and prevents activation of the receptor-mediated cellular survival signal. Therefore, clone 225 conjugated nanoparticles may be used to monitor the targeted delivery of the inhibitors and supply real time therapeutic effects during the treatment of tumor.

For nanorose conjugated with a monolayer of clone 225, a sigmoidal curve of cell uptake versus dosage was observed in Figure 5.5. A high value of ~7,000 nanorose particles per cell was achieved at a dosage of 4.0×10^5 nanoroses/cell, producing a saturated signal for NIR reflectance. For a cell approximated as a 10 μm diameter sphere, this cell uptake corresponds to a 0.030 % packing fraction by volume. For clone 225 coated 50 nm Au nanospheres conjugated by the same protocol, a maximum uptake of 1,160 particle per cell (A431) was obtained at a much higher dosage level of 1.0×10^6 nanospheres/cell.[42] The resulting 0.015 % packing fraction was only half of the value for the nanorose. The higher cancer cell uptake by Ab conjugated nanorose at a lower dosage may be influenced by the smaller overall hydrodynamic diameter, the higher Ab density on the surface, and by the orientation of the Abs with respect to each other, which is influenced by high local surface curvature.

When hydrodynamic diameters of Ab coated Au nanospheres are reduced to less than 70 nm, the biological pathways in targeted cells can undergo profound changes.[28, 59-62] The nanoparticles serve not merely as substrates for the Abs but strongly influence the effect of the Abs on the biological signaling processes. The fact that the curvature of

the Au nanospheres influence binding capacities by nearly 3 orders of magnitude[28] suggests that interactions between multiple Abs on the surface and cell receptors play a key role. However, studies of the effect of curvature are relatively new, and it is not yet known how these effects will vary for different particle shapes, Abs, polymer stabilizers and cell types. For example, shape effects were much smaller for targeting of breast cancer cells (SK-BR-3) in a recent study of nanocages and nanospheres with anti-HER2 on the surface.[38] Anti-HER2 indirect conjugation to 33 nm nanocages through relatively low MW succinimidyl propionyl PEG disulfide (MW 5kDa) gave an uptake of 500 per cell. In this study, N_{Abs} was not reported. However, the small size of the particles and the shape of the nanocage are beneficial for controlling the degree of conjugation and Ab orientation for high uptake. A related example is the highly effective cell targeting of the tyrosine kinase receptors on Jurkat T cells for DNA aptamer conjugated to viral capsid nanoclusters.[63]

The knobby shape of the Au shells on the nanorose particles offers a rich domain of local surface curvatures that would be difficult to achieve for simpler shapes. The curvature of the protuberances (~ 5 nm, Figure 5.3B) on the surface of nanorose particle is similar to that of the protein spheres that make up viral capsids[63]. The multiple number of gold domains of varying curvature for nanoclusters with convex surfaces (Fig. 3) will offer widespread opportunity for varying spacings and orientations of Abs with respect to the receptors on cell surfaces, and thus, ultimately, the therapeutic efficiency. In the current study, only a single nanocluster morphology is considered. However, a homologous series in the sizes and shapes of the Au shells has been accomplished by the mechanism of thin autocatalytic growth on nanoparticles substrates.[47] The thickness of the shells and the local surface curvatures may be adjusted independently.

Not only do the nanorose offer control over surface curvature, but also strong NIR absorbance, despite their small size. In a previous approach, NIR absorbance of Au nanoparticles is achieved upon EGFR-mediated aggregation inside cells.[16, 42, 64] The individual nanoparticles do not absorb in the NIR. Thus, the change in absorbance may be used to identify cancer markers. For the colloidally stable nanorose, the individual particles absorb strongly in the NIR, and provide vivid orange color under dark field microscopy (Figure 5.4). This could be an advantage in cases where cellular uptake of Au nanoparticles doesn't bring the particles closely enough together for NIR absorbance.

5.5 CONCLUSIONS

Multifunctional nanoparticles composed of thin Au coatings on magnetic iron oxide cores, were conjugated with a monolayer of anti-EGFR monoclonal antibodies (clone 225). The number of Abs, as determined from the fluorophore tag, was tuned from 1 to 74 by varying the feed Ab/particle ratio. The respective hydrodynamic diameters, from 35 to 78 nm, were extremely small given the high degree of functionality. The highly asymmetric thin Au shells, synthesized by seeded growth on iron oxide nanoclusters at ultralow supersaturations of Au precursor, produce the strong NIR absorbance. The final Au/Fe mass ratio of 2.5 is smaller than previously reported values on the order of 10.[30] The unusually small volume of the Au is highly beneficial for providing space for other types of functionality, such as targeting and therapeutic Abs, and if desired, magnetic functionality. High surface coverage of Abs is favored by the high density of conjugation sites supplied by Au atoms on the surface and the low cross sectional area of the heterobifunctional dithiol-PEG-hydrazide (MW 708.97) linker. In contrast with this direct conjugation method, in the indirect method the MW of

polymeric linkers is often higher and with a lower density of binding sites, resulting in lower Ab coverage. For 54 Abs, the hydrodynamic diameter indicated coverage of a monolayer for Abs, in agreement with the prediction of a geometric model, by assuming a circular area for the Fab region. Steric stabilization was provided with a combination of Ab as well as mPEG-SH in physiological media, to overcome the VDW attraction.

For the 63 nm particles with 54 Abs in a monolayer, targeting of EGFR overexpressive cancer cells was highly selective, relative to EGFR negative cancer cells. In dark field microscopy, high uptake of the conjugated nanoparticles produced an intense orange signal, resulting from strong NIR scattering. The cellular uptake of nanoparticles/cell of ~7,000, as characterized by AAS, was ~6 fold higher than previously reported for 50 nm Au spheres with the same Ab and cell type.[42] Intense NIR scattering was achieved from both high uptake of nanoparticles in cells and high NIR absorbance/mass Au, as observed in a previous study of the non-conjugated nanoparticles in macrophage cells by hyperspectral microscopy.[7] Colocalization of the NIR scattering and fluorescence indicates the Abs remained attached to the Au surfaces inside the cancer cells. The extremely high curvature of the Au shells with features below 5 nm influence the spacing and orientations of the Abs on the surface, resulting in the high cell uptake. Ultimately, tuning of surface curvature has the potential to have a marked effect on biological pathways within cells.[28, 39-41] The ability to load intense multifunctionality, specifically strong NIR absorbance, conjugation of an Ab monolayer and strong r2 MRI contrast (from previous study[7]) in a total particle size only 63 nm, is an important step forward in achieving both molecular specific imaging and real time feedback on therapeutic efficacy for treatment of cancer.

5.6 SUPPORTING INFORMATION

Table 5.S1. Component of Abs conjugated nanorose particles

Conjugated Ab molecules/ nanorose	Au w/w %	Fe w/w %	Ab w/w %
1	71.38268	28.55307	0.064286
8	71.10934	28.44374	0.448929
18	70.67063	28.26825	1.0725
54	69.21196	27.68478	3.202643
74	68.4465	27.3786	4.356786

5.7 REFERENCES

1. Sokolov, K.; Follen, M.; Aaron, J.; Pavlova, I.; Malpica, A.; Lotan, R.; Richards-Kortum, R., Real-time vital optical imaging of precancer using anti-epidermal growth factor receptor antibodies conjugated to gold nanoparticles. *Cancer Research* **2003,** 63, (9), 1999-2004.

2. Gopalan, B.; Ito, I.; Branch, C. D.; Stephens, C.; Roth, J. A.; Ramesh, R., Nanoparticle based systemic gene therapy for lung cancer: Molecular mechanisms and strategies to suppress nanoparticle-mediated inflammatory response. *Technology in Cancer Research & Treatment* **2004,** 3, (6), 647-657.

3. Loo, C.; Lowery, A.; Halas, N. J.; West, J.; Drezek, R., Immunotargeted nanoshells for integrated cancer imaging and therapy. *Nano Letters* **2005,** 5, (4), 709-711.

4. Huang, X.; El-Sayed, I. H.; Qian, W.; El-Sayed, M. A., Cancer Cell Imaging and Photothermal Therapy in the Near-Infrared Region by Using Gold Nanorods. *Journal of the American Chemical Society* **2006,** 128, (6), 2115-2120.

5. Dames, P.; Gleich, B.; Flemmer, A.; Hajek, K.; Seidl, N.; Wiekhorst, F.; Eberbeck, D.; Bittmann, I.; Bergemann, C.; Weyh, T.; Trahms, L.; Rosenecker, J.;

Rudolph, C., Targeted delivery of magnetic aerosol droplets to the lung. *Nature Nanotechnology* **2007,** 2, (8), 495-499.

6. Bagalkot, V.; Zhang, L.; Levy-Nissenbaum, E.; Jon, S.; Kantoff, P. W.; Langer, R.; Farokhzad, O. C., Quantum dot - Aptamer conjugates for synchronous cancer imaging, therapy, and sensing of drug delivery based on Bi-fluorescence resonance energy transfer. *Nano Letters* **2007,** 7, (10), 3065-3070.

7. Ma, L. L.; Feldman, M. D.; Tam, J. M.; Paranjape, A. S.; Cheruku, K. K.; Larson, T. A.; Tam, J. O.; Ingram, D. R.; Paramita, V.; Villard, J. W.; Jenkins, J. T.; Wang, T.; Clarke, G. D.; Asmis, R.; Sokolov, K.; Chandrasekar, B.; Milner, T. E.; Johnston, K. P., Small Multifunctional Nanoclusters (Nanoroses) for Targeted Cellular Imaging and Therapy. *ACS Nano* **2009,** 3, (9), 2686-2696.

8. Hirsch, L. R.; Stafford, R. J.; Bankson, J. A.; Sershen, S. R.; Rivera, B.; Price, R. E.; Hazle, J. D.; Halas, N. J.; West, J. L., Nanoshell-mediated near-infrared thermal therapy of tumors under magnetic resonance guidance. *Proceedings of the National Academy of Sciences of the United States of America* **2003,** 100, (23), 13549-13554.

9. Shah, J.; Park, S.; Aglyamov, S.; Larson, T.; Ma, L.; Sokolov, K.; Johnston, K.; Milner, T.; Emelianov Stanislav, Y., Photoacoustic imaging and temperature measurement for photothermal cancer therapy. *Journal of biomedical optics* **2008,** 13, (3), 034024.

10. Ferrari, M., Cancer nanotechnology: Opportunities and challenges. *Nature Reviews Cancer* **2005,** 5, (3), 161-171.

11. Maeda, H.; Fang, J.; Inutsuka, T.; Kitamoto, Y., Vascular permeability enhancement in solid tumor: various factors, mechanisms involved and its implications. *International Immunopharmacology* **2003,** 3, (3), 319-328.

12. Matsumura, Y.; Maeda, H., A New Concept for Macromolecular Therapeutics in Cancer-Chemotherapy - Mechanism of Tumoritropic Accumulation of Proteins and the Antitumor Agent Smancs. *Cancer Research* **1986,** 46, (12), 6387-6392.

13. Qian, X. M.; Peng, X. H.; Ansari, D. O.; Yin-Goen, Q.; Chen, G. Z.; Shin, D. M.; Yang, L.; Young, A. N.; Wang, M. D.; Nie, S. M., In vivo tumor targeting and spectroscopic detection with surface-enhanced Raman nanoparticle tags. *Nature Biotechnology* **2008,** 26, (1), 83-90.

14. Wang, S. P.; Mamedova, N.; Kotov, N. A.; Chen, W.; Studer, J., Antigen/antibody immunocomplex from CdTe nanoparticle bioconjugates. *Nano Letters* **2002,** 2, (8), 817-822.

15. Huang, X.; Peng, X.; Wang, Y.; Shin, D. M.; El-Sayed, M. A.; Nie, S., A Reexamination of Active and Passive Tumor Targeting by Using Rod-Shaped Gold Nanocrystals and Covalently Conjugated Peptide Ligands. *ACS Nano* **2010**.

16. Larson, T. A.; Bankson, J.; Aaron, J.; Sokolov, K., Hybrid plasmonic magnetic nanoparticles as molecular specific agents for MRI/optical imaging and photothermal therapy of cancer cells. *Nanotechnology* **2007,** 18, (32), 325101/1-325101/8.

17. Aaron, J. S.; Oh, J.; Larson, T. A.; Kumar, S.; Milner, T. E.; Sokolov, K. V., Increased optical contrast in imaging of epidermal growth factor receptor using magnetically actuated hybrid gold/iron oxide nanoparticles. *Optics Express* **2006,** 14, (26), 12930-12943.

18. Aaron, J.; Nitin, N.; Travis, K.; Kumar, S.; Collier, T.; Park, S. Y.; Jose-Yacaman, M.; Coghlan, L.; Follen, M.; Richards-Kortum, R.; Sokolov, K., Plasmon resonance coupling of metal nanoparticles for molecular imaging of carcinogenesis in vivo. *Journal of Biomedical Optics* **2007,** 12, (3), 034007/1-034007/11.

19. Kumar, S.; Harrison, N.; Richards-Kortum, R.; Sokolov, K., Plasmonic Nanosensors for Imaging Intracellular Biomarkers in Live Cells. *Nano Letters* **2007,** 7, (5), 1338-1343.

20. Kumar, S.; Aaron, J.; Sokolov, K., Directional conjugation of antibodies to nanoparticles for synthesis of multiplexed optical contrast agents with both delivery and targeting moieties. *Nature Protocols* **2008,** 3, (2), 314-320.

21. Aaron, J.; Travis, K.; Harrison, N.; Sokolov, K., Dynamic Imaging of Molecular Assemblies in Live Cells Based on Nanoparticle Plasmon Resonance Coupling. *Nano Letters* **2009,** 9, (10), 3612-3618.

22. Brillhart, K. L.; Ngo, T. T., Use of Microwell Plates Carrying Hydrazide Groups to Enhance Antibody Immobilization in Enzyme Immunoassays. *Journal of Immunological Methods* **1991,** 144, (1), 19-25.

23. Oshannessy, D. J.; Dobersen, M. J.; Quarles, R. H., A Novel Procedure for Labeling Immunoglobulins by Conjugation to Oligosaccharide Moieties. *Immunology Letters* **1984,** 8, (5), 273-277.

24. Ghose, T. I.; Blair, A. H.; Kulkarni, P. N., Preparation of Antibody-Linked Cyto-Toxic Agents. *Methods in Enzymology* **1983,** 93, 280-333.

25. Goldstein, N. I.; Prewett, M.; Zuklys, K.; Rockwell, P.; Mendelsohn, J., Biological efficacy of a chimeric antibody to the epidermal growth factor receptor in a human tumor xenograft model. *Clinical Cancer Research* **1995,** 1, (11), 1311-1318.

26. Ke, S.; Wen, X. X.; Gurfinkel, M.; Charnsangavej, C.; Wallace, S.; Sevick-Muraca, E. M.; Li, C., Near-infrared optical imaging of epidermal growth factor receptor in breast cancer xenografts. *Cancer Research* **2003,** 63, (22), 7870-7875.

27. Farokhzad, O. C.; Langer, R., Nanomedicine: Developing smarter therapeutic and diagnostic modalities. *Advanced Drug Delivery Reviews* **2006,** 58, (14), 1456-1459.

28. Jiang, W.; Kim, B. Y. S.; Rutka, J. T.; Chan, W. C. W., Nanoparticle-mediated cellular response is size-dependent. *Nature Nanotechnology* **2008,** 3, (3), 145-150.

29. Nie, S. M., Understanding and overcoming major barriers in cancer nanomedicine. *Nanomedicine* **2010,** 5, (4), 523-528.

30. Lyon, J. L.; Fleming, D. A.; Stone, M. B.; Schiffer, P.; Williams, M. E., Synthesis of Fe Oxide Core/Au Shell Nanoparticles by Iterative Hydroxylamine Seeding. *Nano Letters* **2004,** 4, (4), 719-723.

31. Park, H.-Y.; Schadt, M. J.; Wang, L.; Lim, I. I. S.; Njoki, P. N.; Kim, S. H.; Jang, M.-Y.; Luo, J.; Zhong, C.-J., Fabrication of Magnetic Core@Shell Fe Oxide@Au Nanoparticles for Interfacial Bioactivity and Bio-separation. *Langmuir* **2007,** 23, (17), 9050-9056.

32. Xu, Z.; Hou, Y.; Sun, S., Magnetic Core/Shell Fe3O4/Au and Fe3O4/Au/Ag Nanoparticles with Tunable Plasmonic Properties. *Journal of the American Chemical Society* **2007,** 129, (28), 8698-8699.

33. Levin, C. S.; Hofmann, C.; Ali, T. A.; Kelly, A. T.; Morosan, E.; Nordlander, P.; Whitmire, K. H.; Halas, N. J., Magnetic-Plasmonic Core-Shell Nanoparticles. *ACS Nano* **2009,** 3, (6), 1379-1388.

34. Rasch, M. R.; Sokolov, K. V.; Korgel, B. A., Limitations on the Optical Tunability of Small Diameter Gold Nanoshells. *Langmuir* **2009,** 25, (19), 11777-11785.

35. Goon, I. Y.; Lai, L. M. H.; Lim, M.; Munroe, P.; Gooding, J. J.; Amal, R., Fabrication and Dispersion of Gold-Shell-Protected Magnetite Nanoparticles: Systematic Control Using Polyethyleneimine. *Chemistry of Materials* **2009,** 21, (4), 673-681.

36. Lim, J.; Tilton, R. D.; Eggeman, A.; Majetich, S. A., Design and synthesis of plasmonic magnetic nanoparticles. *Journal of Magnetism and Magnetic Materials* **2007,** 311, (1), 78-83.

37. Lim, J. K.; Majetich, S. A.; Tilton, R. D., Stabilization of Superparamagnetic Iron Oxide Core-Gold Shell Nanoparticles in High Ionic Strength Media. *Langmuir* **2009,** 25, (23), 13384-13393.

38. Cho, E. C.; Au, L.; Zhang, Q.; Xia, Y., The Effects of Size, Shape, and Surface Functional Group of Gold Nanostructures on Their Adsorption and Internalization by Cells. *Small* **2010,** 6, (4), 517-522.

39. Decuzzi, P.; Pasqualini, R.; Arap, W.; Ferrari, M., Intravascular Delivery of Particulate Systems: Does Geometry Really Matter? *Pharmaceutical Research* **2009,** 26, (1), 235-243.

40. Gratton, S. E. A.; Ropp, P. A.; Pohlhaus, P. D.; Luft, J. C.; Madden, V. J.; Napier, M. E.; DeSimone, J. M., The effect of particle design on cellular internalization pathways. *Proceedings of the National Academy of Sciences of the United States of America* **2008,** 105, (33), 11613-11618.

41. Champion, J. A.; Katare, Y. K.; Mitragotri, S., Making polymeric micro- and nanoparticles of complex shapes. *Proceedings of the National Academy of Sciences of the United States of America* **2007,** 104, (29), 11901-11904.

42. Mallidi, S.; Larson, T.; Tam, J.; Joshi, P. P.; Karpiouk, A.; Sokolov, K.; Emelianov, S., Multiwavelength Photoacoustic Imaging and Plasmon Resonance Coupling of Gold Nanoparticles for Selective Detection of Cancer. *Nano Letters* **2009,** 9, (8), 2825-2831.

43. Kumar, S.; Aaron, J.; Sokolov, K. V., Directional conjugation of antibodies to nanoparticles for synthesis of multiplexed optical contrast agents with both delivery and targeting moieties. *Nature Protocols* **2008,** 3, (2), 314-320.

44. Ryoo, W.; Webber, S. E.; Johnston, K. P., Water-in-Carbon Dioxide Microemulsions with Methylated Branched Hydrocarbon Surfactants. *Industrial & Engineering Chemistry Research* **2003,** 42, (25), 6348-6358.

45. Urbanska, K.; Romanowska-Dixon, B.; Matuszak, Z.; Oszajca, J.; Nowak-Sliwinska, P.; Stochel, G., Indocyanine green as a prospective sensitizer for photodynamic therapy of melanomas. *Acta Biochimica Polonica* **2002,** 49, (2), 387-391.

46. Josephson, L.; Kircher, M. F.; Mahmood, U.; Tang, Y.; Weissleder, R., Near-Infrared Fluorescent Nanoparticles as Combined MR/Optical Imaging Probes. *Bioconjugate Chemistry* **2002,** 13, (3), 554-560.

47. Ma, L. L.; Borwankar, A.; Willsey, B.; Yoon, K. Y.; Tam, J. O.; Sokolov, K.; Feldman, M. D.; Milner, T. E.; Johnston, K. P., Growth of Textured Thin Au Shells on Iron Oxide Nanoparticles. *Prepare for Submitting* **2011**.

48. Xia, Y.; Xiong, Y. J.; Lim, B.; Skrabalak, S. E., Shape-Controlled Synthesis of Metal Nanocrystals: Simple Chemistry Meets Complex Physics? *Angewandte Chemie-International Edition* **2009,** 48, (1), 60-103.

49. Wang, H.; Brandl, D. W.; Le, F.; Nordlander, P.; Halas, N. J., Nanorice: A Hybrid Plasmonic Nanostructure. *Nano Letters* **2006,** 6, (4), 827-832.

50. Knight, M. W.; Halas, N. J., Nanoshells to nanoeggs to nanocups: optical properties of reduced symmetry core-shell nanoparticles beyond the quasistatic limit. *New Journal of Physics* **2008,** 10, (Oct.).

51. Hu, Y.; Noelck, S. J.; Drezek, R. A., Symmetry Breaking in Gold-Silica-Gold Multilayer Nanoshells. *Acs Nano* **2010,** 4, (3), 1521-1528.

52. Pease, L. F.; Elliott, J. T.; Tsai, D. H.; Zachariah, M. R.; Tarlov, M. J., Determination of Protein Aggregation With Differential Mobility Analysis: Application to IgG Antibody. *Biotechnology and Bioengineering* **2008,** 101, (6), 1214-1222.

53. Fetters, L. J.; Lohse, D. J.; Richter, D.; Witten, T. A.; Zirkel, A., Connection between Polymer Molecular-Weight, Density, Chain Dimensions, and Melt Viscoelastic Properties. *Macromolecules* **1994,** 27, (17), 4639-4647.

54. Wang, W., Protein aggregation and its inhibition in biopharmaceutics. *International Journal of Pharmaceutics* **2005,** 289, (1-2), 1-30.

55. Gupta, P.; Hall, C. K.; Voegler, A. C., Effect of denaturant and protein concentrations upon protein refolding and aggregation: A simple lattice model. *Protein Science* **1998,** 7, (12), 2642-2652.

56. Onn, A.; Correa, A. M.; Gilcrease, M.; Isobe, T.; Massarelli, E.; Bucana, C. D.; O'Reilly, M. S.; Hong, W. K.; Fidler, I. J.; Putnam, J. B.; Herbst, R. S., Synchronous overexpression of epidermal growth factor receptor and HER2-neu protein is a predictor of poor outcome in patients with stage I non-small cell lung cancer. *Clinical Cancer Research* **2004,** 10, (1), 136-143.

57. Baselga, J.; Arteaga, C. L., Critical update and emerging trends in epidermal growth factor receptor targeting in cancer. *Journal of Clinical Oncology* **2005,** 23, (11), 2445-2459.

58. Robinson, D. R.; Wu, Y. M.; Lin, S. F., The protein tyrosine kinase family of the human genome. *Oncogene* **2000,** 19, (49), 5548-5557.

59. Ferrari, M., Beyond drug delivery. *Nature Nanotechnology* **2008,** 3, (3), 131-132.

60. Reddy, S. T.; Swartz, M. A.; Hubbell, J. A., Targeting dendritic cells with biomaterials: developing the next generation of vaccines. *Trends in Immunology* **2006,** 27, (12), 573-579.

61. Wang, A. Z.; Bagalkot, V.; Vasilliou, C. C.; Gu, F.; Alexis, F.; Zhang, L.; Shaikh, M.; Yuet, K.; Cima, M. J.; Langer, R.; Kantoff, P. W.; Bander, N. H.; Jon, S.; Farokhzad, O. C., Superparamagnetic iron oxide nanoparticle-aptamer bioconjugates for combined prostate cancer imaging and therapy. *ChemMedChem* **2008,** 3, (9), 1311-1315.

62. Weissleder, R., Molecular Imaging in Cancer. *Science* **2006,** 312, (5777), 1168-1171.

63. Tong, G. J.; Hsiao, S. C.; Carrico, Z. M.; Francis, M. B., Viral Capsid DNA Aptamer Conjugates as Multivalent Cell-Targeting Vehicles. *Journal of the American Chemical Society* **2009,** 131, (31), 11174-11178.

64. Tam, J. M.; Tam, J. O.; Murthy, A.; Ingram, D. R.; Ma, L. L.; Travis, K.; Johnston, K. P.; Sokolov, K. V., Controlled Assembly of Biodegradable Plasmonic Nanoclusters for Near-Infrared Imaging and Therapeutic Applications. *ACS Nano* **2010,** 4, (4), 2178-2184.

Chapter 6: Conclusions

6.1 Small Multifunctional Nanoclusters (Nanoroses) for Targeted Cellular Imaging and Therapy

Strong NIR and magnetic functionality were loaded into very small ~30 nm nanoclusters that were relatively stable for 8 months. The nanoclusters were formed by kinetic assembly of Au/iron oxide nanocomposite building blocks with only a small amount of polymeric stablizers. The closely-spaced and asymmetric thin gold coatings on the primary particles and porosity of the nanoclusters favor high NIR absorbance as a result of collective responses of the electrons and reduced symmetry of the interactions between plasmon modes. The large degree of empty space in the clusters is beneficial for further addition of adsorbed or conjugated (onto gold) drugs, antibodies and aptamers.[1] The primary components of the particles, iron oxide, Au, dextran and poly vinyl alcohol (PVA), are acceptable for administration to humans, without the need for toxic surfactants or toxic metals. The small size of the nanoclusters and the dextran surface coating are shown to facilitate high uptake by macrophages, which contain dextran receptors.[2] The high uptake and intense NIR absorbance are shown to provide high NIR contrast in dark field and hyperspectral microscopy, both in cell culture and an *in vivo* rabbit model of atherosclerosis. A single 50 ns laser pulse at 755 nm is sufficient for photothermal destruction of nanocluster-laden macrophages. Small and stable nanoclusters of nanocomposite primary particles with strong multifunctionality, designed by this general approach, will offer broad opportunities for cellular imaging and altering cell biology, for the treatment of diseases such as atherosclerosis and cancer.

6.2 GROWTH OF TEXTURED THIN AU SHELLS ON IRON OXIDE NANOPARTICLES

Autocatalytic growth of metal shells on metal oxide nanoparticle cores is often excessive as a result of the high metal/metal oxide ratios which are utilized to overcome poor wetting on the low energy substrate. To mitigate the growth, we have introduced a general alternative concept of thin autocatalytic growth on nanparticle substrates (TAGS). The TAGS mechanism may be considered a generalization of the well-known seeded growth mechanism for pure nanoparticles[3-6] to seeded growth of metals on heterogeneous low energy substrates. Low total metal precursor/metal oxide ratios (0.125-0.50 for Au^{3+}/Fe) are chosen to coat a small fraction of the substrate nanoparticles with unusually thin smooth or thin knobby Au shells (< 5 nm) on a 42 nm iron oxide cores. Multiple iterations or continuous addition of Au^{3+} precursor produce the smallest supersaturation values. During nucleation of Au seeds on a given substrate particle, the slow autocatalytic growth, at low supersaturation values, consumes a smaller amount of Au^{3+}. Consequently, new Au nuclei are seeded on a larger fraction of the iron oxide substrate particles, such that subsequent growth results in thinner shells. In essence, the lower supersaturation provides greater separation of nucleation of seeds and growth on them. Coated particles, with relatively monodisperse hydrodynamic diameters distributions, are separated efficiently from uncoated particles by centrifugation, given the large differences in the densities of Au and iron oxide. A covalently bonded polymer, mPEG-SH, provides steric stabilization against van der Waals attraction, while simultaneousy providing passivation of the growth of the Au coating. The less than 5 nm thin coatings along with asymmetry in shell geometries alter the interactions between plasmon modes and shift the SPR peak to the NIR region, with high cross sections, despite the small overall nanoparticle size. Additional asymmetry is introduced with the nanocluster cores, in contrast with spherical cores. Even further asymmetry and thus the

largest red shifts are observed for the highly asymmetric thin knobby shells on nanocluster cores. The thin shells on small nanoparticles produce strong NIR cross sections, while maximizing available effectiveness of the magnetic component. The high degree of multifunctionality in a total particles smaller than 60 nm is desirable for optical, magnetic or multimodal imaging and therapy, with effective permeation of biological barriers.[1, 7-16]

6.3 Tuning the Nucleation and Growth of Au Shells on Iron Oxide Nanoclusters

The relative rates of nucleation and growth were tuned with a solution property, pH, to produce smooth shells from 5 to 40 nm thick, as well as 20 to 40 nm thick knobby shells, on ~42 nm iron oxide core nanoclusters. For a low Au^{3+}/Fe ratio of 0.5, low supersaturation values mitigate otherwise excessive autocatalytic growth. At low Au^{3+}/Fe ratios, intentionally, only a small and controlled fraction of substrate nanoparticles were coated with Au. For high nucleation rates at high pH, Au seeds were deposited on a higher fraction of the iron oxide substrate particles leading to thinner coatings. At lower pH values, slower nucleation led to less separation between nucleation and autocatalytic growth and, consequently, Au seeds on fewer particles, and thicker coatings. Covalently bound mPEG-SH on the Au shells provided steric stabilization and also passivated autocatalytic growth of Au. As the mPEG-SH concentration was lowered, less passivated shells at high pH became thicker, and eventually the concentration became too low for steric stabilization. The ability to control Textured Autocatalytic Growth on the nanoparticles Substrates (TAGS), while simultaneously providing sufficient steric stabilization, enables synthesis of Au shells on nanoparticles cores with total particle sizes in the range of 60 to 150 nm. Together, the tuning of the TAGS mechanism with a

solution property, pH in the current study, as well as the precursor addition rate in our recent study[17] offers a broad platform for designing a wide range of smooth and knobby shell thicknesses on metal oxide cores. Thus, the TAGS mechanism for controlling the separation of nucleation and growth at low supersaturation values to coat high surface energy metals on metal oxide substrates may be expected to be general and applicable to a wide range of materials.

In most previous studies,[18-23] the Au coatings were smooth and sufficiently thick that the peak maximum was in the visible region. The wide range of novel Au coated iron oxide nanoclusters with diameters from 60 to 150 nm were utilized to gain insight into NIR SPR behavior for highly asymmetric Au shell geometries. NIR SPR behavior with high cross-sections was demonstrated for both thin[17] or thick knobby shells, and thin smooth shells[17]. Broad peaks in the range of 700 to 900 nm were produced by the high aspect ratios and asymmetries in the geometries of the cores and shells (Figure 4.7). In many cases, the extinction coefficient per mass of Au in the NIR region (Table 4.3) was quite large for such small nanoparticles.

6.4 Selective Targeting of Antibody Conjugated Multifunctional Nanoclusters (Nanoroses) to Epidermal Growth Factor Receptors in Cancer Cells

Multifunctional nanoparticles composed of thin Au coatings on magnetic iron oxide cores, were conjugated with a monolayer of anti-EGFR monoclonal antibodies (clone 225). The total hydrodynamic diameter, from 35 to 65 nm, was extremely small given the high degree of functionality. The nanoparticles target EGFR overexpressive cancer cells specifically. The highly asymmetric thin Au shells, synthesized by seeded growth on iron oxide nanoclusters at ultralow supersaturations of Au precursor, produce

the strong NIR absorbance. The final Au/Fe mass ratio of 2.5 is smaller than previously reported values on the order of 10.[21] The unusually small volume of the Au is highly beneficial for providing space for other types of functionality, such as targeting and therapeutic Abs, and if desired, magnetic functionality. The Au surfaces enable universal conjugation of Abs with a low MW dithiol-PEG-hydrazide heterobifunctional linker to the non-binding Fc region, without the need for a polymeric stabilizer with reactive binding sites. The number of Abs, tagged with fluorophore, was tuned from 1 to 74 by varying the feed Ab/particle ratio. The hydrodynamic diameter of the conjugated nanoparticles was varied from 35 to 78 nm and correlated to the number of conjugated Abs, as determined by fluorescence spectroscopy. A transition from sub-monolayer to multilayer aggregates of Abs was observed for 54 Abs and a particle diameter of 63 nm. Steric stabilization was provided a combination of Ab as well as mPEG-SH in physiological media, to overcome the VDW attraction.

For the 63 nm particles with 54 Abs in a monolayer, targeting of EGFR overexpressive cancer cells was selective, relative to EGFR negative cancer cells. In dark field microscopy, high uptake of the conjugated nanoparticles produced an intense orange signal, resulting from strong NIR scattering. The cellular uptake of nanoparticles/cell was high, reaching 7,000, as characterized by AAS. The intense NIR scattering from nanoparticles in cells is consistent with the strong NIR absorbance/mass Au, as observed in a previous study of the non-conjugated nanoparticles in macrophage cells by hyperspectral microscopy.[10] Colocalization of the NIR scattering and fluorescence indicates the Abs remained attached to the Au surfaces inside the cancer cells. The extremely high curvature of the Au shells with features below 5 nm influence the spacing and orientations of the Abs on the surface, which has the potential to have a marked effect on biological pathways within cells.[24-27] The ability to load intense

multifunctionality, specifically strong NIR absorbance, conjugation of an Ab monlayer and strong r2 mri contrast (from previous study[10]) in a total particle size only 63 nm is an important step forward in achieving both molecular specific imaging and real time feedback on therapeutic efficacy for treatment of cancer.

6.5 REFERENCES

1. Josephson, L.; Kircher, M. F.; Mahmood, U.; Tang, Y.; Weissleder, R., Near-Infrared Fluorescent Nanoparticles as Combined MR/Optical Imaging Probes. *Bioconjugate Chemistry* **2002,** 13, (3), 554-560.

2. Jaffer, F. A.; Libby, P.; Weissleder, R., Molecular and cellular imaging of atherosclerosis: emergency applications. *Journal of the American College of Cardiology* **2006,** 47, (7), 1328-1338.

3. Jana, N. R.; Gearheart, L.; Murphy, C. J., Evidence for seed-mediated nucleation in the chemical reduction of gold salts to gold nanoparticles. *Chemistry of Materials* **2001,** 13, (7), 2313-2322.

4. Watzky, M. A.; Finke, R. G., Transition metal nanocluster formation kinetic and mechanistic studies. A new mechanism when hydrogen is the reductant: Slow, continuous nucleation and fast autocatalytic surface growth. *Journal of the American Chemical Society* **1997,** 119, (43), 10382-10400.

5. Brown, K. R.; Natan, M. J., Hydroxylamine Seeding of Colloidal Au Nanoparticles in Solution and on Surfaces. *Langmuir* **1998,** 14, (4), 726-728.

6. Brown, K. R.; Walter, D. G.; Natan, M. J., Seeding of colloidal Au nanoparticle solutions. 2. Improved control of particle size and shape. *Chemistry of Materials* **2000,** 12, (2), 306-313.

7. Oh, J.; Feldman, M. D.; Kim, J.; Condit, C.; Emelianov, S.; Milner, T. E., Detection of magnetic nanoparticles in tissue using magneto-motive ultrasound. *Nanotechnology* **2006,** 17, (16), 4183-4190.

8. Mehrmohammadi, M.; Oh, J.; Ma, L.; Yantsen, E.; Larson, T.; Mallidi, S.; Park, S.; Johnston, K. P.; Sokolov, K.; Milner, T.; Emelianov, S.; Ieee, Imaging of iron oxide nanoparticles using magneto-motive ultrasound. In *2007 Ieee Ultrasonics Symposium Proceedings, Vols 1-6*, Ieee: New York, 2007; pp 652-655.

9. Qu, M.; Mallidi, S.; Mehrmohammadi, M.; Ma, L. L.; Johnston, K. P.; Sokolov, K.; Emelianov, S., Combined photoacoustic and magneto-acoustic imaging. *Conf Proc IEEE Eng Med Biol Soc* **2009,** 2009, 4763-6.

10. Ma, L. L.; Feldman, M. D.; Tam, J. M.; Paranjape, A. S.; Cheruku, K. K.; Larson, T. A.; Tam, J. O.; Ingram, D. R.; Paramita, V.; Villard, J. W.; Jenkins, J. T.; Wang, T.; Clarke, G. D.; Asmis, R.; Sokolov, K.; Chandrasekar, B.; Milner, T. E.; Johnston, K. P., Small Multifunctional Nanoclusters (Nanoroses) for Targeted Cellular Imaging and Therapy. *Acs Nano* **2009,** 3, (9), 2686-2696.

11. Aaron, J. S.; Oh, J.; Larson, T. A.; Kumar, S.; Milner, T. E.; Sokolov, K. V., Increased optical contrast in imaging of epidermal growth factor receptor using magnetically actuated hybrid gold/iron oxide nanoparticles. *Optics Express* **2006,** 14, (26), 12930-12943.

12. Larson, T. A.; Bankson, J.; Aaron, J.; Sokolov, K., Hybrid plasmonic magnetic nanoparticles as molecular specific agents for MRI/optical imaging and photothermal therapy of cancer cells. *Nanotechnology* **2007,** 18, (32), 325101/1-325101/8.

13. Shah, J.; Park, S.; Aglyamov, S.; Larson, T.; Ma, L.; Sokolov, K.; Johnston, K.; Milner, T.; Emelianov Stanislav, Y., Photoacoustic imaging and temperature measurement for photothermal cancer therapy. *Journal of biomedical optics* **2008,** 13, (3), 034024.

14. Paranjape, A. S.; Kuranov, R.; Baranov, S.; Ma, L. L.; Villard, J. W.; Wang, T.; Konstantin, S.; Feldman, M. D.; Johnston, K. P.; Milner, T. E., Depth resolved photothermal OCT detection of macrophages in tissue using nanorose. *Biomedical Optics Express* **2010,** 1, (1), 2-16.

15. Weissleder, R., Molecular Imaging in Cancer. *Science* **2006,** 312, (5777), 1168-1171.

16. Hirsch, L. R.; Stafford, R. J.; Bankson, J. A.; Sershen, S. R.; Rivera, B.; Price, R. E.; Hazle, J. D.; Halas, N. J.; West, J. L., Nanoshell-mediated near-infrared thermal therapy of tumors under magnetic resonance guidance. *Proc. Nat. Acad. Sci.* **2003,** 100, (23), 13549-13554.

17. Ma, L. L.; Borwankar, A.; Willsey, B.; Yoon, K. Y.; Tam, J. O.; Sokolov, K.; Feldman, M. D.; Milner, T. E.; Johnston, K. P., Growth of Textured Thin Au Shells on Iron Oxide Nanoparticles. *Prepare for Submitting* **2011**.

18. Wang, L.; Park, H.-Y.; Lim, S. I. I.; Schadt, M. J.; Mott, D.; Luo, J.; Wang, X.; Zhong, C.-J., Core@shell nanomaterials: gold-coated magnetic oxide nanoparticles. *Journal of Materials Chemistry* **2008,** 18, (23), 2629-2635.

19. Rasch, M. R.; Sokolov, K. V.; Korgel, B. A., Limitations on the Optical Tunability of Small Diameter Gold Nanoshells. *Langmuir* **2009,** 25, (19), 11777-11785.

20. Oldenburg, S. J.; Averitt, R. D.; Westcott, S. L.; Halas, N. J., Nanoengineering of optical resonances. *Chemical Physics Letters* **1998,** 288, (2,3,4), 243-247.

21. Lyon, J. L.; Fleming, D. A.; Stone, M. B.; Schiffer, P.; Williams, M. E., Synthesis of Fe oxide core/Au shell nanoparticles by iterative hydroxylamine seeding. *Nano Letters* **2004,** 4, (4), 719-723.

22. Oh, E.; Susumu, K.; Goswami, R.; Mattoussi, H., One-Phase Synthesis of Water-Soluble Gold Nanoparticles with Control over Size and Surface Functionalities. *Langmuir* **2010,** 26, (10), 7604-7613.

23. Goon, I. Y.; Lai, L. M. H.; Lim, M.; Munroe, P.; Gooding, J. J.; Amal, R., Fabrication and Dispersion of Gold-Shell-Protected Magnetite Nanoparticles: Systematic Control Using Polyethyleneimine. *Chemistry of Materials* **2009,** 21, (4), 673-681.

24. Jiang, W.; Kim, B. Y. S.; Rutka, J. T.; Chan, W. C. W., Nanoparticle-mediated cellular response is size-dependent. *Nature Nanotechnology* **2008,** 3, (3), 145-150.

25. Decuzzi, P.; Pasqualini, R.; Arap, W.; Ferrari, M., Intravascular Delivery of Particulate Systems: Does Geometry Really Matter? *Pharm. Res.* **2009,** 26, (1), 235-243.

26. Gratton, S. E. A.; Ropp, P. A.; Pohlhaus, P. D.; Luft, J. C.; Madden, V. J.; Napier, M. E.; DeSimone, J. M., The effect of particle design on cellular internalization pathways. *Proceedings of the National Academy of Sciences of the United States of America* **2008,** 105, (33), 11613-11618.

27. Champion, J. A.; Katare, Y. K.; Mitragotri, S., Making polymeric micro- and nanoparticles of complex shapes. *Proceedings of the National Academy of Sciences of the United States of America* **2007,** 104, (29), 11901-11904.

Bibliography

Aaron, J.; Nitin, N.; Travis, K.; Kumar, S.; Collier, T.; Park, S. Y.; Jose-Yacaman, M.; Coghlan, L.; Follen, M.; Richards-Kortum, R.; Sokolov, K., Plasmon Resonance Coupling of Metal Nanoparticles for Molecular Imaging of Carcinogenesis in Vivo. *Journal of Biomedical Optics* **2007,** 12, 034007/1-034007/11.

Aaron, J.; Travis, K.; Harrison, N.; Sokolov, K., Dynamic Imaging of Molecular Assemblies in Live Cells Based on Nanoparticle Plasmon Resonance Coupling. *Nano Letters* **2009,** 9, 3612-3618.

Aaron, J. S.; Oh, J.; Larson, T. A.; Kumar, S.; Milner, T. E.; Sokolov, K. V., Increased Optical Contrast in Imaging of Epidermal Growth Factor Receptor Using Magnetically Actuated Hybrid Gold/Iron Oxide Nanoparticles. *Optics Express* **2006,** 14, 12930-12943.

Adler, D. C.; Huang, S.-W.; Huber, R.; Fujimoto, J. G., Photothermal Detection of Gold Nanoparticles Using Phase-Sensitive Optical Coherence Tomography. *Optics Express* **2008,** 16, 4376-4393.

Allavena, P.; Sica, A.; Solinas, G.; Porta, C.; Mantovani, A., The Inflammatory Micro-Environment in Tumor Progression: The Role of Tumor-Associated Macrophages. *Critical reviews in oncology/hematology* **2008,** 66, 1-9.

Anker, J. N.; Hall, W. P.; Lyandres, O.; Shah, N. C.; Zhao, J.; Van Duyne, R. P., Biosensing with Plasmonic Nanosensors. *Nature Materials* **2008,** 7, 442-453.

Averitt, R. D.; Westcott, S. L.; Halas, N. J., Linear Optical Properties of Gold Nanoshells. *Journal of the Optical Society of America B-Optical Physics* **1999,** 16, 1824-1832.

Bagalkot, V.; Zhang, L.; Levy-Nissenbaum, E.; Jon, S.; Kantoff, P. W.; Langer, R.; Farokhzad, O. C., Quantum Dot - Aptamer Conjugates for Synchronous Cancer Imaging, Therapy, and Sensing of Drug Delivery Based on Bi-Fluorescence Resonance Energy Transfer. *Nano Letters* **2007,** 7, 3065-3070.

Ban, Z.; Barnakov, Y. A.; Li, F.; Golub, V. O.; O'Connor, C. J., The Synthesis of Core-Shell Iron@Gold Nanoparticles and Their Characterization. *Journal of Materials Chemistry* **2005,** 15, 4660-4662.

Baselga, J.; Arteaga, C. L., Critical Update and Emerging Trends in Epidermal Growth Factor Receptor Targeting in Cancer. *Journal of Clinical Oncology* **2005,** 23, 2445-2459.

Bastos, K. R. B.; Alvarez, J. M.; Marinho, C. R. F.; Rizzo, L. V.; Lima, M. R. D. I., *Journal of Leukocyte Biology* **2002,** 71, 271-278.

Basu, S.; Pande, S.; Jana, S.; Bolisetty, S.; Pal, T., Controlled Interparticle Spacing for Surface-Modified Gold Nanoparticle Aggregates. *Langmuir* **2008,** 24, 5562-5568.

Berret, J.-F.; Schonbeck, N.; Gazeau, F.; El Kharrat, D.; Sandre, O.; Vacher, A.; Airiau, M., Controlled Clustering of Superparamagnetic Nanoparticles Using Block Copolymers: Design of New Contrast Agents for Magnetic Resonance Imaging. *Journal of the American Chemical Society* **2006,** 128, 1755-1761.

Biswas, S. K.; Sica, A.; Lewis, C. E., Plasticity of Macrophage Function During Tumor Progression: Regulation by Distinct Molecular Mechanisms. *Journal of Immunology* **2008,** 180, 2011-2017.

Boal, A. K.; Ilhan, F.; DeRouchey, J. E.; Thurn-Albrecht, T.; Russell, T. P.; Rotello, V. M., Self-Assembly of Nanoparticles into Structured Spherical and Network Aggregates. *Nature* **2000,** 404, 746-748.

Boehm, M. K.; Woof, J. M.; Kerr, M. A.; Perkins, S. J., The Fab and Fc Fragments of Iga1 Exhibit a Different Arrangement from That in Igg: A Study by X-Ray and Neutron Solution Scattering and Homology Modelling. *Journal of Molecular Biology* **1999,** 286, 1421-1447.

Brannon-Peppas, L.; Blanchette, J. O., Nanoparticle and Targeted Systems for Cancer Therapy. *Advanced Drug Delivery Reviews* **2004,** 56, 1649-1659.

Brillhart, K. L.; Ngo, T. T., Use of Microwell Plates Carrying Hydrazide Groups to Enhance Antibody Immobilization in Enzyme Immunoassays. *Journal of Immunological Methods* **1991,** 144, 19-25.

Brown, K. R.; Lyon, L. A.; Fox, A. P.; Reiss, B. D.; Natan, M. J., Hydroxylamine Seeding of Colloidal Au Nanoparticles. 3. Controlled Formation of Conductive Au Films. *Chemistry of Materials* **2000,** 12, 314-323.

Brown, K. R.; Natan, M. J., Hydroxylamine Seeding of Colloidal Au Nanoparticles in Solution and on Surfaces. *Langmuir* **1998,** 14, 726-728.

Brown, K. R.; Walter, D. G.; Natan, M. J., Seeding of Colloidal Au Nanoparticle Solutions. 2. Improved Control of Particle Size and Shape. *Chemistry of Materials* **2000,** 12, 306-313.

Cao, L.; Zhu, T.; Liu, Z., Formation Mechanism of Nonspherical Gold Nanoparticles During Seeding Growth: Roles of Anion Adsorption and Reduction Rate. *Journal of Colloid and Interface Science* **2006,** 293, 69-76.

Caruntu, D.; Cushing, B. L.; Caruntu, G.; O'Connor, C. J., Attachment of Gold Nanograins onto Colloidal Magnetite Nanocrystals. *Chemistry of Materials* **2005,** 17, 3398-3402.

Champion, J. A.; Katare, Y. K.; Mitragotri, S., Making Polymeric Micro- and Nanoparticles of Complex Shapes. *Proceedings of the National Academy of Sciences of the United States of America* **2007,** 104, 11901-11904.

Chen, J.; Saeki, F.; Wiley, B. J.; Cang, H.; Cobb, M. J.; Li, Z. Y.; Au, L.; Zhang, H.; Kimmey, M. B.; Li, X. D.; Xia, Y., Gold Nanocages: Bioconjugation and Their Potential Use as Optical Imaging Contrast Agents. *Nano Letters* **2005,** 5, 473-477.

Chen, R.; Wu, J. L.; Li, H.; Cheng, G.; Lu, Z.; Che, C. M., Fabrication of Gold Nanoparticles with Different Morphologies in Hepes Buffer. *Rare Metals* **2010,** 29, 180-186.

Chen, S.; Reynolds, F.; Yu, L.; Weissleder, R.; Josephson, L., A Screening Paradigm for the Design of Improved Polymer-Coated Superparamagnetic Iron Oxide Nanoparticles. *Journal of Materials Chemistry* **2009,** 19, 6387-6392.

Chen, W. R.; Adams, R. L.; Carubelli, R.; Nordquist, R. E., Laser-Photosensitizer Assisted Immunotherapy: A Novel Modality for Cancer Treatment. *Cancer Letters (Shannon, Ireland)* **1997,** 115, 25-30.

Chithrani, B. D.; Ghazani, A. A.; Chan, W. C. W., Determining the Size and Shape Dependence of Gold Nanoparticle Uptake into Mammalian Cells. *Nano Letters* **2006,** 6, 662-668.

Cho, E. C.; Au, L.; Zhang, Q.; Xia, Y., The Effects of Size, Shape, and Surface Functional Group of Gold Nanostructures on Their Adsorption and Internalization by Cells. *Small* **2010,** 6, 517-522.

Choi, H. S.; Liu, W.; Misra, P.; Tanaka, E.; Zimmer, J. P.; Ipe, B. I.; Bawendi, M. G.; Frangioni, J. V., Renal Clearance of Quantum Dots. *Nature Biotechnology* **2007,** 25, 1165-1170.

Connor, E. E.; Mwamuka, J.; Gole, A.; Murphy, C. J.; Wyatt, M. D., Gold Nanoparticles Are Taken up by Human Cells but Do Not Cause Acute Cytotoxicity. *Small* **2005,** 1, 325-327.

Dames, P.; Gleich, B.; Flemmer, A.; Hajek, K.; Seidl, N.; Wiekhorst, F.; Eberbeck, D.; Bittmann, I.; Bergemann, C.; Weyh, T.; Trahms, L.; Rosenecker, J.; Rudolph, C., Targeted Delivery of Magnetic Aerosol Droplets to the Lung. *Nature Nanotechnology* **2007,** 2, 495-499.

Decuzzi, P.; Pasqualini, R.; Arap, W.; Ferrari, M., Intravascular Delivery of Particulate Systems: Does Geometry Really Matter? *Pharmaceutical Research* **2009,** 26, 235-243.

DeVries, G. A.; Brunnbauer, M.; Hu, Y.; Jackson, A. M.; Long, B.; Neltner, B. T.; Uzun, O.; Wunsch, B. H.; Stellacci, F., Divalent Metal Nanoparticles. *Science* **2007,** 315, 358-361.

Diagaradjane, P.; Orenstein-Cardona, J. M.; Colon-Casasnovas, N. E.; Deorukhkar, A.; Shentu, S.; Kuno, N.; Schwartz, D. L.; Gelovani, J. G.; Krishnan, S., Imaging Epidermal Growth Factor Receptor Expression in Vivo: Pharmacokinetic and Biodistribution Characterization of a Bioconjugated Quantum Dot Nanoprobe. *Clinical Cancer Research* **2008,** 14, 731-741.

Ditsch, A.; Laibinis, P. E.; Wang, D. I. C.; Hatton, T. A., Controlled Clustering and Enhanced Stability of Polymer-Coated Magnetic Nanoparticles. *Langmuir* **2005,** 21, 6006-6018.

Dong, X.; Ji, X.; Wu, H.; Zhao, L.; Li, J.; Yang, W., Shape Control of Silver Nanoparticles by Stepwise Citrate Reduction. *Journal of Physical Chemistry C* **2009,** 113, 6573-6576.

Farokhzad, O. C.; Langer, R., Nanomedicine: Developing Smarter Therapeutic and Diagnostic Modalities. *Advanced Drug Delivery Reviews* **2006,** 58, 1456-1459.

Ferrari, M., Cancer Nanotechnology: Opportunities and Challenges. *Nature Reviews Cancer* **2005,** 5, 161-171.

Ferrari, M., Beyond Drug Delivery. *Nature Nanotechnology* **2008,** 3, 131-132.

Fetters, L. J.; Lohse, D. J.; Richter, D.; Witten, T. A.; Zirkel, A., Connection between Polymer Molecular-Weight, Density, Chain Dimensions, and Melt Viscoelastic Properties. *Macromolecules* **1994,** 27, 4639-4647.

Finney, E. E.; Finke, R. G., Nanocluster Nucleation and Growth Kinetic and Mechanistic Studies: A Review Emphasizing Transition-Metal Nanoclusters. *Journal of Colloid and Interface Science* **2008,** 317, 351-374.

Frey, N. A.; Peng, S.; Cheng, K.; Sun, S., Magnetic Nanoparticles: Synthesis, Functionalization, and Applications in Bioimaging and Magnetic Energy Storage. *Chemical Society Reviews* **2009,** 38, 2532-2542.

Friedlander, S. K., *Smoke, Dust, and Haze: Fundamentals of Aerosol Dynamics, Second Edition*. Oxford University Press: 2000; p 432 pp.

Gachard, E.; Remita, H.; Khatouri, J.; Keita, B.; Nadjo, L.; Belloni, J., Radiation-Induced and Chemical Formation of Gold Clusters. *New Journal of Chemistry* **1998,** 22, 1257-1265.

Ghose, T. I.; Blair, A. H.; Kulkarni, P. N., Preparation of Antibody-Linked Cyto-Toxic Agents. *Methods in Enzymology* **1983,** 93, 280-333.

Gilbert, S. E.; Cavalleri, O.; Kern, K., Electrodeposition of Cu Nanoparticles on Decanethiol-Covered Au(111) Surfaces: An in Situ Stm Investigation. *Journal of Physical Chemistry* **1996,** 100, 12123-12130.

Goldstein, N. I.; Prewett, M.; Zuklys, K.; Rockwell, P.; Mendelsohn, J., Biological Efficacy of a Chimeric Antibody to the Epidermal Growth Factor Receptor in a Human Tumor Xenograft Model. *Clinical Cancer Research* **1995,** 1, 1311-1318.

Goon, I. Y.; Lai, L. M. H.; Lim, M.; Munroe, P.; Gooding, J. J.; Amal, R., Fabrication and Dispersion of Gold-Shell-Protected Magnetite Nanoparticles: Systematic Control Using Polyethyleneimine. *Chemistry of Materials* **2009,** 21, 673-681.

Gopalan, B.; Ito, I.; Branch, C. D.; Stephens, C.; Roth, J. A.; Ramesh, R., Nanoparticle Based Systemic Gene Therapy for Lung Cancer: Molecular Mechanisms and Strategies to Suppress Nanoparticle-Mediated Inflammatory Response. *Technology in Cancer Research & Treatment* **2004,** 3, 647-657.

Gratton, S. E. A.; Ropp, P. A.; Pohlhaus, P. D.; Luft, J. C.; Madden, V. J.; Napier, M. E.; De Simone, J. M., The Effect of Particle Design on Cellular Internalization Pathways. *Proceedings of the National Academy of Sciences of the United States of America* **2008,** 105, 11613-11618.

Gratton, S. E. A.; Ropp, P. A.; Pohlhaus, P. D.; Luft, J. C.; Madden, V. J.; Napier, M. E.; DeSimone, J. M., The Effect of Particle Design on Cellular Internalization Pathways. *Proceedings of the National Academy of Sciences of the United States of America* **2008,** 105, 11613-11618.

Gupta, P.; Hall, C. K.; Voegler, A. C., Effect of Denaturant and Protein Concentrations Upon Protein Refolding and Aggregation: A Simple Lattice Model. *Protein Science* **1998,** 7, 2642-2652.

Hayat, M. A., Cancer Imaging. In Academic Press: 2007.

Hiemenz, P. C.; Rajagopalan, R.; Editors, *Principles of Colloid and Surface Chemistry, Third Edition, Revised and Expanded*. 1997; p 688 pp.

Hirsch, L. R.; Stafford, R. J.; Bankson, J. A.; Sershen, S. R.; Rivera, B.; Price, R. E.; Hazle, J. D.; Halas, N. J.; West, J. L., Nanoshell-Mediated near-Infrared Thermal

Therapy of Tumors under Magnetic Resonance Guidance. *Proceedings of the National Academy of Sciences of the United States of America* **2003,** 100, 13549-13554.

Holmes, J. D.; Johnston, K. P.; Doty, R. C.; Korgel, B. A., Control of Thickness and Orientation of Solution-Grown Silicon Nanowires. *Science* **2000,** 287, 1471-1473.

Hostetler, M. J.; Wingate, J. E.; Zhong, C. J.; Harris, J. E.; Vachet, R. W.; Clark, M. R.; Londono, J. D.; Green, S. J.; Stokes, J. J.; Wignall, G. D.; Glish, G. L.; Porter, M. D.; Evans, N. D.; Murray, R. W., Alkanethiolate Gold Cluster Molecules with Core Diameters from 1.5 to 5.2 Nm: Core and Monolayer Properties as a Function of Core Size. *Langmuir* **1998,** 14, 17-30.

Hu, Y.; Noelck, S. J.; Drezek, R. A., Symmetry Breaking in Gold-Silica-Gold Multilayer Nanoshells. *Acs Nano* **2010,** 4, 1521-1528.

Huang, W.; Tamilmani, S.; Raghavan, S.; Small, R., Dissolution of Copper Thin Films in Hydroxylamine-Based Solutions. *International Journal of Mineral Processing* **2003,** 72, 365-372.

Huang, X.; El-Sayed, I. H.; Qian, W.; El-Sayed, M. A., Cancer Cell Imaging and Photothermal Therapy in the near-Infrared Region by Using Gold Nanorods. *Journal of the American Chemical Society* **2006,** 128, 2115-2120.

Huang, X.; Peng, X.; Wang, Y.; Shin, D. M.; El-Sayed, M. A.; Nie, S., A Reexamination of Active and Passive Tumor Targeting by Using Rod-Shaped Gold Nanocrystals and Covalently Conjugated Peptide Ligands. *ACS Nano* **2010**.

Hyafil, F.; Laissy, J.-P.; Mazighi, M.; Tchetche, D.; Louedec, L.; Adle-Biassette, H.; Chillon, S.; Henin, D.; Jacob, M.-P.; Letourneur, D.; Feldman Laurent, J., Ferumoxtran-10-Enhanced Mri of the Hypercholesterolemic Rabbit Aorta: Relationship between Signal Loss and Macrophage Infiltration. *Arterioscler Thromb Vasc Biol* **2006,** 26, 176-81.

Iglesias-Silva, E.; Vilas-Vilela, J. L.; Lopez-Quintela, M. A.; Rivas, J.; Rodriguez, M.; Leon, L. M., Synthesis of Gold-Coated Iron Oxide Nanoparticles. *Journal of Non-Crystalline Solids* **2010,** 356, 1233-1235.

Jaffer, F. A.; Libby, P.; Weissleder, R., Molecular and Cellular Imaging of Atherosclerosis: Emergency Applications. *Journal of the American College of Cardiology* **2006,** 47, 1328-1338.

Jain, P. K.; Lee, K. S.; El-Sayed, I. H.; El-Sayed, M. A., Calculated Absorption and Scattering Properties of Gold Nanoparticles of Different Size, Shape, and Composition:

Applications in Biological Imaging and Biomedicine. *Journal of Physical Chemistry B* **2006,** 110, 7238-7248.

Jana, N. R.; Gearheart, L.; Murphy, C. J., Evidence for Seed-Mediated Nucleation in the Chemical Reduction of Gold Salts to Gold Nanoparticles. *Chemistry of Materials* **2001,** 13, 2313-2322.

Jans, H.; Liu, X.; Austin, L.; Maes, G.; Huo, Q., Dynamic Light Scattering as a Powerful Tool for Gold Nanoparticle Bioconjugation and Biomolecular Binding Studies. *Analytical Chemistry (Washington, DC, United States)* **2009,** 81, 9425-9432.

Jeong, U.; Teng, X.; Wang, Y.; Yang, H.; Xia, Y., Superparamagnetic Colloids: Controlled Synthesis and Niche Applications. *Advanced Materials (Weinheim, Germany)* **2007,** 19, 33-60.

Ji, X.; Song, X.; Li, J.; Bai, Y.; Yang, W.; Peng, X., Size Control of Gold Nanocrystals in Citrate Reduction: The Third Role of Citrate. *Journal of the American Chemical Society* **2007,** 129, 13939-13948.

Jiang, W.; Kim, B. Y. S.; Rutka, J. T.; Chan, W. C. W., Nanoparticle-Mediated Cellular Response Is Size-Dependent. *Nature Nanotechnology* **2008,** 3, 145-150.

Josephson, L.; Kircher, M. F.; Mahmood, U.; Tang, Y.; Weissleder, R., Near-Infrared Fluorescent Nanoparticles as Combined Mr/Optical Imaging Probes. *Bioconjugate Chemistry* **2002,** 13, 554-560.

Jun, Y.-w.; Lee, J.-H.; Cheon, J., Chemical Design of Nanoparticle Probes for High-Performance Magnetic Resonance Imaging. *Angewandte Chemie, International Edition* **2008,** 47, 5122-5135.

Ke, S.; Wen, X. X.; Gurfinkel, M.; Charnsangavej, C.; Wallace, S.; Sevick-Muraca, E. M.; Li, C., Near-Infrared Optical Imaging of Epidermal Growth Factor Receptor in Breast Cancer Xenografts. *Cancer Research* **2003,** 63, 7870-7875.

Khlebtsov, B.; Zharov, V.; Melnikov, A.; Tuchin, V.; Khlebtsov, N., Optical Amplification of Photothermal Therapy with Gold Nanoparticles and Nanoclusters. *Nanotechnology* **2006,** 17, 5167-5179.

Khoury, C. G.; Vo-Dinh, T., Gold Nanostars for Surface-Enhanced Raman Scattering: Synthesis, Characterization and Optimization. *Journal of Physical Chemistry C* **2008,** 112, 18849-18859.

Kimura, Y. N.; Watari, K.; Fotovati, A.; Hosoi, F.; Yasumoto, K.; Izumi, H.; Kohno, K.; Umezawa, K.; Iguchi, H.; Shirouzu, K.; Takamori, S.; Kuwano, M.; Ono, M.,

Inflammatory Stimuli from Macrophages and Cancer Cells Synergistically Promote Tumor Growth and Angiogenesis. *Cancer Science* **2007,** 98, 2009-2018.

Knight, M. W.; Halas, N. J., Nanoshells to Nanoeggs to Nanocups: Optical Properties of Reduced Symmetry Core-Shell Nanoparticles Beyond the Quasistatic Limit. *New Journal of Physics* **2008,** 10.

Kumar, P. S.; Pastoriza-Santos, I.; Rodriguez-Gonzalez, B.; Garcia de Abajo, F. J.; Liz-Marzan, L. M., High-Yield Synthesis and Optical Response of Gold Nanostars. *Nanotechnology* **2008,** 19, 015606/1-015606/6.

Kumar, S.; Aaron, J.; Sokolov, K., Directional Conjugation of Antibodies to Nanoparticles for Synthesis of Multiplexed Optical Contrast Agents with Both Delivery and Targeting Moieties. *Nat. Protocols* **2008,** 3, 314-320.

Kumar, S.; Harrison, N.; Richards-Kortum, R.; Sokolov, K., Plasmonic Nanosensors for Imaging Intracellular Biomarkers in Live Cells. *Nano Letters* **2007,** 7, 1338-1343.

Larson, T. A.; Bankson, J.; Aaron, J.; Sokolov, K., Hybrid Plasmonic Magnetic Nanoparticles as Molecular Specific Agents for Mri/Optical Imaging and Photothermal Therapy of Cancer Cells. *Nanotechnology* **2007,** 18, 325101/1-325101/8.

Lattuada, M.; Wu, H.; Morbidelli, M., Hydrodynamic Radius of Fractal Clusters. *Journal of Colloid and Interface Science* **2003,** 268, 96-105.

Lazarides, A. A.; Schatz, G. C., DNA-Linked Metal Nanosphere Materials: Structural Basis for the Optical Properties. *Journal of Physical Chemistry B* **2000,** 104, 460-467.

Lee, J.-H.; Huh, Y.-M.; Jun, Y.-W.; Seo, J.-W.; Jang, J.-T.; Song, H.-T.; Kim, S.; Cho, E.-J.; Yoon, H.-G.; Suh, J.-S.; Cheon, J., Artificially Engineered Magnetic Nanoparticles for Ultra-Sensitive Molecular Imaging. *Nature medicine* **2007,** 13, 95-9.

Leff, D. V.; Ohara, P. C.; Heath, J. R.; Gelbart, W. M., Thermodynamic Control of Gold Nanocrystal Size - Experiment and Theory. *Journal of Physical Chemistry* **1995,** 99, 7036-7041.

Levin, C. S.; Hofmann, C.; Ali, T. A.; Kelly, A. T.; Morosan, E.; Nordlander, P.; Whitmire, K. H.; Halas, N. J., Magnetic-Plasmonic Core-Shell Nanoparticles. *Acs Nano* **2009,** 3, 1379-1388.

Libby, P., Inflammation in Atherosclerosis. *Nature (London, United Kingdom)* **2002,** 420, 868-874.

Libby, P.; Aikawa, M., Stabilization of Atherosclerotic Plaques: New Mechanisms and Clinical Targets. *Nature Medicine (New York, NY, United States)* **2002,** 8, 1257-1262.

Lim, J.; Eggeman, A.; Lanni, F.; Tilton, R. D.; Majetich, S. A., Synthesis and Single-Particle Optical Detection of Low-Polydispersity Plasmonic-Superparamagnetic Nanoparticles. *Advanced Materials* **2008,** 20, 1721-1726.

Lim, J.; Tilton, R. D.; Eggeman, A.; Majetich, S. A., Design and Synthesis of Plasmonic Magnetic Nanoparticles. *Journal of Magnetism and Magnetic Materials* **2007,** 311, 78-83.

Lim, J. K.; Majetich, S. A.; Tilton, R. D., Stabilization of Superparamagnetic Iron Oxide Core-Gold Shell Nanoparticles in High Ionic Strength Media. *Langmuir* **2009,** 25, 13384-13393.

Lo, C. K.; Xiao, D.; Choi, M. M. F., Homocysteine-Protected Gold-Coated Magnetic Nanoparticles: Synthesis and Characterization. *Journal of Materials Chemistry* **2007,** 17, 2418-2427.

Loo, C.; Lowery, A.; Halas, N.; West, J.; Drezek, R., Immunotargeted Nanoshells for Integrated Cancer Imaging and Therapy. *Nano Letters* **2005,** 5, 709-711.

Loo, C.; Lowery, A.; Halas, N. J.; West, J.; Drezek, R., Immunotargeted Nanoshells for Integrated Cancer Imaging and Therapy. *Nano Letters* **2005,** 5, 709-711.

Lyon, J. L.; Fleming, D. A.; Stone, M. B.; Schiffer, P.; Williams, M. E., Synthesis of Fe Oxide Core/Au Shell Nanoparticles by Iterative Hydroxylamine Seeding. *Nano Letters* **2004,** 4, 719-723.

Ma, L. L.; Borwankar, A.; Willsey, B.; Yoon, K. Y.; Tam, J. O.; Sokolov, K.; Feldman, M. D.; Milner, T. E.; Johnston, K. P., Growth of Textured Thin Au Shells on Iron Oxide Nanoparticles. *Prepare for Submitting* **2011**.

Ma, L. L.; Feldman, M. D.; Tam, J. M.; Paranjape, A. S.; Cheruku, K. K.; Larson, T. A.; Tam, J. O.; Ingram, D. R.; Paramita, V.; Villard, J. W.; Jenkins, J. T.; Wang, T.; Clarke, G. D.; Asmis, R.; Sokolov, K.; Chandrasekar, B.; Milner, T. E.; Johnston, K. P., Small Multifunctional Nanoclusters (Nanoroses) for Targeted Cellular Imaging and Therapy. *Acs Nano* **2009,** 3, 2686-2696.

Maeda, H.; Fang, J.; Inutsuka, T.; Kitamoto, Y., Vascular Permeability Enhancement in Solid Tumor: Various Factors, Mechanisms Involved and Its Implications. *International Immunopharmacology* **2003,** 3, 319-328.

Mallidi, S.; Larson, T.; Aaron, J.; Sokolov, K.; Emelianov, S., Molecular Specific Optoacoustic Imaging with Plasmonic Nanoparticles. *Optics Express* **2007,** 15, 6583-6588.

Mallidi, S.; Larson, T.; Tam, J.; Joshi, P. P.; Karpiouk, A.; Sokolov, K.; Emelianov, S., Multiwavelength Photoacoustic Imaging and Plasmon Resonance Coupling of Gold Nanoparticles for Selective Detection of Cancer. *Nano Letters* **2009,** 9, 2825-2831.

Mandal, M.; Kundu, S.; Ghosh, S. K.; Panigrahi, S.; Sau, T. K.; Yusuf, S. M.; Pal, T., Magnetite Nanoparticles with Tunable Gold or Silver Shell. *Journal of Colloid and Interface Science* **2005,** 286, 187-194.

Matsumura, Y.; Maeda, H., A New Concept for Macromolecular Therapeutics in Cancer-Chemotherapy - Mechanism of Tumoritropic Accumulation of Proteins and the Antitumor Agent Smancs. *Cancer Research* **1986,** 46, 6387-6392.

Mazumder, V.; Chi, M. F.; More, K. L.; Sun, S. H., Core/Shell Pd/Fept Nanoparticles as an Active and Durable Catalyst for the Oxygen Reduction Reaction. *Journal of the American Chemical Society* **2010,** 132, 7848-7849.

Mehrmohammadi, M.; Oh, J.; Ma, L.; Yantsen, E.; Larson, T.; Mallidi, S.; Park, S.; Johnston, K. P.; Sokolov, K.; Milner, T.; Emelianov, S.; Ieee, Imaging of Iron Oxide Nanoparticles Using Magneto-Motive Ultrasound. In *2007 Ieee Ultrasonics Symposium Proceedings, Vols 1-6*, Ieee: New York, 2007; pp 652-655.

Mirin, N. A.; Halas, N. J., Light-Bending Nanoparticles. *Nano Letters* **2009,** 9, 1255-1259.

Nardin, A.; Abastado, J.-P., Macrophages and Cancer. *Frontiers in Bioscience* **2008,** 13, 3494-3505.

Nie, S. M., Understanding and Overcoming Major Barriers in Cancer Nanomedicine. *Nanomedicine* **2010,** 5, 523-528.

Nikoobakht, B.; El-Sayed, M. A., Preparation and Growth Mechanism of Gold Nanorods (Nrs) Using Seed-Mediated Growth Method. *Chemistry of Materials* **2003,** 15, 1957-1962.

Ntziachristos, V.; Yodh, A. G.; Schnall, M.; Chance, B., Concurrent Mri and Diffuse Optical Tomography of Breast after Indocyanine Green Enhancement. *Proceedings of the National Academy of Sciences of the United States of America* **2000,** 97, 2767-2772.

Ofir, Y.; Samanta, B.; Rotello, V. M., Polymer and Biopolymer Mediated Self-Assembly of Gold Nanoparticles. *Chem. Soc. Rev.* **2008,** 37, 1814-1825.

Oh, E.; Susumu, K.; Goswami, R.; Mattoussi, H., One-Phase Synthesis of Water-Soluble Gold Nanoparticles with Control over Size and Surface Functionalities. *Langmuir* **2010,** 26, 7604-7613.

Oh, J.; Feldman, M. D.; Kim, J.; Condit, C.; Emelianov, S.; Milner, T. E., Detection of Magnetic Nanoparticles in Tissue Using Magneto-Motive Ultrasound. *Nanotechnology* **2006,** 17, 4183-4190.

Oldenburg, S. J.; Averitt, R. D.; Westcott, S. L.; Halas, N. J., Nanoengineering of Optical Resonances. *Chemical Physics Letters* **1998,** 288, 243-247.

O'Neal, D. P.; Hirsch, L. R.; Halas, N. J.; Payne, J. D.; West, J. L., Photo-Thermal Tumor Ablation in Mice Using near Infrared-Absorbing Nanoparticles. *Cancer Letters (Amsterdam, Netherlands)* **2004,** 209, 171-176.

Onn, A.; Correa, A. M.; Gilcrease, M.; Isobe, T.; Massarelli, E.; Bucana, C. D.; O'Reilly, M. S.; Hong, W. K.; Fidler, I. J.; Putnam, J. B.; Herbst, R. S., Synchronous Overexpression of Epidermal Growth Factor Receptor and Her2-Neu Protein Is a Predictor of Poor Outcome in Patients with Stage I Non-Small Cell Lung Cancer. *Clinical Cancer Research* **2004,** 10, 136-143.

Oshannessy, D. J.; Dobersen, M. J.; Quarles, R. H., A Novel Procedure for Labeling Immunoglobulins by Conjugation to Oligosaccharide Moieties. *Immunology Letters* **1984,** 8, 273-277.

Paranjape, A. S.; Kuranov, R.; Baranov, S.; Ma, L. L.; Villard, J. W.; Wang, T.; Konstantin, S.; Feldman, M. D.; Johnston, K. P.; Milner, T. E., Depth Resolved Photothermal Oct Detection of Macrophages in Tissue Using Nanorose. *Biomedical Optics Express* **2010,** 1, 2-16.

Park, H.-Y.; Schadt, M. J.; Wang, L.; Lim, I. I. S.; Njoki, P. N.; Kim, S. H.; Jang, M.-Y.; Luo, J.; Zhong, C.-J., Fabrication of Magnetic Core@Shell Fe Oxide@Au Nanoparticles for Interfacial Bioactivity and Bio-Separation. *Langmuir* **2007,** 23, 9050-9056.

Park, J.; Joo, J.; Kwon, S. G.; Jang, Y.; Hyeon, T., Synthesis of Monodisperse Spherical Nanocrystals. *Angewandte Chemie-International Edition* **2007,** 46, 4630-4660.

Patterson, M. S.; Wilson, B. C.; Wyman, D. R., The Propagation of Optical Radiation in Tissue. Ii: Optical Properties of Tissues and Resulting Fluence Distributions. *Lasers in Medical Science* **1991,** 6, 379-390.

Pease, L. F.; Elliott, J. T.; Tsai, D. H.; Zachariah, M. R.; Tarlov, M. J., Determination of Protein Aggregation with Differential Mobility Analysis: Application to Igg Antibody. *Biotechnology and Bioengineering* **2008,** 101, 1214-1222.

Perez, J. M.; Josephson, L.; Weissleder, R., Use of Magnetic Nanoparticles as Nanosensors to Probe for Molecular Interactions. *ChemBioChem* **2004,** 5, 261-264.

Pham, T.; Jackson, J. B.; Halas, N. J.; Lee, T. R., Preparation and Characterization of Gold Nanoshells Coated with Self-Assembled Monolayers. *Langmuir* **2002,** 18, 4915-4920.

Pissuwan, D.; Valenzuela, S. M.; Killingsworth, M. C.; Xu, X.; Cortie, M. B., Targeted Destruction of Murine Macrophage Cells with Bioconjugated Gold Nanorods. *Journal of Nanoparticle Research* **2007,** 9, 1109-1124.

Pitsillides, C. M.; Joe, E. K.; Wei, X.; Anderson, R. R.; Lin, C. P., Selective Cell Targeting with Light-Absorbing Microparticles and Nanoparticles. *Biophysical Journal* **2003,** 84, 4023-4032.

Prodan, E.; Nordlander, P.; Halas, N. J., Electronic Structure and Optical Properties of Gold Nanoshells. *Nano Letters* **2003,** 3, 1411-1415.

Qian, X. M.; Peng, X. H.; Ansari, D. O.; Yin-Goen, Q.; Chen, G. Z.; Shin, D. M.; Yang, L.; Young, A. N.; Wang, M. D.; Nie, S. M., In Vivo Tumor Targeting and Spectroscopic Detection with Surface-Enhanced Raman Nanoparticle Tags. *Nature Biotechnology* **2008,** 26, 83-90.

Qu, M.; Mallidi, S.; Mehrmohammadi, M.; Ma, L. L.; Johnston, K. P.; Sokolov, K.; Emelianov, S., Combined Photoacoustic and Magneto-Acoustic Imaging. *Conf Proc IEEE Eng Med Biol Soc* **2009,** 2009, 4763-6.

Rasch, M. R.; Sokolov, K. V.; Korgel, B. A., Limitations on the Optical Tunability of Small Diameter Gold Nanoshells. *Langmuir* **2009,** 25, 11777-11785.

Reddy, S. T.; Swartz, M. A.; Hubbell, J. A., Targeting Dendritic Cells with Biomaterials: Developing the Next Generation of Vaccines. *Trends in Immunology* **2006,** 27, 573-579.

Robinson, D. R.; Wu, Y. M.; Lin, S. F., The Protein Tyrosine Kinase Family of the Human Genome. *Oncogene* **2000,** 19, 5548-5557.

Roch, A.; Gossuin, Y.; Muller, R. N.; Gillis, P., Superparamagnetic Colloid Suspensions: Water Magnetic Relaxation and Clustering. *Journal of Magnetism and Magnetic Materials* **2005,** 293, 532-539.

Ross, R., Atherosclerosis--an Inflammatory Disease. *The New England journal of medicine* **1999,** 340, 115-26.

Ryoo, W.; Webber, S. E.; Johnston, K. P., Water-in-Carbon Dioxide Microemulsions with Methylated Branched Hydrocarbon Surfactants. *Industrial & Engineering Chemistry Research* **2003,** 42, 6348-6358.

Sahoo, Y.; Goodarzi, A.; Swihart, M. T.; Ohulchanskyy, T. Y.; Kaur, N.; Furlani, E. P.; Prasad, P. N., Aqueous Ferrofluid of Magnetite Nanoparticles: Fluorescence Labeling and Magnetophoretic Control. *Journal of Physical Chemistry B* **2005,** 109, 3879-3885.

Salgueirino-Maceira, V.; Correa-Duarte, M. A.; Farle, M.; Lopez-Quintela, A.; Sieradzki, K.; Diaz, R., Bifunctional Gold-Coated Magnetic Silica Spheres. *Chemistry of Materials* **2006,** 18, 2701-2706.

Shah, J.; Park, S.; Aglyamov, S.; Larson, T.; Ma, L.; Sokolov, K.; Johnston, K.; Milner, T.; Emelianov Stanislav, Y., Photoacoustic Imaging and Temperature Measurement for Photothermal Cancer Therapy. *Journal of biomedical optics* **2008,** 13, 034024.

Shah, J.; Park, S.; Aglyamov, S.; Larson, T.; Ma, L.; Sokolov, K.; Johnston, K.; Milner, T. E.; Emelianov, S. Y., Photoacoustic Imaging and Temperature Measurement for Photothermal Cancer Therapy. *J. Biomed. Opt.* **2008,** 13, 034024.

Shaw, C. F., III, Gold-Based Therapeutic Agents. *Chem. Rev.* **1999,** 99, 2589-2600.

Shen, T.; Weissleder, R.; Papisov, M.; Bogdanov, A., Jr.; Brady, T. J., Monocrystalline Iron Oxide Nanocompounds (Mion): Physicochemical Properties. *Magnetic Resonance in Medicine* **1993,** 29, 599-604.

Shevchenko, E. V.; Bodnarchuk, M. I.; Kovalenko, M. V.; Talapin, D. V.; Smith, R. K.; Aloni, S.; Heiss, W.; Alivisatos, A. P., Gold/Iron Oxide Core/Hollow-Shell Nanoparticles. *Advanced Materials (Weinheim, Germany)* **2008,** 20, 4323-4329.

Shi, W.; Zeng, H.; Sahoo, Y.; Ohulchanskyy, T. Y.; Ding, Y.; Wang, Z. L.; Swihart, M.; Prasad, P. N., A General Approach to Binary and Ternary Hybrid Nanocrystals. *Nano Letters* **2006,** 6, 875-881.

Skrabalak, S. E.; Au, L.; Li, X.; Xia, Y., Facile Synthesis of Ag Nanocubes and Au Nanocages. *Nature Protocols* **2007,** 2, 2182-2190.

Skrabalak, S. E.; Chen, J.; Au, L.; Lu, X.; Li, X.; Xia, Y., Gold Nanocages for Biomedical Applications. *Advanced Materials (Weinheim, Germany)* **2007,** 19, 3177-3184.

Smith, W. E.; Zukoski, C. F., Hard Structured Particles: Suspension Synthesis, Characterization, and Compressibility. *Langmuir* **2004,** 20, 11191-11200.

Sokolov, K.; Follen, M.; Aaron, J.; Pavlova, I.; Malpica, A.; Lotan, R.; Richards-Kortum, R., Real-Time Vital Optical Imaging of Precancer Using Anti-Epidermal Growth Factor Receptor Antibodies Conjugated to Gold Nanoparticles. *Cancer Research* **2003,** 63, 1999-2004.

Stewart, M. E.; Anderton, C. R.; Thompson, L. B.; Maria, J.; Gray, S. K.; Rogers, J. A.; Nuzzo, R. G., Nanostructured Plasmonic Sensors. *Chemical Reviews* **2008,** 108, 494-521.

Talapin, D. V.; Rogach, A. L.; Haase, M.; Weller, H., Evolution of an Ensemble of Nanoparticles in a Colloidal Solution: Theoretical Study. *Journal of Physical Chemistry B* **2001,** 105, 12278-12285.

Tam, J. M.; Tam, J. O.; Murthy, A.; Ingram, D. R.; Ma, L. L.; Travis, K.; Johnston, K. P.; Sokolov, K. V., Controlled Assembly of Biodegradable Plasmonic Nanoclusters for near-Infrared Imaging and Therapeutic Applications. *Acs Nano* **2010,** 4, 2178-2184.

Tong, G. J.; Hsiao, S. C.; Carrico, Z. M.; Francis, M. B., Viral Capsid DNA Aptamer Conjugates as Multivalent Cell-Targeting Vehicles. *Journal of the American Chemical Society* **2009,** 131, 11174-11178.

Urbanska, K.; Romanowska-Dixon, B.; Matuszak, Z.; Oszajca, J.; Nowak-Sliwinska, P.; Stochel, G., Indocyanine Green as a Prospective Sensitizer for Photodynamic Therapy of Melanomas. *Acta Biochimica Polonica* **2002,** 49, 387-391.

Wang, A. Z.; Bagalkot, V.; Vasilliou, C. C.; Gu, F.; Alexis, F.; Zhang, L.; Shaikh, M.; Yuet, K.; Cima, M. J.; Langer, R.; Kantoff, P. W.; Bander, N. H.; Jon, S.; Farokhzad, O. C., Superparamagnetic Iron Oxide Nanoparticle-Aptamer Bioconjugates for Combined Prostate Cancer Imaging and Therapy. *ChemMedChem* **2008,** 3, 1311-1315.

Wang, H.; Brandl, D. W.; Le, F.; Nordlander, P.; Halas, N. J., Nanorice: A Hybrid Plasmonic Nanostructure. *Nano Letters* **2006,** 6, 827-832.

Wang, H.; Brandl, D. W.; Nordlander, P.; Halas, N. J., Plasmonic Nanostructures: Artificial Molecules. *Accounts of Chemical Research* **2007,** 40, 53-62.

Wang, H.; Goodrich, G. P.; Tam, F.; Oubre, C.; Nordlander, P.; Halas, N. J., Controlled Texturing Modifies the Surface Topography and Plasmonic Properties of Au Nanoshells. *Journal of Physical Chemistry B* **2005,** 109, 11083-11087.

Wang, H.; Huff, T. B.; Zweifel, D. A.; He, W.; Low, P. S.; Wei, A.; Cheng, J.-X., In Vitro and in Vivo Two-Photon Luminescence Imaging of Single Gold Nanorods. *Proceedings of the National Academy of Sciences of the United States of America* **2005,** 102, 15752-15756.

Wang, L.; Luo, J.; Fan, Q.; Suzuki, M.; Suzuki, I. S.; Engelhard, M. H.; Lin, Y.; Kim, N.; Wang, J. Q.; Zhong, C.-J., Monodispersed Core-Shell Fe3o4@Au Nanoparticles. *Journal of Physical Chemistry B* **2005,** 109, 21593-21601.

Wang, L.; Park, H.-Y.; Lim, S. I. I.; Schadt, M. J.; Mott, D.; Luo, J.; Wang, X.; Zhong, C.-J., Core@Shell Nanomaterials: Gold-Coated Magnetic Oxide Nanoparticles. *Journal of Materials Chemistry* **2008,** 18, 2629-2635.

Wang, S. P.; Mamedova, N.; Kotov, N. A.; Chen, W.; Studer, J., Antigen/Antibody Immunocomplex from Cdte Nanoparticle Bioconjugates. *Nano Letters* **2002,** 2, 817-822.

Wang, W., Protein Aggregation and Its Inhibition in Biopharmaceutics. *International Journal of Pharmaceutics* **2005,** 289, 1-30.

Wang, Y.; Xie, X.; Wang, X.; Ku, G.; Gill, K. L.; O'Neal, D. P.; Stoica, G.; Wang, L. V., Photoacoustic Tomography of a Nanoshell Contrast Agent in the in Vivo Rat Brain. *Nano Letters* **2004,** 4, 1689-1692.

Wang, Z.; Zhang, J.; Ekman, J. M.; Kenis, P. J. A.; Lu, Y., DNA-Mediated Control of Metal Nanoparticle Shape: One-Pot Synthesis and Cellular Uptake of Highly Stable and Functional Gold Nanoflowers. *Nano Letters* **2010,** 10, 1886-1891.

Watzky, M. A.; Finke, R. G., Transition Metal Nanocluster Formation Kinetic and Mechanistic Studies. A New Mechanism When Hydrogen Is the Reductant: Slow, Continuous Nucleation and Fast Autocatalytic Surface Growth. *Journal of the American Chemical Society* **1997,** 119, 10382-10400.

Weissleder, R., A Clearer Vision for in Vivo Imaging. *Nature Biotechnology* **2001,** 19, 316-317.

Weissleder, R., Molecular Imaging in Cancer. *Science* **2006,** 312, 1168-1171.

Westcott, S. L.; Oldenburg, S. J.; Lee, T. R.; Halas, N. J., Construction of Simple Gold Nanoparticle Aggregates with Controlled Plasmon-Plasmon Interactions. *Chemical Physics Letters* **1999,** 300, 651-655.

Wilson, B. C.; Patterson, M. S.; Flock, S. T., Indirect Versus Direct Techniques for the Measurement of the Optical Properties of Tissues. *Photochemistry and photobiology* **1987,** 46, 601-8.

Wu, D. J.; Xu, X. D.; Liu, X. J., Influence of Dielectric Core, Embedding Medium and Size on the Optical Properties of Gold Nanoshells. *Solid State Communications* **2008,** 146, 7-11.

Xia, Y.; Xiong, Y. J.; Lim, B.; Skrabalak, S. E., Shape-Controlled Synthesis of Metal Nanocrystals: Simple Chemistry Meets Complex Physics? *Angewandte Chemie-International Edition* **2009,** 48, 60-103.

Xu, Z.; Hou, Y.; Sun, S., Magnetic Core/Shell Fe3o4/Au and Fe3o4/Au/Ag Nanoparticles with Tunable Plasmonic Properties. *Journal of the American Chemical Society* **2007,** 129, 8698-8699.

Yang, X.; Skrabalak, S. E.; Li, Z.-Y.; Xia, Y.; Wang, L. V., Photoacoustic Tomography of a Rat Cerebral Cortex in Vivo with Au Nanocages as an Optical Contrast Agent. *Nano Letters* **2007,** 7, 3798-3802.

Yin, Y.; Alivisatos, A. P., Colloidal Nanocrystal Synthesis and the Organic-Inorganic Interface. *Nature* **2005,** 437, 664-670.

Yu, H.; Chen, M.; Rice, P. M.; Wang, S. X.; White, R. L.; Sun, S. H., Dumbbell-Like Bifunctional Au-Fe3o4 Nanoparticles. *Nano Letters* **2005,** 5, 379-382.

Zeng, H.; Sun, S., Syntheses, Properties, and Potential Applications of Multicomponent Magnetic Nanoparticles. *Advanced Functional Materials* **2008,** 18, 391-400.

Zhang, J.; Sasaki, K.; Sutter, E.; Adzic, R. R., Stabilization of Platinum Oxygen-Reduction Electrocatalysts Using Gold Clusters. *Science* **2007,** 315, 220-222.

Zhang, J.; Tang, Y.; Weng, L.; Ouyang, M., Versatile Strategy for Precisely Tailored Core@Shell Nanostructures with Single Shell Layer Accuracy: The Case of Metallic Shell. *Nano Letters* **2009,** 9, 4061-4065.

Zhang, Q.; Ge, J.; Goebl, J.; Hu, Y.; Sun, Y.; Yin, Y., Tailored Synthesis of Superparamagnetic Gold Nanoshells with Tunable Optical Properties. *Advanced Materials (Weinheim, Germany)* **2010,** 22, 1905-1909.

Zhang, Z.; Horsch, M. A.; Lamm, M. H.; Glotzer, S. C., Tethered Nano Building Blocks: Toward a Conceptual Framework for Nanoparticle Self-Assembly. *Nano Letters* **2003,** 3, 1341-1346.

Zhao, L.; Ji, X.; Sun, X.; Li, J.; Yang, W.; Peng, X., Formation and Stability of Gold Nanoflowers by the Seeding Approach: The Effect of Intraparticle Ripening. *Journal of Physical Chemistry C* **2009,** 113, 16645-16651.

Zharov, V. P.; Kim, J.-W.; Curiel, D. T.; Everts, M., Self-Assembling Nanoclusters in Living Systems: Application for Integrated Photothermal Nanodiagnostics and Nanotherapy. *Nanomedicine* **2005,** 1, 326-345.